High Resolution 3D Functional Anatomy Database of the Kidney

Dissertation

zur

Erlangung der naturwissenschaftlichen Doktorwürde
(Dr. sc. nat.)

vorgelegt der

Mathematisch-naturwissenschaftlichen Fakultät

der

Universität Zürich

von

Willy Kuo

von

Regensdorf ZH

Promotionskommission

Prof. Dr. Vartan Kurtcuoglu (Leitung der Dissertation)

Prof. Dr. Bert Klaus Rainer Müller

Prof. Dr. Roland Hugo Wenger

Dr. Simone Elke Hieber

Zürich, 2019

TABLE OF CONTENTS

1 Abstract

The kidney is the organ responsible for blood filtration and is supplied with blood independently of its oxygen demand. This project was embedded in an overarching research initiative to investigate the properties and behavior of oxygen distribution of the kidney and its effects on oxygen-dependent mechanisms. Computational modeling of oxygen transport and distribution in the murine kidney requires detailed three-dimensional (3D) structural data of blood vessels, the main oxygen suppliers, and tubules, the main oxygen consumers. In order to provide these data on the whole kidney level, vascular casting protocols for X-ray microcomputed tomography imaging were developed. Mouse kidneys were subsequently imaged at synchrotron radiation facilities to acquire vascular and tubular structure datasets with full capillary resolution. Image processing and segmentation was performed on the resulting terabyte-scale dataset using high performance computing clusters, building the first 3D atlas of the vascular and tubular structure of a whole mouse kidney.
To make the process more widely accessible, a cross-linkable, polymeric X-ray contrast agent was developed and used for combined vascular and tubular imaging with widely available laboratory X-ray source micro-CT equipment, which was previously reserved to synchrotron radiation facilities. Vascular and tubular structures were segmented in a simplified workflow based on free software and workstation-grade hardware.

2 Acknowledgements

First I would like to thank my main supervisors, Prof. Vartan Kurtcuoglu and Prof. Bert Müller, for giving me the opportunity to work on this challenging interdisciplinary project, as well as doctoral committee members Prof. Roland Wenger and Simone Hieber for their support and advice.

In the Interface Group, I would like to especially thank the contributors to the project: Anastasios Marmaras for getting me started on transcardial perfusions and infrastructure in general, Virginia Meskenaite for further advice and help with perfusion work, Ufuk Olgaç and Kartik Jain for their work on computational modelling on oxygen transport, and Diego Rossinelli for his work on large scale data processing and modelling.

I would also like to thank Georg Schulz, Griffin Rodgers, Christos Bikis, Hans Deyhle, Peter Thalmann and Anna Khimchenko of the Biomaterials Science Center of the University of Basel for all the discussions and work concerning μCT imaging.

In the University of Zurich, I would like to thank Karen Scholz and Sophie Dahl of the Institute of Physiology for the collaboration on renal erythropoietin producing cells, and Svende Pfundstein for keeping me well supplied with research materials.

In the Department of Chemistry, I would like to thank Phuc Ung and Prof. Gilles Gasser for their help during the initial attempts at synthesizing the first versions of XlinCA, and Ngoc An Le and Prof. Bernhard Spingler for their work on developing the final version.

I would also like to thank José María Mateos Melero and Evgenia Platonova for their work on the Tissue Clearing Platform at the Center for Microscopy and Image Analysis, Jan Czogalla of the Institute of Anatomy for teaching me how to do abdominal aorta perfusions, Axel Lang and Eric Meyer for their support for the PU4ii vascular casting resin, and Àlvaro Gomariz Carrillo and César Nombela Arrieta of the Experimental Hematology Lab for their work on spatial point pattern analysis.

I would further like to extend my thanks to Alexander Rack, Margie Olbinado and Paul Tafforeau for their support during our ESRF beamtimes, Christoph Rau, Marie-Christine Zdora, Malte Storm, Shashidhara Marathe, Andrew Bodey, Silvia Cipiccia and Kaz Wanelik for their support during our Diamond Light Source beamtimes, and Felix Beckmann and Alexander Hipp for their support during our DESY beamtime.

And last but not least, I would like thank all colleagues in the Interface Group, the Institute of Physiology, the Biomaterials Science Center, the NCCR Kidney.ch as well as my friends and family for their friendship and support, which helped me to keep up the enjoyment of my work from the beginning all the way to the end.

3 Introduction

3.1 What is high resolution?

"For me, high resolution means 10 meters."

- *Gerrit Kuhlmann, speaking about imaging from satellites and airplanes* [1]

High resolution has become somewhat a buzzword, used to sell cell phones and cameras as well as scientific imaging equipment and methods. As the above quote illustrates however, context is important. Imaging of a 1 cm mouse kidney with 10 meter resolution is generally not considered high resolution, but this is different when imaging a 10 km × 10 km area. As such, the size of the field of view, the area or volume of the image, is important context when discussing high resolution imaging methods.

The first question that needs to be cleared is the minimum resolution necessary to capture the feature of interest. Capillaries in a mouse kidney are about 4 µm in diameter [2]. This disqualifies imaging methods such as magnetic resonance imaging or ultrasound imaging, which cannot achieve this resolution regardless of the size of the field of view.

On the other end of the spectrum, techniques such as electron microscopy or X-ray ptychography are capable of achieving nanometer-scale resolutions and are well capable of resolving 4 µm capillaries. They would however take an impractically long time to image a mouse kidney, which is typically about 1 cm in length, and the processing of the resulting petabyte-scale datasets is not feasible in practice with current technology.

In order to provide full 3D imaging with capillary resolution on a scale of a whole mouse kidney, there are two imaging methods that were considered as the only feasible ones: 3D light microscopy and X-ray microcomputed tomography.

3.2 The difference between resolution and pixel size

Resolution and pixel size are two terms in digital imaging that are often used interchangeably in general conversation, despite being two distinct concepts and never having the same value in a given image.
Resolution is defined as the minimum distance two objects or features can be apart from each other, so that the imaging method used can still resolve them as two distinct objects, as opposed to blurring together into one indistinct object. Pixel size on the other hand represents the distance between two sampling points of the recording equipment. If the recording equipment is a camera chip, this could mean the size of the light-gathering area on the chip that can be read out as one distinct pixel.

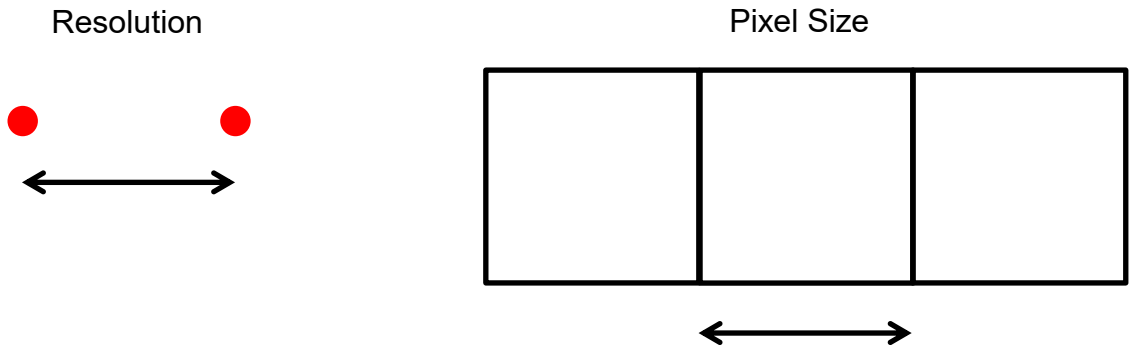

Fig. 1.: Difference between resolution and pixel size

While this distinction may seem academic at first glance, there is a large difference between the two. As an example, two photos of the lunar eclipse on the 28th of September 2015 are shown in Fig. 2, both featuring the same pixel size.

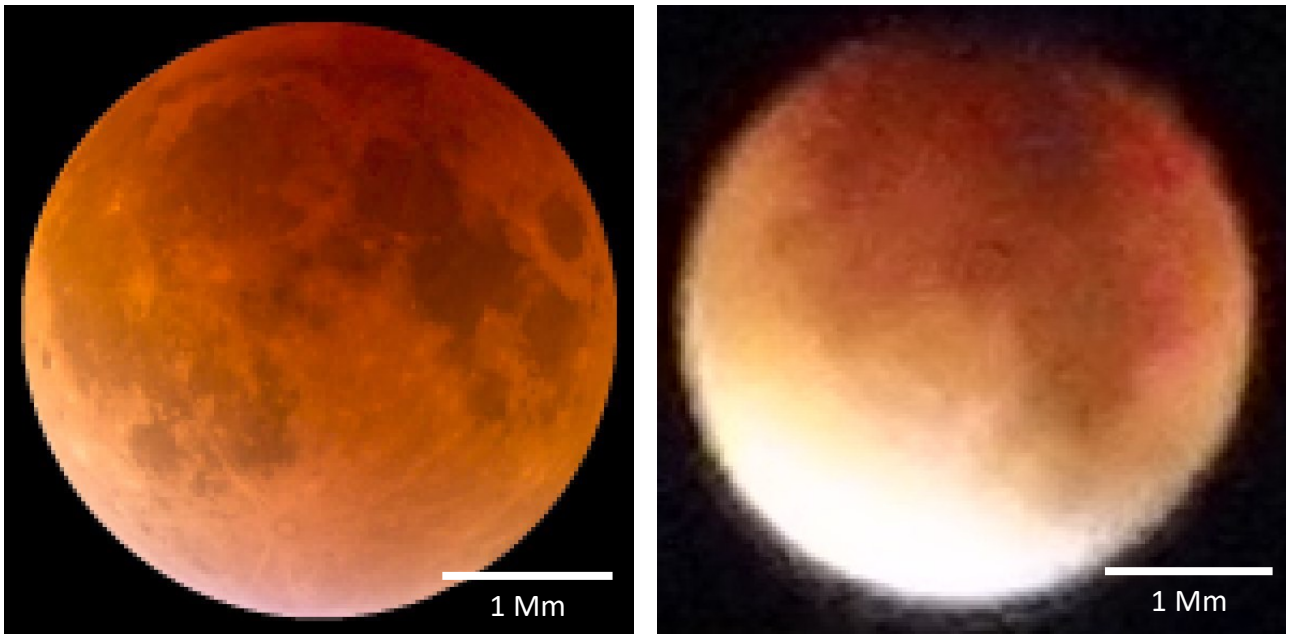

Fig. 2.: Left: Image of the lunar eclipse, downsampled to match the pixel size of the photo on the right. Adapted from a photo taken by Alfredo Garcia Jr., licensed under the terms of the CC BY-SA 2.0. Right: Photo taken by Willy Kuo with a compact camera.

As should be immediately visible, the two photos do not feature the same resolution. The resolution can be affected negatively by factors completely independent of pixel size. In the case of visible light optics, this will be elaborated on in the chapter about light microscopes.

In cases where optics or other factors do not limit the resolution, pixel size can become the limiting factor. However, even in those cases, the two terms cannot be used interchangeably. In fact, they can never have the same value at all. If the pixel size were chosen to be the same as the distance of the two objects to be resolved, the resulting pixel matrix would not be able to show these as two distinct objects, as is shown in Fig. 3.

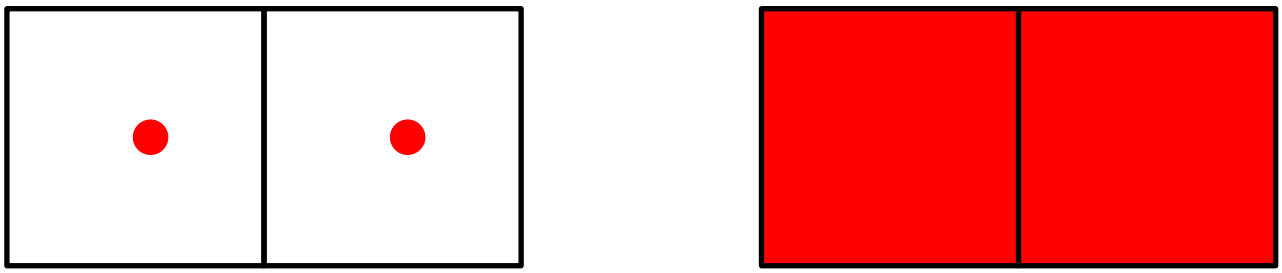

Fig. 3.: Left: Two well resolved red dots. Black squares representing pixels of the same size as the distance between the dots are drawn around them. Right: The same two objects, as they would be represented in a digital image with pixel size equal to the distance between the objects.

To distinguish the two features, there is another pixel in-between required, representing the gap between the two objects.

Fig. 4.: Left: Two well resolved red dots. Squares representing pixels of half the size of the distance between the dots are drawn around them. Right: The same two objects, as they would be represented in a digital image with pixel size half the distance between the objects.

This means that the pixel size needs to be chosen to be less than half the size of the distance between objects that need to be resolved. Exactly half the size would be insufficient, as can be illustrated by the example shown in Fig. 5. In that case, it may be possible for two objects to lie exactly in the middle between two pixels, splitting their contribution to each pixel exactly in half. This would result in an unresolved single object at half intensity.

Fig. 5.: Demonstration of the special case where well resolved dots lie exactly in the middle of two pixels.

This explanation is a descriptive explanation in the special case of digital imaging. The more general mathematical concept [3], which can be applied to any type of signal sampling, is called the Nyquist-Shannon sampling.

3.3 Visible light microscopy

Light microscopes rely on refracting visible light with a lens in order to magnify microscopic features, allowing detection by more coarse sensors, such as camera chips with pixel sizes of tens of micrometers or the human eyeball. There are a variety of different microscopes available, with their own strengths and weaknesses, which are correspondingly used in different applications [4].

3.3.1 Bright-field microscopy

Bright-field microscopy illuminates a sample from the back with white light, and the image is formed by the attenuation of light by the sample. It could also be more descriptively called transmission light microscopy. Bright-field microscopy can only be used on thin or transparent samples that allow sufficient light to be transmitted through the sample. To distinguish different types of soft tissue, which typically have very similar attenuation regardless of their biological composition, a variety of different stains is applied to mark different biological features with different colors. The standard staining protocol is based on hematoxylin and eosin (HE), where hematoxylin stains primarily nuclei and eosin adheres to positively charged molecules, such as proteins with free amine groups.

3.3.2 Fluorescence microscopy

Fluorescence microscopy in contrast does not produce signal directly based on the amount of attenuation incurred by transmitted light, but rather makes use of the wavelength-specific differences in absorption and emission of light. If a molecule is hit by light, the electrons within that molecule can get excited to a higher energy state by absorbing that energy. Since only specific, discrete energy states exist, only discrete transitions are possible. The energy delivered needs to match the energy required to make the transition from one energy state to another. The energy delivered by light is wavelength-specific and the energy difference between electron energy states is molecule-specific. The excited electron can return to its previous, lower energy ground state by emitting light. Since some energy is lost in this process, the emitted light is lower in energy and thus longer in wavelength than the absorbed light.

3.3.3 Diffraction limit and resolution

Resolution of a digital image can be limited by factors independent of the pixel size. In microscopy, the resolution is further limited by the properties of the optical lenses used for magnification. The magnified image arriving at the eye or the camera chip is not perfectly corresponding to the smaller image captured at the sample. If we captured an idealized, infinitely small point, this point would be shown as a much larger, blurred point with fringes around it after magnification by the lens. This pattern, referred to as the point spread function or Airy disk, is caused by interference of the light passing the optical lenses, and limits the resolution achievable by an optical microscope. It is accordingly named the diffraction limit, and depends on the wavelength of the refracted light and the numerical aperture of the objective lens.

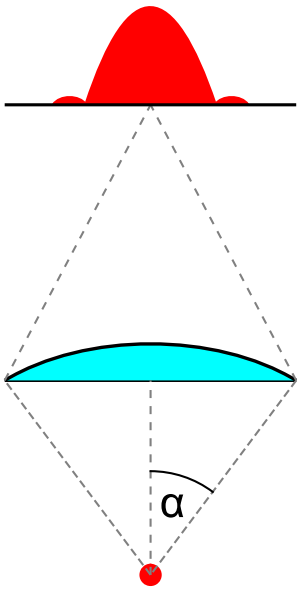

Fig. 6.: Schematic representation of the diffraction pattern of a theoretical infinitesimally small point at the focal spot.

The numerical aperture is a property of the objective lens and a measure independent of the magnification. It is determined by the refractive index of the immersion medium n and the sine of the angle α from the focal point containing the radius of the lens, as shown in Fig. 6. This means that oil immersion objectives (n = 1.5) can achieve higher numerical apertures than water (n = 1.3) or air (n = 1.0) objectives. It also means that objectives with larger working distances, which means the distance between the focal point and the lens, have a lower α and thus a lower numerical aperture.

$$NA = n\,sin\alpha$$

In practical terms, the magnification determines the pixel size, while the numerical aperture determines the diffraction limit. Both numbers are typically indicated next to each other on microscope objectives, separated by a slash (e.g. 40×/1.4). The formula to calculate the diffraction limit according to Abbe takes the form of:

$$R = 0.5\,\frac{\lambda}{NA}$$

R is the resolution, λ the wavelength of the light, and NA the numerical aperture. The constant factor of 0.5 is dependent on which exact diffraction limit formula is used. The Abbe limit uses 0.5 as a

factor and was determined by empirical observation. The Rayleigh limit uses a higher value of 0.61 and is defined as the distance at which the maximum of the point spread function of the one object coincides with the first minimum in the point spread function of the other. The Sparrow limit has a factor of 0.47 and marks the distance at which there is no longer a local minimum in-between the two point spread functions, which can then no longer be separated into two distinct peaks.

Typical values for the diffraction limit according to Abbe for microscopes using ultraviolet to visible light (400 – 700 nm) with low-working distance oil objectives (NA = 1.4) would therefore be 143 – 250 nm, more than enough to resolve capillaries.

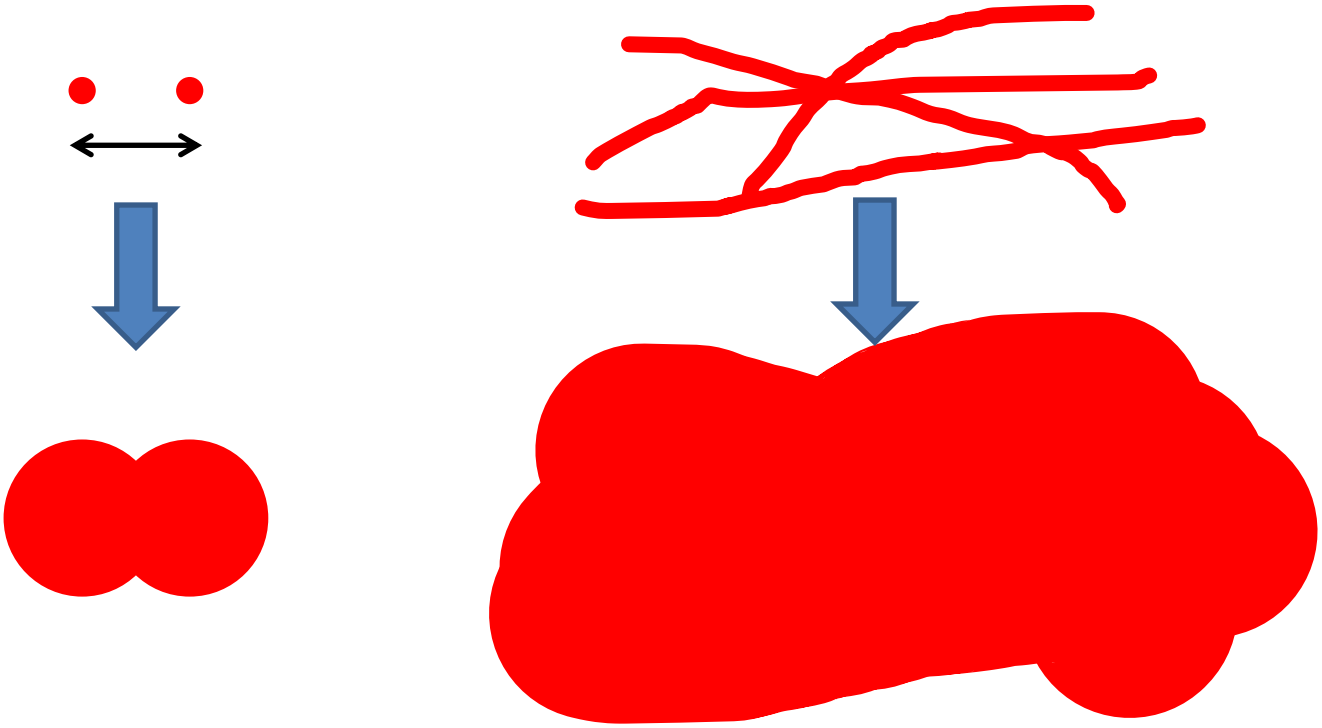

Fig. 7.: Schematic view exemplifying the effects of the diffraction limit on the image quality of round and fibrous features.

3.3.4 Deconvolution

Mathematically, the transformation of the original image into the diffraction image is a convolution of the original image with the point spread function. Since the point spread function of a microscope can either be measured with small fluorescent beads or calculated based on known optical properties of a microscope, deconvolution with this point spread function can be used to reconstruct the original image. Software using iterative algorithms to do this are available. In practice, to make use of such software, images should be sampled well above the normal rate of > 2 times the resolution. For the Huygens Deconvolution software (Scientific Volume Imaging B.V., Netherlands) for example, a pixel size of more than 4 times smaller than the corresponding Abbe refraction limit is recommended.

3.3.5 Aberrations

Quality in microscopy images is further limited by a variety of aberrations. In well corrected objectives, their impact should be minimal on qualitative imaging. However, if highly quantitative imaging or artifact-free imaging are required, these aberrations need to be taken into account and

potentially optimized against. What follows is not an exhaustive list, but a selection of common, high impact aberrations that can be reduced by taking corrective actions.

3.3.5.1 Chromatic aberration

Refraction is wavelength dependent. In an optical lens, longer wavelength light is refracted less than shorter wavelength light, which results in a difference in focal spot location. Additional lenses with different refractive indices are employed by microscope objective manufacturers to correct for this, but corrections can never be entirely perfect and not all objectives feature the same degree of correction, such as the tunable lens employed in the Zurich mesoSPIM. Chromatic aberration can be corrected for to some degree with post-processing, such as deconvolution, and is especially important to correct in colocalization experiments.

3.3.5.2 Spherical aberration

Spherical aberration occurs when the light passing the lens is not perfectly focused to the same spot depending on the light path taken. While this may be the result of imperfections in the lens shape, which is the source for the name, in practice spherical aberration is mainly caused by light scattering objects in the light path, such as thick samples or even the cover slip. Microscope lenses are typically corrected for cover slips of a specific thickness, and using cover slips of the wrong thickness or forgoing them altogether may lead to spherical aberration. The cover slip thickness to use with a given objective is typically indicated on the objective (i.e. 0.17).
Objectives designed to be used with thick materials, such as cleared tissue, may feature a correction collar, which allows the lens to be set to a specific degree of light scattering. This correction collar allows for individual adjustments for different cover slip thicknesses, different sample types and different imaging depths within a sample.

3.3.5.3 Vignetting

Vignetting is characterized by a lower intensity signal towards the edge of the field of view in a microscope. This is due to the lower amount of light gathered at the edge of the objective lens, where light that should contribute to the signal at that location passes by the objective uncollected instead. Vignetting can be compensated for by flat-field correction, which means recording a completely homogeneous object beforehand and scaling the microscopy images accordingly. While flat-field correction can correct the absolute intensity signal of an image, it cannot compensate for the lower amount of photons gathered in those regions. As a result, the signal-to-noise ratio at the edge of the image will still be diminished compared to its center.

3.3.5.4 Geometric distortion

Geometric distortion occurs when the image geometry is not accurately captured by the optics. This distortion is most obvious when looking at a grid of straight lines, such as the ones employed in manual cell counting. In pincushion and barrel distortions, which are the most common geometric distortions, lines that should be straight will appear bent, especially at the edges of the image, as can be seen in Fig. 8.

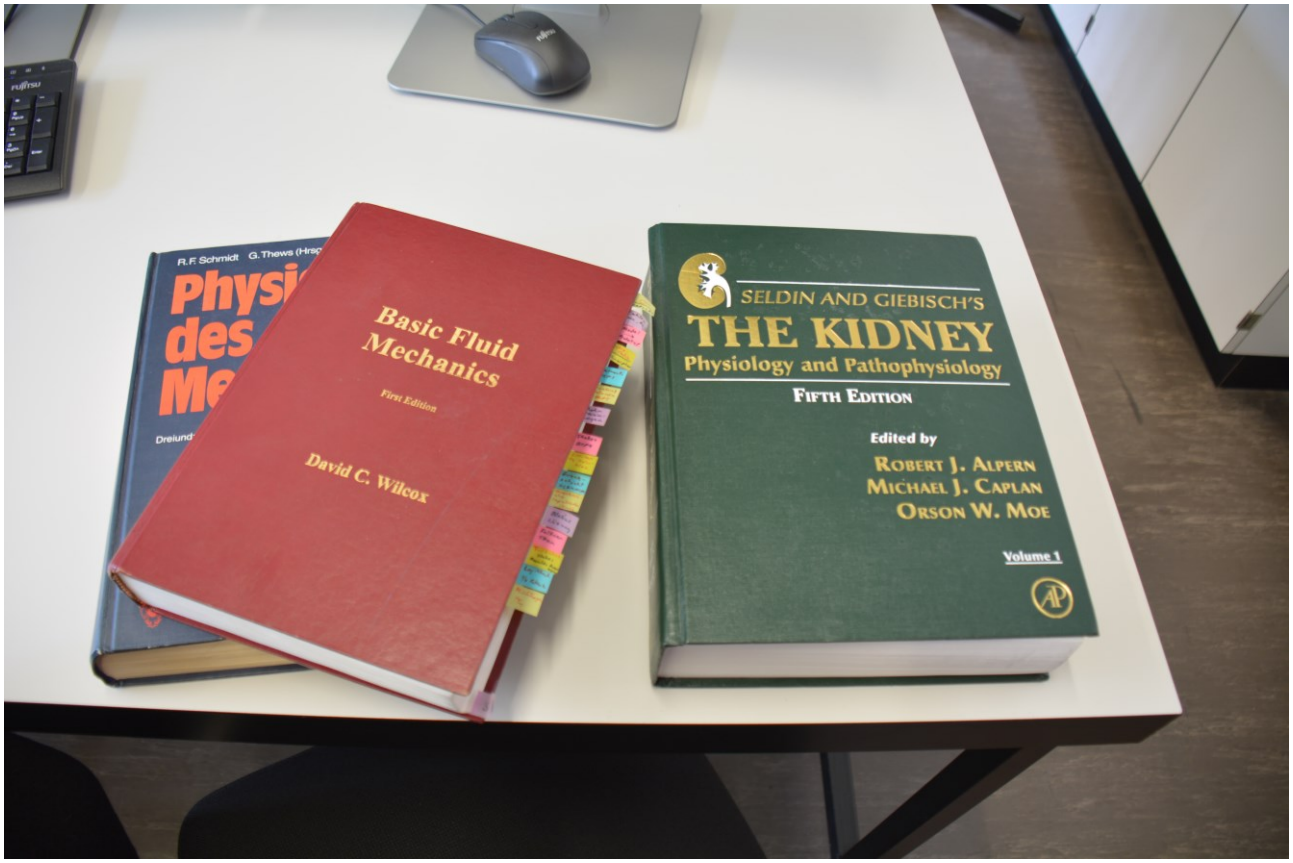

Fig. 8.: Photograph featuring barrel distortion. The straight edges of the table appear bent due to the geometric distortion.

3.4 Light microscopes

3.4.1 Widefield microscope

Advantage: Speed
Disadvantage: No restriction of out-of-focus light
Main application: 2D imaging of sections

In a widefield microscope, a large area of a sample is recorded at once with a camera chip. The main advantage is the fast acquisition enabled by such imaging. The main disadvantage is that all light coming from the sample is gathered, regardless of whether it is coming from the focal plane or not. Light coming from parts of the sample above or below the focal plane, and therefore out of focus, will contribute their blurred signal to the final image and reduce resolution accordingly. Widefield microscopy is therefore only suitable for thin sections, as is bright-field microscopy, which may lead to some people confusing these two terms. Bright-field microscopy refers to the illumination scheme used and is indeed performed with widefield microscopes. The reverse does not apply however: Widefield microscopes can also be used in fluorescence imaging, if they are equipped with the appropriate wavelength light sources and color filters.

3.4.2 Confocal microscope

Advantage: Best resolution in Z
Disadvantage: Slow
Main application: High quality optical sections, 3D imaging

A confocal microscope reduces the blurring introduced by out-of-focus light by introducing a pinhole to block any light not coming from the focal point of the lens. This includes light coming from above and below the focal plane, which gives confocal microscopy better resolution in the Z-dimension, enabling optical sectioning and thus 3D imaging. The fluorescent illumination of a confocal microscope is focused through the same lens onto the focal point, giving the confocal microscope its name.

The confocal microscope, by its very nature, can only record a single point at once instead of an entire area like a widefield microscope. This point needs to be swept across the entire measurement area to record every pixel of the final image individually. As a consequence, recordings with a confocal microscope take considerably longer than they do for a widefield microscope. On the flip side, larger, more sensitive detectors such as photomultiplier tubes can be installed, since the size of an individual pixel on the camera chip is of no consideration in this point-scanning based method.

3.4.3 Spinning disk microscope

Hybrid between widefield and confocal microscope

A spinning disk microscope shares the concept of using a pinhole to restrict out-of-focus light with a confocal microscope. To increase the scan speed, it makes use of multiple pinholes at once, which are mounted as a perforated disk. By spinning this disk, these multiple pinholes are continuously swept across the scan area, which is recorded by a camera chip. In essence, the spinning disk microscope parallelizes the concept of the confocal microscope by installing moving pinholes into a widefield microscope. This increase in speed comes at a cost however. The detector needs to be a pixel array and thus a camera chip instead of a photomultiplier tube, and out-of-focus light from neighboring pinholes can hit the detector, resulting in a lower image quality compared to a confocal microscope.

3.4.4 Two-photon microscope / multiphoton microscope

Advantage: Depth penetration
Disadvantage: Slow
Main application: Deep 3D imaging of thick samples, in vivo imaging

Excitation by a fluorescent molecule in normal fluorescence microscopy is achieved by using light of the wavelength at which the energy of a photon matches the energy required for exciting an electron of the fluorescent molecule. In a two-photon microscope, the same excitation is achieved by two photons, each delivering one half of the required energy at the same time. Since this is a rare occurrence compared to single-photon excitation, only a very small fraction of the incident light will be able to excite a fluorophore. This means that a very high local photon flux is required to give useful amounts of excitation, which is only achieved in the focal point. As the focal point is therefore the only region where fluorophores are excited, two-photon microscopy is another point-scanning technique like confocal microscopy. In contrast to confocal microscopy however, it is the excitation that is restricted to the focal point, and not the collection of emitted light. In two-photon microscopy, all emitted light can be collected, even out of focus light, since the point of origin is well defined.
The main benefit of the multiphoton microscopes is based in the phenomenon that longer wavelength light is scattered less than shorter wavelength light. The double wavelength light of the two-photon microscope can therefore remain coherent and remain focused on a focal point to greater depths within light scattering samples, such as in-vivo tissue or cleared thick organs. Since the fluorescence signal can be collected as a whole without need for focusing, light scattering of the emitted shorter wavelength light is of lesser concern.

3.4.5 Lightsheet microscope / selective plane illumination microscope

Advantage: Speed
Disadvantage: Lightsheet shape highly dependent on sample light scattering
Main application: Fast 3D imaging

Lightsheet microscopy is a wide-field technique, but to increase the resolution in depth and allow 3D imaging, the light coming from above or below the focal plane is restricted by only illuminating the focal plane, giving the technique its names. This is achieved with optical lenses shaping an excitation laser beam into the required sheet or a plane-shaped beam. Since light scattering in the sample distorts the shape of the excitation light from its ideal sheet-like structure, this method is restricted to highly transparent samples, such as zebrafish larvae or cleared tissue, which will be elaborated upon in the next chapter.
The main advantage over the other 3D light microscopy techniques, specifically confocal microscopy and multiphoton microscopy, lies in the acquisition speed. As a widefield technique, an entire area is acquired at once instead of only a single point. As an example, we estimated the required scan time for imaging a whole mouse kidney with a multiphoton microscope to be about 200 days, and only one day with a lightsheet microscope. This comes at the cost of image quality however, since perfect plane-like illumination cannot be achieved due to the limitations of the optics and the light scattering in the sample.

3.5 Tissue clearing

What makes tissue non-transparent? One the one hand, simply looking at any tissue by eye, such as the hand, clearly shows that light does not pass easily through the tissue. On the other hand, unstained tissue sections appear entirely transparent under a bright-field microscope.
On the most fundamental level, lack of transparency is due to a lack of light rays passing through the sample and arriving at the eye. This can happen due to absorption, where the light gets absorbed by the sample matter and converted into a different form of energy, such as heat. It can also happen due to refraction, where the light gets deviated from its straight path and does not hit the retina.
Tissue clearing as a technique relies on the phenomenon that most of the tissue's lack of transparency is due to refraction. Every phospholipid bilayer of a cell or organelle membrane in the body creates a refracting lipid-water interface.
To reduce light scattering and increase the transparency of tissue, a large variety of tissue clearing techniques have been developed. Several different strategies are employed by different techniques to achieve that goal. Most of the below information was taken from the review by Richardson and Lichtman published in Cell in 2015 [5].

3.5.1 Solvent-based clearing methods

Solvent-based clearing methods first dehydrate the tissue and then immerse it in a more hydrophobic medium, which dissolves the lipid bilayers. The solvents also feature high refractive indices which are closer to the refractive index of the remaining tissue, which reduces light scattering due to the smaller mismatch of refractive indices at the remaining interfaces. At 1.55, the refractive index is also close to the refractive index of cover slips and immersion oil, allowing for higher numerical apertures in the objectives used. The main drawback of those hydrophobic solvents is that they denature proteins. This can destroy antigens which would be recognized by antibodies in immunofluorescence and also makes the methods unsuitable for imaging of fluorescent proteins, which lose their fluorescence when denatured.

3.5.2 Aqueous clearing methods

To address this, other methods primarily aimed at preserving fluorescent proteins exist, which take care to retain an aqueous environment throughout the protocol. As a trade-off, they have a more difficult time removing hydrophobic lipids than organic solvent-based clearing methods.

3.5.3 Simple immersion

One basic strategy relies on replacing the water with a medium that is closer to the average refractive index of the non-water-based parts of the tissue. The media employed feature refractive indices between 1.42 and 1.48. In simple immersion-based methods, the lipid – medium interfaces are still present and contribute to light scattering, albeit in a diminished manner due to the smaller refractive index mismatch compared to water. Without removing the lipids however, the degree of transparency that can be achieved by simple immersion is limited.

3.5.4 Hyperhydration

Hyperhydration methods are fundamentally similar to simple immersion-based methods, but aim both at lipid removal and addition of large concentrations of urea or formamide to hydrate proteins in order to reduce the refractive index of the tissue. Refractive index mismatch within the tissue is therefore reduced, despite the immersion media featuring a lower refractive index compared to simple immersion or solvent-based tissue clearing, typically 1.38.

3.5.5 Hydrogel embedding-based clearing methods

Removal of lipids in an aqueous medium can also be achieved by using detergents. These may also denature and solvate proteins, however, removing the very proteins aqueous clearing methods are meant to preserve. To minimize protein loss, a hydrogel backbone is introduced into the tissue to which the proteins are cross-linked with aldehydes. This keeps them physically fixed in location while detergent solutions remove the lipids. Since the hydrogel restricts diffusion of molecules, this can be a very slow process and electrophoresis is used in some protocols to accelerate the movement of the charged detergent micelles. Nevertheless, this also restricts the use of antibodies, which are large proteins. To further minimize light scattering, samples are subsequently immersed in media with higher refractive indices of 1.38 – 1.48.

3.5.6 Limitations of tissue clearing

Tissue clearing methods are not capable of completely removing light scattering from the sample. The problems of optical distortion and loss of focus in thick samples still apply, only at much greater depths than in native tissue. Image quality therefore degrades continuously with increasing depth within the sample. This limits the resolution achievable at a specific depth independently of the diffraction limit, or conversely limits the depth at which a specific resolution can still be achieved. Signal intensity is also reduced as light is lost via light scattering and lack of focus, increasing the complexity of the image processing required to analyze the data.
Cleared tissue is furthermore subject to optical distortion. The difference in average refractive index of a sample compared to the refractive index of the expected immersion medium of the lens distorts the length scales measured. A shift of 1 mm on the objective side may not shift the focal point by the same amount, leading to optical distortion of the Z-dimension, for example.
Physical distortion of the sample is another problem, caused by changes in sample properties during clearing. Solvent-based tissue clearing methods tend to shrink and aqueous tissue clearing methods tend to swell samples physically up to 20 % in length [6]. This effect has even been made use of for expansion microscopy, where the sample was deliberately expanded in size to increase the possible resolution beyond the diffraction limit [7]. Sample size distortions make it more difficult to get accurate structural measurements of an organ, requiring careful calibration and homogeneous expansion or shrinkage of the sample.

3.6 Invisible light – X-rays

As was established in the previous chapter, the lack of transparency in tissue is caused by refraction. Compared to visible light, the refraction of X-rays is negligible. The refractive index, which is unity for vacuum by definition, is 1.33 for visible light in water [8], and 0.99999936 for X-rays at 19 keV [9]. As a result, light in the X-ray range is capable of penetrating whole organs or even whole organisms with minimal optical distortion or loss in intensity.

Contrast in X-ray imaging relies on a difference in how X-rays interact with different matter. Absorption contrast imaging makes use of differences in X-ray absorption of the sample matter, which attenuates the passing X-ray beams to different degrees depending on sample composition, specifically the sample's electron density distribution. In practical X-ray absorption contrast imaging, volumetric mass density and atomic composition are the major contributors to electron density.

X-ray mass attenuation coefficients are dependent on the X-ray energy. While in general, attenuation decreases with increasing X-ray energy, every element has specific absorption edges at which the attenuation increases sharply. This occurs if the energy of the X-ray matches the energy required to excite an electron from its ground state, as in visible light fluorescence microscopy. With the high photon energies of X-rays however, the light is usually absorbed by electrons in the lowest energy state of an atom, the K-shell (also known as 1s orbital). The relevant absorption edge in this energy range is accordingly called the K-edge. The K-edges of three elements used in X-ray contrast agents, iodine, gold and barium, can be seen as peaks in the graph in Fig. 9.

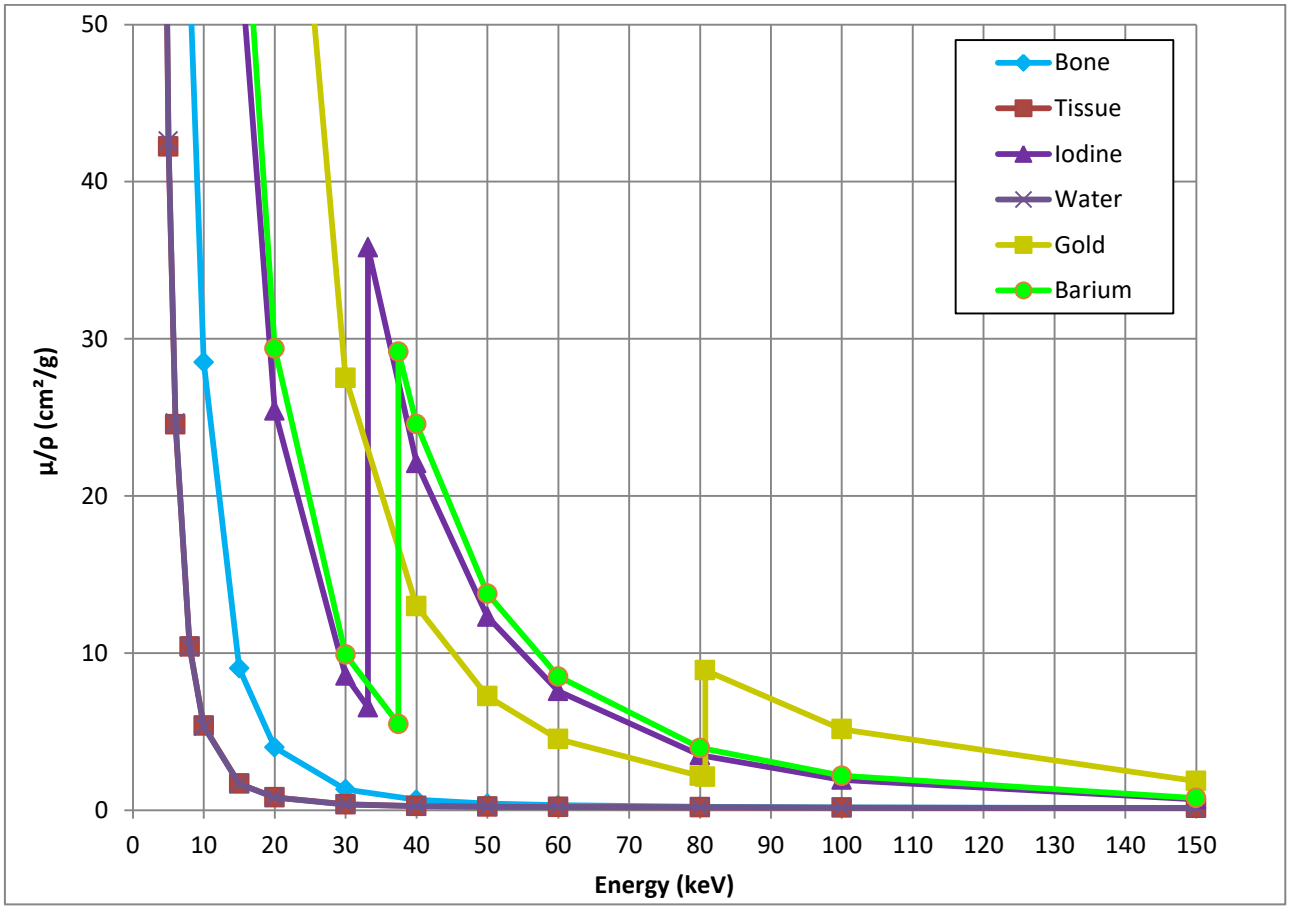

Fig. 9.: X-ray mass attenuation coefficients of soft tissue, bone, water, iodine, gold and barium with normalized volumetric mass density. Data source: NIST Standard Reference Database 126 [10] *Lines are intended as a visual aid only, and do not represent accurate interpolation between measurement points.*

Based on this graph showing the mass attenuation coefficients with normalized volumetric mass density, the best X-ray energy to use for imaging of iodine-based contrast agents in soft tissue would be found at the K-edge of iodine at 33.2 keV and in the range between 10 keV and 20 keV, where attenuation of tissue is low and attenuation of iodine is high. Gold on the other hand may have a K-edge at 80.7 keV, but both the relative increase and the absolute value of the mass attenuation coefficient at this edge are relatively small, making the lower X-ray energies below 40 keV more suitable for gold contrast agent imaging in soft tissue. Below 10 keV however, the X-ray attenuation of water and soft tissue increases dramatically. X-rays at these lower energies have difficulties penetrating soft tissue and are referred to as soft X-rays, whereas the higher energy X-rays with higher penetration power are referred to as hard X-rays.

While the graph for mass attenuation coefficients at normalized volumetric mass densities is useful for establishing the most suitable energy to set an X-ray imaging experiment to, it should not be forgotten that it shows an idealized picture. As an example, X-ray contrast agents are not all used at the same concentration. In this project, gold nanoparticle-based contrast agents were used at approximately one fifth to one quarter of the concentration of iodine-based contrast agents, due to their considerable financial costs and the manufacturer's recommendations. A graph adjusted for tissue and bone densities and using representative X-ray contrast agent concentrations is shown in Fig. 10, using simple linear scaling and ignoring the other elements in the atomic composition of the contrast agents and contributions of the medium they are dissolved in.

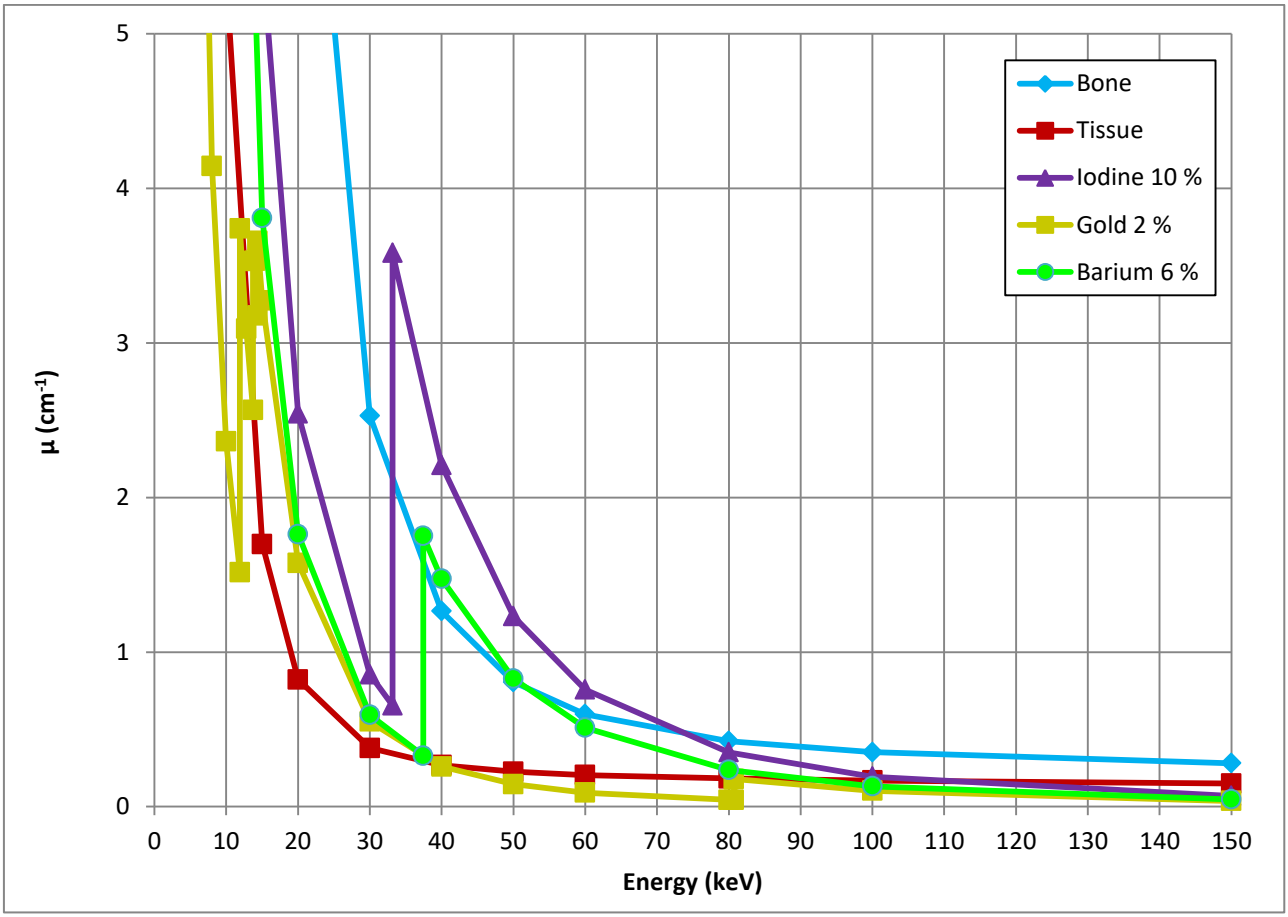

Fig. 10.: X-ray mass attenuation coefficients of soft tissue, bone, water, iodine, gold and barium, adjusted for volumetric mass density. Densities for contrast agent elements were adjusted based on the approximate concentrations used during the thesis. The graph contains only the coefficients of the indicated element and does not contain the contributions of the other elements within the contrast agents or the medium they are suspended in.

As can be seen in the graph, gold at lower concentrations absorbs fewer X-rays than iodine at higher concentrations. The choice of the appropriate element for an X-ray contrast agent is not solely dependent on the mass attenuation coefficient, but on other factors as well, such as solubility, concentration and financial costs.

3.7 X-ray contrast agents

Differences in X-ray attenuation is required in order to obtain contrast in absorption contrast X-ray imaging. In some applications, such as imaging of bone, natural differences in volumetric mass density or elemental composition may provide sufficient contrast. When distinguishing the blood vessel lumen from soft tissue however, the difference in X-ray attenuation yields insufficient contrast for imaging with hard X-rays from laboratory sources. To increase contrast, chemical compounds containing atoms with high atomic mass are injected into the blood vessel lumen, increasing the electron density and thus X-ray absorption within the blood vessels sufficiently to provide contrast against the soft tissue background.

3.7.1 Angiography contrast agents

Standard X-ray contrast agents used in angiography are small, organic molecules carrying iodine as the main absorbing heavy atom.

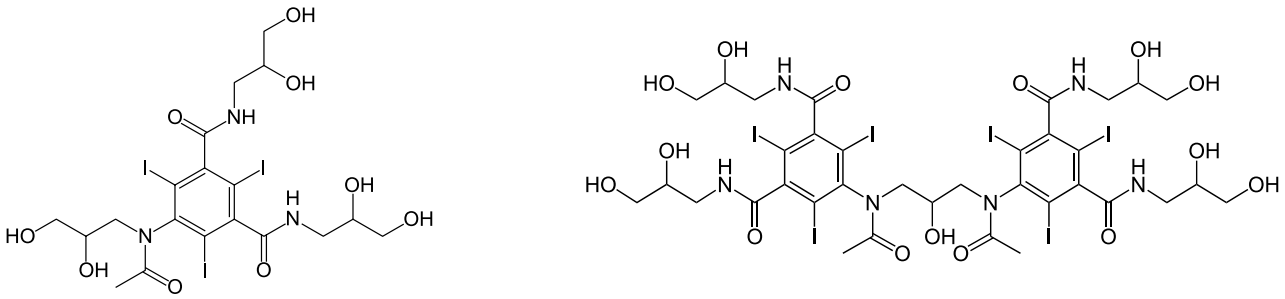

Fig. 11.: Chemical structures of Iohexol (left) and Iodixanol (right), two non-ionic X-ray contrast agents used for clinical imaging.

As small molecules, they are capable of passing the blood vessel walls within minutes of injection, and have to be injected as a bolus and imaged immediately afterwards. This property makes them unsuitable for longer scan times and *ex vivo* applications, as signal in the vasculature decreases and background signal increases when contrast agent diffuses into the tissue. Small molecule contrast agents are freely filtered by the kidney, which is their main pathway for clearance from the body. This prevents distinction of blood vessels from renal tubules and can lead to contrast agent nephropathy, in particular if high concentrations are given intra-arterially to patients already at risk for kidney disease [11].

3.7.2 Blood pool contrast agents

Blood pool contrast agents are much larger compounds, which are retained for longer timeframes within the vasculature. The most common clinical application is magnetic resonance imaging, which employs gadolinium nanoparticles. These could also be used as X-ray contrast agent in principle, but only at a much higher concentration than required in MRI imaging [12]. Surface-functionalized gold-, barium- and iron-nanoparticle-based X-ray contrast agents are available, but at the current stage only for preclinical imaging. Nanoparticles are available in different sizes, some of which are large enough to avoid being filtered via glomerular filtration.

Hydrophobic contrast agents

Hydrophobic contrast agents based on iodized plant oils were also used in medical X-ray imaging applications [13], [14]. These compounds have fallen out of use however, due to the pain response associated with their injection.

3.7.3 Barium sulfate

Barium sulfate is a poorly water-soluble salt that is used in solid form in clinical imaging of the gastrointestinal tract. Barium ions are highly toxic due to their ability to replace calcium in enzymes, rendering them non-functional. When these non-functional enzymes are degraded, the barium ions are released and are then free to replace further calcium ions, leading to catalytic destruction of proteins. Fortunately, due to the poor water-solubility of barium sulfate, barium is not bioavailable in that form and can be excreted safely.
Barium sulfate as contrast agent is also used in the form of micrometer-sized particles and used as radiopaque additive in vascular casting resins [15], [16].

3.8 X-ray sources

With current technologies, X-rays are no longer produced with radioactive elements, but rather generated electrically. In simplified terms, if an electron loses energy, this energy is radiated in the form of light. In order for this light to be in the high energy X-ray range, electrons need to lose a large amount of energy at once.

3.8.1 X-ray tube

In X-ray tubes, electrons are generated with a glowing filament and accelerated in a vacuum tube in an electromagnetic field. This is identical to cathode ray tubes used in old cathode ray tube monitors, but instead of a phosphorescent screen converting the electron beam into visible light, the electrons are instead shot into a metal target. X-ray radiation is produced through two effects, bremsstrahlung and characteristic X-ray emission.

When electrons get shot into a metal target, they are decelerated rapidly. The kinetic energy lost is given off in the form of light, giving bremsstrahlung its name, which is simply “braking radiation” in German. The spectrum of light depends on the amount of kinetic energy lost and results in a continuous, broad distribution.

Knocking out an electron from the lowest energy state, the K-shell, leads to a transition of electrons from a higher energy state to the now vacant energy state, giving off the energy lost as light, exactly as in fluorescence. Just as in fluorescence, only discrete energy states exists and thus only photons with a discrete energy are produced, resulting in sharp peaks in the resulting X-ray spectrum. Since the energy states are element specific, these X-ray lines are characteristic for the elements used in the metal target, resulting in the name characteristic X-ray lines.

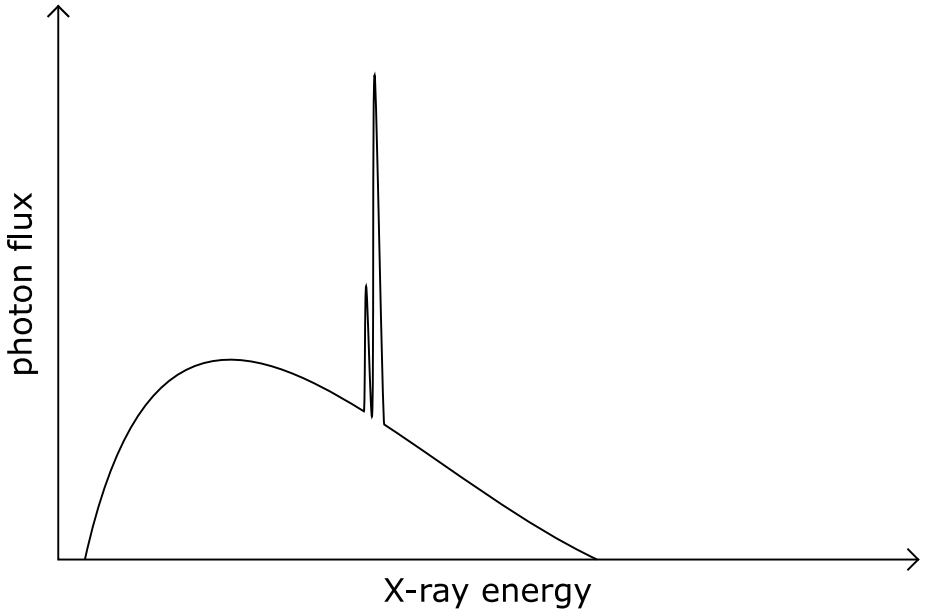

Fig. 12.: Schematic view of an X-ray spectrum coming from an X-ray tube

In practical imaging, it should be noted that the effective X-ray spectrum is lower than the acceleration voltage of the X-ray tube. As an example, if X-ray imaging in the 80 - 90 keV range is desired, such as for matching the absorption edge of gold, then an acceleration voltage of well over 90 kV (generally about 180 kV, see Fig. 12) is required to get sufficient X-rays in the sub 90 keV range.

To get a more narrow spectrum, filtering can be employed. As was shown in a previous chapter, X-ray absorption of matter is higher at lower X-ray energies. By inserting X-ray absorbing matter after the X-ray source, lower energy X-rays can be removed from the spectrum and the mean photon energy increases.

3.8.2 Synchrotron X-rays

In synchrotron X-ray facilities, electrons are not accelerated in a small vacuum tube with a single electromagnetic field, but rather with a particle accelerator, where they are accelerated in a big vacuum ring with multiple electromagnetic fields. They can be accelerated to close to the speed of light and a much larger amount of electrons in flight can be stored within the ring. The main advantages of synchrotron X-ray sources over conventional laboratory sources are the much higher photon flux and spatial and temporal coherence. In practical X-ray μCT imaging, this allows much higher signal-to-noise ratios and the use of phase contrast X-ray imaging techniques that rely on coherent X-rays. Corresponding beamlines (experimental stations which make use of X-ray beams coming from the accelerator) that offer X-ray microtomography imaging at synchrotron facilities in Europe exist at the European Synchrotron Radiation Facility (ESRF) in France, Diamond Light Source (DLS) in the United Kingdom, Deutsches Elektronen-Synchrotron (DESY) in Germany, Source Optimisée de Lumière d'Énergie Intermédiaire du Laboratoire pour l'Utilisation du Rayonnement Électromagnétique (SOLEIL) in France and Swiss Light Source (SLS) in Switzerland.

X-ray generation occurs as in the X-ray tubes by a change of speed of electrons. Unlike X-ray tubes, this is not achieved by electrons being shot into a metal target. X-rays are rather generated by relativistic effects when the electrons are deviated from their path by magnetic fields such as the bending magnets employed in the synchrotron ring to keep them on a circular path [17]. Beamlines using X-rays generated by the bending magnets use the letters BM as designation at the ESRF and the letter B at DLS.

To increase photon flux, other beamlines make use of insertion devices like undulators or wigglers. These are fundamentally a series of magnets with alternating magnetic field inserted along the path of the electron beam, which result in a series of rapid direction changes. Wigglers behave essentially like a series of bending magnets, while undulators produce X-rays with higher temporal coherence [18]. Beamlines using insertion devices use the designation ID at the ESRF and the letter I at DLS.

If an even more narrow X-ray spectrum is required, the low energy X-rays can be filtered by absorbing materials just as with X-ray tubes. A mirror can be used to remove high energy X-rays, which simply pass through the mirror due to the low X-ray attenuation coefficient and thus matter interaction. Such filtered beams are referred as pink beam, to distinguish them from the completely unfiltered white beam coming directly from the synchrotron. If monochromatic beams are required, double-crystal monochromators or multilayer monochromators can be used. Monochromators reduce the photon flux by several orders of magnitude and may introduce beam instability due to vibration, making pink beam preferable in applications where there is no stringent requirement for monochromatic X-rays, such as absorption contrast or single-distance propagation-based phase contrast X-ray μCT.

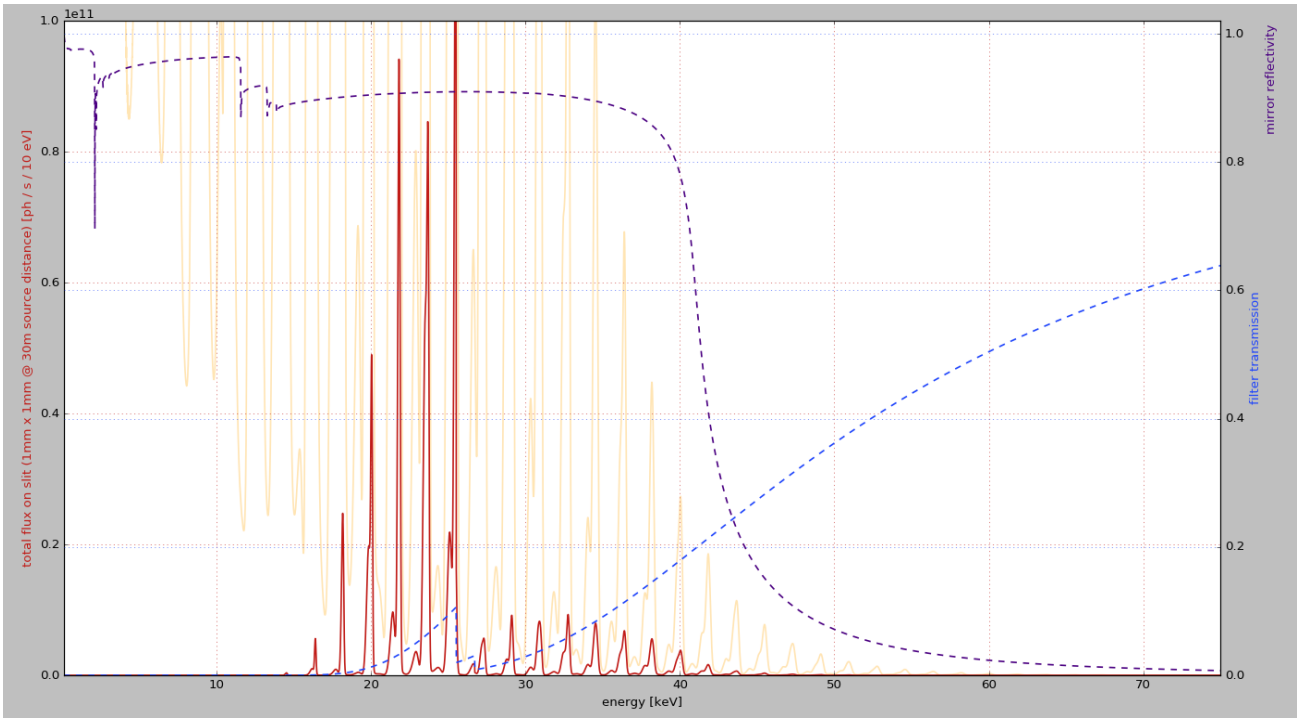

Fig. 13.: Simulated filtered pink beam spectrum of the I13-2 imaging beamline at DLS. Yellow: undulator spectrum, purple: mirror reflectivity, blue: combined filter transmission of C + Al + Ag + Cd filters, red: transmitted harmonics. Simulation software was written by Malte Storm [19].

4 High resolution functional anatomy database of the kidney

4.1 What is a kidney?

The kidney's main function is the removal of waste products from the blood. At first glance, taking out the trash might not seem to be the most important function in the human body, but one only needs to look at the Italian trash crises [20] to see how quickly things can grind to a halt if waste is not properly disposed of. In addition, the kidney not only disposes of waste products that are continuously produced, such as creatinine, but also compensates for fluctuations of nutrients in the body. Water or minerals can be excreted quickly or reabsorbed more efficiently, depending on whether there is an excess or shortage in the body. To coordinate this homeostatic function, the kidney furthermore receives and produces a variety of hormones involved in the regulation of blood pressure, intestinal absorption or red blood cell production.

The way the kidney achieves this feat is by first filtering the entire blood with a simple sieve in the glomeruli. These balls of highly intertwined capillary blood vessels feature a fenestrated endothelium, which is covered by comb-like foot processes, creating slit diaphragms 4 nm × 14 nm in size [21]. These pores have been shown experimentally to retain molecules with more than 6 nm of hydrodynamic diameter [22], while allowing smaller molecules to pass, along with about 25 % of the water as primary urine into the Bowman's capsule. With this passive, broadly selective mechanism, which mostly retains blood cells and large proteins, even unknown toxins can be removed by the kidney without requiring specialized transporter systems. These on the other hand are used subsequently in the renal tubules to selectively reabsorb useful solutes that should not be lost to urinary excretion [23]. They are responsible for the main metabolic energy demand of the kidney and are accordingly the main consumers of oxygen.

Due to the kidney's role in filtering blood, it is supplied with blood well beyond its metabolic needs. As oxygen demand is thus never limited by supply, one might expect oxygen extraction to be constant in the kidney. This is not the case however, and represents one specific aspect of the peculiarities of renal oxygen distribution that will be further explored in the next chapter.

Invited Review

4.2 Renal Arteriovenous Oxygen Shunting

This chapter was first published in Current Opinion in Nephrology and Hypertension as:

W. Kuo and V. Kurtcuoglu, “Renal arteriovenous oxygen shunting,” *Curr. Opin. Nephrol. Hypertens.*, vol. 26, no. 4, pp. 290–295, Jul. 2017. [24].

This invited review describes the developments of computational models of renal oxygen distribution taking place within a one year period in 2015/2016. My personal work on this article consisted of reviewing the literature published on that topic in that period, including associated articles providing necessary context, and to summarize and adapt them towards the intended audience of the journal.

Renal Arteriovenous Oxygen Shunting

Willy Kuo[1,2] and Vartan Kurtcuoglu[1,2]

[1] The Interface Group, Institute of Physiology, University of Zurich, Zurich, Switzerland

[2] National Center of Competence in Research, Kidney.CH, Zurich, Switzerland

4.2.1 Abstract

Purpose of the review:
Renal arterio-venous oxygen shunting has been proposed as a mechanism by which oxygen supplied to the kidney can bypass the renal parenchyma. Shunting could, therefore, play a crucial role in renal hypoxia and hyperoxia. In the absence of suitable quantitative experimental methods, computational modeling has been employed in recent years to estimate the extent and potential impact of oxygen shunting.

Recent findings:
Overestimation of the separation distance between arteries and veins was suggested to be responsible for previous findings that only negligible amounts of oxygen are shunted in the pre-glomerular vasculature. However, models considering the correct separation distance and wrapping of artery-vein pairs still showed shunting at negligible levels of less than 1% of total renal oxygen delivery. The effect of reverse CO_2 shunting on the oxygen-hemoglobin dissociation curve was found to impair, rather than promote pre-glomerular oxygen shunting.

Summary:
Oxygen is unlikely to be shunted along the pre-glomerular vasculature in sufficient quantities to affect renal oxygenation. There may be substantial shunting at the level of the post-glomerular vasculature, but more extensive efforts in structural imaging and computational modeling are needed to quantify it reliably.

Keywords:
renal oxygenation, oxygen shunting, carbon dioxide, Bohr effect, computational modeling

4.2.2 Introduction

The existence of renal arterio-venous oxygen shunting was first demonstrated by Levy and Sauceda in 1959 [1], proposing it as an answer to why the ratio of blood oxygen concentration between the renal artery and renal vein stays largely constant over a wide range of blood flow rates [2].
This phenomenon had been observed in several independent studies at the time. Its presumed cause was the inability of the kidney to extract oxygen from blood to levels below the venous oxygen partial pressure. While this would have been a reasonable explanation for a flow-limited organ where the supply of oxygen is primarily restricted by the flow rate of the incoming blood, it was not for the kidney: The kidneys receive 20-25 % of the cardiac output and are, therefore, supplied with oxygen well above what is necessary for their operation under normal conditions. Oxygen extraction should thus not be a limiting factor.
But what if oxygen could pass through the kidney without contributing to parenchymal oxygenation? Levy [2] proposed that oxygen may be shunted from arteries to veins, as these are arranged in part in countercurrent fashion, which could provide a shortcut to oxygen on its path from renal artery to renal vein. Levy and Sauceda [1] had previously found that oxygen can pass through the kidney more quickly than red blood cells by injecting highly oxygenated blood containing methemoglobin-labeled red blood cells into the renal artery in dogs: The rise in oxygen saturation at the renal vein occurred about a second before the first labeled erythrocytes arrived at the same location.

What Levy and Sauceda could not provide, however, was quantification of the amount of oxygen shunted. Yet this information is needed to assess whether a sufficient quantity of oxygen bypasses the parenchyma to render the kidney a flow-limited organ. It is also needed to evaluate the hypotheses that shunting prevents tissue hyperoxia by routing excess oxygen quickly out of the kidney, and that it exacerbates hypoxia when blood supply is reduced. Evans and co-workers give an excellent overview of the experimental indications for oxygen shunting and its potential implications for kidney oxygenation and disease states [3]. Kidney hypoxia may cause and aggravate acute kidney injury. Along with oxidative stress, it is associated with chronic kidney disease and may progress such towards renal failure.

As there are currently no experimental approaches for quantifying shunting, computational tools have been proposed to fill the gap. Such tools allow for the transformation of purely qualitative models to approximate quantitative ones, thereby enabling hypothesis testing. Concretely, we know that shunting depends on the anatomic arrangement of blood vessels, the permeability of vessel walls and surrounding tissue to oxygen, blood flow rate, oxygen consumption rate and local oxygen gradients, to name a few. What a computational model can do is to determine the combined effect of these factors and yield an estimate of the extent of oxygen shunting in different regions of the kidney under various physiological and pathophysiological conditions.

In the period covered by this review, Evans et al. wrote a letter [4]* in reaction to a model of pre-glomerular oxygen shunting published by our research group [5]*, to which we responded in [6]* and followed up with a further refined model in [7]*.

To provide the necessary context, our original model is comparable, conceptually, to the one published earlier by Gardiner et al. [8]*. Both are based on a dataset by Nordsletten et al. [9], where the renal vascular structure was derived from computed tomography (CT) images of rat kidneys acquired by Garcia-Sanz et al. [10], and ordered into hierarchical vessel segments separated by bifurcations. This Strahler ordering was performed for the pre-glomerular arteries and corresponding veins, yielding two separate vessel trees without the connecting smaller vessels due the limited resolution of the original CT dataset.

4.2.2.1 Hierarchical one-dimensional model suggests shunting is relevant

The model of Gardiner and co-workers [8]* relies on one-dimensional (1D) representations of those two ordered trees. Each hierarchical segment in the Nordsletten data is used as the basis of a computational compartment. In the individual compartments, a single artery and vein are arranged parallel to each other with opposing blood flow directions, using the average vessel diameter and length of the blood vessels of the corresponding Strahler order. Each compartment feeds blood to the next one, and blood exiting the artery in the final compartment is routed back through the corresponding vein after adjusting the blood partial pressure of oxygen (pO_2) for oxygen consumption in the tissue. This countercurrent system produces the pO_2 gradient required for arterio-venous oxygen shunting. The amount of O_2 transferred from the arterial to the venous segment in the respective compartment is considered proportional to that gradient and to the arterial vessel wall surface area.

To account for the effect of parameters that are not explicitly included in the model, a weighting factor is employed. This factor is determined by requiring that the calculated pO_2 in the renal tissue matches the values measured experimentally by Welch et al. [11].

The model output showed that approximately 10% of the total oxygen supplied to the kidney was shunted, which was comparable in magnitude to overall oxygen consumption. It further showed that shunting decreased with increased renal blood flow and hematocrit, and increased with elevated arterial pO_2. Therefore, Gardiner et al. concluded that shunting is a quantitatively significant factor in renal oxygen balance.

4.2.2.2 Higher-dimensional model indicates no substantial shunting

In the model by Olgac and Kurtcuoglu [5]*, the hierarchical structure of the computational compartments is retained, but each level of the vascular tree is represented by a repetitive, idealized three-dimensional (3D) domain. This domain contains artery-vein pairs with tissue in between, and accounts for the effect of capillary blood flow on oxygen transport through tissue by employing the model of Salathé [12]. The blood vessels are not considered homogeneous 1D entities, but the spatial distribution profile of red blood cells as well as the spatial variation of blood flow velocity in the vessel cross-sections are accounted for. Oxygen flux through the arterial and venous walls are calculated by modeling advection, diffusion and consumption in the 3D domain of each hierarchical compartment. Compared to the model of Gardiner et al., this model does not require weighting factors to match experimental data. It rather quantifies oxygen shunting by calculating the total oxygen flux across venous walls.
The model showed that under most of the considered conditions, the amount of oxygen shunted did not exceed consumption in the tissue, with tissue pO_2 staying below venous pO_2. Only when consumption was set to zero, notable shunting occurred, but even then it accounted for just 1.2 % of the total oxygen delivered to the kidney. In that case shunting was limited to the most distal vessels, similar to what was seen in the model of Gardiner et al.

4.2.2.3 Letter to the editor: The model geometry neglects venous wrapping around arteries

Evans et al. [4]* criticized the layout of the three-dimensional units employed by Olgac and Kurtcuoglu, stating that in the kidney larger pre-glomerular arteries and veins are arranged directly adjacent to each other, without capillaries or tubular tissue in between them (Fig. 1).

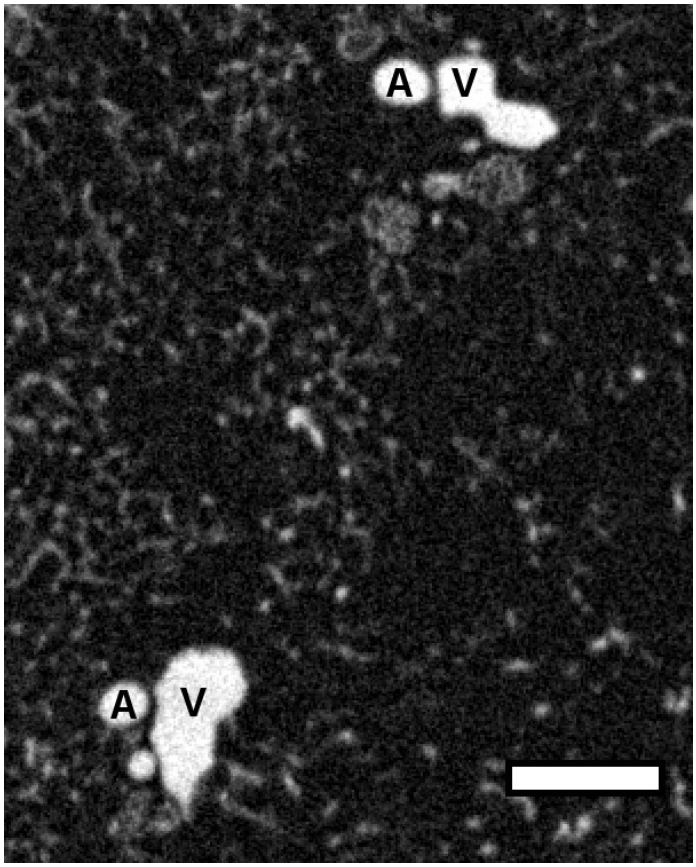

Fig. 1.: X-ray microcomputed tomography scan of a mouse kidney vascular cast showing the relative localization of pre-glomerular arteries (A) and veins (V) at the corticomedullary border. Scale bar: 200 µm. (Original work)

Gardiner et al. [13] and later Ngo et al. [14] had previously created a two-dimensional (2D) model based on histology images, using idealized and realistic vessel geometries, respectively. In the second model, arteries, veins, tubules and capillaries were extracted from histology images and used to calculate oxygen diffusion and consumption in the 2D space of the pictures. It was found that in vessel pairs where the vein partially wrapped around the artery, substantial arterio-venous oxygen shunting occurred, while in non-wrapped pairs most of the oxygen was delivered to the tissue. Evans and co-workers concluded that Olgac and Kurtcuoglu did not find oxygen shunting because their model neglected vessel wrapping.

4.2.2.4 Reply to the letter: Model with full account of wrapped vessels indicates negligible shunting

In response, Olgac and Kurtcuoglu revised the model to treat wrapped and non-wrapped vessels separately. In addition, they extrapolated the 2D model of Ngo et al. to the third dimension by multiplying over the total length of the corresponding blood vessels. Calculations with both showed negligible oxygen shunting, namely 0.13 % and 0.37 % of the total oxygen delivery, respectively. Wrapping occurs predominantly in large vessel pairs, which make up only a small part of the total vascular surface area. Consequently, while there can be shunting in these pairs, there are not enough of them to shunt substantial amounts of oxygen.

4.2.2.5 Model accounting for carbon dioxide transport also shows negligible oxygen shunting

Schurek et al. [15] had hypothesized earlier that carbon dioxide may be shunted from veins to arteries, thereby promoting dissociation of oxygen from hemoglobin through the Bohr effect and thus contributing to oxygen shunting. To test this hypothesis, Olgac and Kurtcuoglu [7]* extended their revised model to include transport of several CO_2 species and take into account the pH dependence of oxygen-hemoglobin binding. Their results showed that CO_2 is shunted only in small quantities, namely in the range of 1 % of the total amount of CO_2 species entering the kidney through the renal artery. In conjunction with the high buffering capacity of blood, only a marginal decrease in arterial pH was seen, which was in addition lower than the decrease in venous pH. Consequently, the Bohr effect appears to impair rather than promote arterio-venous oxygen shunting.

4.2.3 Discussion and outlook

Observations that the ratio of blood oxygen concentration between the renal artery and vein stays largely constant over a wide range of blood flow rates provided the initial impetus for investigations of arterio-venous shunting. Since experimental approaches could not quantify the actual amount of oxygen shunted, the most recent contributions to the field have relied on computational methods instead.

The most current model [7]*, which stands at the end of an evolutionary development that started with the work of Gardiner et al. [8]*, suggests that there is no substantial arterio-venous oxygen shunting in the pre-glomerular vasculature. In the absence of indications that important physiological or anatomical factors with quantitatively large impact were neglected in that model, it is reasonable to assume that pre-glomerular shunting is not responsible for the observed constant oxygen concentration between renal artery and vein. Since the experimental methods of Levy and Sauceda [1] did not allow for drawing conclusions on the quantity of oxygen shunted, their results could be explained either by the very small amount of oxygen shunted in the pre-glomerular vasculature, or by shunting in a different part of the kidney.

To serve as the explanation for the behavior of the kidney as a flow-limited organ as was originally proposed, i.e. an organ in which the supply of oxygen is primarily limited by the flow rate of the incoming blood, oxygen would have to be shunted in large quantities before entering the post-glomerular capillary network, as at that level the oxygen is already distributed by the microvasculature throughout the renal parenchyma. However, the underlying observation of a constant ratio of oxygen concentration between renal artery and vein can also be explained by

increased glomerular filtration at higher renal blood flows, resulting in greater tubular workload and thus increased oxygen consumption [3].
For oxygen shunting to serve as an effective protection mechanism against both whole kidney hyperoxia and hypoxia, it would also have to take place with substantial magnitude in the pre-glomerular vasculature. Furthermore, oxygen shunting would need to be increased under hyperoxic conditions and reduced under hypoxic conditions. However, there is no clear evidence for such behavior. The calculations of Olgac and Kurtcuoglu indicated negligible shunting at high arterial inlet blood pO_2 [5]* and the model of Gardiner et al. [8]* showed a reduction in shunting when renal blood flow and hematocrit were increased. Only when arterial pO_2 was augmented did that model indicate an increase in shunting.
While shunting would have to occur at the level of the pre-glomerular vasculature to fulfill its hypothesized role as a protective mechanism or for rendering the kidney a flow-limited organ, it is conceivable that substantial shunting may only occur along post-glomerular blood vessels, for example at the level of the peritubular capillaries or along the vasa recta in the medulla. Indeed, Zhang and Edwards [16] demonstrated with a computational model shunting between a subset of the ascending and descending vasa recta.
Quantification of shunting along the post-glomerular vasculature is very complex. While from an anatomic point of view highly simplified models can serve as a stepping stone, it is rather likely that more complex 3D models will be needed to accurately determine oxygen transfer at that location. There is currently insufficient structural data available to produce such models: The small size and large number of post-glomerular vessels require micrometer resolution imaging at the organ scale, along with automated processing of the acquired datasets in the terabyte size range. However, with the expected progress in imaging and image processing, it is only a matter of time before we will see the next generation of computational models shed light on oxygen balance in the entire kidney.

4.2.4 Conclusion

In the absence of suitable experimental methods, arterio-venous oxygen shunting has been quantified using computational modeling. The latest of these models indicate that while shunting does occur along the pre-glomerular vasculature, the amount of shunted oxygen is small. They thus do not support the hypothesized role of shunting as a protective mechanism against organ-wide hyperoxia and hypoxia, and its role in rendering the kidney a flow-limited organ. Post-glomerular shunting and its role in localized hyperoxia and hypoxia, on the other hand, is still a field open to investigation (Table 1).

4.2.5 Key points

- Arterio-venous shunting has been proposed as a way for oxygen to bypass the renal parenchyma, possibly playing a crucial role in balancing renal oxygenation.
- To serve as an effective bypass, shunting would need to occur along the pre-glomerular vasculature, before the oxygen reaches the tubular cells, its main consumers.
- There is evidence for shunting, but there are currently no reliable experimental methods that can quantify the amount of oxygen bypass or the location of shunting.
- As an alternative, computational modeling has been used to calculate pre-glomerular oxygen shunting.
- The latest models indicate that only very small amounts of oxygen are shunted along the pre-glomerular vasculature.

Table 1.: Overview of computational models examining pre- and post-glomerular oxygen shunting, and their physiological and pathophysiological relevance.

	Pre-glomerular shunting	Post-glomerular shunting
Evidence		
Support	1D model Gardiner et al. [8]* 2D model Gardiner et al. [13] 2D model Ngo et al. [14]	Partial vasa recta model Zhang and Edwards [16]
Do not support	2D model Ngo et al. extrapolated to 3D [6]* 3D model Olgac and Kurtcuoglu [7]*	
Physiological implications	Renal oxygenation [3] Renal hypoxia response [17]	Corticomedullary oxygen gradient [18] Renal hypoxia response [17]
Pathophysiological significance	Acute Kidney Injury [19] Chronic Kidney Disease [19] and progression to End Stage Renal Disease [20] Renal anemia [17]	Acute Kidney Injury [19] Chronic Kidney Disease [19] Renal anemia [17]

4.2.6 Acknowledgements

Acknowledgements:
We would like to thank Dr. Ufuk Olgac for his assistance in preparation of this review.

Financial support and sponsorship:
We gratefully acknowledge the financial support provided by the Swiss National Science Foundation through grant 205321_153523 HR-Kidney and NCCR Kidney.CH.

Conflicts of interest:
We have no conflicts of interest to declare.

4.2.7 References

[1] M. N. Levy and G. Sauceda, “Diffusion of Oxygen from Arterial to Venous Segments of Renal Capillaries,” *American Journal of Physiology*, vol. 196, no. 6, pp. 1336–1339, 1959.

[2] M. N. Levy, “Influence of variations in blood flow and of dinitrophenol on renal oxygen consumption,” *American Journal of Physiology*, vol. 196, no. 4, pp. 937–942, Apr. 1959, doi: 10.1152/ajplegacy.1959.196.4.937.

[3] R. G. Evans, B. S. Gardiner, D. W. Smith, and P. M. O’Connor, “Intrarenal oxygenation: unique challenges and the biophysical basis of homeostasis,” *American Journal of Physiology-Renal Physiology*, vol. 295, no. 5, pp. F1259–F1270, Nov. 2008, doi: 10.1152/ajprenal.90230.2008.

[4]* R. G. Evans, D. W. Smith, Z. Khan, J. P. Ngo, and B. S. Gardiner, “Letter to the editor: ‘The plausibility of arterial-to-venous oxygen shunting in the kidney: it all depends on radial geometry,’” *American Journal of Physiology-Renal Physiology*, vol. 309, no. 2, pp. F179–F180, Jul. 2015, doi: 10.1152/ajprenal.00094.2015.

Annotation: In this letter it was argued that wrapping of veins around arteries must be taken into account explicitly in the modeling of pre-glomerular oxygen transport.

[5]* U. Olgac and V. Kurtcuoglu, “Renal oxygenation: preglomerular vasculature is an unlikely contributor to renal oxygen shunting,” *American Journal of Physiology-Renal Physiology*, vol. 308, no. 7, pp. F671–F688, Apr. 2015, doi: 10.1152/ajprenal.00551.2014.

Annotation: This publication presents a detailed computational model of pre-glomerular oxygen transport, questioning the results of previous models by finding no substantial oxygen shunting along the pre-glomerular vasculature.

Justification: This model is the basis of the discussions in the two letters of the review period, and is also the basis of the revised model published in 2016.

[6]* U. Olgac and V. Kurtcuoglu, “Reply to ‘Letter to the editor: “The plausibility of arterial-to-venous oxygen shunting in the kidney: it all depends on radial geometry” *American Journal of Physiology-Renal Physiology*, vol. 309, no. 2, pp. F181–F182, Jul. 2015, doi: 10.1152/ajprenal.00221.2015.

Annotation: In this letter it was shown that while explicitly accounting for wrapped vessel pairs yields higher calculated shunting values, the total amount of shunted oxygen remains insubstantial.

[7]* U. Olgac and V. Kurtcuoglu, “The Bohr Effect Is Not a Likely Promoter of Renal Preglomerular Oxygen Shunting,” *Frontiers in Physiology*, vol. 7, Oct. 2016, doi: 10.3389/fphys.2016.00482.

Annotation: In this paper it was shown computationally that explicitly accounting for the effect of various CO_2 species on the hemoglobin-oxygen dissociation curve does not increase but decrease pre-glomerular oxygen shunting.

[8]* B. S. Gardiner, D. W. Smith, P. M. O’Connor, and R. G. Evans, “A mathematical model of diffusional shunting of oxygen from arteries to veins in the kidney,” *American Journal of Physiology-Renal Physiology*, vol. 300, no. 6, pp. F1339–F1352, Jun. 2011, doi: 10.1152/ajprenal.00544.2010.

Annotation: This publication presents the first one-dimensional hierarchical model of renal pre-glomerular oxygen shunting. Oxygen shunting was found to be of similar order of magnitude as oxygen consumption in the kidney.

Justification: The publication contains the hierarchical segment-wise model, explaining the historical context and conceptual basis for the model of Olgac and Kurtcuoglu.

[9] D. A. Nordsletten, S. Blackett, M. D. Bentley, E. L. Ritman, and N. P. Smith, "Structural morphology of renal vasculature," *Am. J. Physiol. Heart Circ. Physiol.*, vol. 291, no. 1, pp. H296-309, Jul. 2006, doi: 10.1152/ajpheart.00814.2005.

[10] Garcia-Sanz Agustin, Rodriguez-Barbero Alicia, Bentley Michael D., Ritman Erik L., and Romero J. Carlos, "Three-Dimensional Microcomputed Tomography of Renal Vasculature in Rats," *Hypertension*, vol. 31, no. 1, pp. 440–444, Jan. 1998, doi: 10.1161/01.HYP.31.1.440.

[11] W. J. Welch, H. Baumgartl, D. Lubbers, and C. S. Wilcox, "Nephron pO(2) and renal oxygen usage in the hypertensive rat kidney," *Kidney International*, vol. 59, no. 1, pp. 230–237, Jan. 2001, doi: DOI 10.1046/j.1523-1755.2001.00483.x.

[12] E. P. Salathé, "Mathematical modeling of oxygen transport in skeletal muscle," *Mathematical Biosciences*, vol. 58, no. 2, pp. 171–184, Apr. 1982, doi: 10.1016/0025-5564(82)90071-2.

[13] B. S. Gardiner *et al.*, "Diffusive oxygen shunting between vessels in the preglomerular renal vasculature: anatomic observations and computational modeling," *Am. J. Physiol. Renal Physiol.*, vol. 303, no. 5, pp. F605-618, Sep. 2012, doi: 10.1152/ajprenal.00186.2012.

[14] J. P. Ngo *et al.*, "Vascular geometry and oxygen diffusion in the vicinity of artery-vein pairs in the kidney," *American Journal of Physiology-Renal Physiology*, vol. 307, no. 10, pp. F1111–F1122, Nov. 2014, doi: 10.1152/ajprenal.00382.2014.

[15] H. J. Schurek, U. Jost, H. Baumgartl, H. Bertram, and U. Heckmann, "Evidence for a Preglomerular Oxygen Diffusion Shunt in Rat Renal-Cortex," *American Journal of Physiology*, vol. 259, no. 6, pp. F910–F915, Dec. 1990.

[16] W. S. Zhang and A. Edwards, "Oxygen transport across vasa recta in the renal medulla," *American Journal of Physiology-Heart and Circulatory Physiology*, vol. 283, no. 3, pp. H1042–H1055, Sep. 2002, doi: 10.1152/ajpheart.00074.2002.

[17] V. H. Haase, "Mechanisms of Hypoxia Responses in Renal Tissue," *JASN*, vol. 24, no. 4, pp. 537–541, Apr. 2013, doi: 10.1681/ASN.2012080855.

[18] D. W. Lübbers and H. Baumgärtl, "Heterogeneities and profiles of oxygen pressure in brain and kidney as examples of the pO2 distribution in the living tissue," *Kidney International*, vol. 51, no. 2, pp. 372–380, Feb. 1997, doi: 10.1038/ki.1997.49.

[19] P. Singh, S.-E. Ricksten, G. Bragadottir, B. Redfors, and L. Nordquist, "Renal oxygenation and haemodynamics in acute kidney injury and chronic kidney disease," *Clin Exp Pharmacol Physiol*, vol. 40, no. 2, pp. 138–147, Feb. 2013, doi: 10.1111/1440-1681.12036.

[20] I. Mimura and M. Nangaku, "The suffocating kidney: tubulointerstitial hypoxia in end-stage renal disease," *Nat Rev Nephrol*, vol. 6, no. 11, pp. 667–678, Nov. 2010, doi: 10.1038/nrneph.2010.124.

4.3 Computational modeling and 3D imaging

The computational models developed so far were based on greatly simplified vascular geometries, resulting in heated discussions concerning the validity of the simplifications and extrapolations required in obtaining the results. More accurate, fully three-dimensional structural data of the entire kidney vasculature were not available, however. The available mathematical representation of the renal vascular tree by Nordsletten et al. [25] was derived from μCT data acquired in 1998 by Garcia-Sanz et al. [26]. These data were limited in resolution and could only resolve the preglomerular vasculature, leaving the entire capillary bed unexplored. In addition, the data was only available for the rat, meaning data from mouse experiments could not be directly transferred to the model. As this included data on the renal oxygen regulation and responses, this PhD-project was conceived. Capillary-level resolution 3D imaging within a whole mouse kidney should finally provide complete structural data of the entire renal vasculature.

4.4 Mouse kidney imaging with tissue clearing and lightsheet microscopy

In the overarching project to investigate the oxygenation of the kidney and its relationship to oxygen-dependent renal erythropoietin (EPO) expression, three features of interest needed to be imaged:

1. Renal blood vessels, the main suppliers of oxygen
2. Renal tubules, the main consumers of oxygen
3. Renal erythropoietin producing cells, the main producers of renal erythropoietin

To localize renal erythropoietin-producing cells, the project was making use of a mouse model that would express tdTomato fluorescent protein in cells with active erythropoietin expression in an inducible manner after Tamoxifen treatment [27]. Since this made preservation of fluorescent proteins a priority, aqueous hydrogel embedding-based tissue clearing was chosen as the most suitable tissue clearing method. Initial trials were performed with the CLARITY protocol [28], which makes use of an acrylamide hydrogels cross-linked with bisacrylamide. for stability. Proteins are linked to the acrylamide backbone with formaldehydes. Lipids are removed with a sodium-dodecyl-sulfate (SDS) detergent solution in borate buffer. This process was accelerated with a custom-built electrophoresis chamber to clear a whole kidney within a week.

The CLARITY-protocol had several drawbacks, most of which were caused by the electrophoresis chamber. Samples were prone to browning due to overheating, greatly reducing transparency if it occurred. Running the electrophoresis chamber was relatively labor-intensive: The pH of the detergent solution had to be checked daily, and the solution exchanged if it had changed. The tubing used to circulate the detergent solution tended to become brittle and break due to the repeated compressions by the peristaltic pump, and required daily supervision and weekly replacement. The platinum electrodes were prone to buildup of black residue on the surface, which could only be removed to a limited degree, making frequent replacement of the electrodes necessary. And finally, since only one full electrophoresis chamber assembly was available, only one sample could be cleared at the same time.

Due to all these drawbacks, the electrophoretic clearing according to the CLARITY protocol was abandoned in favor of passive clearing with the PACT protocol [29]. To accelerate clearing, a hydrogel with considerably larger pores is created by polymerizing the acrylamide hydrogel without bisacrylamide cross-linker and without additional formaldehyde added to the acrylamide solution, relying instead on residual formaldehyde remaining in the tissue after the previous tissue fixation step. Additionally, a higher concentration of SDS detergent in phosphate buffer is employed. While

passive clearing for a whole kidney took approximately a month with this protocol, no electrophoresis chamber was required and samples could instead be cleared in a simple centrifugation tube in an incubator. Since samples could be cleared in parallel, the overall time for clearing more than four samples was less than for sequential clearing using the electrophoresis chamber, despite the faster clearing speed of the latter for a single sample. Passively cleared kidneys furthermore required no supervision, making the process less labor-intensive.

Confocal, two-photon and lightsheet microscopes were evaluated as potential imaging methods. Confocal and two-photon microscopes as point scanning methods were quickly discarded as impractical, as these microscopes were estimated to require 100 – 200 days of continuous scanning for a single kidney. Apart from the logistical problems this would pose, the stability of the fluorescence signal over this length of time could not be guaranteed. Lightsheet microscopy, which could image a whole kidney in approximately one hour, was the only practical option. This came at a cost in image quality however. The Zurich mesoSPIM [30] could be used to image whole mouse kidneys with 6 µm isotropic voxel size by combining images acquired from multiple angles into a single dataset. While this was enough to localize renal erythropoietin producing cells expressing tdTomato fluorescent protein [27], which are sufficiently spaced out to be detected even at low resolution, vascular and tubular structures could only be captured up to a few hundred micrometers in depth.

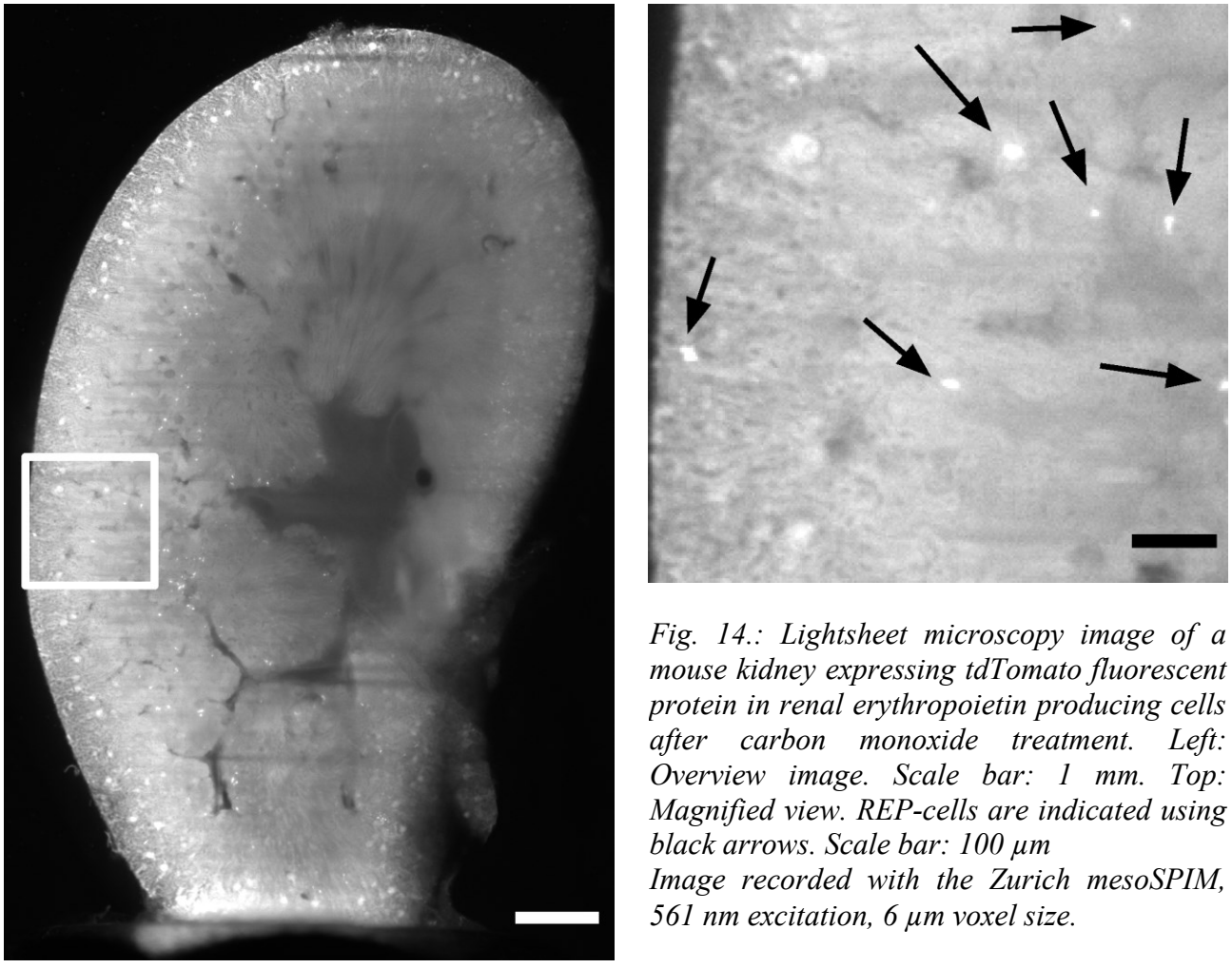

Fig. 14.: Lightsheet microscopy image of a mouse kidney expressing tdTomato fluorescent protein in renal erythropoietin producing cells after carbon monoxide treatment. Left: Overview image. Scale bar: 1 mm. Top: Magnified view. REP-cells are indicated using black arrows. Scale bar: 100 µm
Image recorded with the Zurich mesoSPIM, 561 nm excitation, 6 µm voxel size.

The inability to acquire vascular and tubular structure was primarily an issue of resolution. With 6 µm voxel size, the theoretically achievable resolution is worse than 12 µm. Blood vessels have diameters down to 4 µm at the capillary level. In theory, they could still be captured at sufficient signal-to-background ratios in the cortex, where they are typically spaced apart by proximal tubules with approximately 30 µm diameter. This could not be achieved in practice, as staining of the blood

vessels was performed with fluorescently labeled lectin, which only adheres to the blood vessel surface and does not fill the entire lumen. Accordingly, the blood vessels are represented by hollow structures considerably smaller than 4 µm. Due to partial volume effects, the effective signal-to-background was greatly reduced, preventing reliable imaging of the labeled blood vessels even in the cortex.

In addition, the autofluorescent tubules could also only be captured with useful resolution up to 0.5 mm depth within the kidney. Any vascular or tubular structure deeper within the kidney could not be imaged with the chosen tissue clearing approach, as light scattering degraded the image quality too much at those depths, leading to the lack of sufficient effective resolution. To create a vascular and tubular 3D atlas of the mouse kidney, a different approach was thus required.

4.4.1 Methods

One male HIF1α × EPO-Cre-X × Ai14 mouse was treated with tamoxifen and 0.1 % carbon monoxide as hypoxic stimulus and kept for 4 weeks until sacrifice (SK3550 L/R). The mouse was anaesthetized with 127 mg/kg Ketamine and 25 mg/kg Xylazine, with a second dose of 32 mg/kg and 6 mg/kg given after 15 minutes. The abdominal aorta was cannulated with a 21 G butterfly needle in retrograde direction below the kidneys, and fixed with a constrictor knot ligation. The abdominal aorta above the kidney and the superior mesenteric artery were closed with constrictor knot ligations and a hole was cut into the vena cava as an outlet. Both kidneys were then perfused with 10 ml phosphate-buffered saline (PBS) to flush out the blood, 50 ml 4 % paraformaldehyde (PFA) in PBS to fix the kidneys and 25 ml PBS to flush out excess formaldehyde, all at 37 °C at 150 mmHg of hydrostatic pressure. 50 µg of isolectin B4 from Griffonia simplicifolia dissolved in 17.5 ml PBS were perfused at room temperature at 100 mmHg hydrostatic pressure.
Kidneys were stored in 4 % PFA at 4 °C for one day, immersed in 4 % acrylamide, 0.25 % VA-044 radical initiator in PBS at 4 °C for three days. The acrylamide was polymerized at 37 °C for six hours and left to stand overnight. Kidneys were washed and immersed in 15 ml 8 % SDS in PBS and cleared at 37 °C for 7 months. One kidney was washed in 15 ml PBS overnight and immersed in 1 ml 20 µM DRAQ5 far red nuclear dye for 1 week. The DRAQ5 solution was replaced with a fresh 1 ml 20 µM solution and kept for ten days, then washed in 14 ml PBS for two weeks. The kidney was immersed in 1 ml refractive index matching solution (Histodenz in PBS, n = 1.439) for three days under shaking at room temperature, then scanned on the Zurich mesoSPIM lightsheet microscope.

4.4.2 Acknowledgements

I would like to thank Karen Scholz, my main collaborator on this project, who performed the mouse breeding, genotyping, tamoxifen treatment and carbon monoxide exposure. I would also like to thank José María Mateos Melero and Anastasios Marmaras for help establishing the CLARITY tissue clearing on the mouse kidneys, and Evgenia Platonova for help with tissue clearing and scanning with the Zurich mesoSPIM lightsheet microscope.

My personal contribution to this chapter consisted of evaluating the CLARITY protocol, researching alternatives, implementing the PACT protocol for kidney clearing, developing perfusion and staining protocols for marking the blood vessels, acquiring the confocal and two-photon microscopy images and analyzing the data.

Journal article

4.5 3D atlas of the mouse kidney vascular and tubular structure

This chapter is part of a manuscript in preparation for submission to a peer reviewed journal.

My work consisted of developing the radiopaque PU4ii plastic resin mixture, developing and optimizing the perfusion and vascular casting protocols and preparing and imaging the kidneys with synchrotron propagation-based phase contrast μCT. For processing the resulting data, I reconstructed the datasets and assisted during image processing by managing the data, advising on imaging and anatomical features, checking results and providing training data for classification of glomeruli and artifacts.

3D atlas of the mouse kidney vascular and tubular structure

Willy Kuo[1,2,3,*], Diego Rossinelli[1,2,*], Roland H. Wenger[1,2], Georg Schulz[3], Simone Hieber[3], Bert Müller[3], Vartan Kurtcuoglu[1,2]

[1] Institute of Physiology, University of Zurich, Zurich, Switzerland;

[2] National Centre of Competence in Research, Kidney.CH, Zurich, Switzerland;

[3] Biomaterials Science Center, Department of Biomedical Engineering, University of Basel, Allschwil, Switzerland

* These authors contributed equally

Due to optical and physical distortions, anisotropic image quality and limited resolution, the goal of imaging the complete vascular and tubular structure with full capillary resolution and connectivity could not be achieved by tissue clearing combined with lightsheet microscopy. Other 3D light microscopy methods, such as two-photon microscopy, may have been able to satisfy the quality requirements, but would be too slow to acquire a whole mouse kidney within a useful timeframe.

Hard X-ray imaging on the other hand was capable of providing the necessary high resolution and distortion-free imaging required for this project, due to the minimal refraction of hard X-rays even in native soft tissue. Due to their minimal absorption, fluorescent proteins are expected to survive an X-ray μCT scan with their fluorescence intact. Radiation doses of ten thousands of Grays would be required for a 50 % reduction in fluorescence [12], several orders of magnitudes more than is incurred in a typical X-ray μCT experiment. Therefore, the vascular structure could first be acquired using hard X-ray μCT, followed by tissue clearing and lightsheet microscopy on the same sample to correlate the X-ray data to the location of renal EPO-producing cells. In order to get the tubular structure as well, single-distance propagation-based phase contrast at a synchrotron facility would be employed, which is capable of distinguishing soft tissue and water-filled lumina even without contrast agent. Contrast agents however were still required to distinguish the lumina of the blood vessels from the lumina of the tubules.

To build the first 3D atlas of the complete vascular and tubular structure of a mouse kidney, three methodological developments were necessary:

1. Optimization of vascular casting protocols to get complete filling of the entire capillary bed with a radiopaque plastic resin mixture.

2. Single distance propagation-based hard X-ray phase contrast imaging with micrometer resolution at a synchrotron radiation facility.

3. Image processing and segmentation of the vascular and tubular structure, with artifact removal and connectivity analysis, on the resulting terabyte-scale datasets.

4.5.1 Microparticle-free vascular casting of the mouse kidney

Vascular casting with hardening substances is a centuries-old technique [31] used in the investigation of vascular structures. In corrosion casting, the tissue is subsequently macerated in a potassium hydroxide bath to receive a free-standing cast, which can be visually inspected [32], scanned with electron microscopy [33] or scanned with X-ray μCT [34]. While X-ray μCT scanning of corroded casts against air yields superior contrast, the corrosion process induces considerable

distortions of the vascular cast due to gravity and surface tension during the drying process [35]. There is furthermore no provision for identifying vessels which may have broken off or been insufficiently filled with polymer resin. Tubular imaging is also impossible, since tissue is completely dissolved in the process.
Vascular casting without corrosion was therefore required, which could be performed with commercial radiopaque vascular casting resins. Interrupted or incompletely filled vessels were however frequently observed artifacts in literature using these resins, which were using microparticles such as barium sulfate or lead chromate as the radiopaque component [32], [36], [37]. Since microparticles could potentially clog at the capillary level, a new particle-free radiopaque plastic resin mixture was developed to achieve more reliable vascular casting results. 1,3-Diiodobenzene was identified as a cheap radiopaque additive well soluble in 2-butanone, the solvent used for diluting the PU4ii vascular casting resin. Up to 120 mg iodine per ml resin solutions were tested, yielding excellent contrast in laboratory and synchrotron source hard X-ray µCT imaging.
With occlusion of capillaries through microparticles excluded as an issue, the manner of plastic resin injection was identified as a second obstacle to reliable filling of the vasculature. Standard transcardial perfusions are insufficient to flush kidneys fully of remaining blood. Flow of the perfused solutions has to be diverted entirely to the kidneys, as otherwise most of the perfusion volume would circulate through other organs with lower flow resistance, such as the brain or the liver. Additionally, kidneys need to be fixed under flow to keep up glomerular filtration, to keep up tubular counterpressure and prevent collapse of the tubular lumina. To get kidneys flushed properly from leftover blood and to retain open tubular lumina for tubular imaging, kidneys were perfused by cannulating the abdominal aorta in retrograde direction, closing the access to less flow-resistant organs by ligation, and diverting the entire perfusion volume to the kidney. This procedure was adapted from the isolated perfusion kidney technique [38].
Beyond fixation, the injection of plastic resins for vascular casting poses additional requirements to the quality of the perfusion procedure, requiring additional optimization of the protocol specific for the kidney. Plastic resins are hydrophobic substances, which are not miscible with water and are dependent on physically pushing water out of the vascular lumina. The resin however does not form one unified hydrophobic interface in the vasculature, but rather forms resin droplets suspended in water initially. These can be seen by eye, typically exiting the outlet during injection of the first 0.5 ml of resin volume. If the vasculature is not further flushed with plastic resin, these resin droplets remain as ball shapes within the vasculature instead of fully filled vessels, particularly in the large veins of the kidney [37].
During the next 1 - 2 ml of perfused resin volume, the ratio of water to resin present in the vasculature shifts towards the resin, but water is still present as water inclusions. If these are not completely flushed out with plastic resin, they result in disconnected vessel segments [36].
At least 1.5 ml of vascular casting resin should thus be perfused. However, since the resin begins polymerization within approximately 20-30 minutes, only limited time is available to perfuse this volume before increased viscosity and hardening of the substance prevent further perfusion. Sufficiently high flow rates are therefore required for reliable and complete vascular filling, which are in turn a function of perfusion pressure. During protocol optimization, it was found that between 3 ml and 5 ml of PU4ii could be perfused at pressures between 170 mmHg to 200 mmHg, respectively. Pressures higher than 200 mmHg would lead to bursting of the vessels, first on the surface of the kidney, where resin would then flow into the space between the kidney and the renal capsule, distorting its outer shape [39]. At even higher pressures, bleeding into the renal sinuses would be observed. It is therefore crucial to employ pressure-controlled pumps instead of standard syringe pumps with constant flow rates as commonly used for transcardial perfusions. A pressure-controlled pump can be realized with simple tools by actuating a syringe with a weight providing a constant force via gravity. In addition to the change in pumps, ligations need to be tied using constrictor knots or knots with similar strength, as the standard surgical throw is insufficiently tight at these pressures and would result in immediate leakage [40].

170 mmHg to 200 mmHg are pressures well above physiological blood pressures and cause distension of the blood vessel diameters, as well as tubular collapse due to mechanical compression. At lower pressures however, the reduced flow speed of the resin increases the likelihood of water inclusions remaining in the kidney vasculature. As such, perfusion pressure has to be chosen as a compromise between achieving reliable filling of the vasculature and adhering to physiological pressure ranges. For the 3D atlas project, full connectivity of the vascular structure was considered a priority over accurate diameters of compliant vessels, and thus pressures at the upper end of the range were chosen.

4.5.2 Single distance propagation-based hard X-ray phase contrast imaging

Kidneys were scanned at the ID19 tomography beamline of the ESRF during experiment MD1014. Kidneys were kept in native hydrated state and embedded in agar in 0.5 ml PCR tubes. While embedding in paraffin or epoxy resin would yield better sample stability, dehydration would damage the vascular casts and dissolve the 1,3-diiodobenzene, destroying contrast. Kidneys would furthermore be inaccessible for subsequent tissue clearing.
Kidneys were imaged with pink beam with a mean photon energy of 19 keV. Projections were recorded with a 100 µm LuAG scintillator, 4× magnification lens and a pco.edge 5.5 camera, resulting in a pixel size of 1.625 µm.
The PCR tubes had an inner diameter of 6 mm and an outer diameter of about 7.9 mm. A single scan with asymmetric rotation axis was used to fit the containers into the field of view. In this mode, projections at 180° angle to each other could be stitched with a 180 pixel overlap, resulting in extended field of view of 8.029 mm. This corresponds to 1.93 times the size of a single 2560 pixel array of the pco.edge 5.5 camera. 6 height steps were recorded for each kidney, with 1080 pixels overlap, half the height of the pco.edge 5.5 camera's pixel array, resulting in redundant acquisition of the middle height steps in the kidney.
5125 projections were recorded for each height step with 0.1 s exposure time, resulting in a scan time of 10 min per height step or one hour for a whole kidney. 100 flat-field images were taken before and after each height step and averaged for flat-field correction. Data size was 55 GB per height step, or 330 GB per kidney.
Images were reconstructed using the beamline's in-house PyHST2 software [41], as absorption contrast images and with Paganin-filter [42], choosing a δ/β ratio of 50. Data size for the reconstructed datasets was 193 GB per height step, or 1158 GB per kidney.

4.5.3 Image processing and analysis

4.5.3.1 Vascular segmentation

For the vascular segmentation, the data reconstructed without the Paganin-filter was used. Due to the excellent contrast conferred by the high concentration of contrast agent, retaining maximum resolution had priority over using edge enhancement to increase contrast. As many capillaries were only a few voxels wide and thus consisted entirely of edge voxels, edge enhancement furthermore already contributed to increased contrast without Paganin-filtering.
The six height steps of the dataset were processed individually. First, slices were rescaled based on the grey values of the homogeneous container. The height steps were then denoised using curvelet transform and thresholds were applied based on local statistics within manually set boundaries. The binary masks of the individual height steps were then assembled into the full dataset with an OR operation. All image processing was performed on the Euler high performance computing cluster of the Swiss Federal Institute of Technology in Zurich (ETH) using custom code written by Dr. Diego Rossinelli.

4.5.3.2 Artifact removal

In the resulting blood vessel binary mask, there were three different types of artifacts: 1,3-Diiodobenzene was able to diffuse into white adipose tissue surrounding the kidney resulted in their fat globules being included in the vascular mask. Gas bubbles formed during polymerization of PU4ii plastic resin, leading to holes within the mask in the large vessels. Dust particles on the scintillator could not be compensated for entirely by flat-field correction, leading to severe ring artifacts in the data.
To remove the artifacts, the outline of the adipose tissue was outlined manually in a number of regions of interest to serve as ground truth in machine learning. As fat cells are only found outside of the kidney, the training data could be supplemented by selecting additional regions of interest devoid of fat from within the kidney and declaring the entire region as non-fat without requiring manual outlines. With this approach, fat could be identified and removed from the binary mask.
Gas bubbles within the mask were removed by connected component analysis. All background voxels were grouped according to whether their faces were adjacent, which is also known as d6-connected. The background component was identified, and all components not connected to it were filled, removing holes in the mask that were introduced either by physical gas bubbles in the vascular cast or segmentation artifacts.
Ring artifacts were first identified based on the coordinates of the dust particles visible in the flat-field images. Since this did not remove all the rings in the segment, the entire segment was inspected visually and coordinates of the rings manually marked. Rings were then deleted and replaced by interpolation of neighboring voxels.

4.5.3.3 Connectivity analysis

Connected component analysis was performed on the vascular segment, but with d26-connectivity, meaning voxels touching at the edges were considered to be connected as well. Disconnected components were discarded, yielding a binary vessel mask with full connectivity. A number of capillaries were discarded in this step, meaning that the fully connected vessel mask is less complete than the initial segmentation. A seed point at the papilla was manually chosen, and the shortest path of every voxel to this point along the vasculature calculated by solving the Eikonal equation, creating a path distance map.
Glomeruli were then identified by k-means clustering and manual segmentation of several glomeruli as ground truth data. Similarly to the fat removal, additional training data was generated by taking regions-of-interest from the medulla, where no glomeruli are found. The locations and outlines of 13 000 glomeruli in the mouse kidney were identified, which is a number consistent within the expected number of nephrons for C57BL/6J mice [43]. With the location of all glomeruli identified, the length of the path from the papilla to each of those glomeruli was extracted from the path distance map. The paths could then be traced back to the seeding point and visualized.
A kidney surface hull was created by dilation and erosion. The signed distance transform of the blood vessel mask was calculated and a threshold was set at 400 voxels distance from the mask. Another signed distance transform was calculated, and a threshold of -400 voxels chosen to erode the mask back to the original size. The distance of the identified glomeruli to the kidney surface was calculated with another distance transform based on the kidney hull. These distances representing the depth of the glomeruli within the kidney were then plotted against the path distance to the papilla. There was no indication that cortical and juxtamedullary glomeruli form two distinct classes in either distance from the cortical kidney surface or the path length along the vasculature to the papilla. We found no evidence that the inner medulla is supplied by a separate vascular network originating from juxtamedullary glomeruli. Cortical glomeruli had no physiologically meaningful difference in blood vessel path distances to the papilla compared to juxtamedullary glomeruli.

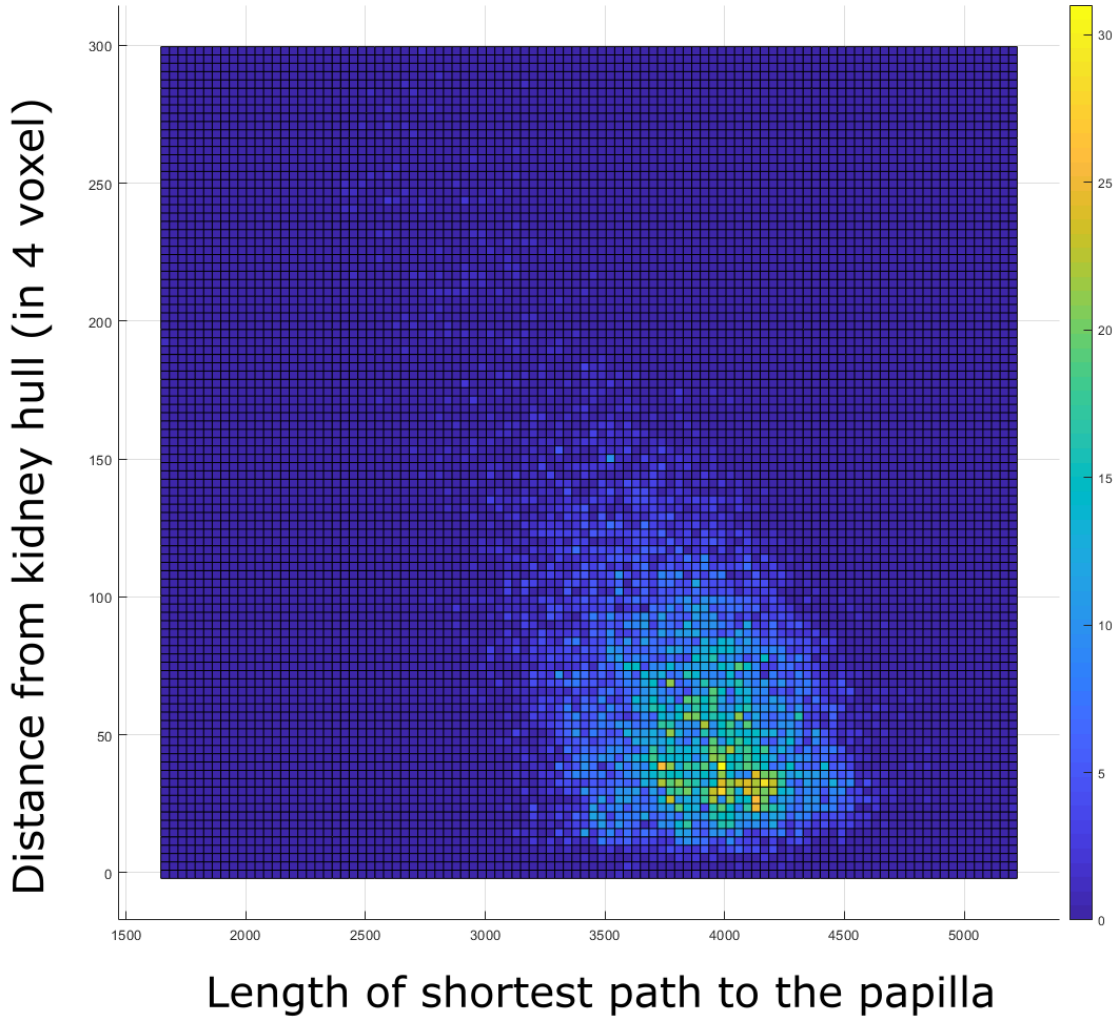

Fig. 15.: Joint histogram of the distance from the kidney hull and shortest path length to the papilla.

4.5.3.4 Tubular segmentation

Tubular lumina were segmented based on the Paganin-filtered data. However, due to the high perfusion pressure and the lack of glomerular filtration during perfusion of the hydrophobic plastic resin, many tubular lumina were mechanically compressed and collapsed. The reduction in diameter resulted in discontinuities in the segmented dataset, leading to an unacceptably large number of discarded tubules when connected component analysis was performed. Furthermore, the smaller size and lower signal-to-background ratio in the inner medulla made the segmentation unreliable in that region. Connectivity analysis was therefore not performed. The tubular structure is nevertheless available as structural data, and can be used for quantifications which do not require full connectivity.

4.5.4 Detailed vascular casting protocol

1. Dissolve 3 g 1,3-Diiodobenzene in 10 g 2-Butanone, mix with 10 g PU4ii resin for an end concentration of 100 mg iodine/g. (This is sufficient for the GE Nanotom µCT, but more is always better.)
2. Anaesthetize the mouse with Ketamine/Xylazine, put a cylindrical object (syringe needle cap) as support under the mouse, pin it to the board. Open up the abdomen and carefully move the intestine to the right side. Make sure to keep the organs, especially the kidneys, wetted with 37 °C 0.9 % saline or equivalent throughout the entire procedure, or blood will start to clot. There is a piece of transparent tissue than connects the intestine with the liver. This must be cut to be able to completely move the intestine out of the way without injuring the liver in the process. Move the cylindrical object below the mouse until the superior mesenteric artery is being moved up for better visibility. It is recognizable by being a horizontal blood vessel going right to the intestine and is surrounded by a thick, white tube. Prepare a ligation with greased surgical suture around this vessel.
   Follow the superior mesenteric artery to its origin at the abdominal aorta, which requires the careful removal of fat. Prepare a ligation using a constrictor knot around the abdominal aorta right above where it connects to the superior mesenteric artery. Standard surgery knots are not sufficiently tight for the used perfusion pressures [40].
3. The vena cava is generally immediately visible. Grab the fat to the right of the vena cava and move it up, take tweezers to split the fat on the right side to reveal the right underside of the vena cava. The abdominal aorta is the white/red blood vessel stuck to the vena cava. Both these blood vessels are surrounded by a tissue tube, which needs to be cut or split with tweezers. Gently grab the abdominal aorta and pull it to the right. If you can see a gap between the abdominal aorta and the vena cava, you can cut it with surgical scissors or stick the sharp end of tweezers or surgical scissors in it to create a separation.
   If the gap is too small to do that, find another position closer to the kidneys or try to grab a part of the tube surrounding the blood vessels with another set of tweezers without grabbing the blood vessels, then release your grip on the abdominal aorta to grab the gap on the other side and pull gently. This will increase the gap.
4. Clamp the abdominal aorta directly below the kidneys and above the lower ligation to stop the blood flow. The more space you have between the clamp and the ligation, the better. You can clamp part of the vena cava as well without problem.
5. Cut partially into the abdominal aorta, below the lower ligation. The lower the better, but if it is too low you may have problem moving the needle all the way up to the ligation. Do not cut through the abdominal aorta, only make a small incision.
   Insert vessel dilating forceps into the hole, spread the vessel and insert a 21 G butterfly needle in-between the arms until it is under the ligation or close enough to it. Pin the butterfly needle to the board, then use tweezers to close the ligation and hold it to move the vessel further over the needle. I recommend using a constrictor knot for this ligation, as it is tightly secured when closed and does not need an additional knot. Remove vessel clamp.
6. Close the ligation of the superior mesenteric artery and ligation of the upper abdominal aorta, above the superior mesenteric artery.
7. Cut out a small window in the vena cava, making sure that it is some distance away from the renal veins to prevent them from collapsing under low pressure. Perfuse with the kidneys with 10 ml PBS/heparin and 50 ml 4 % formaldehyde at 150 mmHg using hydrostatic pressure.

8. Add 1.6 g PU4ii hardener to the plastic resin mix prepared in step 1, mix well and degas in vacuum. Both the mixing and the degassing are important to prevent bubble formation in the plastic later on. Degassing needs a filter paper as seeding stone and should proceed until no more bubbles form.
9. Perfuse with plastic resin at 150 - 200 mmHg, depending on the requirements. I use a 50 ml syringe with 2.8 mm diameter, which is pushed down by a 1.25 kg weight on top, which would give 150 mmHg if the syringe were frictionless. The syringe is inserted over a 3-way valve into the butterfly needle. In this step, there is a tendency for the plastic to exit the abdominal aorta at the needle insertion point rather than going through the kidneys. To prevent this, grab the ligation with tweezers and hold it shut, which is another benefit of using the constrictor knot. The perfusion will proceed with a very low flow rate (somewhere in the range of 0.2 ml/min). At the beginning, you will see plastic bubbles in water leaving the renal veins. Just leave the pressure on until the plastic hardens, as the perfusion will stop on its own once flow resistance increases too much for the perfusion to proceed. You should be able to perfuse for at least 5 ml of plastic resin for a complete casting.
10. Leave the needle in until the plastic hardens to avoid a sudden pressure drop. The plastic can take a variable time to solidify, 1 h is a rough guideline. Once the plastic has solidified fully, the kidneys can be excised and kept in 4 % formaldehyde. Alternatively, one can immerse the entire mouse immediately in 4 % formaldehyde and excise the kidneys at a later date.

4.5.5 Discussion

This project features the completion of the first 3D atlas containing both the vasculature of the whole mouse kidney down to the capillary level with full connectivity and the associated tubular structure. To achieve this, an optimized vascular casting procedure for more reliable and consistent filling of the capillaries in the mouse kidney was developed. State-of-the-art synchrotron hard X-ray μCT was employed to perform micrometer resolution imaging of an entire kidney. Vascular and tubular structures were extracted from the terabyte-scale dataset and are available as binary masks. Connectivity analysis of the vascular segment was performed to yield a single, uninterrupted binary mask. All individual glomeruli were identified and segmented, and paths of every individual glomerulus in the kidney to the papilla were traced along the blood vessels. We expect these data to form a new 3D atlas usable as reference for anatomical studies and computational modeling of kidney transport processes.

There are a few limitations to this atlas. A few capillaries vessels present within the initial segmented vessel mask were discarded during the connectivity analysis, resulting in fewer vessels being included in the connected binary mask. The perfusion pressure was well above physiological pressures, causing an increase of vascular diameter of the preglomerular vessel tree, leading to virtual artificial shortcuts between the arterial tree and the venous tree within the mask. These are the result of compressed blood vessel walls. Visual inspection of the scans revealed that no bleeding took place. The high perfusion pressure is furthermore responsible for the mechanical compression and collapse of parts of the tubular lumina, which led to interruptions in the binary mask that prevented a proper connectivity analysis of the tubular tree.

Since the development of our 3D atlas, another microparticle-free vascular casting resin has become commercially available. μAngiofil is another iodine-based vascular casting resin suitable for capillary level imaging [44], and has recently been used for kidney vascular imaging as well [39]. In our own evaluation, its performance was found to be superior to the PU4ii mixture described, with the main benefit to be found in the lack of diffusion of contrast agent into the adipose tissue. In other aspects however, the performance was comparable to PU4ii. Issues with capillary filling, gas bubble

generation and water inclusions were still present, as they are inherent problems of hydrophobic plastic resins. While less optimization work was performed due to the considerably higher costs of 400 CHF per mouse for µAngiofil compared to the approx. 20 CHF per mouse for PU4ii, a new 3D atlas produced with µAngiofil or any other hydrophobic plastic resin-based vascular casting reagent would share the same limitations as the current PU4ii-based atlas. Instead, further development of water-soluble X-ray contrast agents would be required to overcome those limitations.

4.5.6 Acknowledgements

I would like to thank Anastasios Marmaras, Axel Lang, Jan Czogalla and Eric Meyer for guidance in establishing the vascular casting protocol, Virginia Meskenaite, Karen Scholz and Svende Pfundstein for help with animal experiments, Peter Thalmann, Christos Bikis, Margie Olbinado and Alexander Rack for assistance in X-ray scanning, Ufuk Olgaç and Kartik Jain for assistance during image processing and input concerning computational modeling.

5 Polymeric water-soluble contrast agent

5.1 Limitations of plastic-based vascular casting

In the 3D atlas of the mouse kidney project, several limitations of vascular casting with plastic resins were identified. The most important issue concerned the reliability and consistency of filling all the capillaries. As hydrophobic compounds, plastic resins would frequently contain interrupted blood vessel segments. These were mainly the result of water having been insufficiently flushed out of the vasculature and remaining trapped within the resin. Those water inclusions were frequently found in large vessels and could be recognized and categorized by their shapes. If more water than plastic resin was present in the vasculature, they could be seen interrupting the entire vessel, leaving balls of contrast agent-containing plastic in the middle. If more plastic than water was present, the water inclusions would be either expressed as round bubbles themselves or might show as distorted stripes, depending on the flow and viscosity at the time of hardening of the plastic resin.
In order to remove water inclusions, sufficient volumes of plastic resin have to be in injected before hardening completes. Correspondingly, high flow rates are required, necessitating high perfusion pressures up to 200 mmHg in order to reliably and consistently remove water inclusions. This supraphysiological pressures may cause bleeding of superficial capillaries into the renal capsule or renal sinuses, and will cause distension of the blood vessels and compression of the tubular lumina. The choice of the right perfusion pressure then comes down to a compromise between physiological conditions and reliability of the filling.
The second major source of holes and interrupted vessels was the formation of gas bubbles in the cast. Gas bubbles were either entirely round or assembled from multiple round bubbles in the same location, or could be identified by their lower X-ray absorption compared to the hydrated background. To reduce the number of gas bubbles, extensive degassing has to be applied prior to perfusion. This not only reduces the time available for perfusion before polymerization completes, but also increases viscosity due to evaporation of solvent. The amount of degassing to be applied is therefore difficult to optimize and also subject to compromises.
These drawbacks resulted in a need for alternatives to vascular casting with PU4ii.

Conference Paper

5.2 Evaluation of metal nanoparticle- and plastic resin-based X-ray contrast agents for kidney capillary imaging

This chapter was first published in Developments in X-ray Tomography XII as:

W. Kuo, G. Schulz, B. Müller, and V. Kurtcuoglu, "Evaluation of metal nanoparticle- and plastic resin-based X-ray contrast agents for kidney capillary imaging," in *Developments in X-Ray Tomography XII*, San Diego, United States, 2019, p. 23. [45]

This conference paper reports on results on using blood pool contrast agents and the microparticle-free µAngiofil plastic resin for *ex vivo* high resolution vascular imaging in mouse kidneys. My work on this publication consisted of developing the perfusion protocols for different types of contrast agents, performing the µCT imaging and reconstruction and evaluating the final datasets.

Evaluation of metal nanoparticle- and plastic resin-based X-ray contrast agents for kidney capillary imaging

Willy Kuo[1,2,3], Georg Schulz[3], Bert Müller[3], Vartan Kurtcuoglu[1,2]

[1] Institute of Physiology, University of Zurich, Zurich, Switzerland;

[2] National Centre of Competence in Research, Kidney.CH, Zurich, Switzerland;

[3] Biomaterials Science Center, Department of Biomedical Engineering, University of Basel, Allschwil, Switzerland

5.2.1 Abstract

Injection of radiopaque substances into the vasculature followed by *post mortem* high resolution X-ray μCT imaging currently remains the primary means for capillary imaging in soft tissue. Commercial contrast agents for *in vivo* applications are, however, typically small molecular compounds that can easily diffuse across the blood vessel walls, which makes them unsuitable for *ex vivo* high resolution X-ray μCT imaging. We evaluated the suitability for kidney capillary imaging of the nanoparticle-based blood pool contrast agents Aurovist 15 nm and ExiTron nano 12000, along with the vascular casting resin μAngiofil, by *post mortem* imaging of whole mouse kidneys with 4-5 μm voxel size using the laboratory source μCT system Nanotom m. Based on the results, we identified specific obstacles to reliable capillary filling in the kidney, which will aid in the development of next-generation X-ray contrast agents and protocols.

Keywords
Biological soft tissue, absorption contrast, contrast agents, organ imaging, kidney, vasculature, blood vessels

5.2.2 Introduction

Chronic kidney disease (CKD) is characterized by a decline in renal filtration function and is prevalent in 15% of the population of the United States and 25% of the population above 65 years of age [1]. In 2016, 726,331 patients were in need of a kidney transplant or dialysis, which is required below 12.5% of remaining filtration function. Capillary loss in the kidneys is a hallmark of CKD and three-dimensional (3D) imaging of the kidney vasculature with hard X-ray micro computed tomography (μCT) is employed for quantifying the extent of capillary loss and investigating its effects on hypoxia-dependent disease progression pathways [2]–[4]. Injection of radiopaque substances into the vasculature followed by *post mortem* high resolution X-ray μCT imaging currently remains the primary means for capillary imaging in soft tissue [4], [5]. *In vivo* methods like clinical X-ray CT, magnetic resonance imaging (MRI) [6], ultrasound imaging [7], photoacoustic [8] imaging and intravital multiphoton microscopy [9], [10] feature insufficient resolution or field-of-view for capillary imaging on the whole organ scale. Methods relying on staining the tissue [11], [12] and phase contrast X-ray imaging of unstained tissue [13] are capable of capturing kidney morphology, but are unable to distinguish capillaries from other hollow structures, such as kidney tubuli.

Standard iodine-based angiography X-ray contrast agents are small molecules cleared from the blood via glomerular filtration in the kidney, a process in which molecules smaller than 6 nm in hydrodynamic diameter are sieved as primary urine into the renal tubules [14]. This leads to both a reduction in contrast agent concentration in the blood vessels as well as to an increase thereof in the tubules, preventing distinction of the vascular and tubular lumina and leading to a reduction in contrast-to-noise ratio. To prevent this behavior, contrast agents larger than 6 nm are required, which

are available in the class of blood pool contrast agents. This class consists mainly of surface-functionalized metal nanoparticles whose main clinical application is currently magnetic resonance imaging (MRI) with gadolinium-based contrast agents [15]. Nanoparticles based on high atomic weight elements such as gold, iron and barium are commercially available as X-ray contrast agents for preclinical imaging. These have been used mainly for low resolution *in vivo* imaging studies [16]–[19], but high resolution *ex vivo* imaging is required to capture capillaries. This off-label application creates a different set of requirements. Most importantly, all capillaries need to be completely filled with contrast agent in a reliable and reproducible fashion, in order to judge whether tissue regions without blood vessels represent genuine capillary rarefaction or simply contrast agent filling artifacts. In this study, the reliability of two blood-pool contrast agents when filling the renal capillary network was investigated: Aurovist 15 nm, a gold-nanoparticle-based blood pool contrast agent, and ExiTron nano 12000, an alkaline earth metal-nanoparticle-based blood pool contrast agent. The performance of these agents was compared to that of µAngiofil, an iodine-based vascular casting resin. Mouse kidneys were imaged *post mortem* with 4 to 5 µm voxel size using a laboratory source absorption-contrast µCT device (GE Nanotom m). Specific obstacles to reliable capillary filling in the kidney were identified, which will aid in development of specialized contrast agents and protocols for *ex vivo* capillary X-ray imaging of the kidney.

5.2.3 Materials and methods

5.2.3.1 Animal husbandry

C57BL/6J mice were kept in individually ventilated cages with ad libitum access to water and standard rodent food (Kliba Nafag 3436) in 12 h light/dark cycles. All animal experiments were approved by the veterinary office of the canton Zurich (license numbers ZH177/13 and ZH233/15).

5.2.3.2 Abdominal aorta perfusion

Mice were anaesthetized with ketamine / xylazine and kidneys were perfused retrogradely via the abdominal aorta based on the isolated perfused kidney technique described by Czogalla et al. [20]. Constrictor knot ligations [21] were applied to the abdominal aorta superior of the renal artery and on the superior mesenteric artery to direct all flow to the kidneys. The kidneys were flushed with 10 ml phosphate-buffered saline (PBS) and fixed with 150 mmHg hydrostatic pressure. With the exception of µAngiofil, all contrast agent solutions were injected using a syringe actuated by a constant weight.

5.2.3.3 X-ray micro computed tomography

All kidneys were scanned on a Nanotom m X-ray µCT scanner (General Electric, USA) equipped with a water-cooled tungsten target. The X-ray tube was used in mode 0 with an acceleration voltage of 50 kV or 60 kV and a beam current of 310 µA. No additional X-ray filter was applied.

5.2.3.4 µAngiofil

Kidneys were flushed with 10 ml PBS and fixed with 100 ml 4% formaldehyde / 0.5% glutaraldehyde in PBS at 150 mmHg hydrostatic pressure. µAngiofil (Fumedica AG, Switzerland) was injected at a constant flow rate of 0.45 ml/min, according to the manufacturer's instructions. Kidneys were excised after polymerization and embedded in 1.5% agar in PBS in a 1.5 ml centrifugation tube. Kidneys were scanned with an acceleration voltage of 50 kV and 4.889 µm voxel size.

5.2.3.5 µAngiofil degassed

Kidneys were flushed with 10 ml PBS and fixed with 100 ml 4% formaldehyde / 0.5% glutaraldehyde in PBS at 150 mmHg hydrostatic pressure. µAngiofil was degassed in a vacuum chamber at 90 mbar and injected at a constant flow rate of 0.45 ml/min. Kidneys were excised after

polymerization and embedded in 1.5% agar in PBS in a 1.5 ml centrifugation tube. Kidneys were scanned with an acceleration voltage of 50 kV and 4.889 µm voxel size.

5.2.3.6 Aurovist 15 nm unfiltered

Kidneys were flushed with 10 ml PBS and fixed with 50 ml 4% formaldehyde at 150 mmHg hydrostatic pressure. Free aldehydes were flushed out with 5 ml PBS and a mixture of 150 µl Aurovist 15 nm (Nanoprobes Inc., USA) with 3% gelatin in 2 ml PBS was injected (15 mg gold/ml). Kidneys were excised, immersed briefly in 4% formaldehyde and embedded in 3% gelatin in PBS in a 1.5 ml centrifugation tube. Kidneys were scanned with an acceleration voltage of 50 kV and 4.444 µm voxel size.

5.2.3.7 Aurovist 15 nm filtered

Kidneys were flushed with 10 ml PBS and fixed with 100 ml 2% glutaraldehyde in PBS at 150 mmHg hydrostatic pressure. 200 µl Aurovist 15 nm were mixed with 1.5 ml PBS (23.6 mg gold/ml), pressed through a 1.2 µm pore size syringe filter and injected into the kidneys. Renal artery and vein of each kidney were ligated immediately afterwards. Kidneys were excised and embedded in 1% agar in PBS in a 0.5 ml PCR tube. Kidneys were scanned with an acceleration voltage of 60 kV and 3.2 µm voxel size.

5.2.3.8 ExiTron nano 12000 unfiltered

Kidneys were flushed with 10 ml PBS and fixed with 100 ml 4% formaldehyde / 1% glutaraldehyde in PBS at 150 mmHg hydrostatic pressure. Free aldehydes were flushed out with 15 ml PBS and 0.4 ml ExiTron nano 12000 nanoparticles (nanoPET Pharma GmbH, Germany) in 1.6 ml PBS were injected. Renal artery and vein of each kidney were ligated immediately afterwards. Kidneys were excised and embedded in 6% gelatin with 1% glutaraldehyde in PBS. Kidneys were scanned with an acceleration voltage of 60 kV and 4.4 µm voxel size.

5.2.3.9 ExiTron nano 12000 filtered

Kidneys were flushed with 10 ml PBS and fixed with 100 ml 4% formaldehyde / 1% glutaraldehyde in PBS at 150 mmHg hydrostatic pressure. Free aldehydes were flushed out with 20 ml PBS. 0.5 ml ExiTron nano 12000 nanoparticles were mixed with 1.5 ml PBS, filtered through a 0.45 µm pore size syringe filter and injected into the kidneys. Renal artery and vein of each kidney were ligated immediately afterwards. Kidneys were excised and embedded in 1% agar in PBS in a 0.5 ml PCR tube. Kidneys were scanned with an acceleration voltage of 60 kV and 4.444 µm voxel size.

5.2.3.10 ExiTron nano 12000 filtered in mannitol

Kidneys were flushed with 10 ml PBS and fixed with 100 ml 4% formaldehyde / 1% glutaraldehyde in PBS at 150 mmHg hydrostatic pressure. 0.5 ml ExiTron nano 12000 nanoparticles were mixed with 1.5 ml isosmotic mannitol solution, filtered through a 1.2 µm pore size syringe filter and injected into the kidneys. Renal artery and vein of each kidney were ligated immediately afterwards. Kidneys were excised and embedded in 1% agar in PBS in a 1.5 ml centrifugation tube. Kidneys were scanned with an acceleration voltage of 60 kV and 4.444 µm voxel size.

5.2.3.11 Visualization

Contrast of the virtual sections was manually adjusted for optimal visibility of relevant features of interest using Fiji/ImageJ [22]. Maximum intensity projections were rendered using Bitplane Imaris 8.4.1.

5.2.4 Results

5.2.4.1 µAngiofil

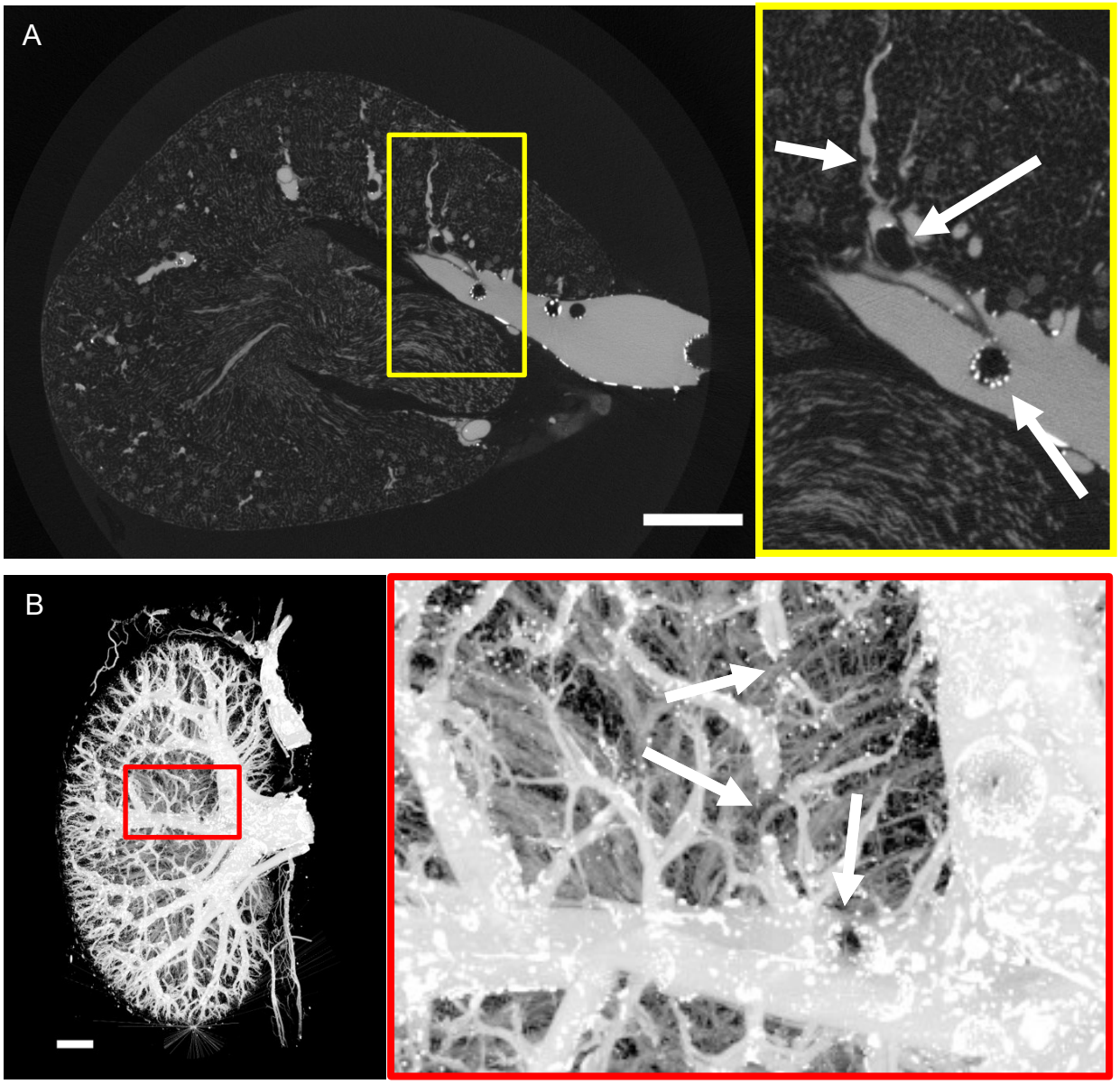

Fig. 1.: Virtual section (A) and maximum intensity projection (B) of a mouse kidney perfused with µAngiofil. White arrows indicate gas bubbles in the cast large enough to interrupt the blood vessel. The scale bars correspond to a length of 1 mm.

µAngiofil reached the entire blood vessel system when used according to the manufacturer's instructions. Many gas bubbles, however, formed during polymerization of the contrast agent, best visible in the larger vessels. These bubbles were of sufficient size to interrupt blood vessels (Fig. 1), which would disturb thickness determination and connectivity analysis. Highly X-ray absorbing particles were found primarily at the phase boundaries, likely having formed due to phase separation and accumulation of the radiopaque component of the plastic resin after polymerization.

5.2.4.2 µAngiofil degassed

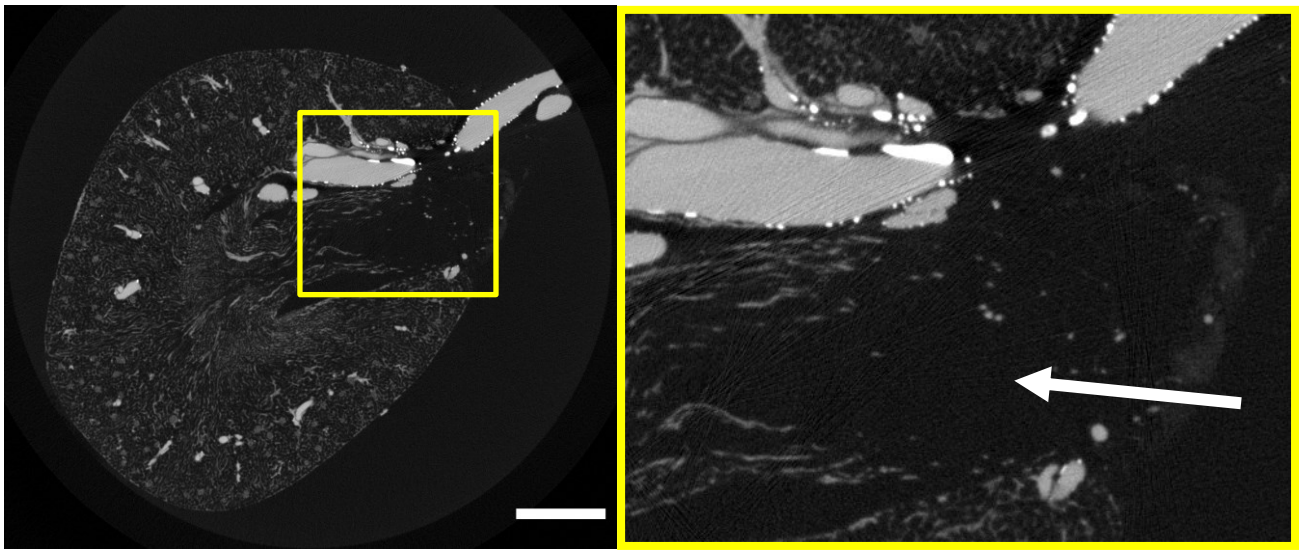

Fig. 2.: Mouse kidney perfused with degassed µAngiofil. The white arrow indicates non-filled vasculature in the inner medulla. The scale bar corresponds to a length of 1 mm.

Degassing of the µAngiofil plastic resin solution in a vacuum chamber prior to perfusion suppressed the formation of gas bubbles (Fig. 2). The vasculature in the inner medulla was no longer completely filled, however, which was likely caused by changes in viscosity of the plastic resin due to evaporation of the solvent during degassing. As the chemical composition of µAngiofil is proprietary information, supplementation of the solvent was not possible for the present study.

5.2.4.3 Aurovist 15 nm unfiltered

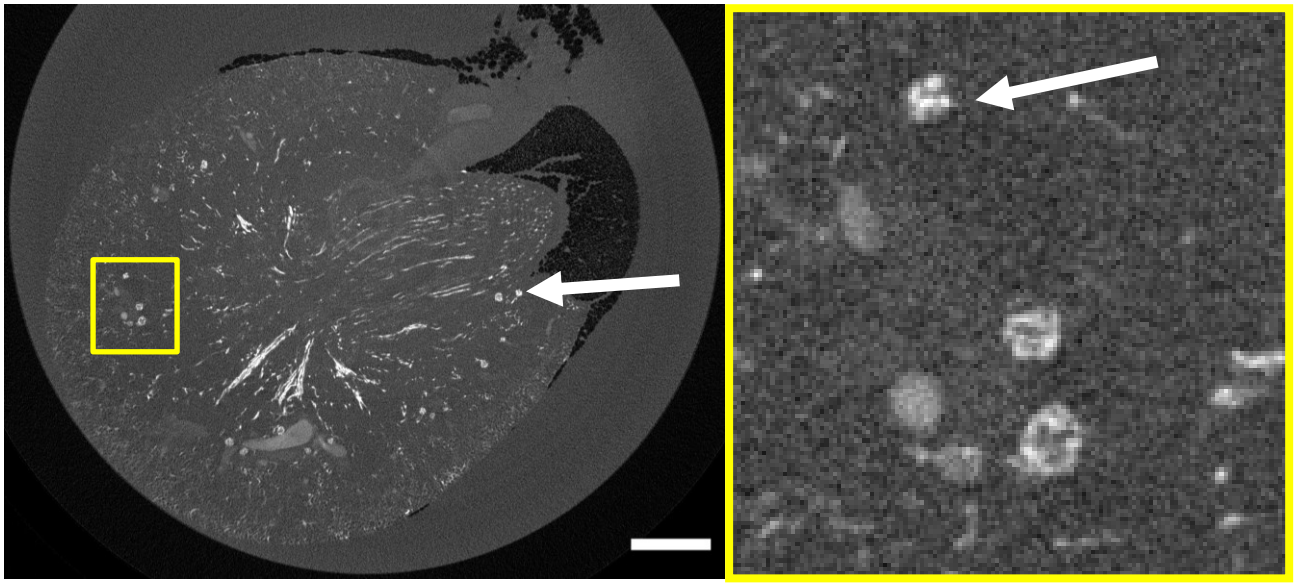

Fig. 3.: Mouse kidney perfused with Aurovist 15 nm. The white arrows indicate glomeruli containing highly absorbing species, suggesting blockage of the capillary loops by aggregated nanoparticles. The scale bar corresponds to a length of 1 mm.

Aurovist 15 nm gold nanoparticles suspended in gelatin did not fill the entire capillary network. Patches of missing vasculature could be found homogeneously distributed throughout the whole kidney volume. Highly absorbing species in the glomeruli suggest that blockage of the capillary loops by aggregated nanoparticles may prevent proper perfusion of the capillary bed. Despite the gelatin perfusion, nanoparticles also slowly diffuse out of the vasculature, reducing contrast over time.

5.2.4.4 Aurovist 15 nm filtered

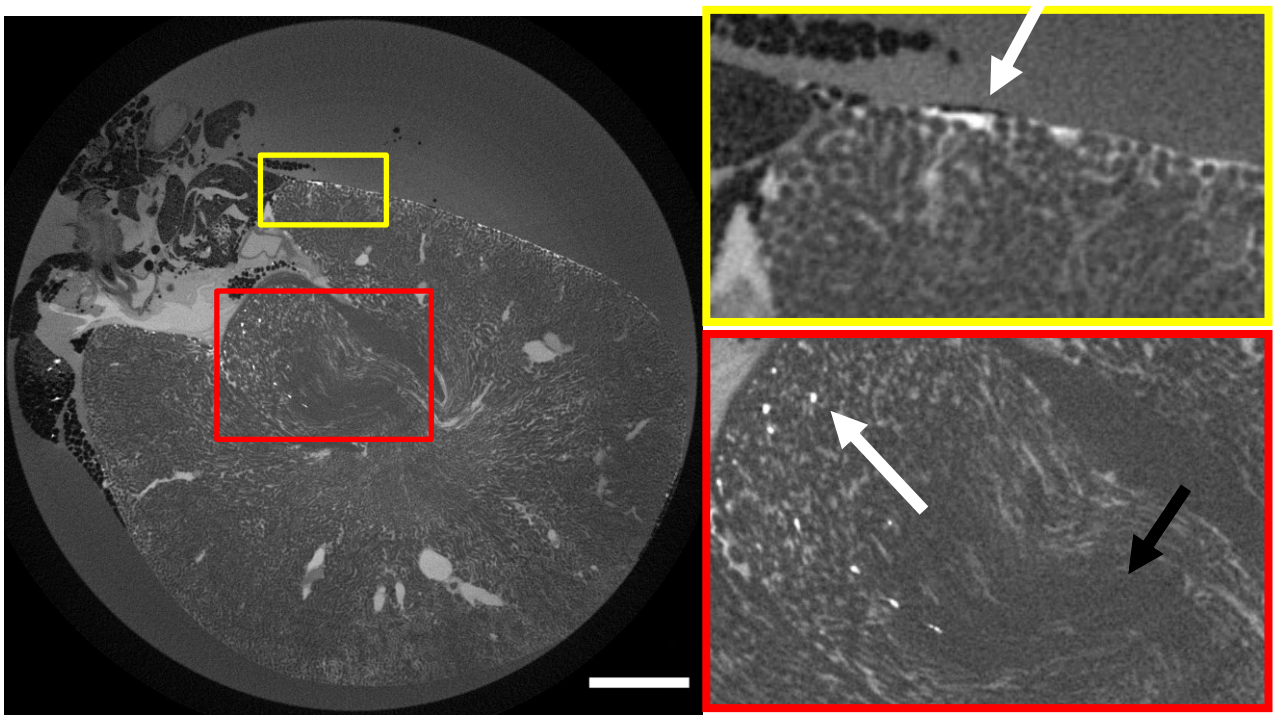

Fig. 4.: Mouse kidney perfused with filtered Aurovist 15 nm. The black arrow indicates non-filled vasculature in the inner medulla. The white arrows indicate highly absorbing species in the vasa recta and superficial cortical capillaries, suggesting blockage by aggregated nanoparticles. The scale bar corresponds to a length of 1 mm.

Filtered Aurovist 15 nm without gelatin filled almost all of the capillaries in the kidney. A subset of the vasa recta in the inner medulla were not filled, and part of the cortical capillary network showed lower concentrations of contrast agent. Highly absorbing species could be identified in the inner medulla and at the superficial cortical capillaries, suggesting blockage owing to remaining or newly formed aggregates of nanoparticles.

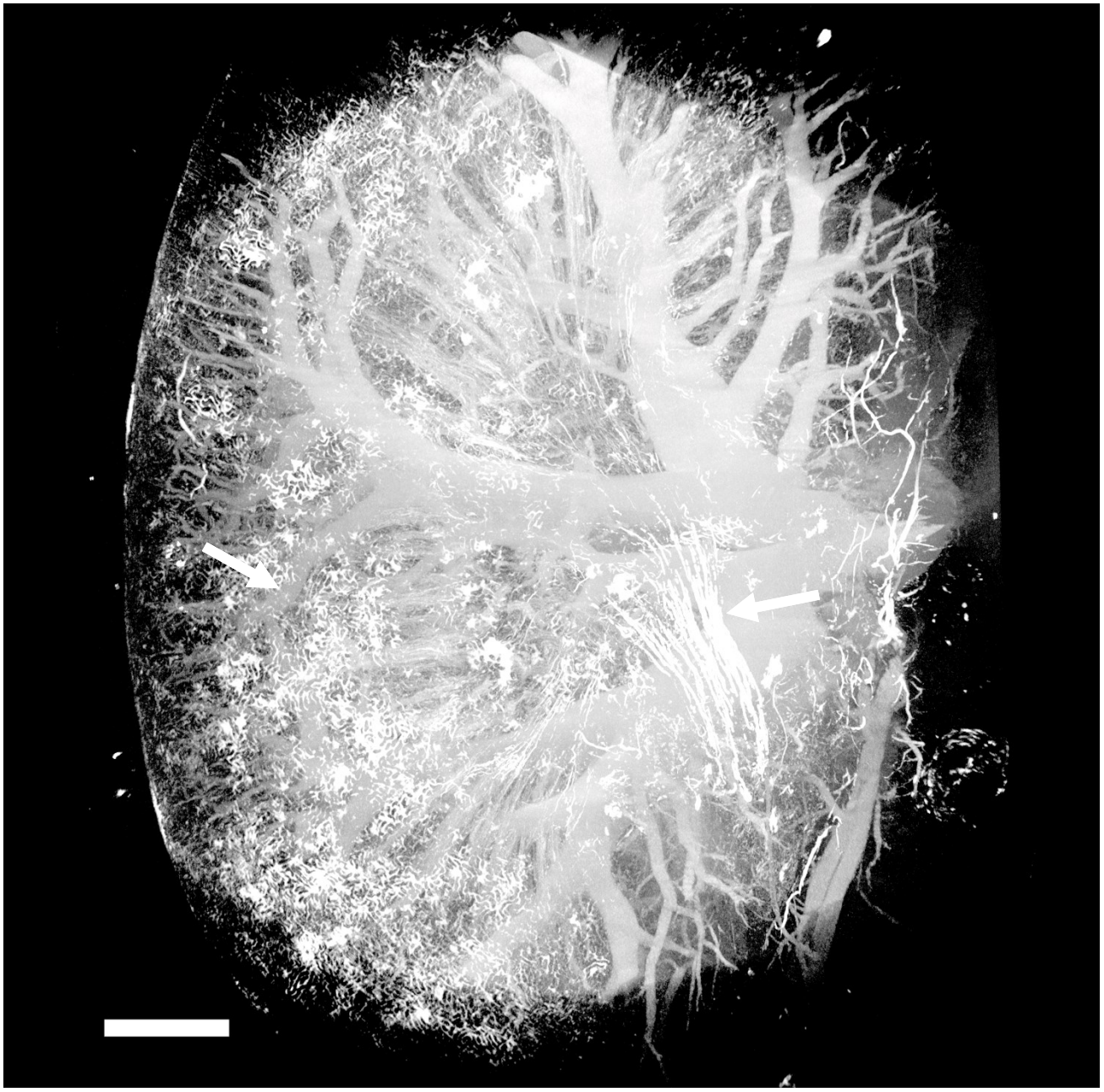

Fig. 5.: Maximum intensity projection displaying a single height step of a mouse kidney perfused with filtered Aurovist 15 nm. The white arrows indicate highly absorbing species in the vasa recta and superficial cortical capillaries, suggesting blockage by aggregated nanoparticles. The scale bar corresponds to a length of 1 mm.

5.2.4.5 ExiTron nano 12000 unfiltered

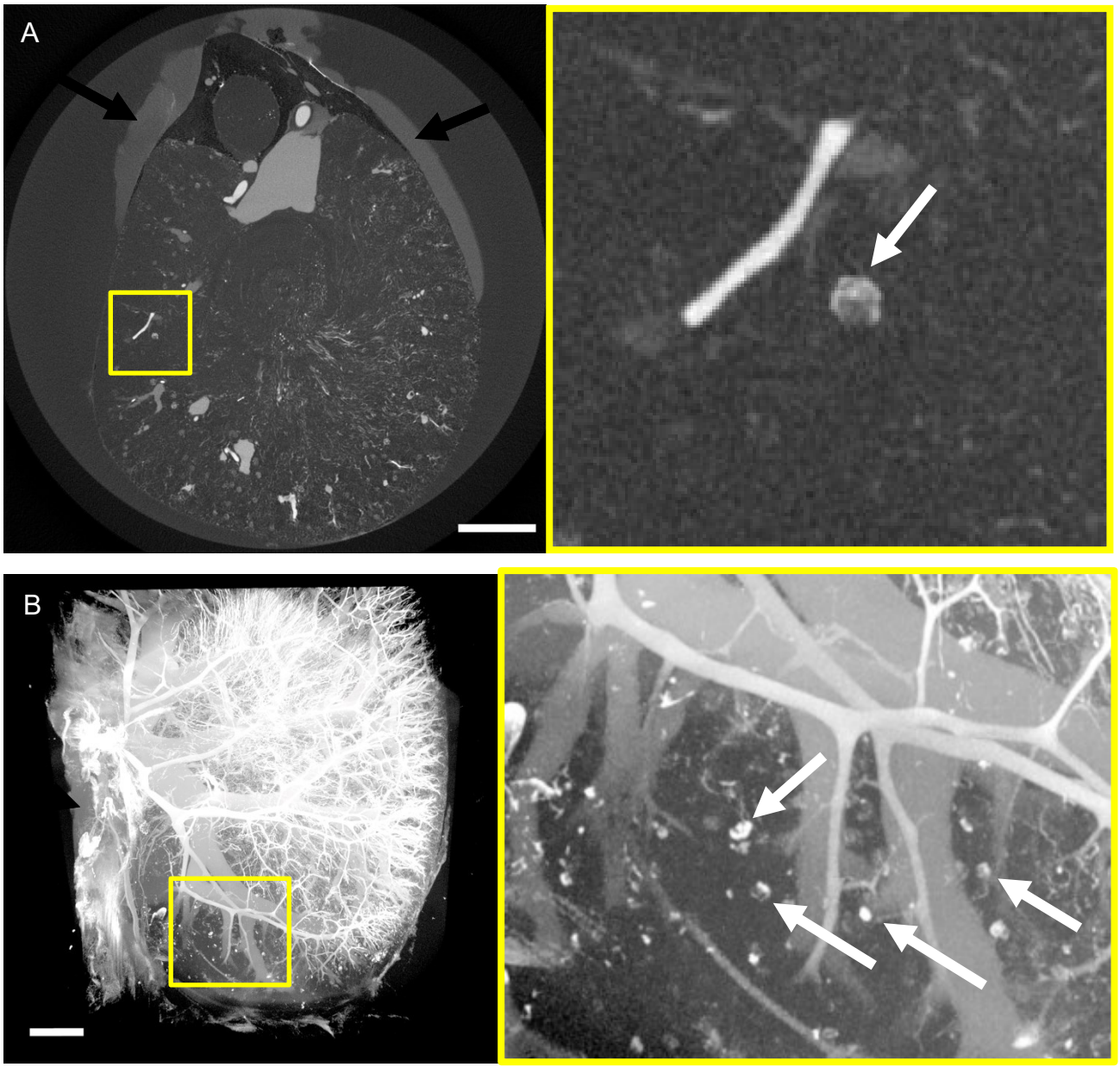

Fig. 6.: Virtual section (A) and maximum intensity projection (B) of a mouse kidney perfused with unfiltered ExiTron nano 12000. The white arrows indicate glomeruli containing highly X-ray absorbing species, suggesting blockage of the capillary loops by aggregated nanoparticles. The black arrows indicate accumulation of contrast agent leaking into the surrounding agar medium through the renal artery and vein. The scale bars correspond to a length of 1 mm.

Unfiltered ExiTron nano 12000 nanoparticles yielded results similar to unfiltered Aurovist 15 nm nanoparticles. Non-filled capillaries were found in one large cortical region and the associated parts in the medulla. Further small regions with missing vessels were homogeneously distributed throughout the rest of the kidney. Aggregates in the glomeruli suggest that the blockage of the capillary loops prevents further perfusion of the nanoparticles.

5.2.4.6 ExiTron nano 12000 filtered

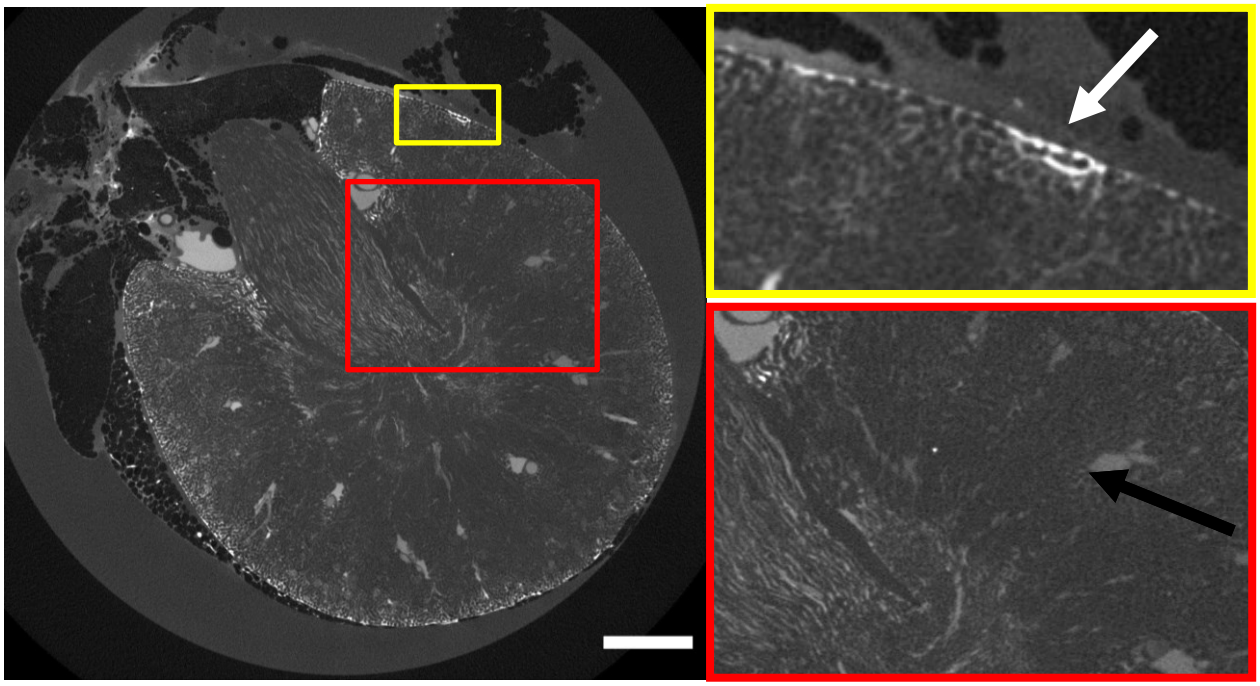

Fig. 7.: Mouse kidney perfused with filtered ExiTron nano 12000. The white arrow indicates highly absorbing species in superficial cortical capillaries. The black arrow indicates unfilled vasculature in the cortex and the outer medulla. The scale bar corresponds to a length of 1 mm.

As with Aurovist 15 nm, filtering ExiTron nano 12000 nanoparticles resulted in improved, but still incomplete filling. Empty regions were found in the cortex and the outer medulla. Aggregates could be seen primarily in the superficial capillary network.

5.2.4.7 ExiTron nano 12000 filtered in mannitol

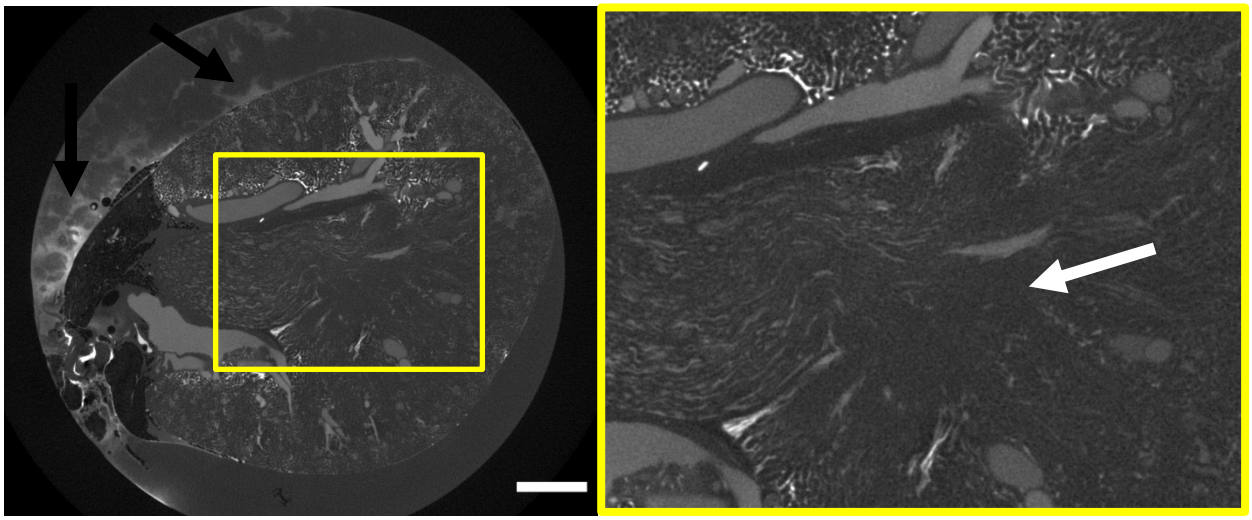

Fig. 8.: Mouse kidney perfused with filtered ExiTron nano 12000, suspended in an isosmotic mannitol solution. The white arrow indicates incompletely filled vasculature in the outer medulla. The black arrows indicate accumulation of contrast agent leaking into the surrounding agar medium through superficial capillaries or the renal artery and vein. The scale bar corresponds to a length of 1 mm.

Based on suggestions from the manufacturer, ExiTron nano 12000 nanoparticles were suspended in isosmotic mannitol solution instead of PBS to reduce aggregation of the particles. Regions with

incompletely filled capillaries could still be found. Aggregated nanoparticles were still present, albeit in capillaries in the vicinity of large vessels, rather than superficial capillaries.

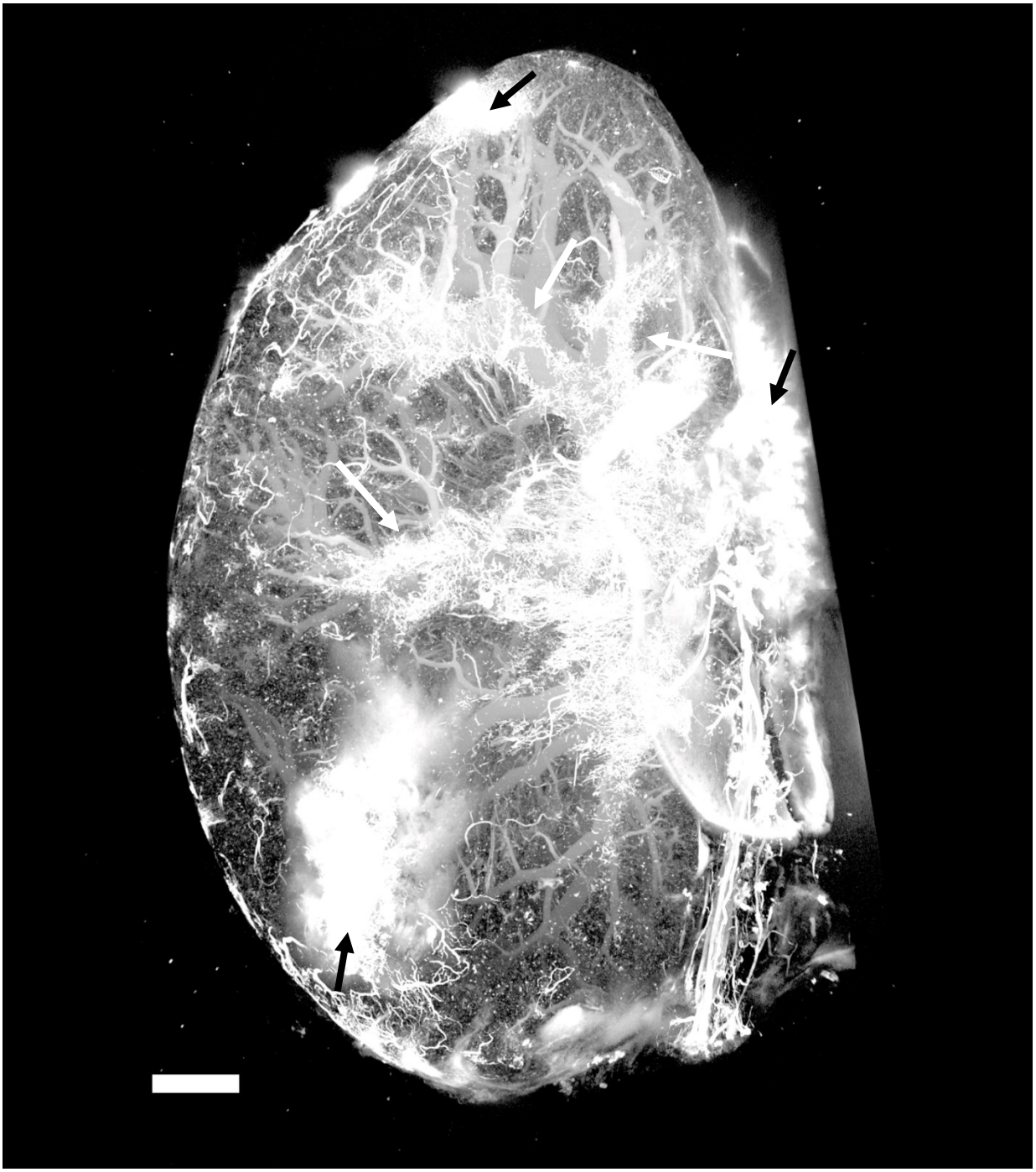

Fig. 9.: Maximum intensity projection of a mouse kidney perfused with filtered ExiTron nano 12000, suspended in an isosmotic mannitol solution. The white arrows indicate capillaries filled with aggregates surrounding large blood vessels. The black arrows indicate accumulation of contrast agent leaking into the surrounding agar medium through superficial capillaries or the renal artery and vein. The scale bar corresponds to a length of 1 mm.

5.2.5 Discussions

In preclinical studies investigating capillary rarefaction, it is crucial that vascular imaging data is reliable, complete and representative of the vasculature in order to prevent false-negatives. In this study, contrast agents were evaluated solely based on their ability to fill the entire renal vasculature. Contrast-to-noise is influenced by factors independent of the choice of contrast agent, such as the type and quality of µCT equipment. Contrast agents feature different heavy elements as radiopaque component, were used in different concentrations and scanned at comparable but slightly different photon energies. Intensity values and contrast-to-noise therefore should not be compared across contrast agents based on the data presented in this study, and structures could not be segmented on an equivalent basis. In addition, there is no single objective measure capable of encompassing the widely differing types of filling artifacts. Quantitative measures such as vessel density and non-perfused area would not accurately reflect issues with vessel discontinuities. Conversely, connectivity analysis would not accurately reflect non-perfused kidney regions, when the perfused regions show no discontinuities within themselves. Comparisons of different protocols would therefore only be possible based on subjective weighting of multiple factors, even if segmentation on equal grounds had been achieved. Contrast agent filling was thus evaluated only on a qualitative basis.

The vascular casting resin µAngiofil was capable of filling all capillaries, but produced a large amount of gas bubbles during polymerization, leading to disconnected vessel segments. Since µAngiofil is a hydrophobic plastic resin, particular care has to be taken to ensure thorough flushing of the kidney vasculature from any remaining water, which could otherwise lead to water inclusions, which are another source of vessel discontinuities. Plastic resins also feature higher viscosities than water-soluble X-ray contrast agents. Flow rates have to be optimized and adjusted individually when perfusing kidneys with capillary rarefaction, as these feature a lower blood flow capacity. Otherwise, high pressures during perfusion may lead to bursting vessels, distension of blood vessels and collapse of tubular lumina.

Aurovist 15 nm and ExiTron nano 12000 are both surface-functionalized metal nanoparticles, and their results were comparable to each other, despite their different particle sizes of 15 nm and 110 nm, respectively. Unfiltered nanoparticles were unable to fill the whole capillary bed of the kidneys. Highly X-ray absorbing species visible in the glomeruli suggest that nanoparticle aggregates block the glomerular capillary loops, which are located at the beginning of the capillary network. Blockage at this location would result in the observed lack of perfusion in various kidney regions, as these are downstream of the glomeruli.

Filtering the nanoparticles with syringe filters greatly reduced the number of aggregates, but was unable to remove them completely. Accordingly, unfilled capillaries remained, although at much lower numbers. The aggregates were considerably larger than the pore size of the filters, which suggests that they were formed after filtration within the kidney. To reduce aggregation, ExiTron nano 12000 was suspended in isosmotic mannitol solution instead of PBS in accordance to suggestions from the manufacturer. However, capillary filling did not improve. While aggregation behavior was successfully altered, it only resulted in a shift in location of the aggregates from the kidney surface to the capillaries close to the large blood vessels. Nanoparticles also diffused out of the kidney over time, resulting in loss of signal and increase of background over time, requiring X-ray scans to be performed immediately after sample preparation.

Co-injecting Aurovist 15 nm with gelatin did not prevent diffusion of the nanoparticles out of the vasculature. Capillary filling was negatively affected. Since gelatin solidifies based on temperature, accurate control of this process is challenging and premature solidification can cause incompletely perfused vessels. Gelatin perfusions are therefore not recommended.

Based on these results, the following requirements were identified for a contrast agent to be used in kidney capillary imaging:

1. The contrast agent should be highly water-soluble to prevent issues with discontinuous vessel segments caused by water inclusions of hydrophobic resins and issues of aggregation of suspended particles.
2. The contrast agent needs to be large enough to avoid extravasation or glomerular filtration.
3. The contrast agent should be cross-linkable to prevent loss of contrast and increase of background over time.

A highly water-soluble blood pool contrast agents exists in the form of ExiTron P, a polymeric iodine-based contrast agent. However, this contrast agent has a molecular weight of around 20 000 g/mol and is thus too small to avoid glomerular filtration. As such, while nanoparticle-based blood pool contrast agents represent a substantial advancement over microparticle-based protocols [23], [24], there is currently no ideal X-ray contrast agent for *ex vivo* capillary imaging of the kidney available, creating a demand for the development of compounds that fulfill the requirements summarized above. The benefits of such a development would not be limited to studies of the mouse kidney, but also extend to studies of other tissue featuring permeable vasculature, such as tumors [25] or the circumventricular organs in the brain [26].

5.2.6 Acknowledgements

µAngiofil was provided by Fumedica AG. ExiTron nano 12000 was provided by nanoPET Pharma GmbH. This study was funded by the Swiss National Science Foundation through NCCR Kidney.CH and grant 205321_153523.

5.2.7 References

[1] R. Saran *et al.*, "US Renal Data System 2018 Annual Data Report: Epidemiology of Kidney Disease in the United States," *American Journal of Kidney Diseases*, vol. 73, no. 3, pp. A7–A8, Mar. 2019, doi: 10.1053/j.ajkd.2019.01.001.

[2] Y. Kida, B. N. Tchao, and I. Yamaguchi, "Peritubular capillary rarefaction: a new therapeutic target in chronic kidney disease," *Pediatr. Nephrol.*, vol. 29, no. 3, pp. 333–342, Mar. 2014, doi: 10.1007/s00467-013-2430-y.

[3] G. Mayer, "Capillary rarefaction, hypoxia, VEGF and angiogenesis in chronic renal disease," *Nephrology Dialysis Transplantation*, vol. 26, no. 4, pp. 1132–1137, Apr. 2011, doi: 10.1093/ndt/gfq832.

[4] J. Ehling *et al.*, "Quantitative Micro-Computed Tomography Imaging of Vascular Dysfunction in Progressive Kidney Diseases," *J. Am. Soc. Nephrol.*, vol. 27, no. 2, pp. 520–532, Feb. 2016, doi: 10.1681/ASN.2015020204.

[5] R. Hlushchuk *et al.*, "Cutting-edge microangio-CT: new dimensions in vascular imaging and kidney morphometry," *Am J Physiol Renal Physiol*, vol. 314, no. 3, pp. F493–F499, Mar. 2018, doi: 10.1152/ajprenal.00099.2017.

[6] I. S. Tuna and S. Tatli, "Contrast-enhanced CT and MR imaging of renal vessels," *Abdom Imaging*, vol. 39, no. 4, pp. 875–891, Aug. 2014, doi: 10.1007/s00261-014-0105-1.

[7] T. D. Hull, A. Agarwal, and K. Hoyt, "New Ultrasound Techniques Promise Further Advances in AKI and CKD," *JASN*, vol. 28, no. 12, pp. 3452–3460, Dec. 2017, doi: 10.1681/ASN.2017060647.

[8] O. Ogunlade *et al.*, "In vivo three-dimensional photoacoustic imaging of the renal vasculature in preclinical rodent models," *American Journal of Physiology-Renal Physiology*, vol. 314, no. 6, pp. F1145–F1153, Jun. 2018, doi: 10.1152/ajprenal.00337.2017.

[9] A. M. Hall, C. D. Schuh, and D. Haenni, "New frontiers in intravital microscopy of the kidney:," *Current Opinion in Nephrology and Hypertension*, vol. 26, no. 3, pp. 172–178, May 2017, doi: 10.1097/MNH.0000000000000313.

[10] R. M. Sandoval and B. A. Molitoris, “Intravital multiphoton microscopy as a tool for studying renal physiology and pathophysiology,” *Methods*, vol. 128, pp. 20–32, Sep. 2017, doi: 10.1016/j.ymeth.2017.07.014.
[11] M. Busse *et al.*, “Three-dimensional virtual histology enabled through cytoplasm-specific X-ray stain for microscopic and nanoscopic computed tomography,” *Proc Natl Acad Sci USA*, vol. 115, no. 10, pp. 2293–2298, Mar. 2018, doi: 10.1073/pnas.1720862115.
[12] J. Missbach-Guentner *et al.*, “3D virtual histology of murine kidneys – high resolution visualization of pathological alterations by micro computed tomography,” *Sci Rep*, vol. 8, no. 1, p. 1407, Dec. 2018, doi: 10.1038/s41598-018-19773-5.
[13] R. Shirai *et al.*, “Enhanced renal image contrast by ethanol fixation in phase-contrast X-ray computed tomography,” *J Synchrotron Rad*, vol. 21, no. 4, pp. 795–800, Jul. 2014, doi: 10.1107/S1600577514010558.
[14] J. R. Pappenheimer, E. M. Renkin, and L. M. Borrero, “Filtration, diffusion and molecular sieving through peripheral capillary membranes; a contribution to the pore theory of capillary permeability,” *Am. J. Physiol.*, vol. 167, no. 1, pp. 13–46, Oct. 1951, doi: 10.1152/ajplegacy.1951.167.1.13.
[15] H. Lusic and M. W. Grinstaff, “X-ray-Computed Tomography Contrast Agents,” *Chem. Rev.*, vol. 113, no. 3, pp. 1641–1666, Mar. 2013, doi: 10.1021/cr200358s.
[16] L. Nebuloni, G. A. Kuhn, and R. Muller, “A comparative analysis of water-soluble and blood-pool contrast agents for in vivo vascular imaging with micro-CT,” *Acad Radiol*, vol. 20, no. 10, pp. 1247–55, Oct. 2013, doi: 10.1016/j.acra.2013.06.003.
[17] J. F. Hainfeld, H. M. Smilowitz, M. J. O’Connor, F. A. Dilmanian, and D. N. Slatkin, “Gold nanoparticle imaging and radiotherapy of brain tumors in mice,” *Nanomedicine*, vol. 8, no. 10, pp. 1601–1609, Oct. 2013, doi: 10.2217/nnm.12.165.
[18] H. Boll *et al.*, “Comparison of Fenestra LC, ExiTron nano 6000, and ExiTron nano 12000 for Micro-CT Imaging of Liver and Spleen in Mice,” *Academic Radiology*, vol. 20, no. 9, pp. 1137–1143, Sep. 2013, doi: 10.1016/j.acra.2013.06.002.
[19] S. A. Detombe, J. Dunmore-Buyze, and M. Drangova, “Evaluation of eXIA 160XL cardiac-related enhancement in C57BL/6 and BALB/c mice using micro-CT: EVALUATION OF EXIA 160XL CARDIAC ENHANCEMENT,” *Contrast Media Mol. Imaging*, vol. 7, no. 2, pp. 240–246, Mar. 2012, doi: 10.1002/cmmi.488.
[20] J. Czogalla, F. Schweda, and J. Loffing, “The Mouse Isolated Perfused Kidney Technique,” *Journal of Visualized Experiments*, vol. 117, p. 54712, Nov. 2016, doi: 10.3791/54712.
[21] K. M. Hazenfield and D. D. Smeak, “In vitro holding security of six friction knots used as a first throw in the creation of a vascular ligation,” *J Am Vet Med Assoc*, vol. 245, no. 5, pp. 571–7, Sep. 2014, doi: 10.2460/javma.245.5.571.
[22] J. Schindelin *et al.*, “Fiji: an open-source platform for biological-image analysis,” *Nat Methods*, vol. 9, no. 7, pp. 676–82, Jun. 2012, doi: 10.1038/nmeth.2019.
[23] F. Plouraboue, P. Cloetens, C. Fonta, A. Steyer, F. Lauwers, and J.-P. Marc-Vergnes, “X-ray high-resolution vascular network imaging,” *J Microsc*, vol. 215, no. 2, pp. 139–148, Aug. 2004, doi: 10.1111/j.0022-2720.2004.01362.x.
[24] B. Müller, J. Fischer, U. Dietz, P. J. Thurner, and F. Beckmann, “Blood vessel staining in the myocardium for 3D visualization down to the smallest capillaries,” *Nuclear Instruments and Methods in Physics Research Section B: Beam Interactions with Materials and Atoms*, vol. 246, no. 1, pp. 254–261, May 2006, doi: 10.1016/j.nimb.2005.12.048.
[25] S. Lang *et al.*, “Three-dimensional quantification of capillary networks in healthy and cancerous tissues of two mice,” *Microvascular Research*, vol. 84, no. 3, pp. 314–322, Nov. 2012, doi: 10.1016/j.mvr.2012.07.002.
[26] W. F. Ganong, “Circumventricular organs: definition and role in the regulation of endocrine and autonomic function,” *Clin. Exp. Pharmacol. Physiol.*, vol. 27, no. 5–6, pp. 422–427, Jun. 2000.

5.3 Early designs of a dedicated contrast agent for ex vivo hard X-ray imaging

In order to design a contrast agent fulfilling the requirements described in chapter 5.2.4, multiple approaches were considered.

5.3.1 Copolymer of diiodotyrosine and lysine

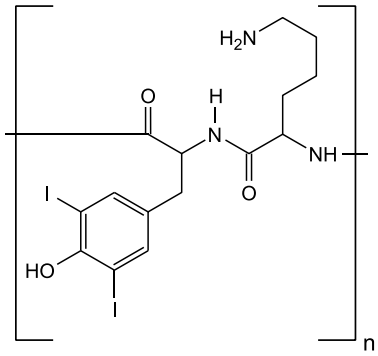

Fig. 16.: Chemical structure of the envisioned copolymer of diiodotyrosine and lysine

One of the very first designs suggested the use of radiopaque polymers, containing specifically iodinated tyrosine as the iodine-carrying monomer. When coupled with lysine, the resulting polymer would be aldehyde-fixable as well. This was quickly discarded, as the costs of production at the scale required would have been prohibitive, whether it would be synthesized with protein chemistry or by bacterial protein expression systems. Besides the costs however, this compound would have had a considerably lower iodine content than a polymer derived from 5-amino-2,4,6-triiodoisophthalic acid, resulting in less contrast at the same molecular weight. Alternatively, at equal contrast, the low iodine content would require either higher molecular weight or higher concentrations of contrast agent, both of which would increase viscosity.

5.3.2 Copolymer of 5-Amino-2,4,6-triiodoisophthalic acid-derived monomer with acrylamide

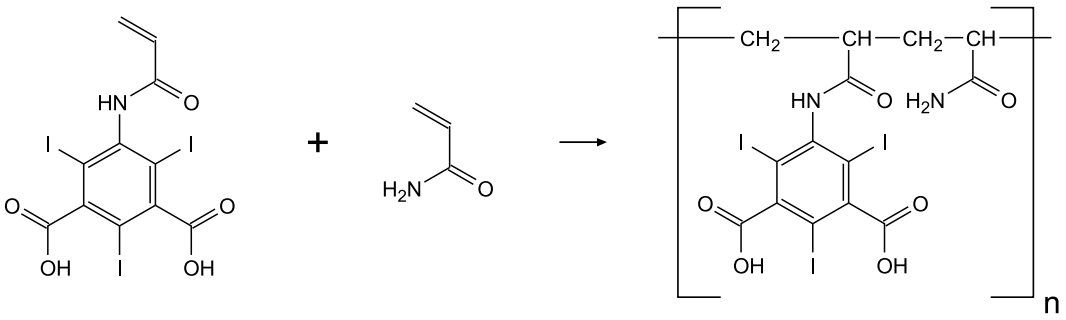

Fig. 17.: Chemical structure of the envisioned copolymer of 5-Amino-2,4,6-triiodoisophthalic acid-derived monomer with acrylamide

Another design proposed to create a copolymer of a 5-amino-2,4,6-triiodoisophthalic acid-derived monomer with acrylamide to add the necessary NH_2-groups. This design has the advantage of requiring fewer reaction steps, being able to insert the amide groups during the already existing polymerization reaction step. There are several disadvantages to this approach, however. Firstly, the ratio of acrylamide to 5-amino-2,4,6-triiodoisophthalic acid may be difficult to control. Secondly, a high acrylamide content would directly lead to a low ratio of iodine to molecular weight. As the third disadvantage, the aldehyde-crosslinking efficiency of amide groups is lower than the one of amine groups, and the cross-linkable NH_2-groups are sterically hindered in this design. A different design was thus chosen in the end, which will be presented in the next chapter.

Journal article

5.4 Cross-linkable polymeric contrast agent for high-resolution X-ray imaging of the vascular system

This chapter was first published in Chemical Communications as:

N. A. Le, W. Kuo, B. Müller, V. Kurtcuoglu, and B. Spingler, "Crosslinkable polymeric contrast agent for high-resolution X-ray imaging of the vascular system," *Chem. Commun.*, vol. 56, no. 44, pp. 5885–5888, 2020. [46]

My work on this publication included the initial design of the contrast agent as described in the previous chapter, the unsuccessful attempts at synthesis of compound **2** via direct reaction of 5-amino-2,4,6-triiodoisophthalic acid with acryloyl chloride and literature research and pilot experiments using RAFT-controlled radical polymerization. On the application side, my work encompassed the development and optimization of the perfusion procedure, μCT image acquisition, visualization, data analysis, providing feedback during the development of XlinCA and coming up with its name.

Cross-linkable polymeric contrast agent for high-resolution X-ray imaging of the vascular system

Ngoc An Le[1,*], Willy Kuo[2,3,4,*], Bert Müller[4], Vartan Kurtcuoglu[2,3,+], Bernhard Spingler[1,+]

[1] Department of Chemistry, University of Zurich, 8057 Zurich, Switzerland;

[2] Institute of Physiology, University of Zurich, 8057 Zurich, Switzerland;

[3] National Centre of Competence in Research, Kidney.CH, 8057 Zurich, Switzerland;

[4] Biomaterials Science Center, Department of Biomedical Engineering, University of Basel, 4123 Allschwil, Switzerland

*, [+] These authors contributed equally to this work respectively.

5.4.1 Abstract

A contrast agent for X-ray micro computed tomography (μCT), called *XlinCA*, that combines reliable perfusion and permanent retention and contrast properties was developed for *ex-vivo* imaging. The new imaging agent *XlinCA* features high molecular weight, low viscosity and a high iodine content.

5.4.2 Introduction

Qualitative and quantitative assessment of vascular physiology, pathology and angiogenesis under various circumstances such as cancer, myocardial infarction, stroke, atherosclerosis, vasculitis, and inflammation requires accurate three-dimensional (3D) structural data [1-4]. A large number of different 3D imaging techniques can provide morphometric parameters including vessel volume, connectivity, number, thickness, thickness distribution, separation, and degree of anisotropy [2, 4, 5]. These parameters are not only useful for investigating diseases that affect the vasculature, but are also crucial for proper evaluation of pro- and anti-angiogenic therapies in preclinical models [6-8].
Micro computed tomography (μCT) allows for non-destructive 3D imaging with isotropic quality and micrometer resolution. The geometric magnification used in cone-beam μCT allows for continuously variable effective pixel sizes and for hierarchical imaging on low-resolution animal scale and high-resolution organ scale in a single device [9-11]. Whole small animals and organs can be imaged in their entirety in their native hydrated state, minimizing sample distortion through sample preparation artefacts, dehydration, realignment artefacts or optical distortion.
Ex vivo high-resolution X-ray imaging is not limited by movement during respiratory and cardiac cycles [12], anaesthetic tolerance or the dose of ionizing radiation [13, 14]. In addition, organs can be extracted and imaged at smaller fields of view, resulting in a corresponding increase of resolution in cone-beam μCT. The density difference between blood and soft tissue is, however, too small to be captured with standard absorption contrast using laboratory sources. Radiopaque X-ray contrast agents featuring heavy atomic elements have to be injected into the vasculature to provide the necessary contrast [15, 16].
Currently available contrast agents have various limitations when used for *ex vivo* vascular imaging. Standard clinical angiography contrast agents, such as iopamidol and iohexol, are small molecular compounds capable of passing through blood vessel walls, which also leads to a loss of contrast between the vascular lumen and the surrounding tissue within a few minutes [17]. This issue can be addressed by the use of blood pool contrast agents, which are large nanoparticles or polymeric compounds that can achieve vascular circulation times on the scale of hours [18-20]. In an *ex vivo* setting, blood pool contrast agents tend to sediment and aggregate, and can slowly leak out of the

vasculature as well [21]. These limitations make both types of angiography contrast agents unsuitable for capillary resolution *ex vivo* vascular imaging.
For such application, the current gold standard consists of vascular casting with plastic resins, e.g. Microfil (Microfil, Flow Tech, Carver, MA), PU4ii (vasQtec, Zurich, Switzerland) and µAngiofil (Fumedica AG, Muri, Switzerland) [22-24]. These hydrophobic resins are incapable of passing through the hydrated endothelial cell layer and polymerize after injection. They are thus permanently retained within the vasculature and provide excellent contrast. Perfusion of these resins is, however, technically challenging. The plastic resin may polymerize prematurely before the vasculature has been fully perfused, leading to incompletely filled blood vessels. Water inclusions and gas bubble formation are frequently occurring artefacts that cause disconnected vessel segments [22, 25-28]. Well-optimized injection techniques, closure of blood vessels via ligation in order to divert all flow to the organ of interest and high perfusion pressures are, therefore, required to obtain consistent perfusion results [22]. While some of these problems can be attributed to the high viscosity of the polymerizing plastic resins, they are inherent limitations shared by hydrophobic casting materials.
While plastic resins can provide reasonable vascular filling, extensive practice is required to reliably prevent frequent sample preparation failures and incomplete vessel filling [29]. Reliable vessel filling is, however, absolutely required for the quantitative characterization of pathological processes and the comparison of vascular phenotypes, as the resulting structural data is otherwise dominated by sample preparation artefacts and not representative of the true vascular structure.
In this paper, we address the shortcomings of current X-ray contrast agents in high resolution *ex vivo* imaging of the vascular network with µCT. We have developed a crosslinkable polymeric contrast agent, *XlinCA*, that combines the simple and reliable perfusion of the hydrophobic angiography contrast agents with the permanent retention and high contrast of the hydrophobic vascular casting resins. We demonstrate its application for capillary-level imaging of a brain hemisphere and vascular imaging of an entire mouse with a non-optimized transcardial perfusion. *XlinCA* was designed to fulfil a specific set of criteria to resolve issues encountered in *ex vivo* vascular imaging with current contrast agents:

- Highly water-soluble, so as to avoid incomplete vascular filling and interrupted vessel segments.
- Higher molecular weight than 65 kDa, for the prevention of the immediate leakage through blood vessel walls.
- Crosslinkable with free primary amine groups as targets for glutaraldehyde fixation, which enables crosslinking via imine formation [30, 31] in order to prevent leakage over time.
- High X-ray attenuation coefficient with a high iodine content [32], for reducing the required contrast agent concentration, viscosity and osmolarity.

After considering all the above criteria, we designed the crosslinkable polymeric contrast agent *XlinCA* represented schematically in Fig. 1. The theoretical iodine content is 49.5 m/m %, which is comparable to standard small molecule angiography iodine contrast agents and considerably higher than what could be achieved by other typical approaches, such as linkage to polyethylene glycol (PEG) [33].

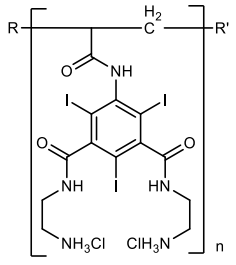

Fig. 1.: Chemical formula of the crosslinkable polymeric X-ray contrast agent XlinCA.

5.4.3 Results and Discussion

The contrast agent was synthesized through a multi-step process, see Fig. S1. Starting from the commercially available 5-amino-2,4,6-triiodoisophthalic acid **1**, the acryloyl group was added through reaction with acrylic anhydride and a catalytic amount of sulfuric acid. The key step in this synthesis was the polymerization of **2** to give polymer **3** by reversible addition-fragmentation chain transfer (RAFT) polymerization [34-37]. Trithiocarbonate **7** was chosen as RAFT agent for polymerization of **2** due to the reported compatibility with various acrylamide derivatives [38]. We found that dimethylformamide (DMF) is the most suitable solvent for RAFT polymerization of **2**. It provides high solubility of both starting materials as well as polymeric products and allows a high degree of conversion of the monomers. The optimal reaction temperature was 70 °C. The concentrations of monomer, RAFT agent and AIBN as radical initiator were optimized (Table S2). The average molecular weight of the synthesized polymer increases with the ratio of monomer to RAFT agent [37]. The optimal ratio of monomer : RAFT agent : AIBN was found to be 400 : 2 : 1. Lower ratios of RAFT and AIBN to **2** led to higher conversion degrees, but lowered the molecular weight of **3**, while higher ratios led to precipitates of both starting material and product. The molecular weight of **3** could not be measured with gel permeation chromatography (GPC) even in warm DMF due to low solubility and the tendency of the polymer towards aggregation. However, the molecular weight and polydispersity index of **3** could be estimated indirectly from the GPC result of the final product **6**, which is water soluble and stable against aggregation. Based on the ratio of the molecular weights of the monomers and the average molecular weight of **6** (Fig. S6), we calculated the average molecular weight of **3** to be 30400 Da. Ethylenediamine was added to the polymer **3** after activation of the carboxylic groups with oxalyl chloride. The obtained **5** dissolved easily in dilute hydrochloric acid solution to give the contrast agent *XlinCA* (**6**), which is water soluble and can be crosslinked with aldehydes due to the presence of the amine groups.

The ability to be crosslinked not only enables polymerization of *XlinCA* after injection into the vasculature, but also facilitates the increase of the contrast agent molecular weight by pre-crosslinking with glutaraldehyde (Fig. S7). In order to obtain the desired molecular weight of 65 kDa, required to prevent diffusion through the blood vessel walls, *XlinCA* was pre-crosslinked with different amounts of 25 % glutaraldehyde prior to perfusion into the mouse. The highest amount that could be introduced without inducing gelation was found to be 30 µL of 25 % glutaraldehyde solution per 1 g of *XlinCA* dissolved in 4 mL water. This ratio led to a limited increase in viscosity through an increase in the molecular weight of the polymer by pre-crosslinking. The pre-crosslinked contrast agent was dialysed with a 100 kDa dialysis membrane to remove all compounds below the size threshold and lyophilised. In this form it should be used within a week, as its solubility reduces over time. After the contrast agent was administered into the vasculature, further crosslinking of the contrast agent with glutaraldehyde led to gelation of the contrast agent, preventing any leakage and loss of contrast over time (Fig. S7).

Mice perfused with vascular casting resin PU4ii and polymeric contrast agent *XlinCA* were compared by using low-resolution µCT with a voxel size of 80 µm. In the PU4ii-perfused mouse, numerous water inclusions and gas bubbles could be observed in the descending aorta, vena cava and larger vessels in the kidneys and the liver. Correspondingly, one liver lobe, the adrenal glands and part of the kidneys were only partially filled with PU4ii. Certain large blood vessels, such as the naso-frontal vein and anterior vein, remained completely devoid of PU4ii (Fig. 2A), while their counterparts in the mouse perfused with *XlinCA* were filled in their entirety (Fig. 2B and S8). In order to evaluate completeness of the vessel filling further, the *XlinCA*-perfused mouse was scanned with a voxel size of 20 µm. Brain, heart, lungs, liver, kidneys and adrenal glands appeared well-perfused, see Fig. 2C, 2D, S9 and S10. No discontinuous vessel segments could be found, as expected for a water-soluble compound. Vascular filling with *XlinCA* was not entirely complete. Small vessels posterior to the kidneys were ill-defined. Parts of the capillaries were missing in the renal medulla of the kidney (Fig. S10) and the spleen. Leftover blood seen in the histological examination indicated that this was caused by incomplete flushing of blood prior to contrast agent injection, and thus not due to any contrast agent-related property.

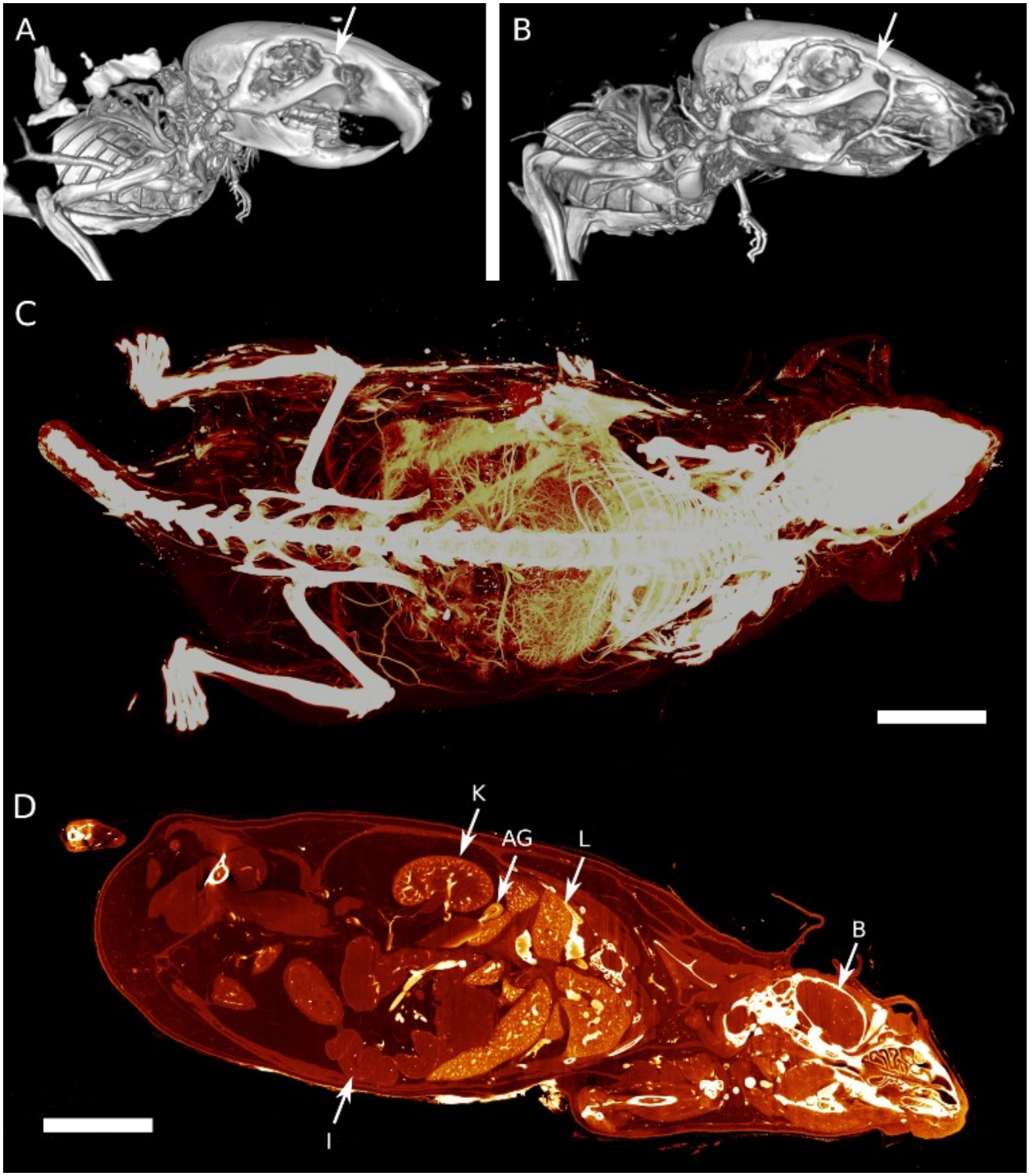

Fig. 2.: Conventional µCT images of mice heads perfused with PU4ii (A) and XlinCA (B). In the PU4ii-filled mouse, the supraorbital vein (white arrow) is partially filled up to the bifurcation to the naso-frontal vein and anterior facial vein, which do not appear. In contrast, these vessels, along with the anterior facial vein, are completely filled in the XlinCA-perfused mouse. C: Maximum intensity projection of the higher resolution XlinCA-perfused whole mouse dataset. Voxel size: 20 µm, scale bar: 1 cm. D: Virtual section of the µCT dataset shown in C. Intestine (I), kidney (K), adrenal gland (AG) liver (L) and brain (B) are clearly visible. Scale bar: 1 cm.

The brain of the *XlinCA*-perfused mouse was removed and the right brain hemisphere was scanned with a voxel size of 4.4 µm, as the smaller field of view allowed for scans with approximately twice

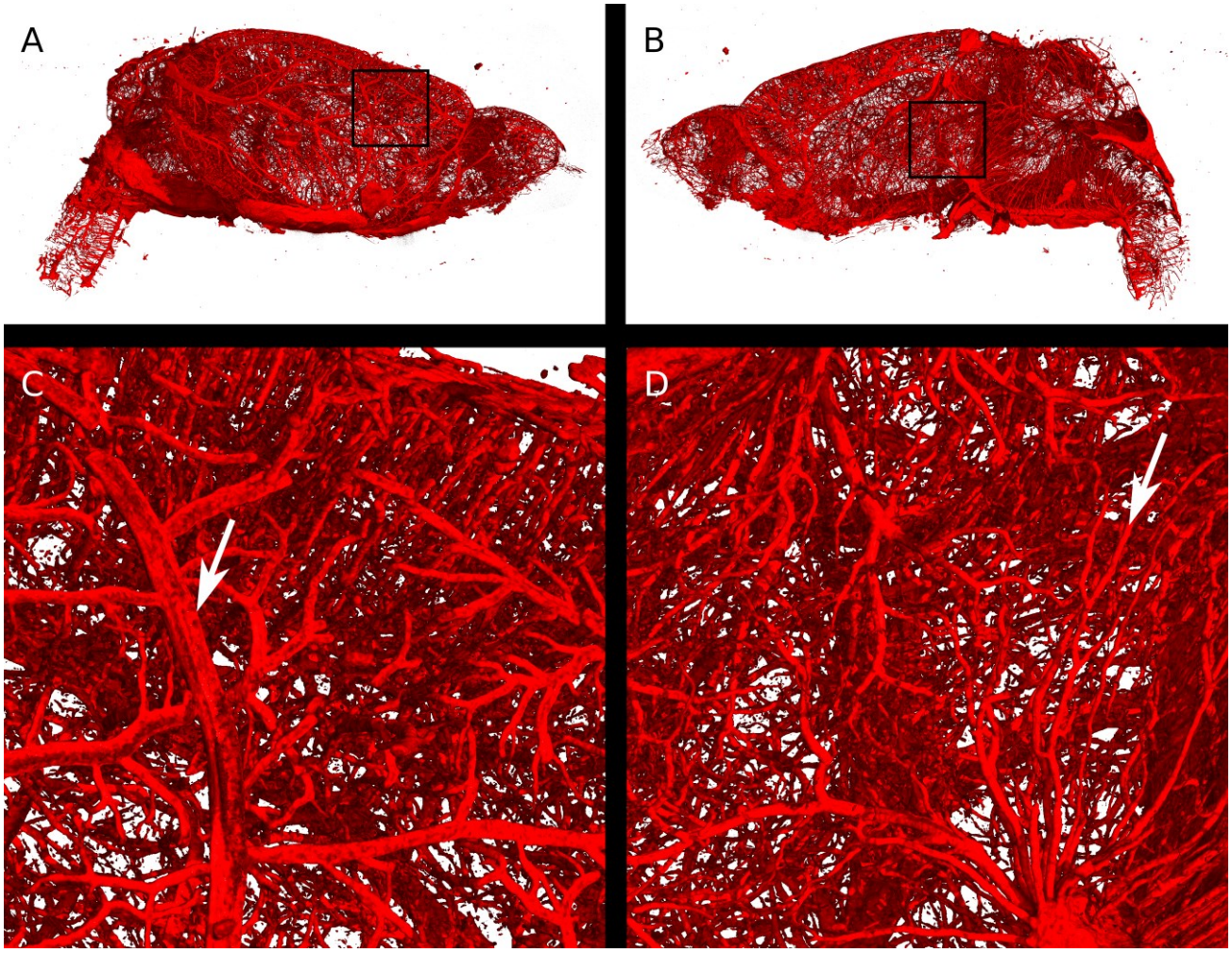

Fig. 3.: 3D rendering of the brain hemisphere vasculature perfused with XlinCA. A: Outside view. B: Inside view. C: Magnified view of the region indicated by the black square in Fig. 4A. Diameter of blood vessel indicated by the white arrow: 70 µm. D: Magnified view of Fig. 4B. Diameter of blood vessel indicated by the white arrow: 15 µm.

the resolution compared to a full brain. There were no large areas of missing vasculature as has been reported for optimized Microfil perfusions [22]. Neither vessel discontinuities through insufficient filling nor gas bubbles could be identified (Fig. 3). Independent of the choice of vascular casting agent, non-optimized transcardial perfusion techniques cannot entirely outperform optimized perfusion techniques in specific organs. On equal terms, however, *XlinCA* provided more complete and reliable filling of multiple organs in an entire mouse with a simple transcardial injection, without requiring clamping or ligation of the descending aorta and vena cava. The procedure is thus much simpler to perform and allows multiple organs to be harvested and used in the analysis of the vasculature, which reduces the number of animals required and the variance in multi-organ correlation studies.

Factors such as injection volume and flow rate did not have to be optimized, as crosslinking can be initiated at any time after perfusion is complete. In contrast, Microfil polymerizes within approximately 20 minutes [22], limiting the perfusion volume before viscosity and thus resistance to flow increases. With the time constraints removed, flow rate and thus perfusion pressure are no longer factors that require optimization. Perfusion pressure in our experiment was 150 mmHg, which is consistent with the pressure used in the transcardial perfusion reported by Chugh et al. [26], but lower pressures can be used without risk of premature polymerization and resulting incomplete filling. Higher perfusion pressures are still of advantage in the prior perfusion steps required for flushing the vasculature of remaining blood, however.

In conclusion, we have shown that our new imaging agent *XlinCA* circumvents the limitations of current vascular casting with plastic resins. As *XlinCA* is a water-soluble compound, water

inclusions are inherently avoided. The contrast agent is free of microparticles, thereby preventing blockage of capillaries by solid aggregates. Crosslinking can be initiated after perfusion is complete, allowing perfusion to be conducted for any desired period of time without an increase in viscosity limiting the amount of contrast agent volume that can be injected. The flow rate does not need optimization, and perfusion pressure ceases to be an important factor for contrast agent filling.
Vascular casting with *XlinCA* thus requires not only considerably less technical expertise and time, but also permits perfusion of both the brain and the whole mouse in a single procedure. We envision that these features will enable hierarchical imaging of organs in their original spatial context and identification of areas with vascular abnormalities, which can then be excised for higher resolution imaging. The vasculature of more than one organ of the same animal could be analysed, which would reduce the number of animals required and reduce the variance in multi-organ correlation studies.

5.4.4 Acknowledgements

This work was financially supported by University of Zurich and the Swiss National Science Foundation through NCCR Kidney.CH and grant 205321_153523. We thank Dr. Thomas Fox for recording the ^{1}H-NMR of *XlinCA* (**6**).

Conflicts of interest
A patent application for the polymeric contrast agent described in this publication has been filed by the University of Zurich.

5.4.5 References

[1] Z. Starosolski, C. A. Villamizar, D. Rendon, M. J. Paldino, D. M. Milewicz, K. B. Ghaghada*, et al.*, "Ultra High-Resolution *In vivo* Computed Tomography Imaging of Mouse Cerebrovasculature Using a Long Circulating Blood Pool Contrast Agent," *Sci. Rep.,* vol. 5, p. 10178, May 18 2015, doi: 10.1038/srep10178.

[2] J. Ehling, J. Babickova, F. Gremse, B. M. Klinkhammer, S. Baetke, R. Knuechel*, et al.*, "Quantitative Micro-Computed Tomography Imaging of Vascular Dysfunction in Progressive Kidney Diseases," *J. Am. Soc. Nephrol.,* vol. 27, pp. 520-32, Feb 2016, doi: 10.1681/asn.2015020204.

[3] J. López-Guimet, L. Peña-Perez, R. S. Bradley, P. Garcia-Canadilla, C. Disney, H. Geng*, et al.*, "MicroCT imaging reveals differential 3D micro-scale remodelling of the murine aorta in ageing and Marfan syndrome," *Theranostics,* vol. 8, pp. 6038-6052, 2018, doi: 10.7150/thno.26598.

[4] J. Epah, K. Palfi, F. L. Dienst, P. F. Malacarne, R. Bremer, M. Salamon*, et al.*, "3D Imaging and Quantitative Analysis of Vascular Networks: A Comparison of Ultramicroscopy and Micro-Computed Tomography," *Theranostics,* vol. 8, pp. 2117-2133, 2018, doi: 10.7150/thno.22610.

[5] L. Zagorchev, P. Oses, Z. W. Zhuang, K. Moodie, M. J. Mulligan-Kehoe, M. Simons*, et al.*, "Micro computed tomography for vascular exploration," *J. Angiogenes Res.,* vol. 2, p. 7, Mar 5 2010, doi: 10.1186/2040-2384-2-7.

[6] J. Ehling, B. Theek, F. Gremse, S. Baetke, D. Mockel, J. Maynard*, et al.*, "Micro-CT Imaging of Tumor Angiogenesis Quantitative Measures Describing Micromorphology and Vascularization," *Am. J. Pathol.,* vol. 184, pp. 431-441, Feb 2014, doi: 10.1016/j.ajpath.2013.10.014.

[7] L. Ayala-Dominguez and M. E. Brandan, "Quantification of tumor angiogenesis with contrast-enhanced x-ray imaging in preclinical studies: a review," *Biomed. Phys. Eng. Express,* vol. 4, p. 062001, Nov 2018, doi: 10.1088/2057-1976/aadc2d.

[8] S. Gu, J. Xue, Y. Xi, R. Tang, W. Jin, J.-J. Chen*, et al.*, "Evaluating the effect of Avastin on breast cancer angiogenesis using synchrotron radiation," *Quant. Imaging Med. Surg.,* vol. 9, pp. 418-426, Mar 2019, doi: 10.21037/qims.2019.03.09.

[9] L. A. Walton, R. S. Bradley, P. J. Withers, V. L. Newton, R. E. B. Watson, C. Austin*, et al.*, "Morphological Characterisation of Unstained and Intact Tissue Micro-architecture by X-ray Computed Micro- and Nano-Tomography," *Sci. Rep.,* vol. 5, p. 10074, May 15 2015, doi: 10.1038/srep10074.
[10] E. L. Ritman, "Role of microcomputed tomography in microvascular imaging," *Proc. SPIE,* vol. 7898, p. 78980I, 2011,
[11] T. Salditt, T. Aspelmeier, and S. Aeffner, *Biomedical Imaging: Principles of Radiography, Tomography and Medical Physics*, 1st ed. Berlin, Boston: De Gruyter, 2017.
[12] R. J. Alfidi, W. J. Mac Intyre, and Haaga, "The effects of biological motion on CT resolution," *Am. J. Roentgenol.,* vol. 127, pp. 11-15, 1976/07/01 1976, doi: 10.2214/ajr.127.1.11.
[13] J. Lerch, L. Gazdzinski, J. Germann, J. Sled, R. M. Henkelman, and B. Nieman, "Wanted dead or alive? The tradeoff between *in-vivo* versus *ex-vivo* MR brain imaging in the mouse," *Front. Neuroinform.,* vol. 6, p. 6, 2012,
[14] S. K. Carlson, K. L. Classic, C. E. Bender, and S. J. Russell, "Small Animal Absorbed Radiation Dose from Serial Micro-Computed Tomography Imaging," *Mol. Imaging Biol.,* vol. 9, pp. 78-82, 2007/03/01 2007, doi: 10.1007/s11307-007-0080-9.
[15] B. Müller, J. Fischer, U. Dietz, P. J. Thurner, and F. Beckmann, "Blood vessel staining in the myocardium for 3D visualization down to the smallest capillaries," *Nucl. Instrum. Methods Phys. Res., Sect. B,* vol. 246, pp. 254-261, 2006/05/01/ 2006, doi: 10.1016/j.nimb.2005.12.048.
[16] E. Eggl, K. Mechlem, E. Braig, S. Kulpe, M. Dierolf, B. Günther*, et al.*, "Mono-Energy Coronary Angiography with a Compact Synchrotron Source," *Sci. Rep.,* vol. 7, p. 42211, 2017/02/09 2017, doi: 10.1038/srep42211.
[17] M. Bourin, P. Jolliet, and F. Ballereau, "An Overview of the Clinical Pharmacokinetics of X-Ray Contrast Media," *Clin. Pharmacokinet.,* vol. 32, pp. 180-193, Mar 1997, doi: Doi 10.2165/00003088-199732030-00002.
[18] F. Hallouard, N. Anton, P. Choquet, A. Constantinesco, and T. Vandamme, "Iodinated blood pool contrast media for preclinical X-ray imaging applications – A review," *Biomaterials,* vol. 31, pp. 6249-6268, Aug 2010, doi: 10.1016/j.biomaterials.2010.04.066.
[19] L. Nebuloni, G. A. Kuhn, and R. Müller, "A Comparative Analysis of Water-Soluble and Blood-Pool Contrast Agents for *in vivo* Vascular Imaging with Micro-CT," *Acad. Radiol.,* vol. 20, pp. 1247-1255, Oct 2013, doi: 10.1016/j.acra.2013.06.003.
[20] C. Gao, Y. Zhang, Y. Zhang, S. Li, X. Yang, Y. Chen*, et al.*, "cRGD-modified and disulfide bond-crosslinked polymer nanoparticles based on iopamidol as a tumor-targeted CT contrast agent," *Polym. Chem.,* vol. 11, pp. 889-899, 2020, doi: 10.1039/C9PY01418G.
[21] W. Kuo, G. Schulz, B. Müller, and V. Kurtcuoglu, "Evaluation of metal nanoparticle- and plastic resin-based x-ray contrast agents for kidney capillary imaging," in *Developments in X-Ray Tomography XII*, San Diego, California, United States, 2019, p. 111130Q.
[22] S. Ghanavati, L. X. Yu, J. P. Lerch, and J. G. Sled, "A perfusion procedure for imaging of the mouse cerebral vasculature by X-ray micro-CT," *J. Neurosci. Meth.,* vol. 221, pp. 70-77, Jan 15 2014, doi: 10.1016/j.jneumeth.2013.09.002.
[23] T. Krucker, A. Lang, and E. P. Meyer, "New Polyurethane-Based Material for Vascular Corrosion Casting with Improved Physical and Imaging characteristics," *Microsc. Res. Techn.,* vol. 69, pp. 138-147, Feb 2006, doi: 10.1002/jemt.20263.
[24] L. Schaad, R. Hlushchuk, S. Barre, R. Gianni-Barrera, D. Haberthur, A. Banfi*, et al.*, "Correlative Imaging of the Murine Hind Limb Vasculature and Muscle Tissue by MicroCT and Light Microscopy," *Sci. Rep.,* vol. 7, p. 41842, Feb 7 2017, doi: 10.1038/srep41842.
[25] S. Grabherr, V. Djonov, K. Yen, M. J. Thali, and R. Dirnhofer, "Postmortem angiography: review of former and current methods," *Am. J. Roentgenol.,* vol. 188, pp. 832-838, Mar 2007, doi: 10.2214/AJR.06.0787.
[26] B. P. Chugh, J. P. Lerch, L. X. Yu, M. Pienkowski, R. V. Harrison, R. M. Henkelman*, et al.*, "Measurement of cerebral blood volume in mouse brain regions using micro-computed tomography," *NeuroImage,* vol. 47, pp. 1312-1318, Oct 1 2009, doi: 10.1016/j.neuroimage.2009.03.083.

[27] S. X. Vasquez, F. Gao, F. Su, V. Grijalva, J. Pope, B. Martin*, et al.*, "Optimization of microCT imaging and blood vessel diameter quantitation of preclinical specimen vasculature with radiopaque polymer injection medium," *PLOS ONE,* vol. 6, p. e19099, 2011, doi: 10.1371/journal.pone.0019099.
[28] L. Fan, S. Wang, X. He, E. Gonzalez-Fernandez, C. Lechene, F. Fan*, et al.*, "Visualization of the intrarenal distribution of capillary blood flow," *Physiol. Rep.,* vol. 7, p. e14065, Apr 2019, doi: 10.14814/phy2.14065.
[29] D. S. Perrien, M. A. Saleh, K. Takahashi, M. S. Madhur, D. G. Harrison, R. C. Harris*, et al.*, "Novel methods for microCT-based analyses of vasculature in the renal cortex reveal a loss of perfusable arterioles and glomeruli in eNOS-/- mice," *BMC Nephrol.,* vol. 17, p. 24, Mar 2 2016, doi: 10.1186/s12882-016-0235-5.
[30] D. T. Cheung and M. E. Nimni, "Mechanism of Crosslinking of Proteins by Glutaraldehyde. 1. Reaction with Model Compounds," *Connect. Tissue Res.,* vol. 10, pp. 187-199, 1982, doi: Doi 10.3109/03008208209034418.
[31] I. Migneault, C. Dartiguenave, M. J. Bertrand, and K. C. Waldron, "Glutaraldehyde: behavior in aqueous solution, reaction with proteins, and application to enzyme crosslinking," *BioTechniques,* vol. 37, pp. 790-802, Nov 2004, doi: Doi 10.2144/04375rv01.
[32] H. Lusic and M. W. Grinstaff, "X-ray-Computed Tomography Contrast Agents," *Chem. Rev.,* vol. 113, pp. 1641-1666, Mar 2013, doi: 10.1021/cr200358s.
[33] E. Jin and Z.-R. Lu, "Biodegradable iodinated polydisulfides as contrast agents for CT angiography," *Biomaterials,* vol. 35, pp. 5822-5829, Jul 2014, doi: 10.1016/j.biomaterials.2014.03.054.
[34] J. Chiefari, Y. K. Chong, F. Ercole, J. Krstina, J. Jeffery, T. P. T. Le*, et al.*, "Living Free-Radical Polymerization by Reversible Addition-Fragmentation Chain Transfer: The RAFT Process," *Macromolecules,* vol. 31, pp. 5559-5562, Aug 11 1998, doi: DOI 10.1021/ma9804951.
[35] C. Boyer, V. Bulmus, T. P. Davis, V. Ladmiral, J. Liu, and S. Perrier, "Bioapplications of RAFT Polymerization," *Chem. Rev.,* vol. 109, pp. 5402-5436, Nov 2009, doi: 10.1021/cr9001403.
[36] D. J. Keddie, "A guide to the synthesis of block copolymers using reversible-addition fragmentation chain transfer (RAFT) polymerization," *Chem. Soc. Rev.,* vol. 43, pp. 496-505, 2014, doi: 10.1039/c3cs60290g.
[37] S. Perrier, "50th Anniversary Perspective: RAFT Polymerization–A User Guide," *Macromolecules,* vol. 50, pp. 7433-7447, Oct 10 2017, doi: 10.1021/acs.macromol.7b00767.
[38] G. Moad, E. Rizzardo, and S. H. Thang, "Living Radical Polymerization by the RAFT Process – A Third Update," *Aust. J. Chem.,* vol. 65, pp. 985-1076, 2012, doi: 10.1071/Ch12295.

5.4.6 Supplementary information

5.4.6.1 Methods

5.4.6.1.1 General

Unless otherwise stated, all chemicals were of reagent grade and purchased from *Sigma–Aldrich*. All solvents were of analytical grade. The synthesis and characterization of acrylic anhydride were performed in accordance with the literature [1]. Dialysis tubings were purchased from *Sigma–Aldrich* (cellulose, 12 kDa cut-off) and from *Spectrum* (cellulose ester, 100 kDa cut-off). The ^{1}H NMR and ^{13}C NMR spectra were recorded on a Bruker 400 MHz spectrometer. IR spectra were recorded on a Spectrum Two FT-IR Spectrometer (Perkin–Elmer) equipped with a Specac Golden Gate™ ATR accessory. Low resolution mass spectroscopic analysis was performed with a Waters AQUITY-Bruker UPLC-MS system. Elemental microanalyses were performed on a LECO CHNS-932 elemental analyser. Analytical gel permeation chromatography was performed by the analytical service of PSS Polymer (Mainz, Germany) using columns PSS-NovemaMax_F 5µm: Guard + 30Å + 1000Å +1000Å with UV/VIS and differential refractometer RID detectors. An aqueous solution of 0.1 M NaCl and 0.1 vol.-% TFA was used as an eluent. The average molecular weight and the molecular weight distribution of the samples were calculated relative to a standard calibration with pullulan.

5.4.6.1.2 Synthesis of the contrast agent

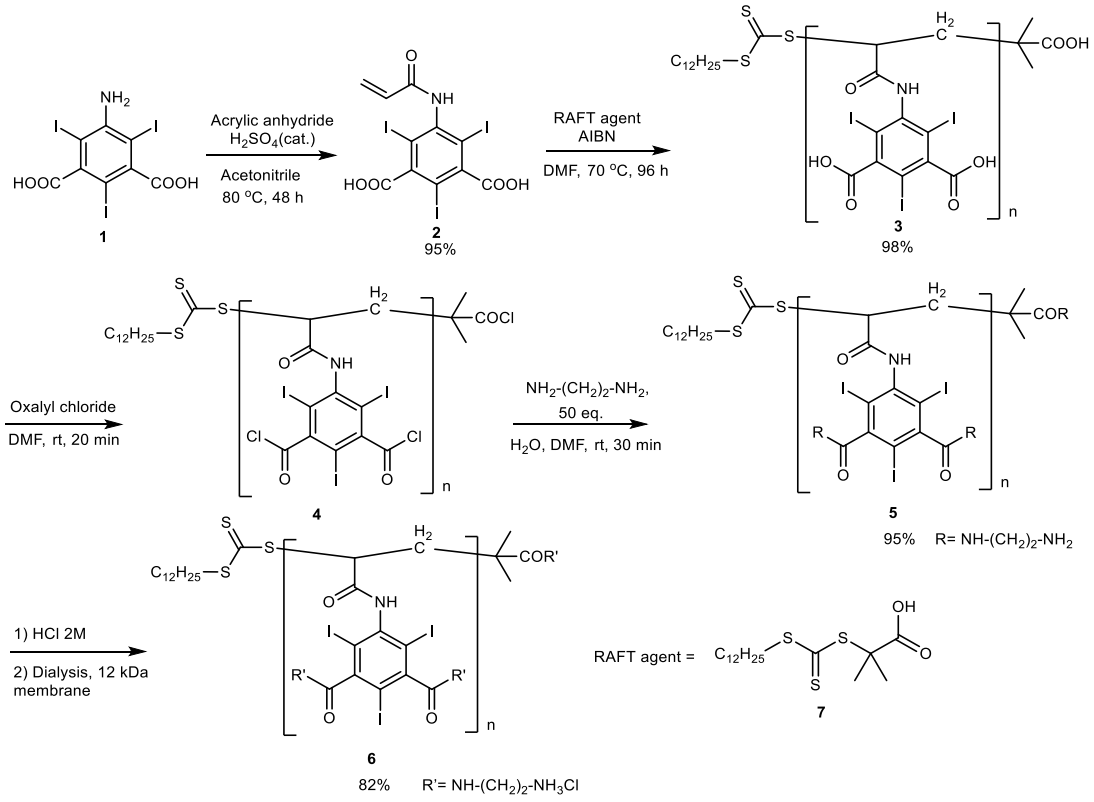

*Fig. S1.: Synthesis pathway for polymeric contrast agent XlinCA (**6**) using RAFT polymerization.*

2,4,6-triiodo-5-(prop-2-enamido)benzene-1,3-dicarboxylic acid (2)
To a suspension of 5-amino-2,4,6-triiodobenzene-1,3-dicarboxylic acid (**1**) (20 g, 35.8 mmol) and concentrated sulfuric acid (0.04 mL) in acetonitrile (40 mL), acrylic anhydride (12 mL, 107 mmol) was added drop-wise while the reaction mixture was being cooled in an ice bath. The reaction mixture was stirred at 80 °C for 36 h until no 5-amino-2,4,6-triiodobenzene-1,3-dicarboxylic acid (**1**) was detected by UPLC. The mixture was cooled down to room temperature, then filtered under

vacuum and washed with acetonitrile (20 mL). The solid was dried in high vacuum for two days to yield 20.8 g (95%) of a white product. Multiple attempts to synthesize compound **2** with the help of the cheaper acryloyl chloride reagent were unsuccessful. UV-Vis spectrum (methanol, λ; nm): 243; IR [KBr, cm^{-1}]: 3247, 3000, 1725, 609, 508; ^{1}H NMR (400 MHz, DMSO-d_6): 5.82 (dd, J^2 =1.8 Hz, J^3cis =10.2 Hz, 1H, H(15)), 6.30 (dd, J^2 =1.7 Hz, J^3trans =17.2 Hz, 1H, H(16)), 6.44 (dd, J^3cis =10.2 Hz, J^3trans =17.1 Hz, 1H, H(17)), 10.22 (s, 1H, H(7)), 14.0 (s, broad, 2H, H(20,23)), proton assignment: see Fig. S2. ^{13}C NMR (101 MHz, DMSO-d_6): 169.9 C(18,21), 163.5 C(8), 149.7 C(2,4), 143.8 C(6), 131.5 C(10), 128.1 C(11), 98.6 C(1,5), 87.7 C(3), the carbon assignment was done with the help of ChemDraw Professional 19: see Fig. S3. ESI-MS: m/z = 613.74 $[M+H]^+$; Elemental analysis calcd (%) for $C_{11}H_6I_3NO_5$: C 21.56, H 0.99, N 2.29; found: C 21.75, H 0.93, N 2.36.

Poly(2,4,6-triiodo-5-(prop-2-enamido)benzene-1,3-dicarboxylic acid) (3)

2,4,6-triiodo-5-(prop-2-enamido)benzene-1,3-dicarboxylic acid (**2**) (25.12 g, 40 mmol) was dissolved in DMF (40 mL). Then, 2-(dodecylthiocarbonothioylthio)-2-methylpropionic acid (**7**) (72.8 mg, 0.2 mmol) and AIBN (16.4 mg, 0.1 mmol) were added. The solution was degassed by three freeze-evacuate-thaw cycles and transferred to an oil bath preheated at 70 °C under nitrogen flow. The polymerization was carried out for 96 h under slow stirring and then was quenched by cooling in an ice bath under atmospheric air for 30 minutes (conversion degree 78 %). DMF was removed on a rotovap at 10 mbar, 50 °C and the product was dried under high vacuum for 2 days to give polymer **3** (24.6 g, 95%) as a yellowish solid. The proton nuclear magnetic resonance (NMR) spectrum was measured at the end of the reaction to calculate the conversion degree of the polymerization process, which was determined to be 78 %. It was obtained via the ratio of the integral of the methine proton signal at 2.54 to 2.60 ppm to half of the integral of the carboxylic group proton signal at 13.4 to 14.5 ppm. (*Suppl. Fig. S2*). ^{1}H NMR (400 MHz, DMSO-d_6): 5.82 (dd, J^2 =1.8 Hz, J^3cis =10.2 Hz, 0.22 H), 6.30 (dd, J^2 =1.7 Hz, J^3trans =17.2 Hz, 0.26 H), 6.44 (dd, J^3cis =10.2 Hz, J^3trans =17.1 Hz, 0.22 H), 10.22 (s, 0.26 H), 14.01 (s, broad, 2 H), see Fig. S4. Elemental analysis calcd (%) for $C_{15.35}H_{16.15}I_3N_{2.45}O_{6.45}$ (M+1.45 DMF): C, 25.65; H, 2.26; N, 4.77 Found: C, 25.57; H, 2.56; N, 4.41.

XlinCA (6)

The polymer **3** was re-dissolved in 40 mL of DMF before the oxalyl chloride-DMF adduct was added in small portions. The oxalyl chloride-DMF adduct was synthesized by adding oxalyl chloride (15 mL) dropwise over 15 min to a solution of 40 mL of DMF in 300 mL of DCM, while the reaction was being cooled in an ice bath. After 15 min, DCM was evaporated giving the mixture of adduct in DMF, then the whole mixture was used to treat the polymer **3**.

The reaction mixture was stirred at room temperature for 30 min. Afterwards, the solution was added quickly to 500 mL of water to precipitate the product. The precipitate was filtered, washed with 100 mL of water, and dried under high vacuum overnight to give the chlorinated polymer **4**.

Chlorinated polymer **4** was dissolved in DMF (100 mL) and the solution was added quickly to the ice-cold mixture of ethylene diamine (100 mL) and water (100 mL) under vigorous stirring. After 30 min, the solvents were evaporated *in vacuo*. Water (50 mL) was added to the residue and the mixture was lyophilized under high vacuum to give **5** (23.4 g, 95 %). Polymer **5** was found not to be soluble in all tested solvents tested solvents (D_2O, MeOH, DMSO and DMF). Therefore, it was converted to a water-soluble salt form (polymer **6**) without characterisation. **5** was dissolved in HCl solution (100 mL, 2 M). The solution was dialyzed with a 12 kDa membrane against NaCl solution (10 L, 0.2%), changing the solution after 3 h, 8 h and 24 h; then against deionized water (10 L) for 6 h more. Afterwards, pH was readjusted to 7 by adding NaOH 1M solution and the solution lyophilized to give the final product *XlinCA* **6** as a white to yellowish powder (19.2 g, 82 %). IR [KBr, cm^{-1}]: 3420, 3231, 3053, 1647, 1546, 1384, 1351, 1270, 1171, 1030, 618. GPC (M_n= 33700, PDI= 3.16). Unfortunately, no high-resolution ^{1}H-NMR spectra could be obtained for **6**. The ^{1}H-NMR of

polymer **6** in D_2O gave broad signals (see Fig. S5). Other tested solvents (MeOH, DMSO and DMF) did not dissolve the compound.

GPC measurement of contrast agent *XlinCA* (6)
GPC measurements were done by PSS Polymer Standards Service GmbH, Mainz, Germany.
Sample preparation: About 2 mg of each sample were weighed in on an analytical balance. 2 mL of eluent were added to the sample and left to dissolve at room temperature. After 2 hours, the sample was completely dissolved and could be measured. The sample solution was not filtrated before the measurement and 100 µL were injected by an autosampler (Fig. S6).
Calibration and Calculation: Pullulan-standards with different molecular weights were analyzed first in order to get a calibration curve. The calculations of the average molecular weights and the molecular weight distribution of the samples were done by the so-called slice by slice method based on the pullulan-calibration.

Table S1.: Calculation of the average molecular weights and the molecular weight distribution. M_n: Number average molecular weight, M_w: Weight average molecular weight, M_z: Size average molecular weight, PDI: Polydispersity index, V_p: Elution volume at peak maximum, M_p: Molecular weight at the peak maximum, Area: Total area under elugram.

	Detector	M_n /Da	M_w /Da	M_z /Da	PDI (=M_w/M_n)	V_p /mL	M_p /Da	Area
	UV@230 nm	33700	107000	324000	3,16	22,58	39900	2686,9200
	RID	33400	105000	325000	3,16	22,60	39400	16,6182

5.4.6.1.3 Mouse husbandry

C57BL/6J mice were purchased from Charles River Laboratories and Janvier Labs and were housed in individually ventilated cages in 12 h light/dark cycles with ad libitum access to water and standard rodent food (Kliba Nafag 3436). All animal experiments were approved by the veterinary office of the canton of Zurich (license number ZH233/15).

5.4.6.1.4 Pre-crosslinking of contrast agent

Contrast agent *XlinCA* (5 g) was dissolved in water (20 mL). 150 µL of an aqueous glutaraldehyde solution (25 %) were added and mixed well. The mixture was left to rest at room temperature for 20 min. 30 mL of water were then added, and the solution was dialysed through a 100 kDa dialysis membrane against NaCl solution (5 L, 0.2 %), changing the solution after 3 h, 8 h and 24 h; then against deionized water for 6 h. The solution was centrifuged to remove all insoluble particles and lyophilized to give 4 g of a solid, pre-crosslinked contrast agent.

5.4.6.1.5 Transcardial whole body perfusion with polymeric contrast agent

A 9 month old mouse was euthanized with ketamine/ xylazine. The chest cavity was opened, a blunted 21 G butterfly needle inserted into the left ventricle and the right atrium cut as an outlet. Blood was flushed out with approx. 10 mL of phosphate-buffered saline (PBS) and the mouse fixed with 100 mL 4 % formaldehyde and 1 % glutaraldehyde in PBS. The aldehydes were flushed out with 50 mL PBS and quenched with 50 mL 0.5 % glycine in PBS. The mouse was finally flushed with 25 mL PBS and perfused with 14 mL contrast agent solution filtered through a 1.2 µm pore syringe filter (2.7 g of pre-crosslinked above contrast agent in 14 mL H_2O, 100 mg iodine/ml prior to filtering). To close the outlet, 4 % glutaraldehyde in PBS was dripped onto the heart to initiate crosslinking. Gelation of superficial *XlinCA* on the heart and in the thoracic cavity started within 30

s, and did not visibly proceed further after 5 min. The entire mouse was subsequently immersed in 500 mL 4 % glutaraldehyde in PBS.

5.4.6.1.6 Transcardial whole body perfusion with vascular casting resin PU4ii

The left ventricle was cannulated as above, and the blood was flushed out with approx. 10 mL of PBS and the mouse fixed with 100 mL 4 % formaldehyde in PBS. Vascular casting was performed using a mixture of 3.7 g 1,3-diiodobenzene (Sigma-Aldrich, USA) with the vascular casting resin PU4ii (vasQtec, Switzerland), which consists of 10 g 2-butanone, 10 g PU4ii resin and 1.6 g PU4ii hardener. The final contrast agent concentration of the PU4ii mixture was 110 mg iodine/ml.

5.4.6.1.7 X-ray µCT scans

For the low-resolution comparison scans, the heads of the PU4ii- and *XlinCA*-perfused mice were scanned with 80 µm voxel size using a QuantumFX *in vivo* µCT scanner (PerkinElmer, USA) with an acceleration voltage of 70 kV and a tube current of 200 µA. High-resolution scans were performed on a Nanotom m µCT scanner (General Electric, USA) using an X-ray tube with a water-cooled tungsten target set to an acceleration voltage of 60 kV and a tube current of 310 µA. 1440 projections per height step were acquired with 0.5 s exposure time using a scintillator-coupled flat-panel detector. The mouse was removed from the fixation solution, mounted in a plastic cup using polyurethane foam and scanned with 20 µm voxel size. The skull was scanned in the same configuration with 14.5 µm voxel size. The brain was excised, cut in the middle with a razor blade. The right brain hemisphere and the kidney were embedded in 1% agar in 1.5 mL centrifugation tubes and scanned with 4.4 µm voxel size.
The whole mouse and skull were visualized using Arivis4D 2.12.4 (Arivis, Germany). The brain hemisphere, kidney and adrenal gland were visualized using VGStudio Max 2.1 (Volume Graphics, Germany).
Fractional vessel volume (*FVV*) was estimated by dividing the overall mean intensity values of regions of interests (I_{ROI}) by the intensity values of contrast-agent filled, fully resolved vessels (I_{Ves}), after first subtracting intensity values of non-perfused tissue as background (I_{Bkg}) [2]. Regions of interest were measured in the brain, liver and kidneys.

$$FVV = \frac{I_{ROI} - I_{Bkg}}{I_{Ves} - I_{Bkg}}$$

5.4.6.2 References

[1] Z. B. Jian, M. C. Baier, and S. Mecking, "Suppression of Chain Transfer in Catalytic Acrylate Polymerization via Rapid and Selective Secondary Insertion," *J. Am. Chem. Soc.,* vol. 137, pp. 2836-2839, Mar 4 2015, doi: 10.1021/jacs.5b00179.

[2] A. Garcia-Sanz, A. Rodriguez-Barbero, M. D. Bentley, E. L. Ritman, and J. C. Romero, "Three-dimensional microcomputed tomography of renal vasculature in rats," *Hypertension,* vol. 31, pp. 440-4, Jan 1998, doi: 10.1161/01.hyp.31.1.440.

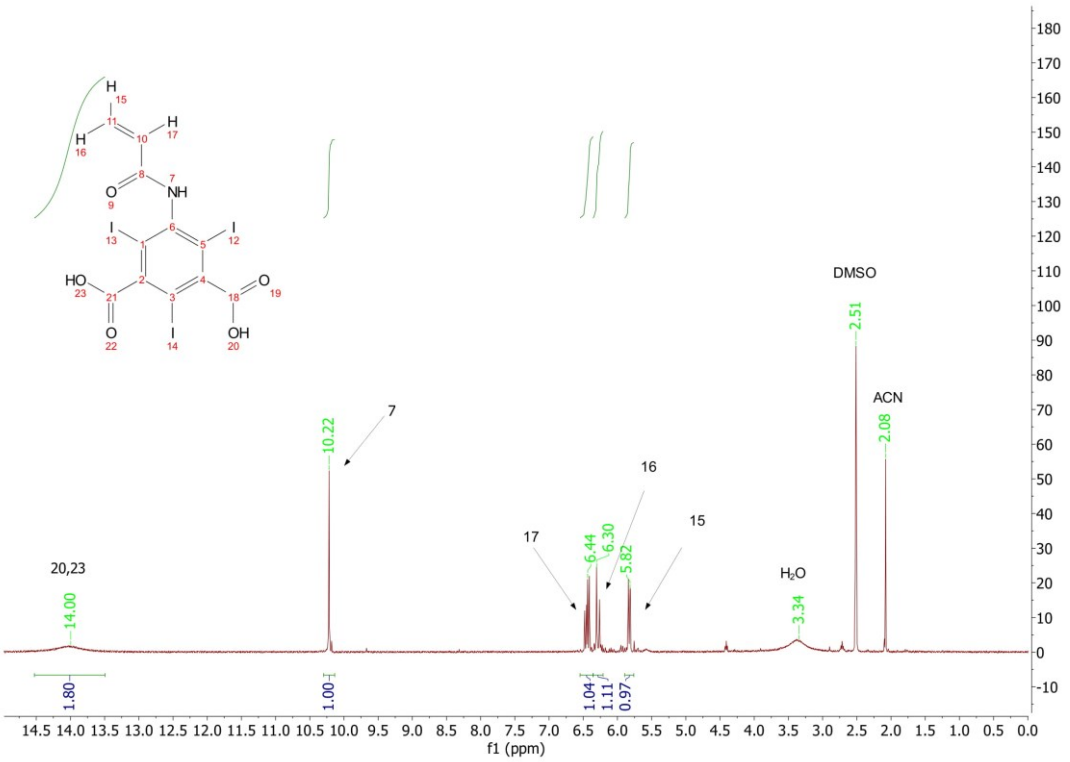

Fig. S2.: ^{1}*H NMR of* ***2*** *in DMSO-d*$_6$

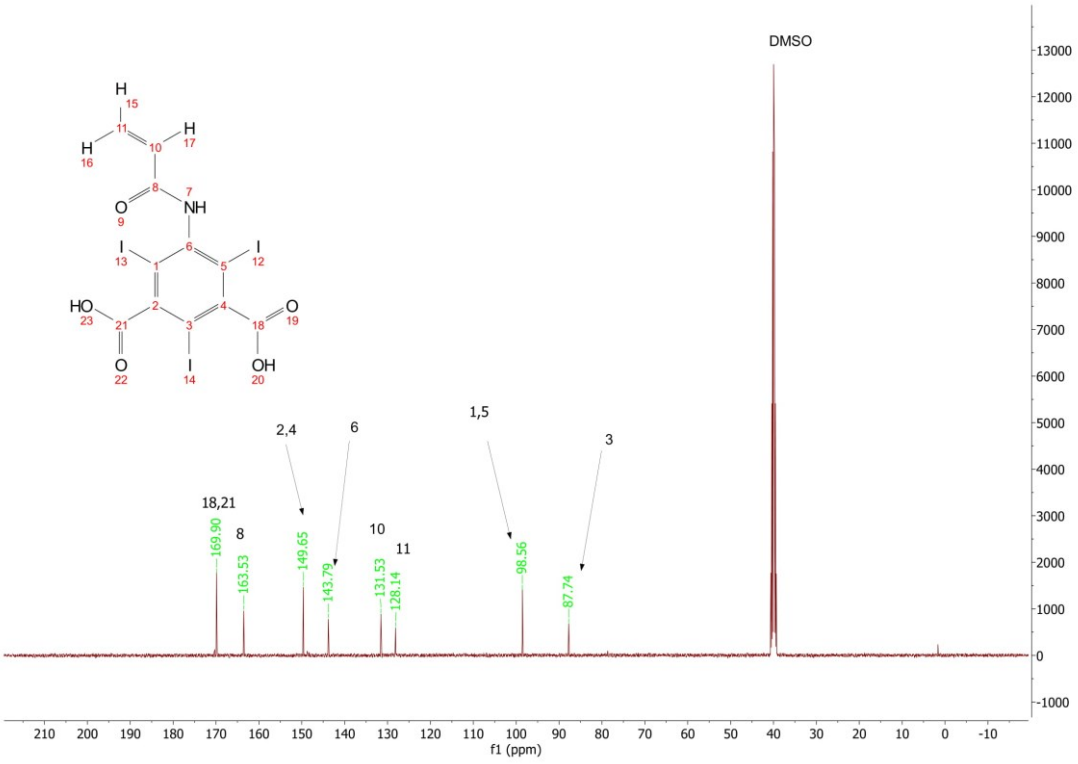

Fig. S3.: ^{13}*C NMR of* ***2*** *in DMSO-d*$_6$

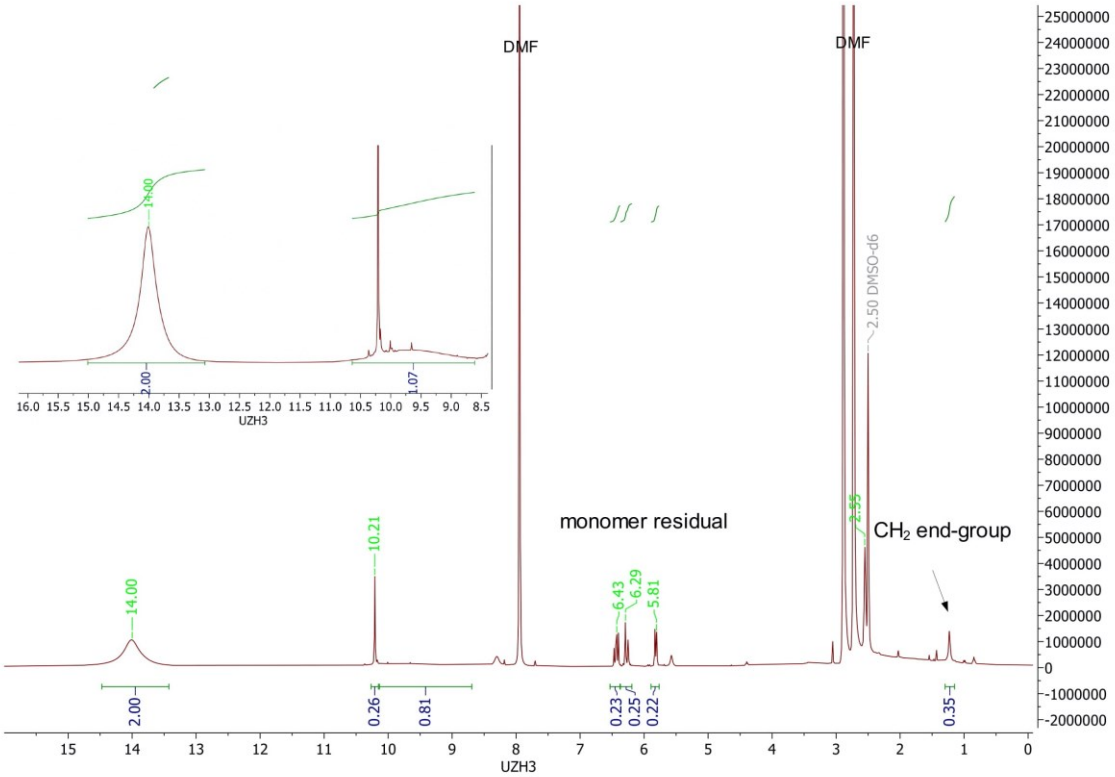

*Fig. S4.: ^{1}H NMR of polymer **3** in DMSO-d_6*

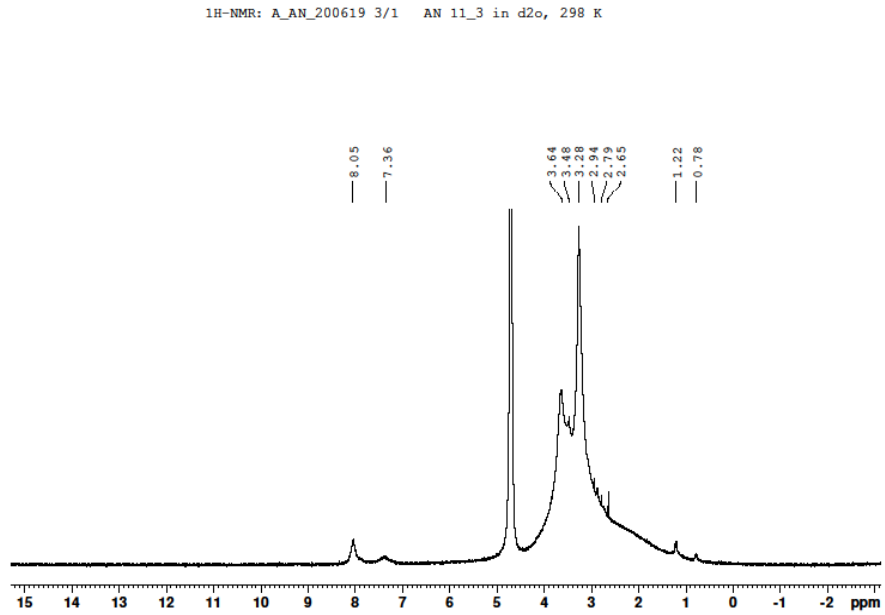

*Fig. S5.: ^{1}H NMR of XlinCA (**6**) in D_2O.*

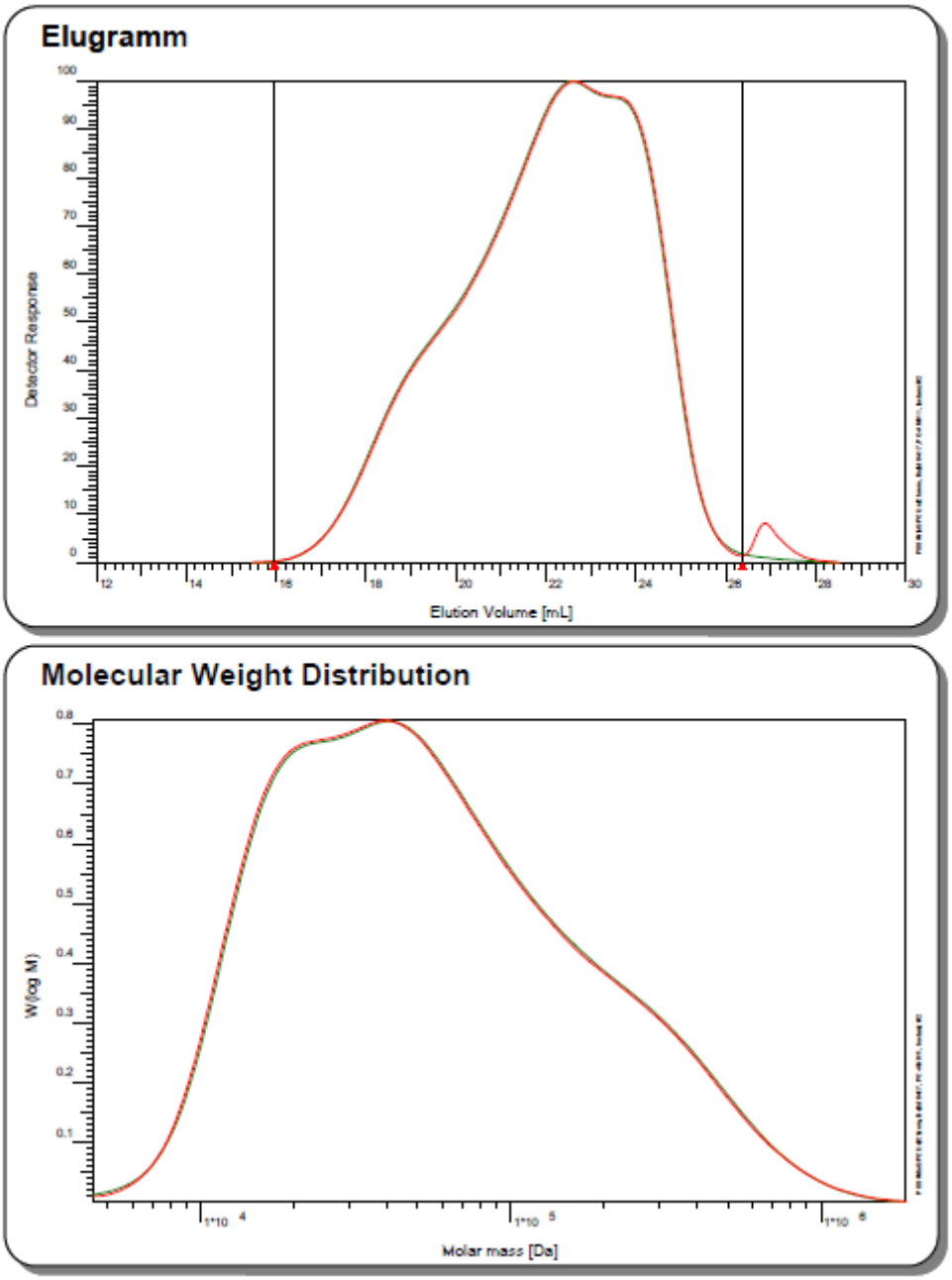

Fig. S6.: Elugram and molecular weight distribution diagram of XlinCA ***(6)***

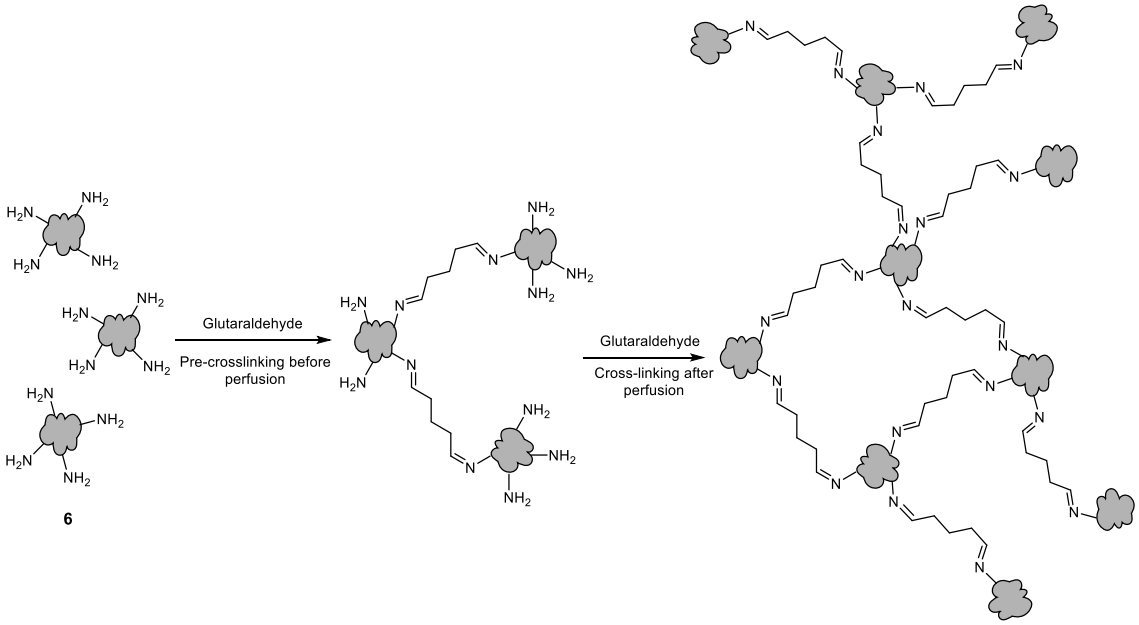

*Fig. S7.: Crosslinking of the contrast agent XlinCA (**6**) by imine formation through reaction of amine groups with glutaraldehyde.*

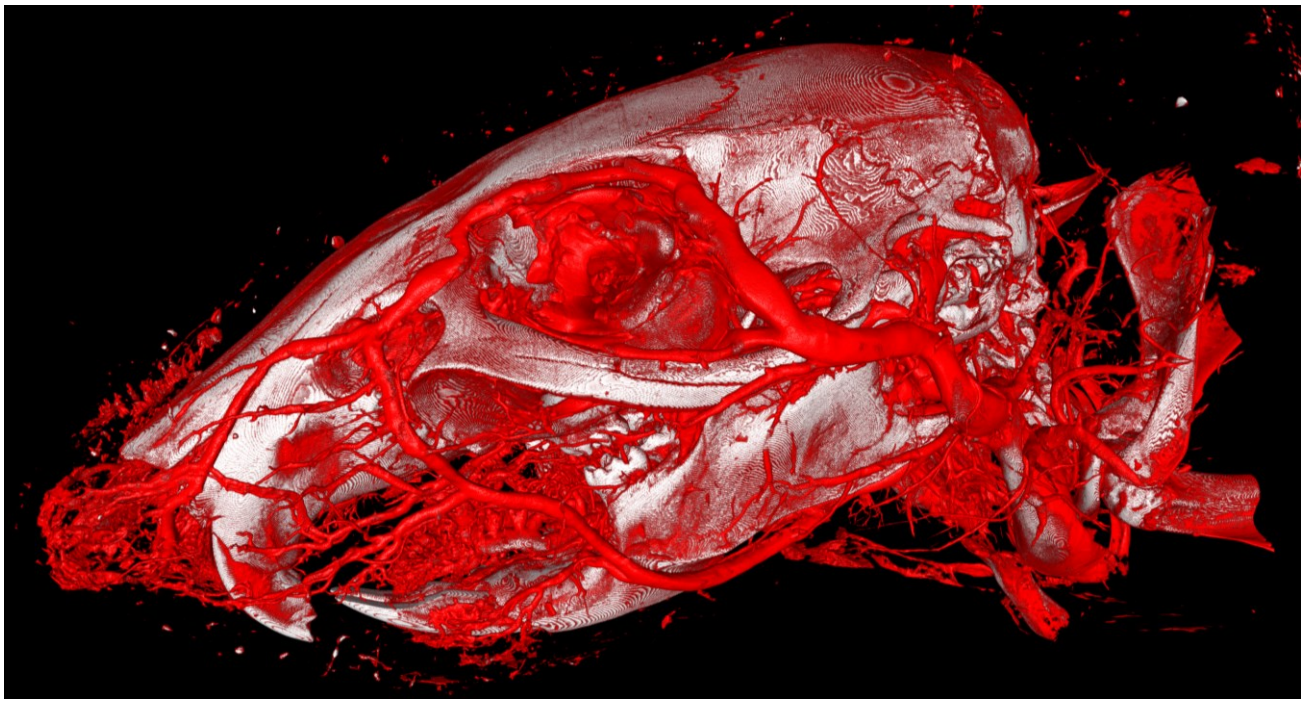

Fig. S8.: 3D visualization of the skull vasculature perfused with XlinCA and imaged with 14.5 µm voxel size using X-ray µCT.

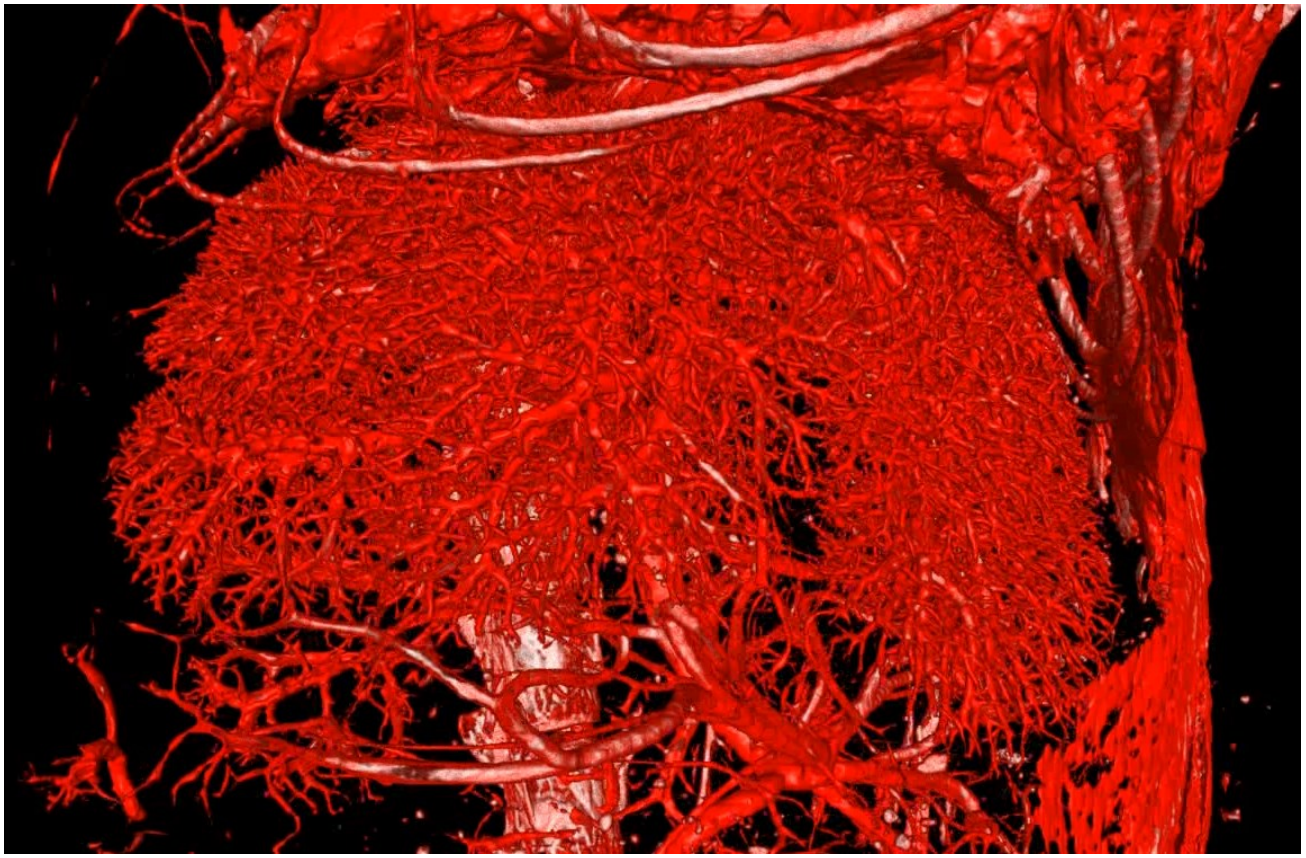

Fig. S9.: 3D visualization of the liver vasculature perfused with XlinCA, derived from the whole mouse µCT dataset acquired with 20 µm voxel size.

Fig. S10.: 3D visualization of microvasculature in the kidney and adrenal gland imaged with 4.4 µm voxel size. The organs are well perfused with XlinCA, with the exception of parts of the capillaries missing in the renal medulla. This issue is caused by incomplete flushing of blood prior to contrast agent injection, and can be resolved by employing kidney-specific, optimized perfusion protocols.

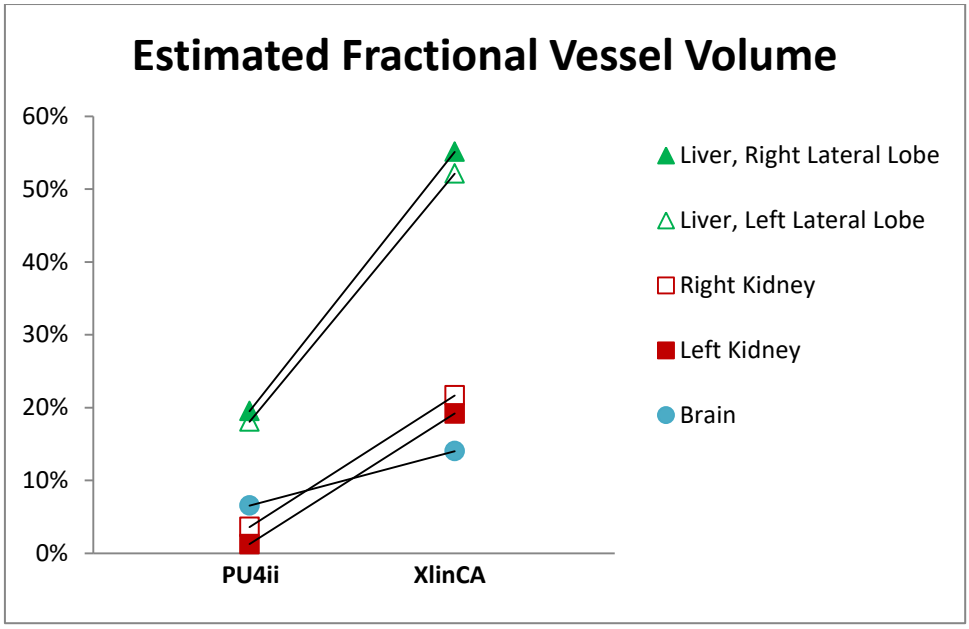

*Fig. S11.: Estimated fractional vessel volume of independently vascularized regions of interest in the brain, liver and kidney. XlinCA (**6**) demonstrates higher fractional vessel volume (32.4 % ± 19.6 %, mean ± SD) than PU4ii (9.8 % ± 8.4 %, mean ± SD), suggesting a larger proportion of filled vasculature (p = 0.01336, two-tailed paired Student's t-test, n = 5).*

Table S2.: Optimization of the synthesis of polymer **3**. The reaction temperature was 70 ^{o}C. M: monomer, R: RAFT agent, I: AIBN. MW of polymer **3** was calculated indirectly from GPC data of polymer **6**.

conditions	**[M]: [R]: [I] [mmol]**	**Reaction time**	**Precipitation**	**Conversion degree by ^{1}H NMR**	**MW (Da) By GPC**
1	2 : 0.04 : 0.02 (= 100 : 2 : 1)	18 h	no	95%	17500
2	2 : 0.02 : 0.01 (= 200 : 2 : 1)	28 h	no	92%	24600
3	2 : 0.01 : 0.005 (= 400 : 2 : 1)	3 days	no	78%	30400
4	2 : 0.01 : 0.01 (= 400 : 2 : 2)	3 days	no	77%	29200
5	2 : 0.008 : 0.004 (500 : 2 : 1)	4 days	+	no NMR	-
6	2 : 0.0067 : 0.0033 (= 600 : 2 : 1)	5 days	++	no NMR	-
7	2 : 0.0057 : 0.029 (= 700 : 2 : 1)	7 days	+++	no NMR	-
8	2 : 0.005 : 0.0025 (= 800 : 2 : 1)	7 days	+++	no NMR	-

Journal article

5.5 Simultaneous three-dimensional vascular and tubular imaging of whole mouse kidneys with X-ray µCT

This chapter has been accepted for publication in Microscopy and Microanalysis.

My work on this publication consisted of developing and optimizing the perfusion protocols, µCT image acquisition, image processing, visualization and quantitative analysis. The contributions to the prerequisite work of developing the contrast agent XlinCA are described in the previous chapter 4.4.

Simultaneous three-dimensional vascular and tubular imaging of whole mouse kidneys with X-ray µCT

Willy Kuo[a,b,c], Ngoc An Le[d], Bernhard Spingler[d], Roland H. Wenger[a,b], Anja Kipar[e], Udo Hetzel[f], Georg Schulz[c], Bert Müller[c,*], Vartan Kurtcuoglu[a,b,g*]

[1] Institute of Physiology, University of Zurich, Winterthurerstrasse 190, 8057 Zurich, Switzerland;

[2] National Centre of Competence in Research, Kidney.CH, University of Zurich, Winterthurerstrasse 190, 8057 Zurich, Switzerland;

[3] Biomaterials Science Center, Department of Biomedical Engineering, University of Basel, Gewerbestrasse 14, 4123 Allschwil, Switzerland

[4] Department of Chemistry, University of Zurich, Winterthurerstrasse 190, 8057 Zurich, Switzerland;

[5] Laboratory for Animal Model Pathology (LAMP), Institute of Veterinary Pathology, Vetsuisse Faculty, University of Zurich, Winterthurerstrasse 268, 8057 Zurich, Switzerland

[6] Electron Microscopy Unit, Institute of Veterinary Pathology, Vetsuisse Faculty, University of Zurich, Winterthurerstrasse 268, 8057 Zurich, Switzerland

[7] Zurich Center for Integrative Human Physiology, University of Zurich, Zurich, Switzerland

* These authors contributed equally

5.5.1 Abstract

Concurrent three-dimensional imaging of the renal vascular and tubular systems on the whole kidney scale with capillary level resolution is labor intensive and technically difficult. Approaches based on vascular corrosion casting and X-ray micro computed tomography (µCT), for example, suffer from vascular filling artifacts, and necessitate imaging with an additional modality to acquire tubules. In this work, we report on a new sample preparation, image acquisition and quantification protocol for simultaneous vascular and tubular µCT imaging of whole, uncorroded mouse kidneys. The protocol consists of vascular perfusion with the water-soluble, aldehyde-fixable, polymeric X-ray contrast agent XlinCA, followed by laboratory-source µCT imaging and structural analysis using the freely available Fiji/ImageJ software. We achieved consistent filling of the entire capillary bed and staining of the tubules in the cortex and outer medulla. After imaging at isotropic voxel sizes of 3.3 and 4.4 µm, we segmented vascular and tubular systems and quantified luminal volumes, surface areas, diffusion distances and vessel path lengths. This protocol permits analysis of vascular and tubular parameters with higher reliability than vascular corrosion casting, less labor than serial sectioning and leaves tissue intact for subsequent histological examination with light and electron microscopy.

Keywords:
Vascular imaging; contrast agents; angiography; tissue staining; kidney; X-ray; computed tomography

5.5.2 Introduction

Renal function is dependent on the intricate three-dimensional (3D) arrangement of the kidney's vascular and tubular structures on both the local and whole-organ scales [1-5]. Pathologies such as autosomal dominant polycystic kidney disease or fibrosis following acute kidney injury change renal structure and may thereby affect renal function beyond the primary disease mechanism [6-8]. Whole-kidney imaging can be used to quantify structures and structural changes, yielding otherwise inaccessible entities such as whole-organ diffusion distances [9], connectivity [10] and distribution of compounds such as oxygen [11-14], both of which may be affected by pathologies. Sampling of the entire organ is crucial when investigating phenotypes that are constricted to small, specific regions that may be overlooked in 2D sampling-based approaches [15]. However, concurrent whole-kidney imaging of vascular and tubular systems at capillary resolution is time-consuming, error prone and technically difficult.

Micro computed tomography (μCT) combined with vascular casting has been utilized in the evaluation of capillary rarefaction in ischemia-reperfusion, unilateral ureteral obstruction and Alport models of kidney disease [16], measurement of vascular volume in different kidney regions [17], changes in kidney cortical vascular volume in a chronic bile duct ligation model of liver cirrhosis [18], measurement of vessel area of wrapped artery-vein pairs permitting oxygen shunting [19], and in the analysis of blood vessel hierarchy and bifurcations [20].

In vascular corrosion casting, polymerizing plastic resin is injected into the vasculature and the organ tissue is dissolved to yield a solid plastic cast that can be imaged with light or electron microscopy [7, 21-25]. Since this approach destroys the tissue, concurrent or subsequent analysis of renal tubules or other structures is impossible. For corrosion-free vascular casting, plastic resins with radiopaque additives such as lead chromate, barium sulfate or iodine compounds are available, permitting non-destructive imaging with X-ray μCT [16, 24, 26-29]. Without such additives, vascular lumina or renal tubular tissue cannot be distinguished from water or agar background with standard laboratory X-ray source μCT.

As the plastic resins employed in vascular casting are hydrophobic, any water-based fluid present in the vasculature must be displaced physically during the injection. This requires well optimized injection procedures combined with ligations to divert all resin flow to the organ of interest [30]. If water is incompletely removed, water inclusions can result in visible bubbles instead of fully filled large vessels [16, 29]. To reduce this problem, flow rate and thus perfusion pressure is typically increased, which, in the kidney, may lead to bleeding into the renal capsule, visible as shape distortion of the kidney surface. Tubules may also collapse during perfusion with hydrophobic substances due to the lack of tubular counter pressure in the absence of glomerular filtration [31]. These challenges make the preparation of an artifact-free sample technically difficult, frequently resulting in large numbers of samples with incomplete filling that have to be excluded from the respective study [32, 33].

To simplify the procedure of vascular imaging and allow for simultaneous acquisition of the cortical tubular network, we developed a new approach around XlinCA, an iodine-based contrast agent developed specifically for ex vivo X-ray μCT [34]. XlinCA is a water-soluble polymer large enough to avoid glomerular filtration. It can be cross-linked with glutaraldehyde to be retained within the vasculature permanently. As a water-soluble compound, the issue of water inclusions common to hydrophobic vascular casting resins is inherently avoided. Polymerization can be initiated from outside the organ at any time, obviating the need for optimization of injection time. Perfusion with XlinCA can therefore proceed for as long as is required to achieve proper filling of the vasculature. Beyond resolving these artifacts, XlinCA features limited passive accumulation in the tubular walls in the cortex and outer medulla and enables visualization of these features within the same μCT scan.

The protocol presented herein allows for imaging the renal vascular and tubular systems in 3D with a single μCT acquisition. In addition, it provides a simple step-by-step image processing and quantification workflow that requires no specialized image processing expertise and relies solely on

the freely available Fiji/ImageJ software platform. Overall, it enables quantification of vascular parameters with higher reliability than vascular corrosion casting, permits analysis of tubular parameters with less labor than serial sectioning, and allows for subsequent histological examination with light and electron microscopy.

5.5.3 Materials and Methods

Detailed methods, including chemical suppliers, surgical guide, detailed scan parameters and exact image processing steps are provided as supplemental data.

5.5.3.1 X-ray contrast agent synthesis

The contrast agent was synthesized as described previously [34]. In brief, an acryloyl group was added to the amine of 5-amino-2,4,6-triiodoisophthalic acid. The resulting compound was polymerized via reversible addition−fragmentation chain-transfer polymerization [35, 36] to a molecular weight of approximately 30 000 g/mol. Ethylenediamine was coupled with the carboxylic acid groups of the polymer to add free amine groups, enabling aldehyde fixation. The chemical structure of the compound is given in Suppl. Fig. S1. To increase the size of the polymer, it was pre-crosslinked with a small amount of glutaraldehyde and dialyzed using a membrane with a cut-off of 100 000 g/mol.

5.5.3.2 Mouse husbandry

Three female C57BL/6J mice were purchased from Charles River Laboratories and Janvier Labs and were kept until the age of 7 or 10 months in individually ventilated cages with ad libitum access to water and standard rodent food (Kliba Nafag 3436) in 12 h light/dark cycles. All animal experiments were approved by the veterinary office of the canton of Zurich (license number ZH233/15).

5.5.3.3 Abdominal aorta perfusion

Mice were anaesthetized with ketamine/xylazine, and kidneys were perfused retrogradely via the abdominal aorta [37] with a 21 G butterfly needle connected via a 2.5 m long silicone tube to a reservoir providing 150 mmHg of hydrostatic pressure, which resulted in flow rates of about 5 ml / min. Kidneys were flushed with approximately 10 ml of phosphate-buffered saline (PBS) and fixed with 100 ml 4% formaldehyde / 1% glutaraldehyde in PBS. Remaining aldehydes were flushed out with 20 ml PBS and quenched with 50 ml glycine solution (5 mg / ml in PBS), then flushed again with another 40 ml PBS. All perfused solutions were kept at 37°C.
4 ml of XlinCA contrast agent solution (75 mg iodine/ml) were perfused using a 10 ml syringe, actuated with a constant weight to provide 150 mmHg of pressure. Flow rates were typically between 0.3 and 0.5 ml / min. The abdominal cavity was then filled with 4% glutaraldehyde in PBS to crosslink the contrast agent, and the kidneys were removed afterwards and kept in 4% glutaraldehyde / PBS. These solutions were kept at room temperature.
Fixed kidneys were mounted in 1% agar in PBS in either standard 1.5 ml centrifugation tubes or 0.5 ml PCR tubes for scanning, depending on their size.

5.5.3.4 X-ray µCT image acquisition

The X-ray µCT data were acquired with a General Electric Phoenix Nanotom m, equipped with a tungsten target and diamond window. Acceleration voltage was set to 60 kV, current to 310 µA. 1440 projections were acquired per height step with a GE DXR detector with a 3072 × 2400 pixel array with 0.5 s exposure time. Kidneys mounted in 1.5 ml tubes were scanned with 4.4 µm isotropic voxel size. Three frames per projection were recorded and averaged, resulting in a scan

time of approximately 3 h per kidney. The one kidney mounted in a 0.5 ml tube was scanned with 3.3 µm isotropic voxel size with 12 frames per projection averaged, resulting in 10 h of scan time. Four height steps were required for each kidney. Reconstruction was performed with the manufacturer's GE phoenix datos|x software.

5.5.3.5 Histological examination

Fixed kidneys were trimmed (midline longitudinal or cross-section) and paraffin wax embedded. Consecutive sections (3-5 µm) were stained with hematoxylin-eosin (HE) and the periodic acid Schiff reaction for histological examination, or were deparaffinized and left unstained for assessment of fluorescence. Slides were photographed through a Nikon Eclipse Ni-U microscope with digital camera and scanned using a digital slide scanner with 40× magnification (NanoZoomer-XR C12000, Hamamatsu, Japan).

5.5.3.6 Transmission electron microscopy examination

A slice of fixed kidney (midline cross-section) was trimmed and embedded in epoxy resin. Toluidine blue-stained semithin (1.5 µm) sections were prepared to select areas of interest for the preparation of ultrathin (75 nm) sections that were either directly viewed with a Philips CM10 microscope, operating with a Gatan Orius SC1000 digital camera (Gatan Microscopical Suite, Digital Micrograph), or were contrasted with lead citrate and uranyl acetate and viewed subsequently.

5.5.3.7 Example segmentation and quantification

The 3.3 µm dataset was segmented using the free Fiji/ImageJ software [38, 39] with the MorphoLibJ [40] and 3D ImageJ Suite plugins [41] installed. A 3D Gauss filter with $\sigma = 1$ pixel was applied, and the blood vessel lumina were extracted by setting manual thresholds. A rough kidney mask was created with a lower threshold, then erosion and connected component analysis with the MorphoLibJ plugin [40] were used to remove areas of contrast outside the kidney. This mask was then applied to the blood vessel segment.
The blood vessel segment was transformed into a more refined kidney mask by dilation, 3D hole filling using the 3D ImageJ Suite plugin [41] and subsequent erosion. This mask was combined with thresholding of the water background to obtain the tubular lumina. Any remaining volume within the mask that was part of neither the blood vessels nor the tubular lumina was declared kidney tissue. The binary representations of the segmented vascular lumina, tubular lumina and kidney tissue are available together with the original µCT dataset on the *Zenodo* public repository, DOI: 10.5281/zenodo.3354338.
Blood vessel and tubular volumes were calculated by adding up the number of voxels in the binary segments. The blood vessel and tubuli surface areas were estimated with the MorphoLibJ plugin by counting the number of line probe intersections in 13 different directions. A marker point was manually selected at the papilla of the kidney in the blood vessel segment, and the geodesic distance map was calculated using the same plugin. The Euclidean distance map and all histograms were calculated using default Fiji/ImageJ functions.
Image processing was performed on a workstation equipped with 256 GB RAM and two 8-core Intel Xeon E5-2670 processors. 3D computer graphic images of the segmentation were rendered with Arivis4D 2.12.4 (Arivis, Germany) on a virtual machine with 174 GB of RAM, 7 Intel Xeon E5-2680 v2 cores and pass-through Nvidia GRID K2 graphics.

5.5.4 Results

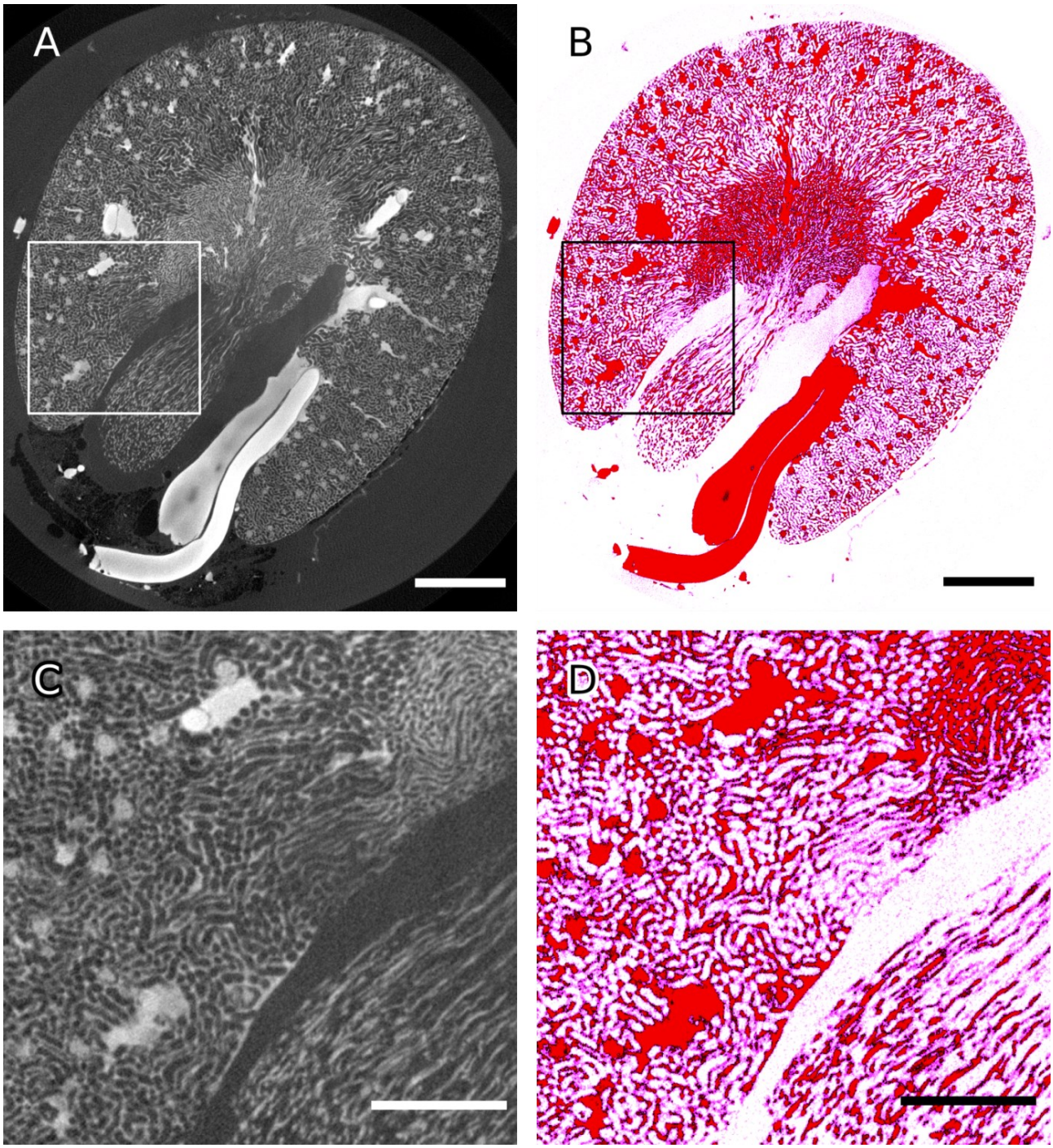

Fig. 1.: A: Virtual section of the 3.3 µm voxel size µCT dataset displaying blood vessels (white and light grey) and tubular walls (grey). B: False-color image of the same virtual section of the µCT dataset, approximating the appearance of a HE-stained histological section. Red: blood vessels, purple: tubular walls. Scale bars: 1 mm. C, D: Magnified views of the boxed regions in the top panels containing parts of the cortex, outer medulla and inner medulla. Scale bars: 0.5 mm.

Vascular casting of mouse kidneys with the water-soluble, cross-linkable contrast agent XlinCA was carried out at a fixed perfusion pressure without the need to maintain a minimum flow rate. No water inclusions or disconnected vessels could be identified, even in kidneys perfused at low flow rates that would result in severe filling artifacts with conventional plastic resin-based vascular casting materials.

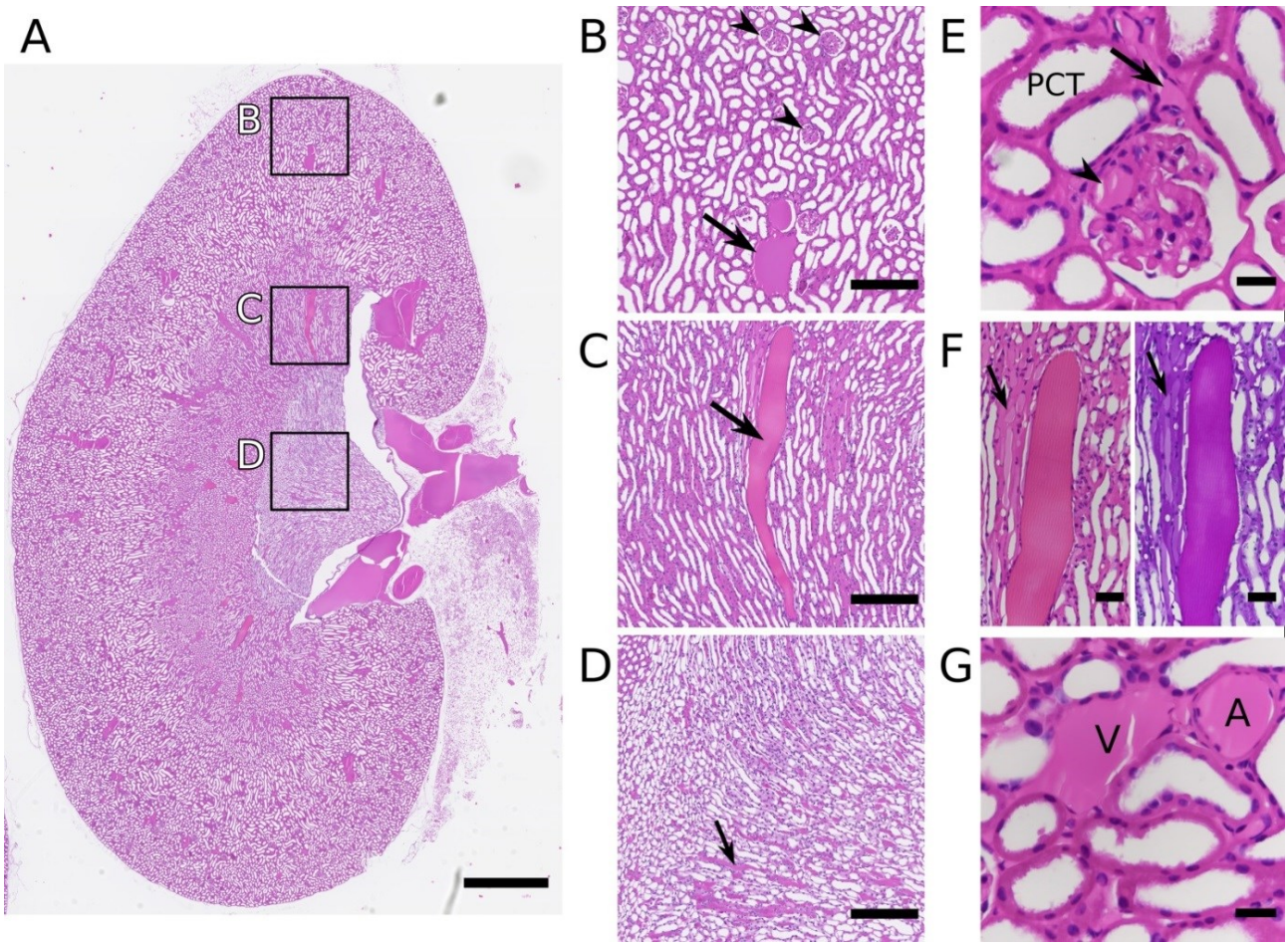

Fig. 2.: Long axis midline section of mouse kidney after perfusion with the contrast agent; HE stain. A: Overview. Scale bar: 1 mm. B: Part of renal cortex, containing glomeruli (arrowhead) and an artery-vein pair. The contrast agent is visible as homogenous, amorphous eosinophilic material due to the abundance of primary amine groups in its structure (arrow). Scale bar: 200 µm. C: Inner stripe of the outer medulla, with one longitudinally cut tubule filled with an eosinophilic protein cast (arrow). Scale bar: 200 µm. D: Inner medulla, containing contrast agent-filled vasa recta (arrow). Scale bar: 200 µm. E: Cortex with glomerulus and proximal convoluted tubules (PCT). Contrast agent is seen within glomerular capillaries (arrowhead) and interstitial blood vessels (arrow). Scale bar: 20 µm. F: Closer view of tubule in Fig. 2C, filled with protein cast. Adjacent blood vessels contain contrast agent (arrow). Left: HE stain; right: PAS reaction. Scale bars: 40 µm. G: Contrast agent in an artery (A) and a vein (V) in the cortex. Scale bar: 20 µm.

µCT datasets of 6 mouse kidneys were acquired with 4.4 µm voxel size and sufficient contrast to distinguish vascular and tubular lumina, as is shown in Fig. 1 using both the original grayscale and a false-color map mimicking the appearance HE-stained histological sections. Contrast retention within the vascular lumen and cortical tubular tissue was permanent. One additional dataset with 3.3 µm voxel size was acquired after one month of storage and did not exhibit any reduction in contrast between blood vessels, surrounding tissue and background.

Fluid-filled longitudinal structures in the inner stripe of the outer medulla could be identified in the µCT data in all mice, despite using healthy mice with non-transgenic background and without any intervention (Suppl. Fig. S2). These structures would not have been captured with previous vascular casting methods, which provide no direct means of identifying specific structures in the tissue. The histological examination shown in Fig. 2 identified those as protein casts within thin ascending tubules, and the PAS reaction confirmed that, unlike the contrast agent, these casts contained some polysaccharides. There was no histological evidence of tissue damage. The latter was confirmed also at ultrastructural level. Cellular ultrastructures were well preserved in transmission electron microscopy images (Suppl. Fig. S3). Capillaries were found to be well filled with contrast agent and

their diameter increased compared to unperfused kidneys, although the change in capillary diameter is too small to be captured by µCT with 3.3 µm wide voxels. The increase is a consequence of the 150 mmHg of perfusion pressure employed during fixation, which was chosen to increase the reliability of the initial flushing step to remove blood. While this is well above resting blood pressure, it represents the upper end of blood pressure during physical activity [42, 43] and is in keeping with or lower than perfusion pressures typically used in vascular casting [30, 33, 44].
Tubular lumina were also found to be slightly dilated, featuring diameters in the range of 20 – 40 µm compared to the *in vivo* situation where tubular diameters are closer to 20 – 30 µm in mice [45]. This deviation lies within the variability of other sample preparation methods and other factors such as choice of anesthetic *in vivo*.
To determine the contrast agent behavior under suboptimal conditions, a kidney with incomplete perfusion due to surgical mistakes was evaluated. The presence of erythrocytes in blood vessels not filled with contrast (Suppl. Fig. S4) suggests that the lack of filling is caused by insufficient flushing of the blood vessels prior to contrast agent injection. It is thus not an issue directly related to the agent. Filling with contrast is likely primarily dependent on the quality of the initial blood removal step.
The quality of the µCT data with a voxel size of 3.3 µm enabled us to extract the vascular and tubular lumina of a single kidney as binary masks using a semiautomatic workflow in Fiji/ImageJ, and to visualize them with Arivis4D as shown in Fig. 3 and the Supplemental Video available on the *Zenodo* public repository, DOI: 10.5281/zenodo.3354338. These segmented 3D data can be employed to determine quantities such as blood vessel density - a measure used to quantitatively characterize capillary rarefaction [16] - by computing the number of voxels of the masks with standard Fiji/ImageJ functions. This approach is mathematically identical to the point probe intersection method used in stereological quantification of histological sections. The volume of the segmented blood vessel lumina was 65.6 mm^3, of the tubular lumina 58.5 mm^3, of the tissue 42.6 mm^3 and of the whole kidney 166.7 mm^3, resulting in a vessel density of 39%. While this value is considerably higher than the 25.1 % Garcia-Sanz et al. calculated based on rat kidney vascular casts [17], their dataset was unable to fully resolve capillaries, and vascular density was therefore estimated by assuming a linear relationship between vessel density and mean gray value of the kidney. We expect our measurement to be the more accurate one, as capillaries were identified explicitly, could be validated visually and the discrepancy is consistent with similar underestimation of vascular density based on under-resolved µCT images [44].
Line probe intersection can be used in stereological quantification of histological sections to measure surface area. Instead of using a counting frame, we applied it to the binary masks in a fully automatic manner using MorphoLibJ. Surface areas were 8433 and 8775 mm^2 for the segmented blood vessels and tubules, respectively. This information can be used, for example, to quantify the diffusion of oxygen across the blood vessel walls, which is proportional to the surface area [19]. We are certain to have underestimated total surface area: Some vessels, such as the glomerular capillaries or vessels of the vascular bundles, are located too close together to be distinguished at the given resolution. The numbers reported represent, therefore, a lower limit. They are also usable for comparative quantification of datasets with identical resolution.
The 3D Euclidean distance of each voxel to the nearest blood vessel was calculated. This represents the minimal diffusion distance of a given location of the kidney to the nearest source of oxygen and nutrients [46], and can be used to quantify the amount of tissue that is insufficiently supplied [9]. The 3D Euclidean distance was determined for the entire space of the kidney devoid of blood vessels, creating a map as shown in Fig. 4A. We also evaluated the distribution of the distances within the kidney accounting for either the whole non-blood vessel space, or only the renal tissue (Fig. 4C). 43% of the considered non-blood vessel space is contained within the first neighboring voxel adjacent to a blood vessel if the whole space, including tubular lumina, is evaluated. However, if tubular lumina are excluded and only tissue is considered, 83% of the tissue is contained within the first voxel. This result demonstrates the potential for misinterpretation when evaluating the diffusion distances of oxygen or nutrients based solely on vascular data.

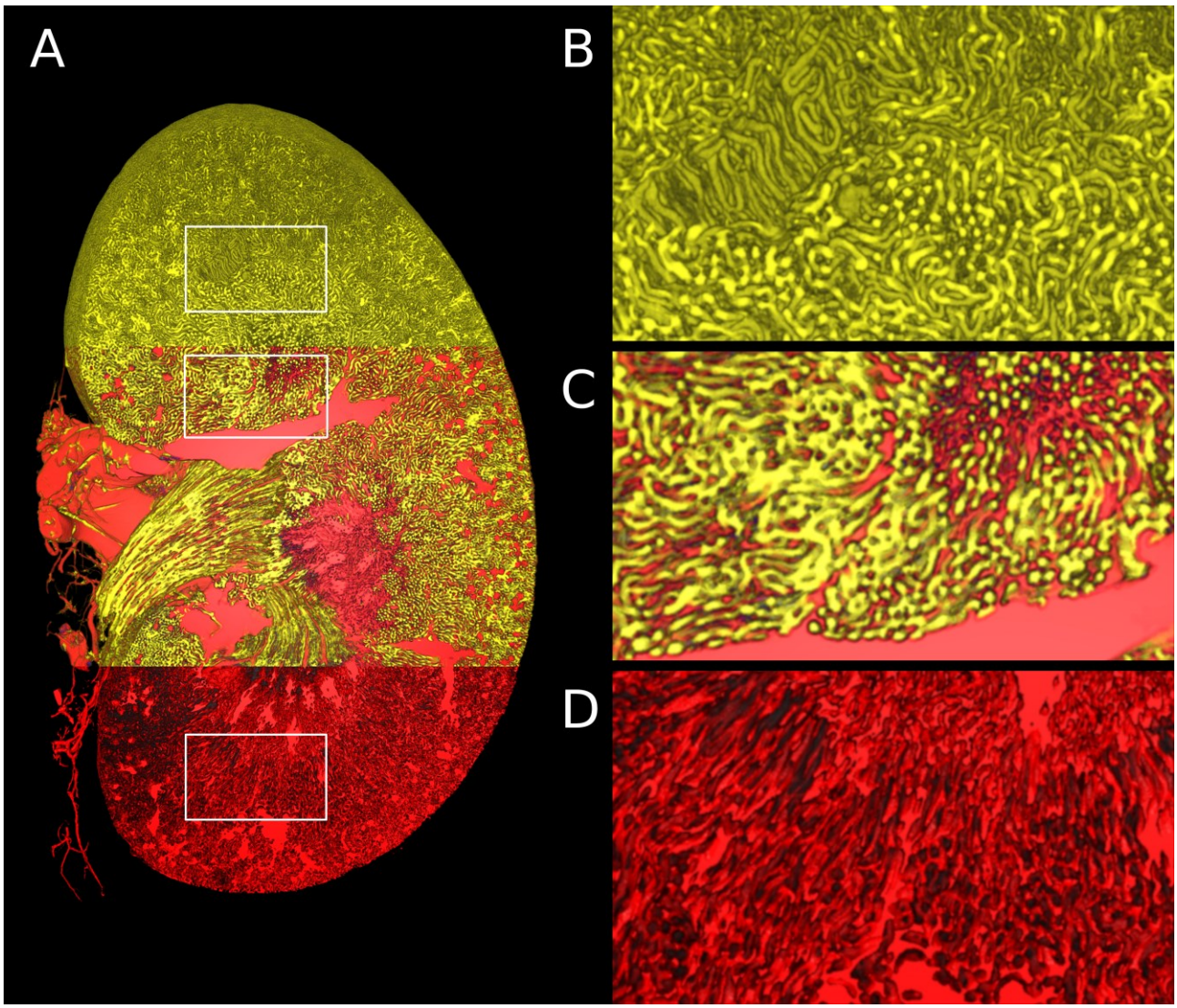

Fig. 3.: Computer rendering of the vascular and tubular structures segmented from the µCT dataset with 3.3 µm voxel size. A: Overview image including rectangles indicating the origin of the regions of interest shown on the right with higher magnification. In the top section, only tubular lumina (yellow) are displayed. Vascular lumina (red) are shown in the bottom section and both segments are shown in the middle section. Height of the kidney: 10.3 mm. B: Magnified view of segmented tubular lumina. C: Magnified view of both tubular and vascular lumina. D: Magnified view of segmented vascular lumina.

To illustrate the potential of 3D data for blood vessel path analysis, which is a measure inaccessible to 2D analysis, an arbitrary marker point in the blood vessel segment of the papilla was set and the lengths of the shortest path along the vasculature from every voxel to that marker were calculated. The resulting false-color map shown in Fig. 4B indicates 4 mm path length as the cut-off distance at which the blood vessels exit the inner and enter the outer medulla. Calculating the cumulative distribution function revealed that only 1.5% of the blood vessel volume is contained in the inner medulla (Fig. 4D). In principle, this quantification method allows determining the length of any blood vessel or tubule [10], provided that the image resolution is sufficiently high to avoid artificial shortcuts.

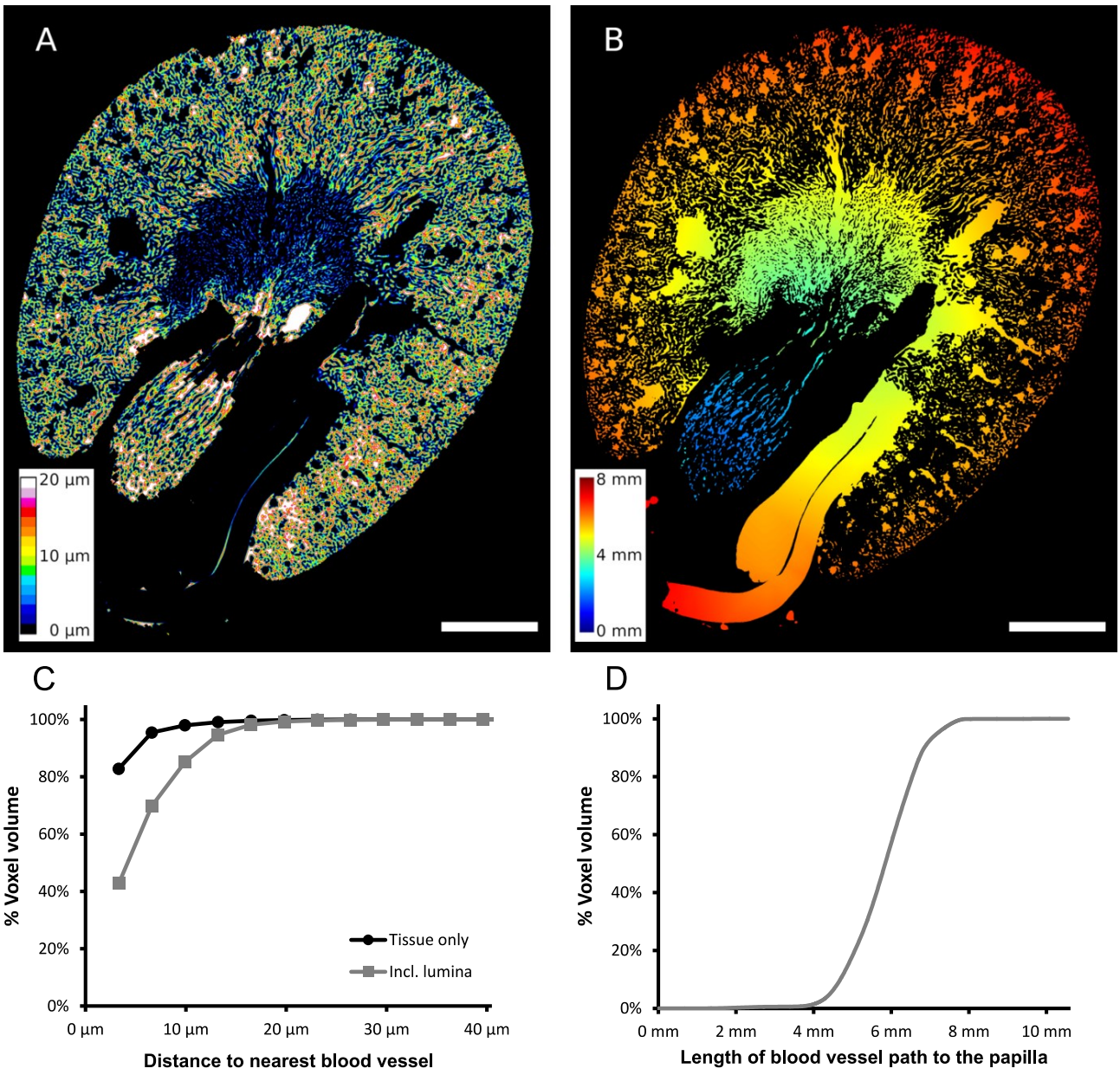

Fig. 4.: A: A kidney virtual section showing the diffusion distance of each voxel within the kidney to the nearest blood vessel. B: Virtual section displaying the lengths of the shortest paths along blood vessels of each voxel to the papilla of the kidney. Scale bars: 1 mm. C: Cumulative distribution function of the diffusion distances. D: Cumulative distribution function of the blood vessel path lengths to the papilla.

5.5.5 Discussion

5.5.5.1 Advantages in vascular imaging over previous high-resolution CT protocols

Our protocol represents an orthogonal approach to reducing artifacts encountered in 3D renal vascular imaging. We made use of a water-soluble contrast agent, XlinCA, to circumvent the problem of water inclusions caused by vascular casting with hydrophobic plastic resins. XlinCA features low viscosity and flow resistance, and polymerization can be initiated from outside the organ independent of the perfusion. This contrasts with vascular casting resins, for which polymerization and perfusion are not independent: Perfusion must be concluded within a fixed time frame - typically 20 minutes - before the resin is polymerized. Since perfusion with a minimum volume of resin is required to flush out all residual water inclusions, a certain minimum flow rate

has to be ensured. As higher flow rates require higher perfusion pressures, the casting process must be optimized to achieve the required minimum flow rate without exceeding the maximum permissible perfusion pressure.
Since XlinCA only solidifies after addition of glutaraldehyde, there is no upper time limit on how long an organ perfusion may proceed. Correspondingly, flow rate does not need to be optimized, and it does not need to be taken into consideration for optimizing perfusion pressure. These properties allowed us to achieve reliable filling of the renal vasculature with a higher success rate than using plastic-based vascular casting, while requiring little optimization of parameters such as flow rate, perfusion pressure and polymerization time.
The histologic examination revealed microscopic gas bubbles in the polymerized contrast agent hydrogel. These bubbles were invisible in the µCT datasets, since they were typically below the resolution limit and of much smaller size than the gas bubbles common in plastic-resin based vascular casting. It is therefore unclear whether these bubbles were present during the cross-linking of the contrast agent, or were introduced only later during the processing steps required for the histologic examination. As a precaution, the contrast agent solution should be degassed extensively prior to perfusion if higher resolution scans are foreseen.
Standard clinical angiography contrast agents are water-soluble compounds unsuitable for high resolution *ex vivo* vascular imaging, since these low molecular weight compounds can pass through the blood vessel walls within minutes. They are furthermore cleared via glomerular filtration. While this is necessary to prevent their accumulation in patients' bodies, it also introduces contrast agent into the tubular lumina, preventing a clear distinction between vascular and tubular structures [47]. Blood pool contrast agents are designed for longer circulation times, and surface-functionalized metal nanoparticles are available in sizes that avoid glomerular filtration. However, in *ex vivo* settings, they tend to sediment, aggregate and diffuse out of the vasculature, making them often unsuitable for capillary imaging in the kidney [48].
To resolve these issues encountered with water-soluble X-ray angiography contrast agents when used for high-resolution *ex vivo* imaging, XlinCA was designed as a polymeric compound with sufficiently large molecular weight to avoid extravasation or glomerular filtration. As a polymer of a 5-amino-2,4,6-triiodoisophthalic acid-derived monomer, the iodine content of 49.5% is considerably higher than contrast agents that rely on increasing their molecular weight by linkage to large molecules such as polyethylene glycol [49]. Free amine groups allow for covalent cross-linking with glutaraldehyde, resulting in a sample with stable contrast for months or longer.

5.5.5.2 Tubular imaging with laboratory-based µCT in absorption contrast mode

The most important advantage of the protocol lies in the ability to image tubular walls in the cortex and outer medulla concurrently with the vasculature in the same µCT scan. This is contrary to conventional casting protocols where the contrast agent only labels the vascular lumina, leaving the native tissue essentially invisible for conventional µCT. We hypothesize that limited diffusion of the polydisperse XlinCA contrast agent into the tubular walls and fixation by unquenched aldehydes within the intracellular space of the tubules is responsible for this behavior. This interpretation is supported by the electron microscopy images, where no contrast agent could be found in Bowman's space or tubular lumen, and no aggregation was observed in the extracellular space.
The exact mechanism by which XlinCA accumulates in the tubular walls is unclear. Active uptake mechanisms can be excluded, since XlinCA is perfused only after extensive aldehyde fixation of the organ. The polymer is too large to pass through channels such as aquaporins, and the presence of large amounts of small molecule fractions can be excluded due to the lack of contrast agent in Bowman's space. Passage through fenestrated epithelial layers would leave contrast agent in the extracellular space. Embedment of the hydrophobic parts of XlinCA in the lipid bilayer is unlikely, since the inner medulla is not stained.
While the exact mechanism of XlinCA accumulation in the tubular walls remains to be elucidated, tubular lumina and interstitial space remain free of contrast agent. Tubular walls contain small concentrations and vascular lumina large concentrations of XlinCA, permitting concurrent imaging

of these features in a single µCT scan. Tubular structure can thus be obtained without requiring subsequent serial sectioning, which is highly labor-intensive and may suffer from various sample preparation artifacts, notably shrinkage during dehydration and damage to the sections during sample handling. These artifacts complicate realignment and virtual reassembly of the sections, requiring non-rigid registration algorithms if structural data need to be preserved [50].
The importance of visualizing tubules along with the vasculature should not be underestimated: The amount of tissue in direct contact with blood vessels is underestimated by about 50% if the tubular lumen is not taken into account when determining the distribution of diffusion distances (Fig. 4C). Tubules provide important context when investigating the effect of renal diseases on the vasculature. Here, kidneys of aged mice featured areas not perfused by the vasculature, which could have been interpreted erroneously as signs of capillary rarefaction. With tubular imaging, we were able to identify those regions as liquid-filled structures instead, which were confirmed by histology to be eosinophilic protein casts, a common finding in healthy, aged mice.

5.5.5.3 Comparison to 3D light microscopy

3D imaging with microscopy on the whole organ scale has been made possible in recent years via the introduction of tissue clearing, allowing for light sheet microscopy on intact, uncut tissue by reducing light scattering via, e.g., refractive index matching or lipid removal [51]. However, residual light scattering reduces the achievable resolution at depth and leads to optical distortion. In addition, the clearing process typically introduces swelling or shrinkage of the sample by 20% by length [52]. Tissue clearing with light sheet microscopy is, therefore, well suited for large, well-separated features at the renal surface, such as glomeruli [53, 54], but not for capturing the dense capillary network in the deeper regions of the kidney.
Compared to visible light, X-rays penetrate soft tissue with negligible absorption and refraction, which allows X-ray µCT to provide 3D data with isotropic quality and resolution regardless of depth within the sample. Organs can be imaged fully intact in their hydrated state, preventing any further sample distortion beyond the minor volume changes introduced by fixation [55, 56]. X-ray absorption is furthermore not dependent on chemically labile fluorescence reporters and does not incur any photobleaching. Samples can be imaged repeatedly at high photon fluxes with no contrast degradation, enabling hierarchical imaging.

5.5.5.4 Image quality was achieved with a previous-generation X-ray µCT scanner

The Nanotom m employed in this study uses a water-cooled tungsten target and a scintillator-coupled flat panel detector, which is representative of advanced µCT scanners introduced almost a decade ago. Accordingly, the image quality presented in this work is achievable by a wide base of currently installed hard X-ray µCT systems and thus accessible to many research labs. Higher resolution and better image quality may be required if segmentation with higher precision is needed for a specific study. As samples do not degrade upon repeated measurements, they can be imaged with more expensive laboratory or synchrotron radiation-based µCT instrumentation if such a need is identified. The results presented in this work therefore do not represent the upper limits of the protocol, but rather a baseline that should be achievable by most existing µCT devices.

5.5.5.5 Simple segmentation based on Fiji/ImageJ

The presented image segmentation workflow is simple, relies solely on freely available software and can be implemented without specialized knowledge in image processing or programming (see Supplemental Methods). To segment larger numbers of datasets in a consistent fashion, more advanced algorithms that do not rely on human manipulation of individual datasets should be applied. The choice of the most suitable algorithm depends on factors such as contrast-to-noise ratio and the type and quantity of artifacts (e.g., beam hardening or ring artifacts), which are dependent on the settings and specifications of the employed scanning equipment, requiring a case-by-case

evaluation. The segmentation workflow presented here relies instead on manual determination of the intensity threshold, which is robustly applicable to any µCT data with sufficiently high contrast-to-noise ratio.
The methods used to quantify the segmented binary vascular and tubular structural data are mathematically identical to and thus a suitable replacement for manual quantification via counting frames, the gold standard in histology. They are agnostic to the means by which these binary masks were created, are therefore applicable regardless of the choice of segmentation protocol and can be performed entirely independent of manual user interaction in a fully automatic manner with Fiji/ImageJ.

5.5.5.6 Limitations of the protocol

The tissue in the inner medulla did not contain detectable amounts of XlinCA despite its close proximity to the *vasa recta* through which it could have been supplied with the contrast agent. We speculate that the passive accumulation of XlinCA is specific to proximal and distal tubular cells, as other organs such as the brain did not display similar staining of tissue in our previous studies. µCT imaging of the inner medulla can be provided by other tissue staining protocols [57] that are in principle compatible with our protocol, but would require careful optimization of the different contrast levels between vascular lumen, tubular walls and background. Incomplete tubular wall staining with XlinCA may also occur in certain pathological phenotypes that display large kidney areas fully devoid of blood vessels, since the contrast agent is distributed via the vasculature.
The presence of tubular walls as a third feature of interest besides vascular and tubular lumina reduces the signal over background for the vascular lumen alone. While the X-ray absorption values for blood vessels are well separated from the background, as can be seen in the histogram shown in Suppl. Fig. S6., the related values of tissue have considerable overlap with both background and blood vessels. This results in a lower contrast-to-noise ratio, which requires either more advanced algorithms or better µCT systems to achieve vascular segmentation results comparable to methods providing vascular imaging only. Limited contrast-to-noise ratio combined with limited imaging resolution causes small features such as capillary bundles to appear as connected entities, even when they are separate in reality. Consequently, calculated path lengths as shown in Figs. 4B and D may include, in some cases, virtual connections between adjacent vessels where, in reality, no such connections exist. The calculations should thus be seen as lower thresholds of the real path lengths. This limitation may be removed by imaging with more advanced µCT scanners.
Hard X-ray µCT can only provide structural images and cannot capture changes in protein expression or mRNA levels. Correlative microscopy is, therefore, still required for functional imaging, but limited by the high concentration of glutaraldehyde, which results in antigen masking and high autofluorescence in the kidney. The X-ray contrast agent itself has no specific fluorescence in the visible light range (Suppl. Fig. S8). The exceedingly high concentration compared to fluorescent staining nevertheless produces strong signal despite the low attenuation coefficient. However, it is only higher than background autofluorescence in the TRITC channel (Ex: 563 nm, em: 607 nm, Suppl. Fig. S9).

5.5.6 Conclusions

Previous approaches based on vascular casting with hydrophobic plastic resins required a large amount of optimization to avoid filling artifacts and were unable to provide both vascular and tubular structure simultaneously. This work describes a kidney preparation, image acquisition and quantification protocol that provides full 3D imaging of these structures in whole mouse kidneys with a single procedure, and can be implemented with common imaging equipment and image processing software. The protocol greatly reduces the amount of labor and skill required for providing standard quantitative measures such as vessel density and surface areas, features fewer artifacts than vascular corrosion casting and is able to provide structural parameters inaccessible to 2D analysis such as 3D diffusion distances and path tracing.

5.5.7 Acknowledgements

ExiTron nano 12000 nanoparticles were provided by Viscover. Computing resources for image rendering were provided by the Center for Microscopy and Image Analysis, University of Zurich.

Funding
This study was financially supported by the Swiss National Science Foundation through NCCR Kidney.CH and grant 205321_153523 HR-Kidney, as well as by the University of Zurich.

Disclosures
A patent application for the cross-linkable contrast agent XlinCA has been filed by the University of Zurich.

Author Contributions
W.K. and V.K. conceived and designed the research. W.K. prepared the kidneys, acquired and analyzed the X-ray datasets and drafted the manuscript. N.A.L. synthesized the contrast agent. A.K. performed the histological evaluation and U.H. performed the electron microscopy evaluation, and both contributed the corresponding sections of the manuscript. G.S. designed the X-ray scanning parameters. B.S., R.H.W., B.M. and V.K. analyzed the data, edited and revised the manuscript. All authors approved the final version of the manuscript.

5.5.8 References

[1] T. L. Pallone, Z. Zhang, and K. Rhinehart, "Physiology of the renal medullary microcirculation," *Am J Physiol Renal Physiol,* vol. 284, pp. F253-66, Feb 2003, doi: 10.1152/ajprenal.00304.2002.

[2] X. Y. Zhai, J. S. Thomsen, H. Birn, I. B. Kristoffersen, A. Andreasen, and E. I. Christensen, "Three-dimensional reconstruction of the mouse nephron," *J Am Soc Nephrol,* vol. 17, pp. 77-88, Jan 2006, doi: 10.1681/ASN.2005080796.

[3] W. Kriz, "Structural organization of the renal medulla: comparative and functional aspects," *Am J Physiol,* vol. 241, pp. R3-16, Jul 1981, doi: 10.1152/ajpregu.1981.241.1.R3.

[4] R. Beeuwkes, 3rd and J. V. Bonventre, "Tubular organization and vascular-tubular relations in the dog kidney," *Am J Physiol,* vol. 229, pp. 695-713, Sep 1975, doi: 10.1152/ajplegacy.1975.229.3.695.

[5] L. Bankir, L. Figueres, C. Prot-Bertoye, N. Bouby, G. Crambert, J. H. Pratt*, et al.*, "Medullary and cortical thick ascending limb: similarities and differences," *Am J Physiol Renal Physiol,* vol. 318, pp. F422-F442, Feb 1 2020, doi: 10.1152/ajprenal.00261.2019.

[6] T. Tanaka and M. Nangaku, "Angiogenesis and hypoxia in the kidney," *Nat Rev Nephrol,* vol. 9, pp. 211-22, Apr 2013, doi: 10.1038/nrneph.2013.35.

[7] W. Wei, V. Popov, J. A. Walocha, J. Wen, and E. Bello-Reuss, "Evidence of angiogenesis and microvascular regression in autosomal-dominant polycystic kidney disease kidneys: a corrosion cast study," *Kidney Int,* vol. 70, pp. 1261-8, Oct 2006, doi: 10.1038/sj.ki.5001725.

[8] M. A. Venkatachalam, J. M. Weinberg, W. Kriz, and A. K. Bidani, "Failed Tubule Recovery, AKI-CKD Transition, and Kidney Disease Progression," *J Am Soc Nephrol,* vol. 26, pp. 1765-76, Aug 2015, doi: 10.1681/ASN.2015010006.

[9] H. U. Prommer, J. Maurer, K. von Websky, C. Freise, K. Sommer, H. Nasser*, et al.*, "Chronic kidney disease induces a systemic microangiopathy, tissue hypoxia and dysfunctional angiogenesis," *Sci Rep,* vol. 8, p. 5317, Mar 28 2018, doi: 10.1038/s41598-018-23663-1.

[10] C. Lantuejoul and S. Beucher, "On the Use of the Geodesic Metric in Image-Analysis," *J Microsc,* vol. 121, pp. 39-49, 1981, doi: 10.1111/j.1365-2818.1981.tb01197.x.

[11] B. S. Gardiner, D. W. Smith, P. M. O'Connor, and R. G. Evans, "A mathematical model of diffusional shunting of oxygen from arteries to veins in the kidney," *Am J Physiol Renal Physiol,* vol. 300, pp. F1339-52, Jun 2011, doi: 10.1152/ajprenal.00544.2010.
[12] U. Olgac and V. Kurtcuoglu, "Renal oxygenation: preglomerular vasculature is an unlikely contributor to renal oxygen shunting," *Am J Physiol Renal Physiol,* vol. 308, pp. F671-88, Apr 1 2015, doi: 10.1152/ajprenal.00551.2014.
[13] U. Olgac and V. Kurtcuoglu, "The Bohr Effect Is Not a Likely Promoter of Renal Preglomerular Oxygen Shunting," *Front Physiol,* vol. 7, p. 482, 2016, doi: 10.3389/fphys.2016.00482.
[14] W. Kuo and V. Kurtcuoglu, "Renal arteriovenous oxygen shunting," *Curr Opin Nephrol Hypertens,* vol. 26, pp. 290-295, Jul 2017, doi: 10.1097/MNH.0000000000000332.
[15] D. M. Hyde, N. K. Tyler, and C. G. Plopper, "Morphometry of the respiratory tract: avoiding the sampling, size, orientation, and reference traps," *Toxicol Pathol,* vol. 35, pp. 41-8, Jan 2007, doi: 10.1080/01926230601059977.
[16] J. Ehling, J. Babickova, F. Gremse, B. M. Klinkhammer, S. Baetke, R. Knuechel*, et al.*, "Quantitative Micro-Computed Tomography Imaging of Vascular Dysfunction in Progressive Kidney Diseases," *J Am Soc Nephrol,* vol. 27, pp. 520-32, Feb 2016, doi: 10.1681/ASN.2015020204.
[17] A. Garcia-Sanz, A. Rodriguez-Barbero, M. D. Bentley, E. L. Ritman, and J. C. Romero, "Three-dimensional microcomputed tomography of renal vasculature in rats," *Hypertension,* vol. 31, pp. 440-4, Jan 1998, doi: 10.1161/01.hyp.31.1.440.
[18] M. C. Ortiz, A. Garcia-Sanz, M. D. Bentley, L. A. Fortepiani, J. Garcia-Estan, E. L. Ritman*, et al.*, "Microcomputed tomography of kidneys following chronic bile duct ligation," *Kidney Int,* vol. 58, pp. 1632-40, Oct 2000, doi: 10.1111/j.1523-1755.2000.00324.x.
[19] J. P. Ngo, S. Kar, M. M. Kett, B. S. Gardiner, J. T. Pearson, D. W. Smith*, et al.*, "Vascular geometry and oxygen diffusion in the vicinity of artery-vein pairs in the kidney," *Am J Physiol Renal Physiol,* vol. 307, pp. F1111-22, Nov 15 2014, doi: 10.1152/ajprenal.00382.2014.
[20] D. A. Nordsletten, S. Blackett, M. D. Bentley, E. L. Ritman, and N. P. Smith, "Structural morphology of renal vasculature," *Am J Physiol Heart Circ Physiol,* vol. 291, pp. H296-309, Jul 2006, doi: 10.1152/ajpheart.00814.2005.
[21] F. E. Hossler and J. E. Douglas, "Vascular Corrosion Casting: Review of Advantages and Limitations in the Application of Some Simple Quantitative Methods," *Microscopy and Microanalysis,* vol. 7, pp. 253-264, 2001/05 2001, doi: 10.1007/S10005-001-0006-2.
[22] F. E. Hossler, A. Lametschwandtner, R. Kao, and F. Finsterbusch, "Microvascular architecture of mouse urinary bladder described with vascular corrosion casting, light microscopy, SEM, and TEM," *Microsc Microanal,* vol. 19, pp. 1428-35, Dec 2013, doi: 10.1017/S143192761301341X.
[23] R. C. Wagner, K. Czymmek, and F. E. Hossler, "Confocal microscopy, computer modeling, and quantification of glomerular vascular corrosion casts," *Microsc Microanal,* vol. 12, pp. 262-8, Jun 2006, doi: 10.1017/S143192760606034X.
[24] R. Wagner, D. Van Loo, F. Hossler, K. Czymmek, E. Pauwels, and L. Van Hoorebeke, "High-resolution imaging of kidney vascular corrosion casts with Nano-CT," *Microsc Microanal,* vol. 17, pp. 215-9, Apr 2011, doi: 10.1017/S1431927610094201.
[25] T. Krucker, A. Lang, and E. P. Meyer, "New polyurethane-based material for vascular corrosion casting with improved physical and imaging characteristics," *Microsc Res Tech,* vol. 69, pp. 138-47, Feb 2006, doi: 10.1002/jemt.20263.
[26] S. Grabherr, A. Hess, M. Karolczak, M. J. Thali, S. D. Friess, W. A. Kalender*, et al.*, "Angiofil-mediated visualization of the vascular system by microcomputed tomography: a feasibility study," *Microsc Res Tech,* vol. 71, pp. 551-6, Jul 2008, doi: 10.1002/jemt.20585.

[27] K. Haenssgen, A. N. Makanya, and V. Djonov, "Casting materials and their application in research and teaching," *Microsc Microanal,* vol. 20, pp. 493-513, Apr 2014, doi: 10.1017/S1431927613014050.
[28] D. S. Perrien, M. A. Saleh, K. Takahashi, M. S. Madhur, D. G. Harrison, R. C. Harris*, et al.*, "Novel methods for microCT-based analyses of vasculature in the renal cortex reveal a loss of perfusable arterioles and glomeruli in eNOS-/- mice," *BMC Nephrol,* vol. 17, p. 24, Mar 2 2016, doi: 10.1186/s12882-016-0235-5.
[29] S. X. Vasquez, F. Gao, F. Su, V. Grijalva, J. Pope, B. Martin*, et al.*, "Optimization of microCT imaging and blood vessel diameter quantitation of preclinical specimen vasculature with radiopaque polymer injection medium," *PLoS One,* vol. 6, p. e19099, Apr 18 2011, doi: 10.1371/journal.pone.0019099.
[30] S. Ghanavati, L. X. Yu, J. P. Lerch, and J. G. Sled, "A perfusion procedure for imaging of the mouse cerebral vasculature by X-ray micro-CT," *J Neurosci Methods,* vol. 221, pp. 70-7, Jan 15 2014, doi: 10.1016/j.jneumeth.2013.09.002.
[31] R. Hlushchuk, C. Zubler, S. Barre, C. Correa Shokiche, L. Schaad, R. Rothlisberger*, et al.*, "Cutting-edge microangio-CT: new dimensions in vascular imaging and kidney morphometry," *Am J Physiol Renal Physiol,* vol. 314, pp. F493-F499, Mar 1 2018, doi: 10.1152/ajprenal.00099.2017.
[32] L. Fan, S. Wang, X. He, E. Gonzalez-Fernandez, C. Lechene, F. Fan*, et al.*, "Visualization of the intrarenal distribution of capillary blood flow," *Physiol Rep,* vol. 7, p. e14065, Apr 2019, doi: 10.14814/phy2.14065.
[33] B. P. Chugh, J. P. Lerch, L. X. Yu, M. Pienkowski, R. V. Harrison, R. M. Henkelman*, et al.*, "Measurement of cerebral blood volume in mouse brain regions using micro-computed tomography," *Neuroimage,* vol. 47, pp. 1312-8, Oct 1 2009, doi: 10.1016/j.neuroimage.2009.03.083.
[34] N. A. Le, W. Kuo, B. Müller, V. Kurtcuoglu, and B. Spingler, "Crosslinkable polymeric contrast agent for high-resolution X-ray imaging of the vascular system," *Chemical Communications,* vol. 56, no. 44, pp. 5885–5888, 2020, doi: 10.1039/C9CC09883F.
[35] J. T. Lai, D. Filla, and R. Shea, "Functional Polymers from Novel Carboxyl-Terminated Trithiocarbonates as Highly Efficient RAFT Agents," *Macromolecules,* vol. 35, pp. 6754-6756, 2002, doi: 10.1021/ma020362m.
[36] J. Chiefari, Y. K. Chong, F. Ercole, J. Krstina, J. Jeffery, T. P. T. Le*, et al.*, "Living Free-Radical Polymerization by Reversible Addition−Fragmentation Chain Transfer: The RAFT Process," *Macromolecules,* vol. 31, pp. 5559-5562, 1998, doi: 10.1021/ma9804951.
[37] J. Czogalla, F. Schweda, and J. Loffing, "The Mouse Isolated Perfused Kidney Technique," *J Vis Exp,* p. 54712, Nov 17 2016, doi: 10.3791/54712.
[38] J. Schindelin, I. Arganda-Carreras, E. Frise, V. Kaynig, M. Longair, T. Pietzsch*, et al.*, "Fiji: an open-source platform for biological-image analysis," *Nat Methods,* vol. 9, pp. 676-82, Jun 28 2012, doi: 10.1038/nmeth.2019.
[39] C. A. Schneider, W. S. Rasband, and K. W. Eliceiri, "NIH Image to ImageJ: 25 years of image analysis," *Nat Methods,* vol. 9, pp. 671-5, Jul 2012, doi: 10.1038/nmeth.2089.
[40] D. Legland, I. Arganda-Carreras, and P. Andrey, "MorphoLibJ: integrated library and plugins for mathematical morphology with ImageJ," *Bioinformatics,* vol. 32, pp. 3532-3534, Nov 15 2016, doi: 10.1093/bioinformatics/btw413.
[41] J. Ollion, J. Cochennec, F. Loll, C. Escude, and T. Boudier, "TANGO: a generic tool for high-throughput 3D image analysis for studying nuclear organization," *Bioinformatics,* vol. 29, pp. 1840-1, Jul 15 2013, doi: 10.1093/bioinformatics/btt276.
[42] D. Adlam, J. P. De Bono, E. J. Danson, M. H. Zhang, B. Casadei, D. J. Paterson*, et al.*, "Telemetric analysis of haemodynamic regulation during voluntary exercise training in mouse models," *Exp Physiol,* vol. 96, pp. 1118-1128, Nov 2011, doi: 10.1113/expphysiol.2011.059261.

[43] K. Burgess, S. Jovanovic, R. Sudhir, and A. Jovanovic, "Area under the curve analysis of blood pressure reveals increased spontaneous locomotor activity in SPAK knock-in mice: relevance for hypotension induced by SPAK inhibition?," *Physiol Rep,* vol. 7, p. e13997, Feb 2019, doi: 10.14814/phy2.13997.
[44] J. Epah, K. Palfi, F. L. Dienst, P. F. Malacarne, R. Bremer, M. Salamon*, et al.*, "3D Imaging and Quantitative Analysis of Vascular Networks: A Comparison of Ultramicroscopy and Micro-Computed Tomography," *Theranostics,* vol. 8, pp. 2117-2133, 2018, doi: 10.7150/thno.22610.
[45] A. M. Hall, G. J. Rhodes, R. M. Sandoval, P. R. Corridon, and B. A. Molitoris, "In vivo multiphoton imaging of mitochondrial structure and function during acute kidney injury," *Kidney Int,* vol. 83, pp. 72-83, Jan 2013, doi: 10.1038/ki.2012.328.
[46] G. Borgefors, "On digital distance transforms in three dimensions," *Comput Vis Image Underst,* vol. 64, pp. 368-376, Nov 1996, doi: DOI 10.1006/cviu.1996.0065.
[47] H. Lusic and M. W. Grinstaff, "X-ray-computed tomography contrast agents," *Chem Rev,* vol. 113, pp. 1641-66, Mar 13 2013, doi: 10.1021/cr200358s.
[48] S. Grabherr, V. Djonov, K. Yen, M. J. Thali, and R. Dirnhofer, "Postmortem angiography: review of former and current methods," *AJR Am J Roentgenol,* vol. 188, pp. 832-8, Mar 2007, doi: 10.2214/AJR.06.0787.
[49] E. Jin and Z. R. Lu, "Biodegradable iodinated polydisulfides as contrast agents for CT angiography," *Biomaterials,* vol. 35, pp. 5822-9, Jul 2014, doi: 10.1016/j.biomaterials.2014.03.054.
[50] N. Roberts, D. Magee, Y. Song, K. Brabazon, M. Shires, D. Crellin*, et al.*, "Toward routine use of 3D histopathology as a research tool," *Am J Pathol,* vol. 180, pp. 1835-42, May 2012, doi: 10.1016/j.ajpath.2012.01.033.
[51] D. S. Richardson and J. W. Lichtman, "Clarifying Tissue Clearing," *Cell,* vol. 162, pp. 246-257, Jul 16 2015, doi: 10.1016/j.cell.2015.06.067.
[52] H. Kolesova, M. Capek, B. Radochova, J. Janacek, and D. Sedmera, "Comparison of different tissue clearing methods and 3D imaging techniques for visualization of GFP-expressing mouse embryos and embryonic hearts," *Histochem Cell Biol,* vol. 146, pp. 141-52, Aug 2016, doi: 10.1007/s00418-016-1441-8.
[53] B. Yang, J. B. Treweek, R. P. Kulkarni, B. E. Deverman, C. K. Chen, E. Lubeck*, et al.*, "Single-cell phenotyping within transparent intact tissue through whole-body clearing," *Cell,* vol. 158, pp. 945-958, Aug 14 2014, doi: 10.1016/j.cell.2014.07.017.
[54] A. Klingberg, A. Hasenberg, I. Ludwig-Portugall, A. Medyukhina, L. Mann, A. Brenzel*, et al.*, "Fully Automated Evaluation of Total Glomerular Number and Capillary Tuft Size in Nephritic Kidneys Using Lightsheet Microscopy," *J Am Soc Nephrol,* vol. 28, pp. 452-459, Feb 2017, doi: 10.1681/ASN.2016020232.
[55] R. E. Stowell, "Effect on Tissue Volume of Various Methods of Fixation, Dehydration, and Embedding," *Stain Technology,* vol. 16, pp. 67-83, 2009, doi: 10.3109/10520294109106200.
[56] T. Tran, C. P. Sundaram, C. D. Bahler, J. N. Eble, D. J. Grignon, M. F. Monn*, et al.*, "Correcting the Shrinkage Effects of Formalin Fixation and Tissue Processing for Renal Tumors: toward Standardization of Pathological Reporting of Tumor Size," *J Cancer,* vol. 6, pp. 759-66, 2015, doi: 10.7150/jca.12094.
[57] M. Busse, M. Muller, M. A. Kimm, S. Ferstl, S. Allner, K. Achterhold*, et al.*, "Three-dimensional virtual histology enabled through cytoplasm-specific X-ray stain for microscopic and nanoscopic computed tomography," *Proc Natl Acad Sci U S A,* vol. 115, pp. 2293-2298, Mar 6 2018, doi: 10.1073/pnas.1720862115.

5.5.9 Supplementary Information

5.5.9.1 Supplemental Fig. S1: Polymeric X-ray contrast agent formula

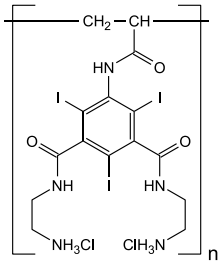

Fig. S1.: Chemical formula of the polymeric X-ray contrast agent prior to pre-crosslinking with glutaraldehyde.

5.5.9.2 Supplemental Fig. S2: Fluid-filled structures in kidneys of aged mice

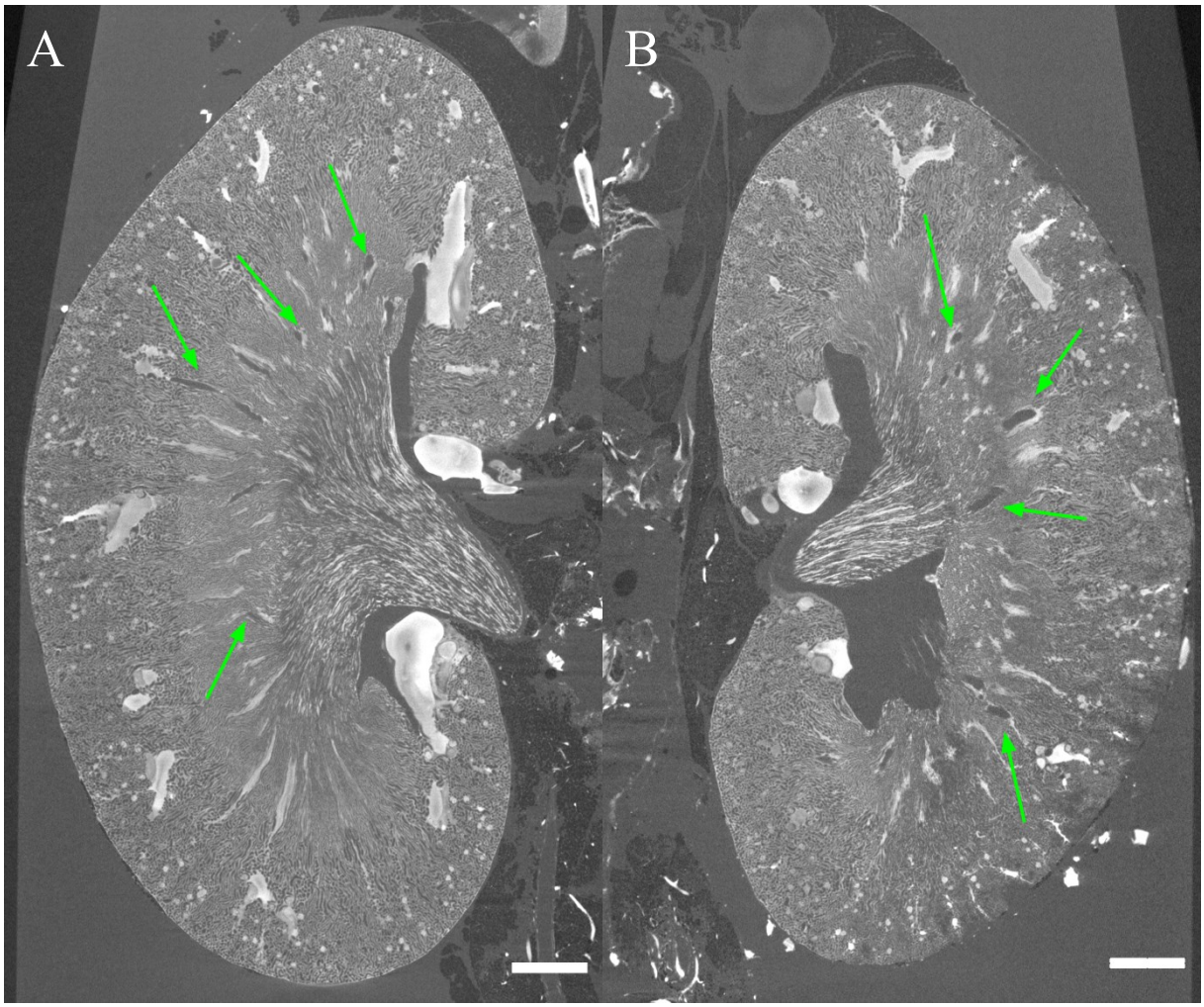

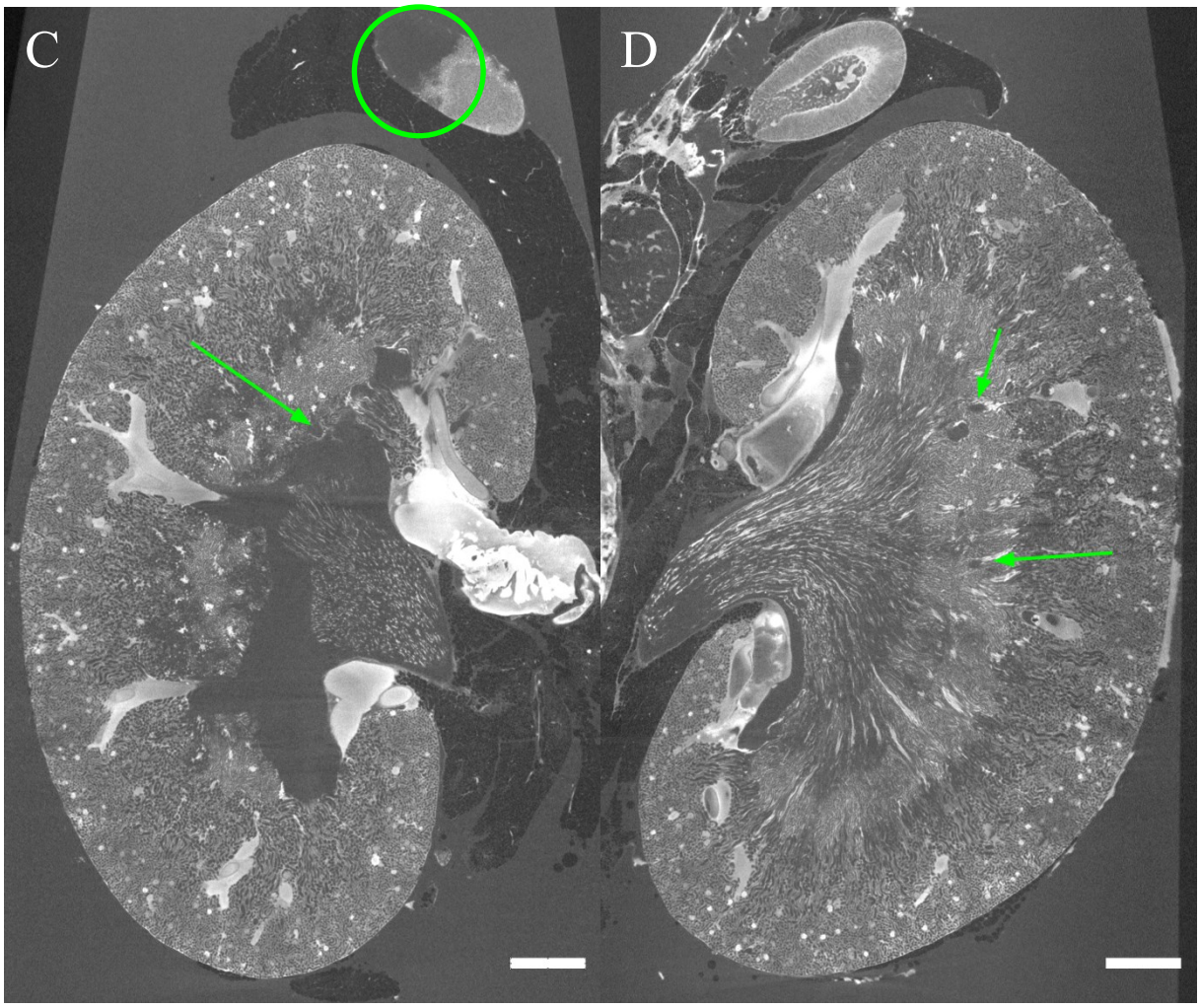

Fig. S2.: A: Left kidney of a 10 month old female C57BL/6J mouse. A number of fluid-filled structures are indicated by green arrows. These structures cannot be captured by previous vascular casting protocols, and were identified as tubular protein casts based on the subsequent histological examination (Fig 2.). Voxel size 4.4 µm. Scale bar: 1 mm. B: Right kidney of the same mouse. C: Left kidney of a different 10 month old female C57BL/6J mouse. Fluid-filled structures are indicated by green arrows. Part of the left adrenal gland is unperfused, while the rest is completely perfused (green circle). This region is likely supplied by vessels other than the renal artery and were not perfused due to the ligations applied to the abdominal aorta and superior mesenteric artery. Voxel size 4.4 µm. Scale bar: 1 mm. D: Right kidney of the same mouse. The right adrenal gland is fully perfused.

5.5.9.3 Supplemental Fig. S3: Transmission electron microscopy

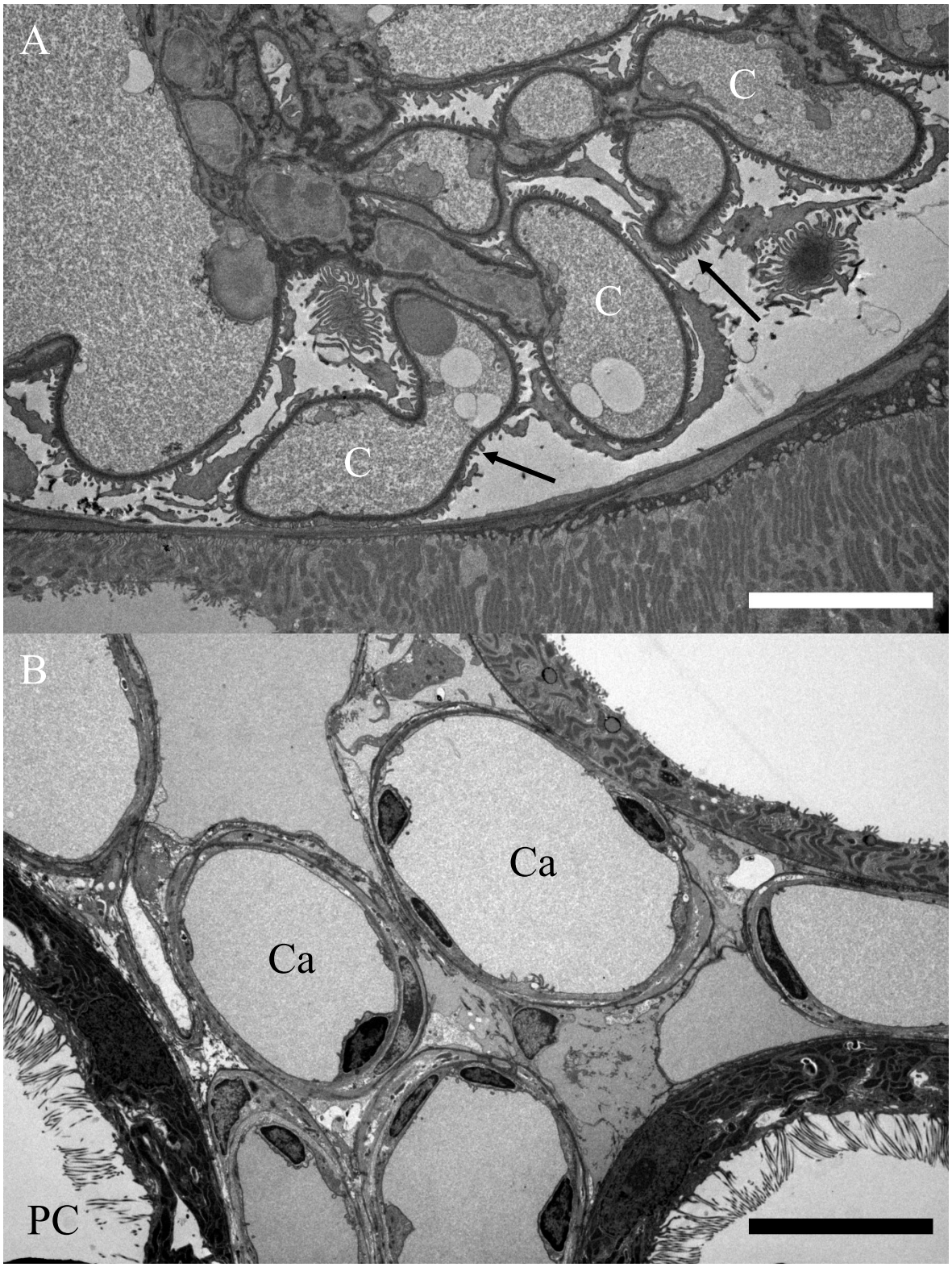

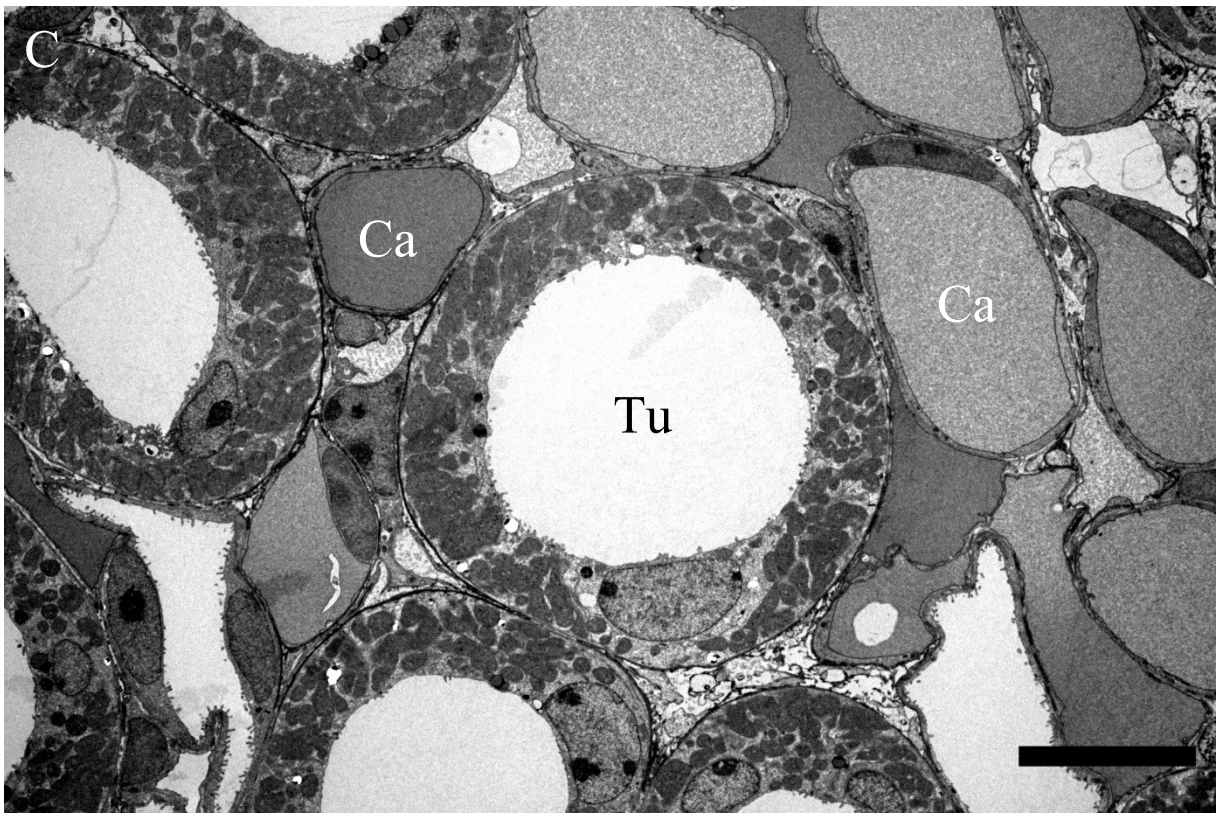

Fig. S3.: Transmission electron microscopy (TEM) images confirm that instillation of the contrast agent does not induce any tissue damage. A: Cortex. Non-contrasted TEM image of part of a glomerulus. Contrast agent is visible as coarsely granular material within the lumen of mesangial capillary loops (CL), and not found in the Bowman's space. Capillary loops are delineated by basement membrane with podocyte foot processes (arrows). Scale bar: 10 µm. B: Cortex. Contrasted TEM image of interstitial cortical capillaries (Cap) containing finely granular contrast agent. PCT - proximal convoluted tubule with intact ciliated epithelial cells. C: Medulla. Contrasted TEM image of interstitial cortical capillaries (Cap) containing moderately granular contrast agent of variable electron density. Tub - tubule with intact non-ciliated mitochondria rich epithelial cell. Scale bar: 10 µm.

5.5.9.4 Supplemental Fig. S4: Histology of inadequately perfused kidney region

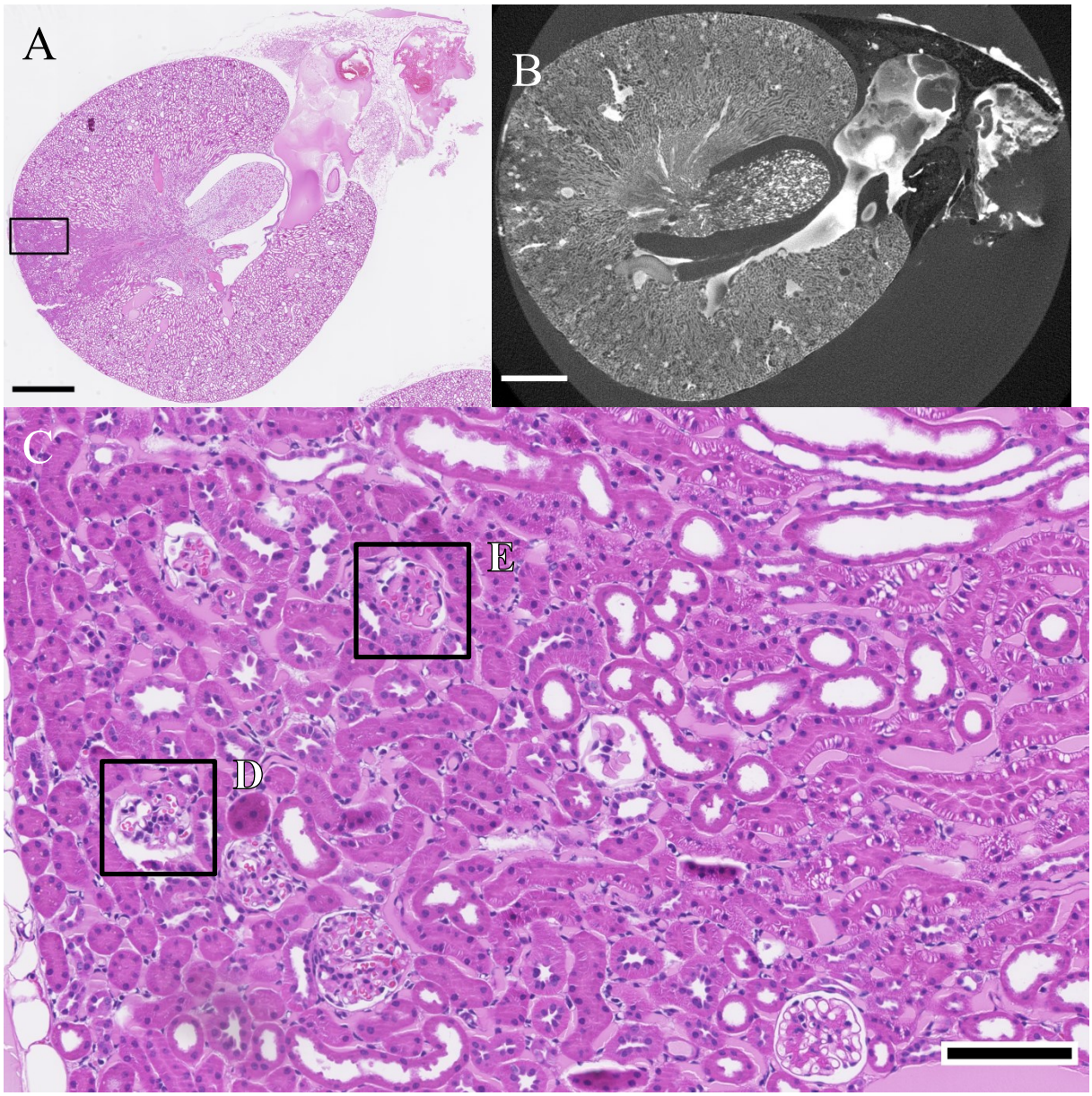

Fig. S4.: A: Overview image of an HE-stained histological section showing an inadequately perfused region. HE-stained slides and unstained slides for evaluation of fluorescence were scanned using a digital slide scanner (NanoZoomer-XR C12000; Hamamatsu, Hamamatsu City, Japan) with 40× magnification. Pixel size: Downsampled 8× to 1.8 µm. Scale bar: 1 mm. B: Similar virtual section from the X-ray µCT dataset. Pixel size: 4.4 µm. Scale bar: 1 mm C: Higher magnification of the improperly perfused region highlighted in A. Glomeruli show abundant red blood cells (D), indicating an insufficient initial flushing of the glomeruli as the cause of the collapsed tubuli. Contrast agent is visible in some of the glomeruli along with the red blood cells in both the histology and the X-ray µCT dataset (E), indicating filling of the vessels despite blockage via remaining red blood cells. Pixel size: 227 nm. Scale bar: 100 µm.

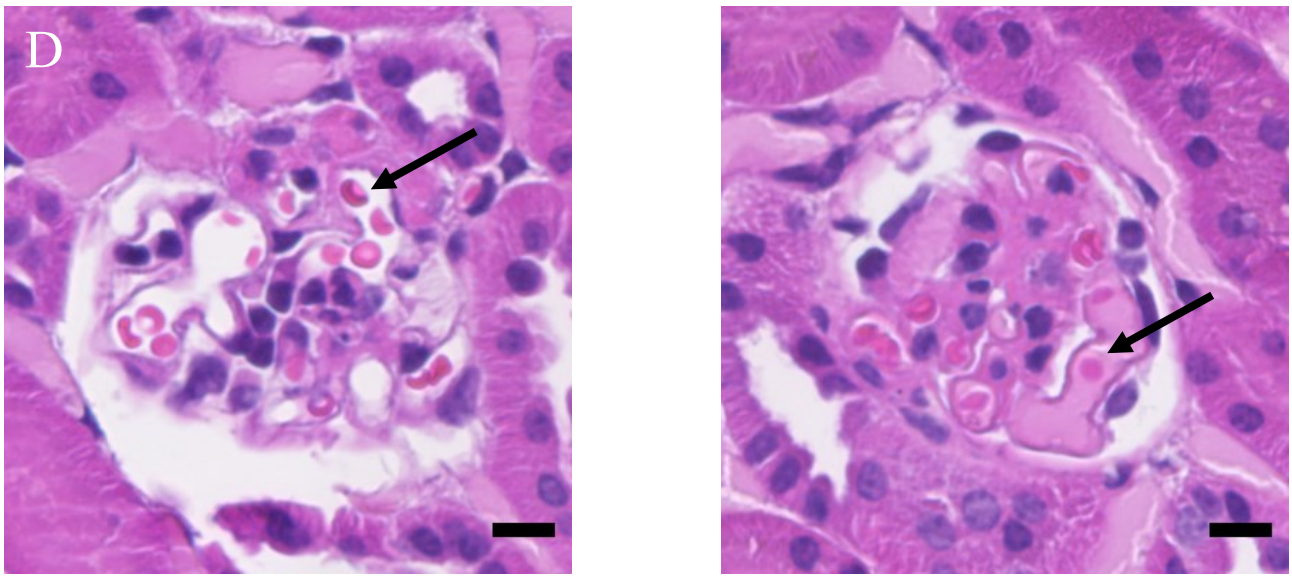

Fig. S4.: D: Higher magnification of a glomerulus showing abundant red blood cells highlighted in C. Scale bar: 10 µm. E: Higher magnification of a glomerulus filled with X-ray contrast agent and red blood cells highlighted in C.

5.5.9.5 Supplemental Fig. S5: Histology of low contrast region in renal vein

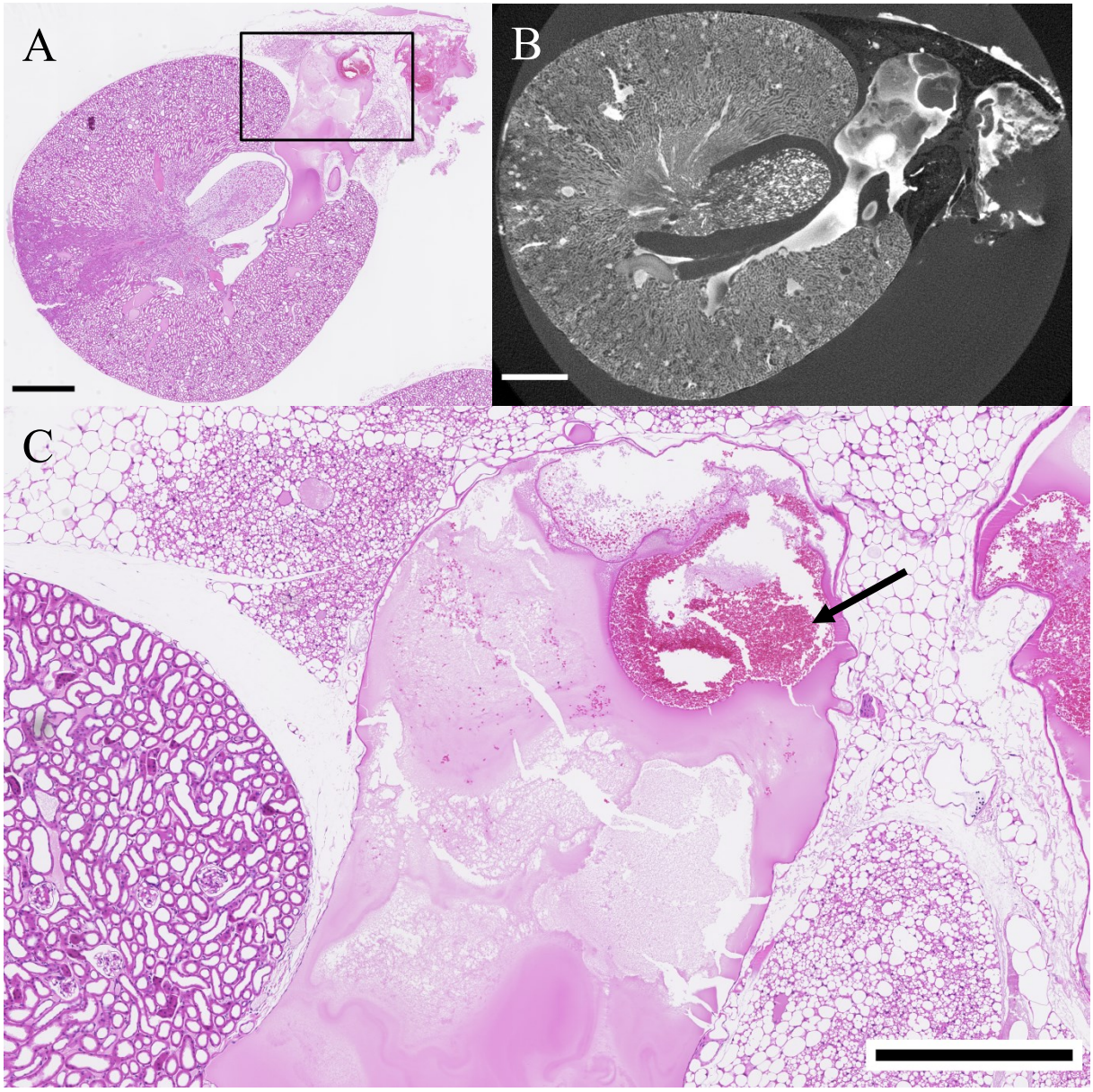

Fig. S5.: A: Overview image of an HE-stained histological section showing an improperly perfused region. Pixel size: Downsampled 8× to 1.8 µm. Scale bar: 1 mm. B: Similar virtual section from the X-ray µCT dataset. Pixel size: 4.4 µm. Scale bar: 1 mm C: Region of interest showing the renal vein. The low contrast regions seen in the X-ray µCT dataset are represented by a foam-like mixture of contrast agent with water or blood (aggregates of red blood cells (arrow) and/or fibrin), which may be caused by backflow of blood from the non-perfused parts of the remaining mouse body and resulting dilution of the contrast agent. Pixel size: Downsampled 2× to 454 nm. Scale bar: 500 µm.

5.5.9.6 Supplemental Fig. S6: Histogram and segmentation

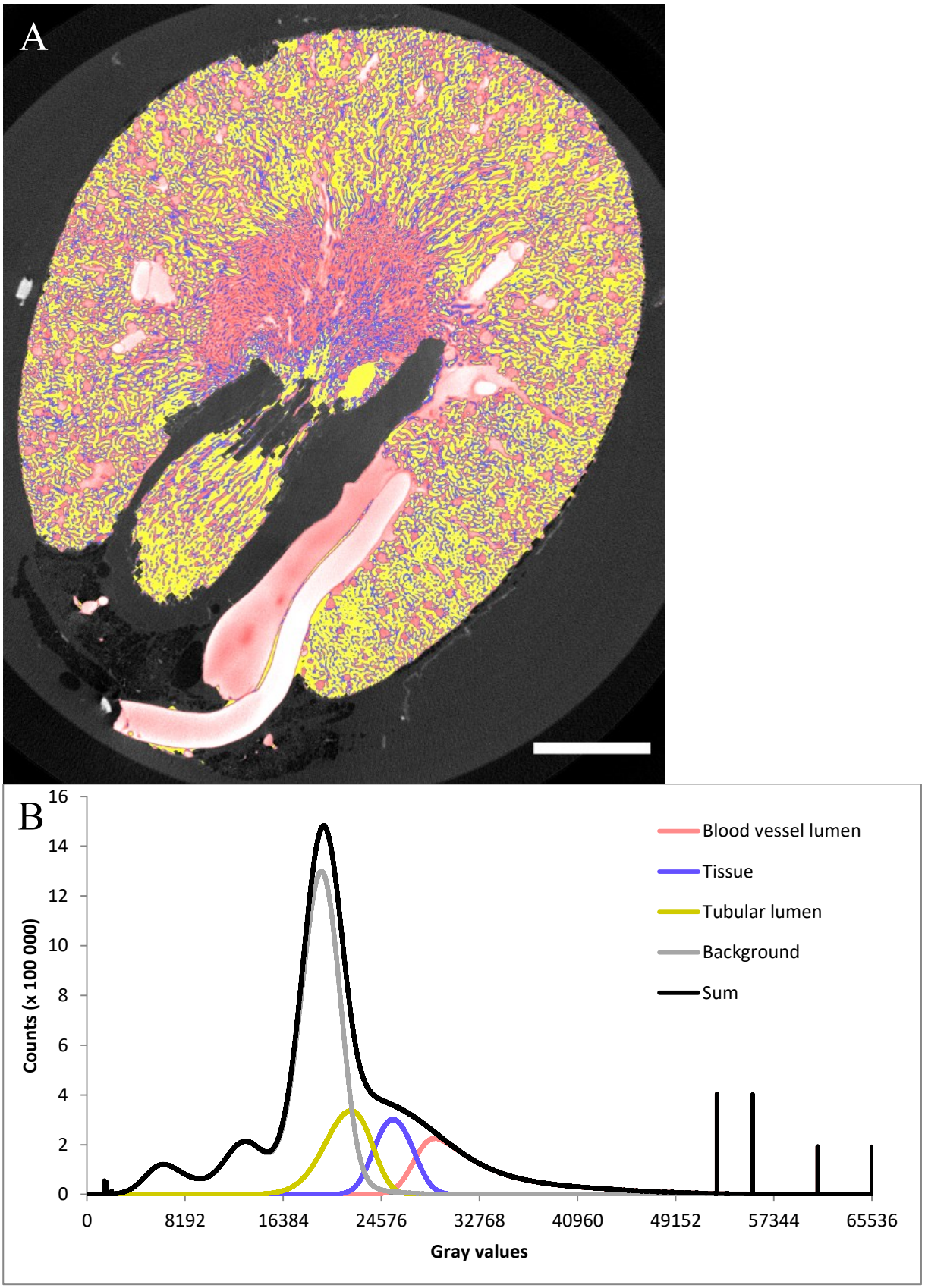

Fig. S6.: A: Overlay of segmentations of blood vessels (red), tissue (blue) and tubules over original raw data. Scale bar: 1 mm. B: Histogram of the whole dataset.

5.5.9.7 Supplemental Fig. S7: Line intensity profile

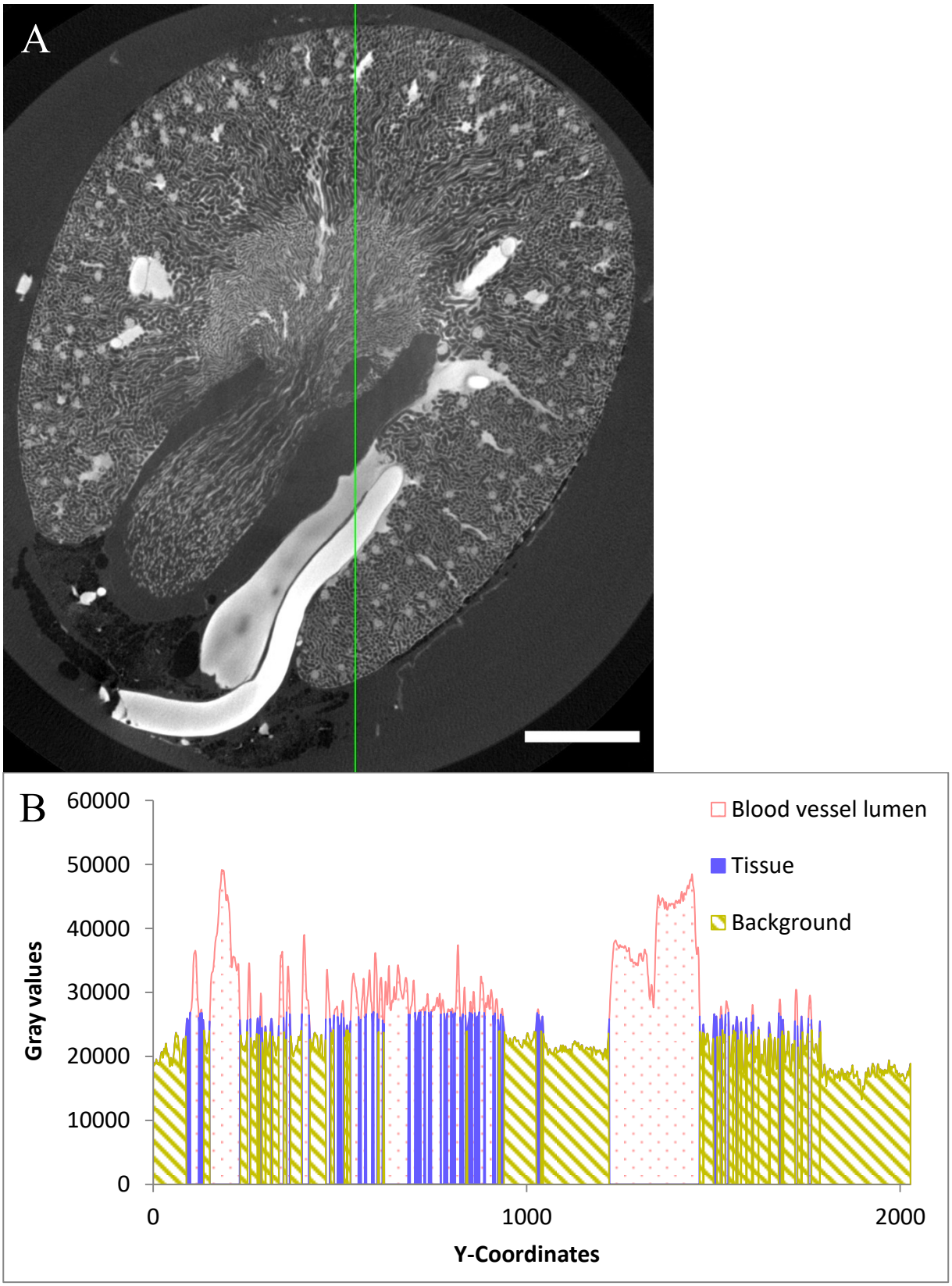

Fig. S7.: A: Single virtual section of the Gauss-filtered 3.3 µm voxel size dataset. The green line indicates line probe location. Scale bar: 1 mm. B: Profile along the line probe colored according to the thresholds used for segmentation.

5.5.9.8 Supplemental Fig. S8: UV-Vis spectrum of the contrast agent

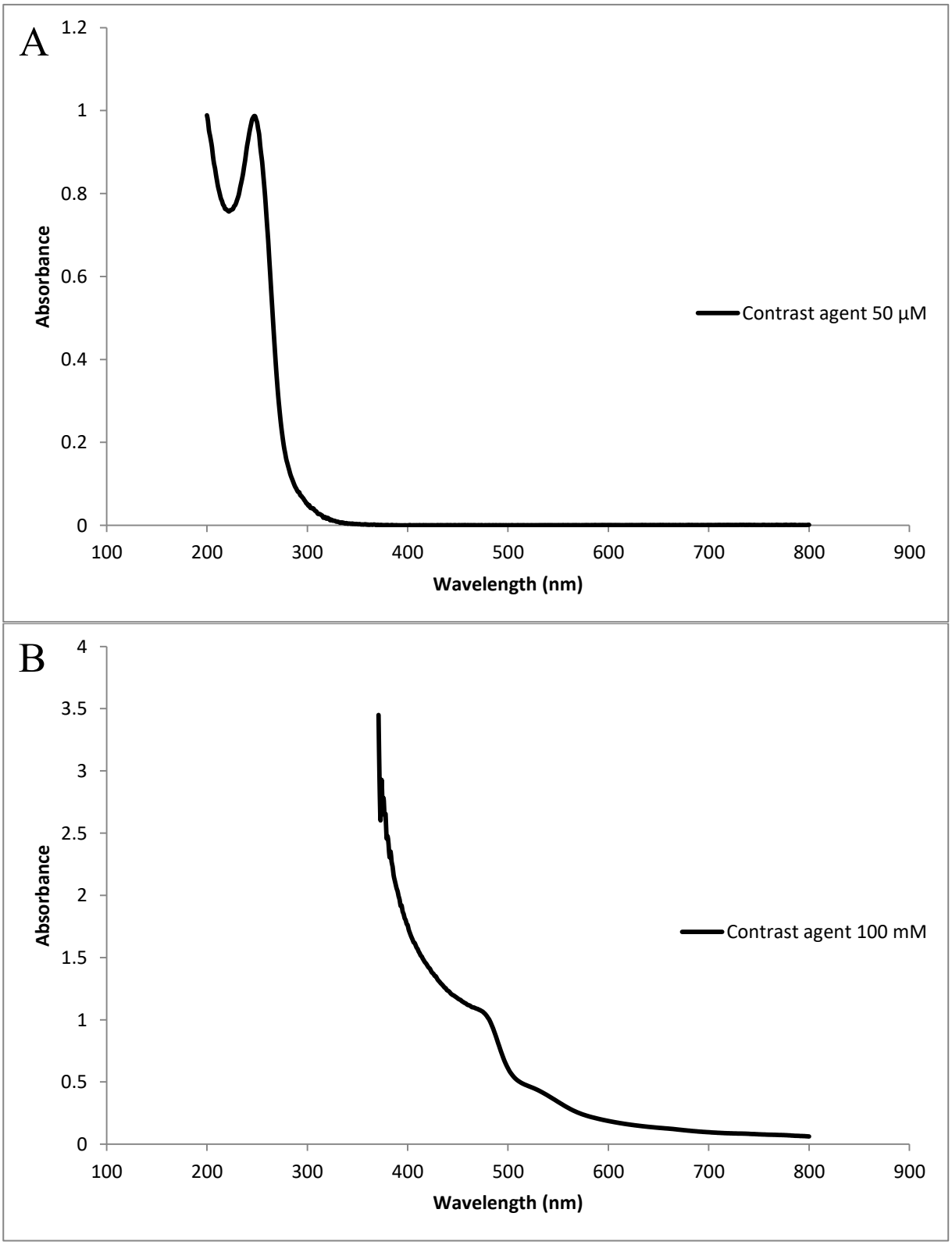

Fig. S8.: Absorption spectrum of the contrast agent. A: At a concentration of 50 µM, the contrast agent shows no absorption in the wavelengths used in fluorescence microscopy. B: At a concentration of 100 mM, there is absorption at those wavelengths due to the high concentration.

5.5.9.9 Supplemental Fig. S9: Fluorescent microscopy

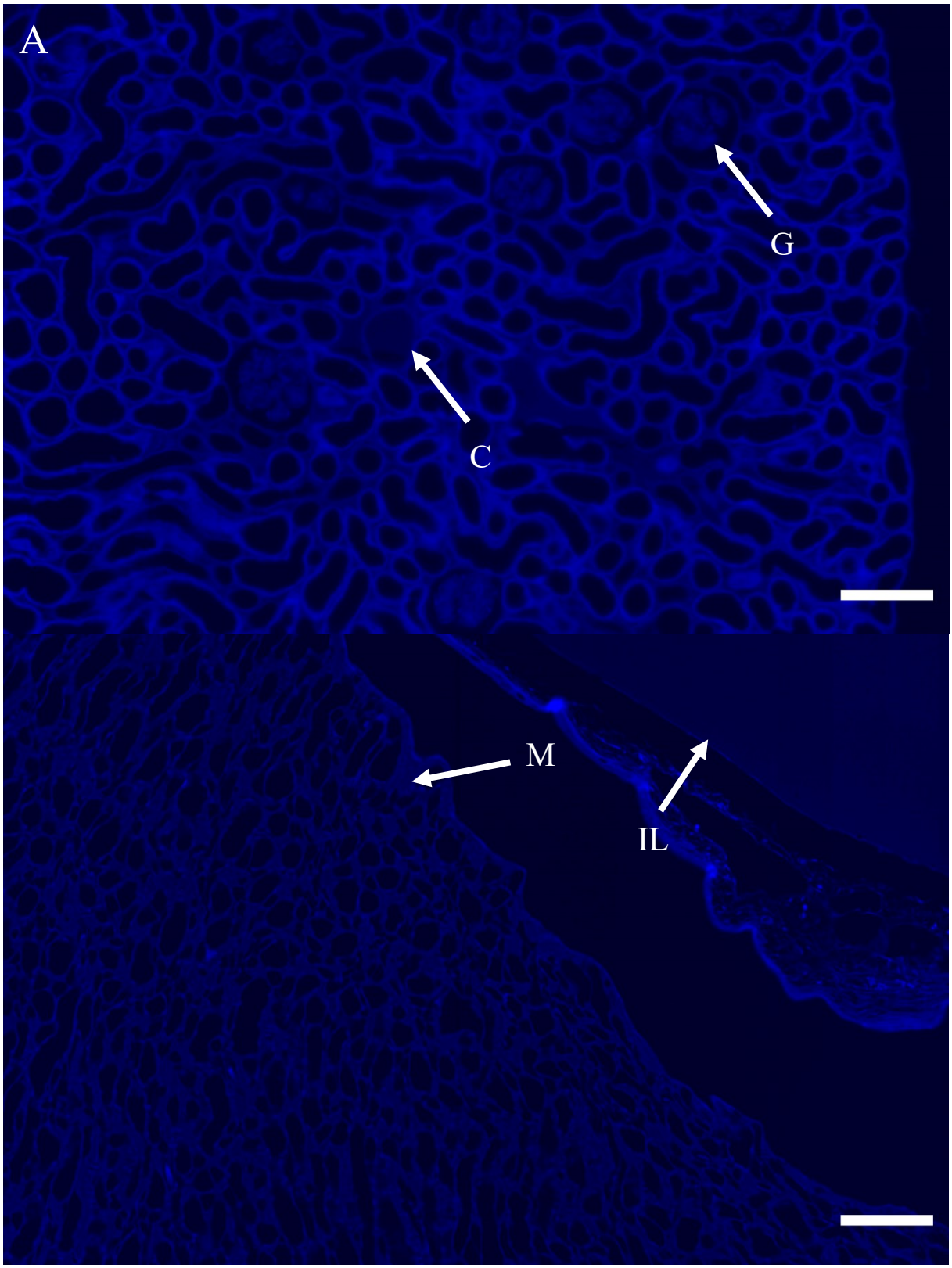

Fig. S9.: Fluorescent microscopy of the cortex and inner medulla in unstained kidney sections. Scale bars: 100 µm. A: DAPI channel, ex: 387 nm, em: 440 nm. X-ray contrast agent in glomerular tufts (G), cortical vessels (C) medullary capillaries (M) and an interlobar vessel (IL) shows less intense fluorescence compared to strong autofluorescence of the kidney.

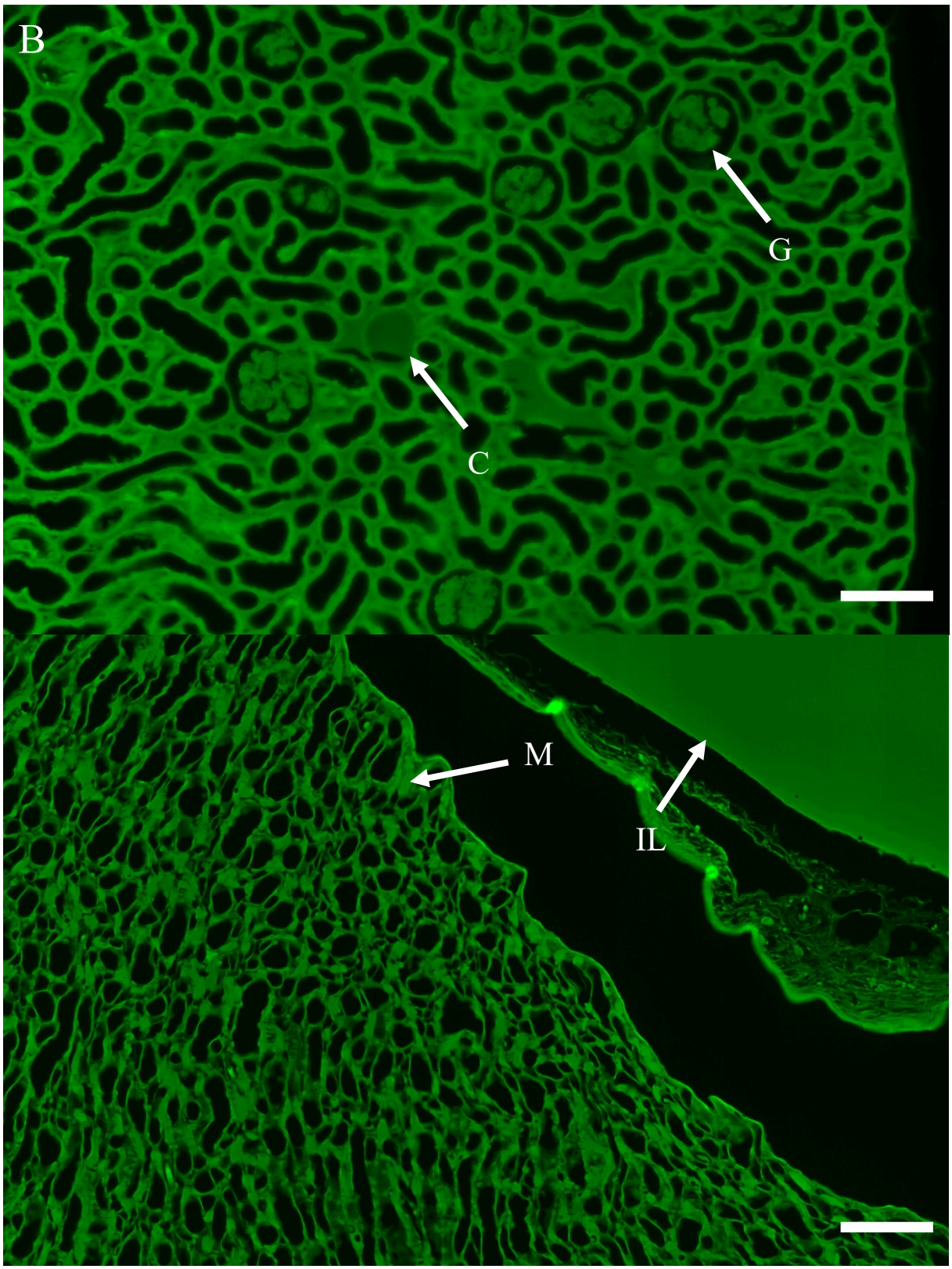

Fig. S9.: B: FITC channel, ex: 482 nm, em: 525 nm. X-ray contrast agent in glomerular tufts (G) and cortical capillaries (C) shows less intense fluorescence compared to strong autofluorescence of the kidney, while contrast agent capillaries in the inner medulla (M) shows comparable levels of fluorescence.

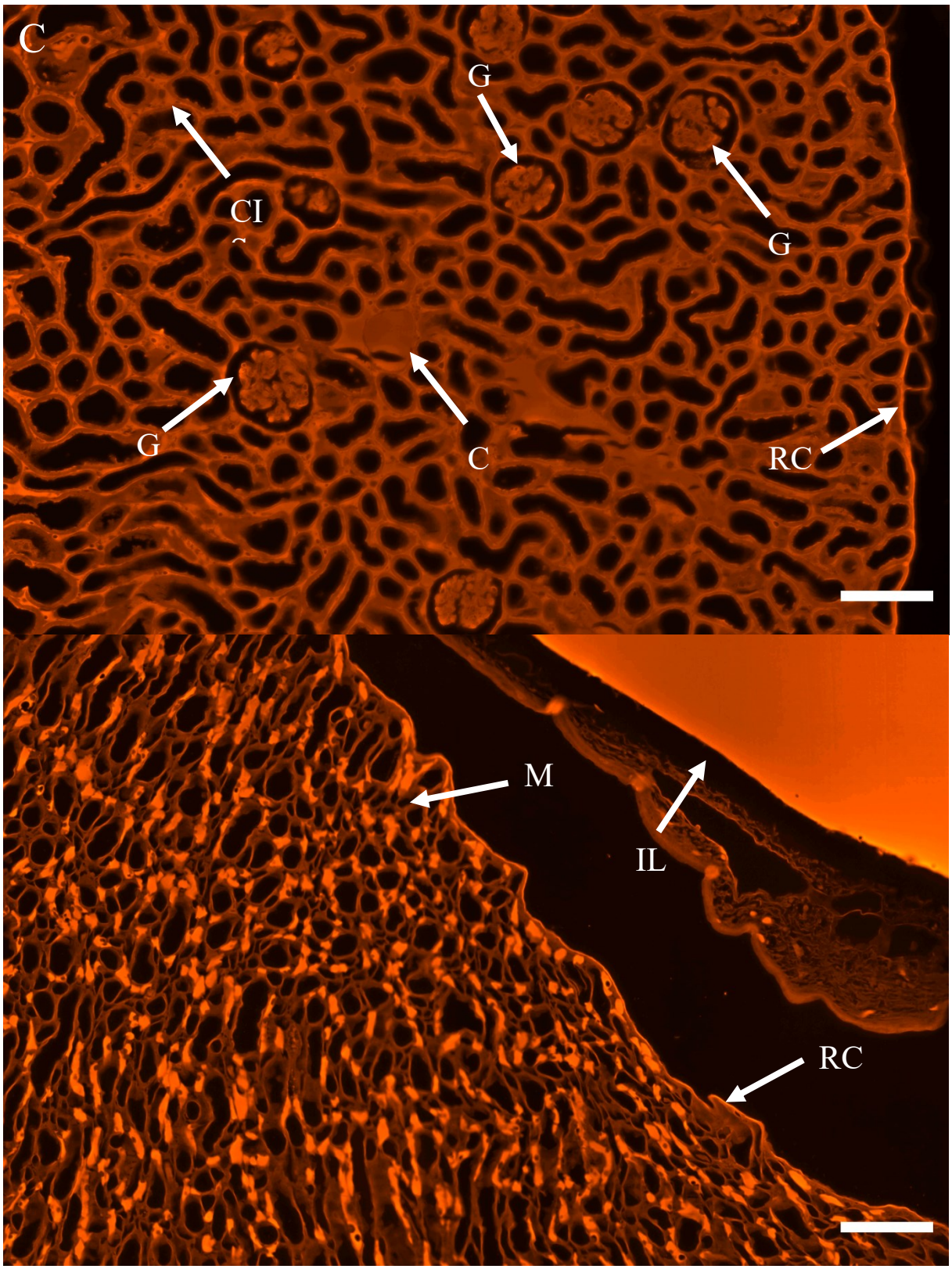

Fig. S9.: C: TRITC channel, ex: 563 nm, em: 607 nm. X-ray contrast agent shows much higher fluorescence than kidney autofluorescence in the interlobar vessel (IL) and capillaries of the inner medulla (M), and slightly elevated fluorescence in cortical vessels and glomerular tufts (G). Fluorescent signal can be seen in the cortical interstitium (CIS) and the renal capsule (RC), but these structures are not visible in X-ray μCT or electron microscopy, and are likely due to autofluorescence.

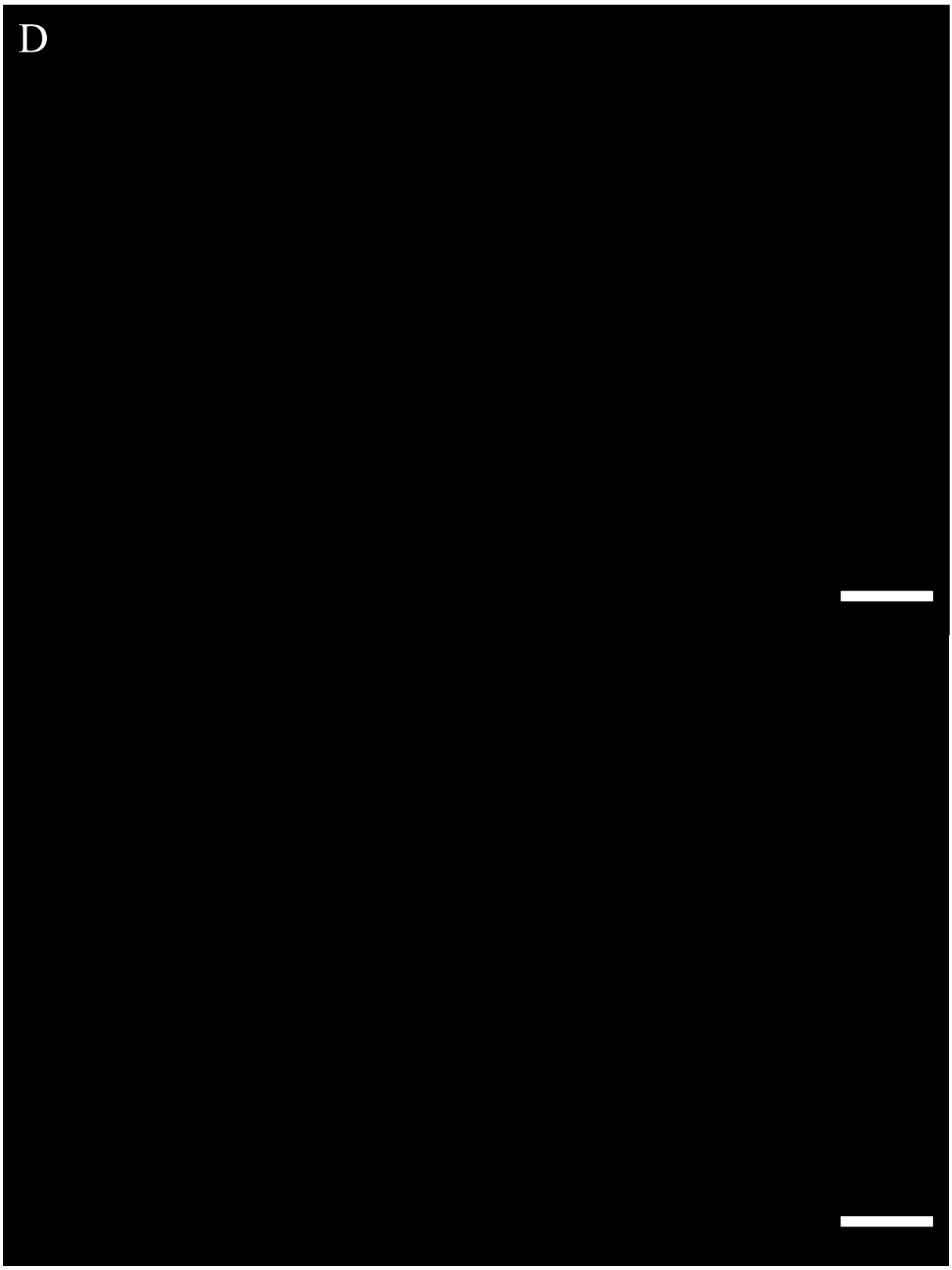

Fig. S9.: D: Cy5 channel, ex: 640 nm, em: 676 nm. No fluorescence of the contrast agent or autofluorescence of the kidney can be seen.

5.5.9.10 Detailed methods

5.5.9.10.1 Abdominal aorta perfusion

Kidneys were perfused retrogradely via the abdominal aorta based on a modified version of the isolated perfused kidney protocol by Czogalla et al. [1].
A 50 ml syringe serving as reservoir was connected to a 2.5 m long silicone tube, and kept 2 m above the mouse for a hydrostatic pressure of 150 mmHg. A 3-way stopcock to control flow and a blunted butterfly needle were connected to the tubing with a Luer-lock connector. The whole tubing was then flushed thoroughly with water until all air bubbles had been removed. Perfusion solutions could later be added to the open reservoir on the top as needed, even under flow.
Mice were anaesthetized with ketamine/xylazine, using an initial dose of 100 mg/kg ketamine and 20 mg/kg xylazine. Additional doses of 25 mg/kg ketamine and 5 mg/kg xylazine were given in 15 min intervals if necessary. For each perfusion, three constrictor knot ligations had to be prepared: Two around the abdominal aorta, one above the renal artery and one below the renal artery, and one at the superior mesenteric artery. The constrictor knot was chosen, since the surgical knot does not hold sufficiently tight at pressures used in perfusion [2]. Blood vessels were freed from surrounding fat, and silk sutures soaked in mineral oil were pulled under the vessel to be ligated using angled forceps. Abdominal aorta and vena cava had to be separated carefully from each other by pulling apart the fascia tubing holding them together without injuring either vessel.
The abdominal aorta was clamped above the lower abdominal aorta ligation. A small hole was cut into the abdominal aorta below the ligation, through which closed vessel dilating forceps could be inserted. The forceps were spread to insert a blunted 21 G butterfly needle between the tips deep enough to lie under the prepared ligation. The butterfly needle was first loosely fixed by pinning a pin behind one of the butterfly wings, then fixed properly to the abdominal aorta by tightening the prepared constrictor knot. The arterial clamp was removed, and the kidneys flushed with about 10 ml phosphate-buffered saline (PBS) and 100 ml 4% formaldehyde / 1% glutaraldehyde in PBS to fix the kidney under pressure and retain open tubular lumina. To prevent clogging of the capillaries, the aldehyde solution was pressed through a 1.2 µm syringe filter prior to perfusion. To quench leftover aldehydes prior to contrast agent perfusion, 20 ml PBS, 50 ml glycine solution (5 mg/ml in PBS) and another 40 ml PBS were perfused. All the above solutions were perfused at 37°C with 150 mmHg constant hydrostatic pressure.
Four ml of X-ray contrast agent solution (75 mg iodine/ml) were perfused using a 10 ml syringe, actuated with a 460 g weight to provide a constant pressure of around 150 mmHg. 4 ml are insufficient volume to build up the necessary hydrostatic pressure via the same silicon tubing as above.
Once contrast agent had been fully perfused, 4% glutaraldehyde in PBS was dripped into the abdominal cavity to start polymerization. Kidneys were cut out and kept in 4% glutaraldehyde in PBS. Care needs to be taken that renal artery and vein are cut cleanly in order to avoid accidentally pulling out the polymerized contrast agent hydrogel from the kidney vasculature.
For scanning, kidneys were mounted in 1% agar in PBS in 1.5 ml centrifugation tubes or 0.5 ml PCR tubes, depending on their diameter. Kidneys of mice with body weight below 25 g can typically fit into 0.5 ml PCR tubes.

5.5.9.10.2 Laboratory source X-ray microCT image acquisition

Laboratory source X-ray microCT images were acquired with a General Electric Phoenix Nanotom m system equipped with a water-cooled tungsten target and diamond window. Acceleration voltage was set to 60 kV, current 310 µA, no filter, Mode 0 for 2.2 – 2.7 µm focal spot size. The Nanotom m is equipped with a GE DXR Detector with 3072 × 2400 pixels, which was set to sensitivity setting 4, 0.5 s exposure time, 1440 projections per height step. The option to reduce ring artifacts through random detector position shift was turned on. Source detector distance was set to the minimum 225 mm, and sample was moved towards to a position close to the source to achieve 4.4

µm pixel size for standard 1.5 ml Eppendorf tubes and 3.3 µm pixel size for 0.5 ml PCR tubes. Directly before each scan, a 4-point calibration with 100, 170, 240, 310 µA was performed, with 50 flat-field frames recorded for each point and 50 dark-field frames recorded with the X-rays turned off.
For the 4.4 µm voxel size, 1.5 ml tube scans, 3 frames per projection were recorded and averaged per projection, resulting in a scan time of around 3.5 h per kidney.
For the 3.3 µm voxel size, 0.5 ml tube scan, 12 frames per projection were recorded and averaged per projection, resulting in a scan time of around 10 h per kidney.
Reconstruction was performed with the manufacturer's GE phoenix datos|x software. Projections were median filtered using a 3×3 kernel prior to reconstruction. Center of rotation calibration correction was optimized manually by reconstructing a single slice multiple times with different calibration values and selecting the best value via visual inspection. Images were cropped and exported as unsigned 16 bit values in a raw binary .vol file. Dimensions and other metadata were stored in the accompanying .pcr file.

5.5.9.10.3 Image processing – vascular and tubular segmentation of the 3.3 µm voxel size dataset

Segmentation of the 3.3 µm voxel size X-ray data was performed using Fiji/ImageJ [3, 4] with the MorphoLibJ [5] and 3D ImageJ Suite plugins [6]. These can be installed by adding the following update sites: http://sites.imagej.net/IJPB-plugins/ and http://sites.imagej.net/Tboudier/ .
The kidney dataset was imported via raw import and cropped again, reducing the data size from 46 GB to 21 GB. The whole volume was filtered with the Fiji 3D Gauss filter function, using an isotropic $\sigma = 1$ voxel. Blood vessels and tubules were extracted by setting manual thresholds. As the first height step of the scan had a deviating intensity distribution from the other height steps, thresholds were set separately from the rest of the scan.
For blood vessels, a lower threshold of 27700 was chosen for the first height step, and a lower threshold of 27000 for the rest of the dataset. To remove contrast from contrast agent stuck to the outside of the kidneys, a mask was created by choosing another threshold of 23000 for the whole kidney, performing MorphoLibJ's 6-connected component labeling function to label and remove unconnected areas via thresholding. As the first mask still left some areas connected to the kidney, a single 3D erosion was performed and the connected component labeling repeated. The mask was 3D dilated two times and applied to the blood vessel segmentation, yielding the blood vessel segment.
For tubules, upper thresholds of 25000 and 24200 were chosen, respectively. To separate tubules from the water background with the same intensity, a kidney shape mask was created from the blood vessel segment by dilating at first 10 times and using 3D ImageJ Suite 3D hole filling. As there were still holes remaining, we dilated the mask another 3 times, repeated the 3D hole filling, then eroded the shape back 13 times. The resulting kidney shape mask was applied to the thresholds to receive the tubule segment.
Quantification of vessel and tubular volumes and surface was performed with Analyze Regions 3D of the MorphoLibJ plugin. The plugin calculated the volume based on the number of voxels in the binary segment, and surface was estimated by counting the number of line probe intersections in 13 different directions. Details can be found in the MorphoLibJ documentation:
https://imagej.net/MorphoLibJ
We manually chose a marker point at the papilla of the kidney in the blood vessel segment at X: 370, Y: 1671, Z: 1194 and calculated the lengths of the shortest path along the blood vessels using the Geodesic Distance Map 3D function of MorphoLibJ. The Euclidean distance map and all histograms were calculated using default Fiji/ImageJ functions.
All image processing was performed on a workstation equipped with 256 GB RAM and two eight-core Intel Xeon E5-2670 processors clocked at 2.60 GHz. 3D computer graphic images of the segmentation were rendered with Arivis4D 2.12.4 (Arivis, Germany) on a virtual machine with 174 GB of RAM, 7 Intel Xeon E5-2680 v2 cores and pass-through Nvidia Grid K2 graphics.

5.5.9.11 Materials and Suppliers List

5.5.9.11.1 Perfusion reagents

Phosphate Buffered Saline (PBS)	Oxoid Phosphate Buffered Saline Tablets (Dulbecco A) BR0014G , ThermoFisher Scientific, United States
Ketamine 100 mg/ml	Ketasol®-100 ad us. vet., Injektionslösung Dr. E. Graeub AG, Switzerland
Xylazine 20 mg/ml	Xylazin Streuli ad us. vet., Injektionslösung Streuli Pharma AG, Switzerland
Paraformaldehyde	Paraformaldehyde prilled, 95% 441244, Sigma Aldrich, Germany
Glycine	Glycine Molecular biology 07132391, Biosolve Chimie, France
Agar	Agar for microbiology 05039, Sigma Aldrich, Germany
Mineral oil	Mineral oil, light oil (neat), BioReagent M8410, Sigma Aldrich, Germany

5.5.9.11.2 Surgical Tools

Fine scissors	Vannas Spring Scissors - 2.5mm Blades 15000-08, Fine Science Tools, Germany
Arterial clamp	Micro Serrefine - 10 x 2 mm 18055-01, Fine Science Tools, Germany
Arterial clamp applying forceps	Micro-Serrefine Clip Applying Forceps 18057-14, Fine Science Tools, Germany
Vessel dilating forceps	S&T Vessel Dilating Forceps - 11cm 00125-11, Fine Science Tools, Germany
Angled forceps	S&T 0.3mm x 0.25mm Forceps 00649-11, Fine Science Tools, Germany
Straight forceps	Rubis Switzerland Tweezers 5-SA 232-1221, VWR, United States
Silk suture for ligations	Non-Sterile Silk Suture Thread 5/0 18020-50, Fine Science Tools, Germany

5.5.9.11.3 Perfusion Consumables

1 ml syringe	Injekt F 1 ml 9166017V , B. Braun, Germany
26 G needle	Sterican 26 G x ½ “ 466 5457, B. Braun, Germany
10 ml syringe Luer Lock	NORM-JECT 10 ml (12 ml) 4100-X00V0, Henke Sass Wolf, Germany
50 ml syringe Luer Lock	Omnifix 50 ml (60 ml) 4617509F , B. Braun, Germany
1.2 µm syringe filter	Chromafil Xtra PET-120/25 729229, Macherey-Nagel, Germany
3-way stopcock	Discofix C 3-way Stopcock 16494C , B. Braun, Germany
21 G butterfly needle	Venofix Safety G21 4056521-01, B. Braun, Germany
0.5 ml PCR tubes	PCR Single tubes, PP, 0,5 ml 781310, Brand, Germany
1.5 ml centrifugation tubes	Micro tube 1.5ml 72.690.001, Sarstedt, Germany

5.5.9.12 References

[1] J. Czogalla, F. Schweda, and J. Loffing, "The Mouse Isolated Perfused Kidney Technique," *J Vis Exp,* p. 54712, Nov 17 2016, doi: 10.3791/54712.

[2] K. M. Hazenfield and D. D. Smeak, "In vitro holding security of six friction knots used as a first throw in the creation of a vascular ligation," *J Am Vet Med Assoc,* vol. 245, pp. 571-7, Sep 1 2014, doi: 10.2460/javma.245.5.571.

[3] J. Schindelin, I. Arganda-Carreras, E. Frise, V. Kaynig, M. Longair, T. Pietzsch*, et al.*, "Fiji: an open-source platform for biological-image analysis," *Nat Methods,* vol. 9, pp. 676-82, Jun 28 2012, doi: 10.1038/nmeth.2019.

[4] C. A. Schneider, W. S. Rasband, and K. W. Eliceiri, "NIH Image to ImageJ: 25 years of image analysis," *Nat Methods,* vol. 9, pp. 671-5, Jul 2012, doi: 10.1038/nmeth.2089.

[5] D. Legland, I. Arganda-Carreras, and P. Andrey, "MorphoLibJ: integrated library and plugins for mathematical morphology with ImageJ," *Bioinformatics,* vol. 32, pp. 3532-3534, Nov 15 2016, doi: 10.1093/bioinformatics/btw413.

[6] J. Ollion, J. Cochennec, F. Loll, C. Escude, and T. Boudier, "TANGO: a generic tool for high-throughput 3D image analysis for studying nuclear organization," *Bioinformatics,* vol. 29, pp. 1840-1, Jul 15 2013, doi: 10.1093/bioinformatics/btt276.

6 Discussion

6.1 Context

The specific aims of this PhD-project can be summarized as acquiring data on the following three features of renal anatomy:

1. Structure of the vascular system
2. Structure of the tubular system
3. Localization of renal erythropoietin-producing cells

The overarching goal of acquiring these data was to gain further insights into the oxygen-dependent regulation of renal erythropoietin production. The local oxygen concentrations within the kidney could not be measured experimentally with the necessary resolution to correlate them with the localization of the renal erythropoietin-producing cells. This necessitated the use of computational modeling to calculate more detailed oxygen concentration maps based on less highly resolved experimental measurements of oxygen, knowledge of physics of flow and diffusion processes and knowledge of renal physiological oxygen supply and consumption. The structural data of the vascular and tubular system required for the latter was not available in sufficient detail to build an accurate computational model with realistic geometries and spatial distribution. This necessitated the use of idealized, simplified geometries, as was outlined in the review on renal arteriovenous oxygen shunting, which has been reproduced in chapter 4.2 of this thesis. Replacing these idealized geometries with realistic geometries was the main purpose of this PhD project.

The envisioned use in computational modeling created additional requirements for the imaging data. Specifically, the vascular structure, tubular structure and renal erythropoietin-producing cells had to be acquired:

4. in full 3D
5. in the whole kidney
6. in the same kidney

Simulation of blood flow, the primary means of oxygen distribution from the renal artery throughout the kidney, also required imaging with:

7. full connectivity of the vascular structure

Achieving all of these additional conditions made the development and optimization of specialized imaging protocols necessary. Individually, these aims could be achieved easily with well-established standard methods. The main challenge lay in achieving these aims all at the same time.

6.2 Methodology

6.2.1 Multi-modal imaging

The initial research plan split the imaging into two modalities: The vascular system was to be imaged with conventional laboratory source µCT, whereas the tubular system and renal erythropoietin-producing cells were to be imaged with 3D light microscopy.

Due to the small size and high density of capillaries in the kidney, imaging of the vascular structure had the highest resolution requirements of the three features of interest. µCT was the most suitable method for imaging the vasculature due to the high resolution, lack of optical distortion, isotropic image quality and accessibility towards injection with X-ray contrast agents. The tubular structure could not be perfused independently with contrast agent from the vasculature, but featured larger diameters and thus required lower resolution. The renal erythropoietin-producing cells could only be distinguished from interstitial cells by their expression of tdTomato fluorescent protein, and thus could only be captured with fluorescence microscopy methods. These cells individually had a smaller size than the capillaries, but were typically spaced apart sufficiently that they could be separated even at lower imaging resolutions than required for the capillaries.

6.2.2 3D light microscopy and X-ray microtomography

The experiments described in chapter 4.4 revealed that the resolution achievable with lightsheet microscopy on CLARITY- or PACT-cleared kidney tissue was insufficient to image the tubular structure. 3D light microscopy techniques capable of higher resolutions such as confocal microscopy and multiphoton microscopy were impractically slow, requiring scan times that exceeded the expected shelf life of the samples under measurement conditions. Confocal microscopy was furthermore incapable of providing the necessary resolution beyond a depth of 1 mm. Therefore, the decision was made to employ synchrotron X-ray propagation-based phase contrast imaging, which features higher density resolution compared to laboratory source X-ray imaging and would be able to image tubular structure without contrast agent enhancement. Vascular structure could be imaged concurrently in the same scan, obviating the need for image registration.

Separating the vascular lumen from the tubular lumen still required contrast agent injection. Without contrast agent, the water-filled vascular lumen would feature exactly the same X-ray absorption and thus grey values as the water-filled tubular lumen. While in theory, the two lumina could be separated during post-processing by employing connectivity analysis to define the fully connected vascular tree and the fully connected tubular tree separately, in practice this requires the segmented data to be free of any artificial connections between the two trees. These may be introduced by lack of resolution, noise or artifacts, and could not be excluded for our dataset. The 1.625 µm voxel size would have been insufficient to ensure proper separation of vascular and tubular lumina, in particular in the inner medulla. The resulting partial volume effects would also require a much higher contrast-to-noise ratio than was achieved during our measurements. Ring artifacts could not be removed entirely and would have caused artificial connections.

Contrast agent-free imaging would only have been feasible if the vasculature had been the sole feature to be imaged. In that case, the two lumina could, for be distinguished if the blood was allowed to remain in the vascular lumen, for example. Tubular lumina on the other hand collapse at death, because the post-mortem drop in blood pressure results in a lack of glomerular filtration and tubular counterpressure. Tubules thus require fixation while upholding liquid flow and pressure, which is achieved by perfusion of the kidneys with liquid fixative solutions. Since this results in the removal of the blood, contrast between the now solution-filled vasculature and the solution-filled tubules then has to be established by injection of new contrast agent after fixation.

6.2.3 Vascular casting

As is described in chapter 4.5, vascular casting with radiopaque, hardening plastic resins was employed to this end. This had been a well-established technique for microvascular imaging in the rat. The vascular dataset [25] used for the previous computational models of renal oxygen transport [47]–[49] was based on μCT images of a vascular cast [26]. For this PhD-project, the procedure had to be adapted to the mouse, as the localization of the renal erythropoietin-producing cells relied on a mouse model. The smaller size of murine kidneys would also permit a smaller field of view and thus higher resolution, allowing imaging of the capillaries that was not possible on the whole organ scale in the previous rat kidney μCT datasets. Getting the fully connected vascular tree for computational modeling also required uninterrupted filling of the capillaries throughout the whole organ.

Vascular casts of the murine kidney were found to be lacking in this regard compared to vascular casts of the rat. Insufficient filling of both capillaries and larger vessels, in particular in the venous tree, was described in the literature [37], [50] or could be observed in the presented data [36]. It was assumed that the microparticle-based radiopaque components of the employed Microfil plastic resin were responsible for the lack of reliable and consistent perfusion. This view was supported by the higher quality exhibited by vascular casts without radiopaque component [51]. On the other hand, this view was not supported by the higher quality exhibited by vascular casts of rat kidneys [26], [52]. On the gripping hand, as rat kidneys could not be imaged down to the capillary level in their entirety, it could not be ascertained that capillary filling was indeed complete.

These assessments led to the development of the microparticle-free mixture of PU4ii with dissolved 1,3-diiodobenzene as the radiopaque component. It should be noted that, at that point in time, kidney vascular casting using the commercial microparticle-free μAngiofil vascular casting resin had not been demonstrated yet [39]. The newly developed PU4ii mixture initially featured the similar issues with blood vessel filling as the microparticle-based Microfil did. After thorough optimization of the mixture established sufficient trust that this result was not caused by any issues of the mixture itself, microparticles were excluded as the sole source of the observed deficits in vessel filling. The transcardial injection procedure then became the focus of the investigation, with arterial clamping being employed to divert a larger fraction of the flow to the kidneys. It was then observed that blood remained in the renal veins and vena cava after the first perfusion step with PBS. This meant that blood vessels were insufficiently flushed already prior to the injection of any contrast agent, which clearly indicated that transcardial perfusions were insufficient for kidney vascular casting. Improving the injection procedure was thus paramount irrespective of the choice and properties of the employed X-ray contrast agent, and became the next focus of the PhD project. Further research on developing new contrast agents was mostly put on hold until this issue could be resolved.

Fortunately, the expertise on the isolated kidney procedure in mice was available within the NCCR Kidney.ch framework and the University of Zurich [38], and only a simplified procedure was required, namely the perfusion of the kidneys via the abdominal aorta. Unfortunately, the surgery for the abdominal aorta perfusion is still considerably more difficult than the procedure for the transcardial perfusion. As a matter of comparison, learning to reliably perform the abdominal aorta perfusion took me several months of practice, whereas learning to reliably perform the transcardial perfusion can be done in a single day.

Once learned, the abdominal aorta perfusion had to be further adapted to and optimized for the specific requirements of vascular casting. The plastic resins are more viscous and have higher resistance to flow than the water-based solutions employed in the isolated perfused kidney protocol. Flow speed is furthermore a critical factor for complete vascular filling, as all water in the vascular

lumen needs to be replaced by radiopaque resin before polymerization and thus hardening of the resin completes. This may then require much higher perfusion pressures, which in turn requires the ligations to be tied with constrictor knots instead of the standard surgeon's throw [40]. The hardening of vascular casting resins also means that the entire perfusion apparatus has to be disposable, since it is rendered unusable after a single attempt. This necessitated the development of the weight-actuated pressure-controlled syringe pump, which is a cheap and disposable alternative to the expensive pressure-sensor controlled peristaltic pump used in the isolated perfusion kidney technique, albeit at a cost in precision.

6.2.4 Single distance propagation-based hard X-ray phase contrast imaging

The combination of optimized perfusion surgery and the microparticle-free vascular casting mixture permitted imaging of the whole vascular and tubular structure with synchrotron hard X-ray single-distance propagation-based phase contrast μCT. Fourteen mouse kidneys were scanned with 1.625 μm voxel size at the ID19 microtomography beamline of the European Synchrotron Radiation Facility. Employing pink beam at 19 keV, a single height step could be acquired within 10 minutes, which proved to be close to the optimum, since the radiation exposure would start to create gas bubbles in the agar medium surrounding the kidneys after 15 minutes, leading to movement artifacts. The chosen acquisition settings thus allowed us to make the most use out of the available photon flux at that energy, while keeping measurement times low.
Imaging with smaller voxel sizes of 1.125 μm and 1.25 μm at the I13-2 beamline of Diamond Light Source and P05 beamline of Deutsches Elektronen-Synchrotron was performed as well. These smaller voxel sizes came at a cost: The higher number of projections required and the slower read-out times of the larger camera arrays increased the measurement time per height step well above the time limit by which bubble formation would occur. Photon flux had to be reduced in those cases, increasing the time required for a height step to the order of two hours. Due to limited beam time, compromises had to be made in terms of exposure time for those datasets. The larger camera arrays also increased the geometric distortion along the borders of the acquired projections, since the tomography beamlines make use of standard microscopy optical lenses to magnify the visible light image formed by converted X-rays at the scintillator. Most crucially, however, the PyHST2 reconstruction software at ID19 was capable of reconstructing scans with asymmetric rotation axis, whereas the reconstruction pipelines at I13-2 and P05 did not feature this capability at the time, requiring the development of in-house code for reconstruction. Such code would have to be written by our group, and would be missing features such as corrections for geometric distortion [53]. These drawbacks, especially the last one, still made the datasets acquired at ID19 the best suited datasets for further image processing at that time. Further developments of the reconstruction pipelines at the various tomography beamlines in the meantime have made smaller voxel sizes more feasible since then.

6.2.5 Image Processing

Due to the large file size of 1158 GB of a single reconstructed dataset of a whole mouse kidney at 1.625 μm voxel size, none of the available commercial or free and open source image processing tools were suitable for segmentation. The first main roadblock were limited or lacking capabilities of out-of-core processing, the capability to process data without having to load the entire dataset into main memory (RAM). The largest amount of RAM available to us on a single node was only 512 GB (on the Euler high performance computing cluster), well below the requirements of processing the whole dataset in RAM. The second main roadblock was the lack of parallelization in many implemented image processing algorithms. This meant that these algorithms were only capable of using a fraction of the computing power of contemporary multi-core central processing units (CPU), leading to impractically long processing times.

Processing of these large datasets therefore required the development of dedicated processing code, which required specialized knowledge in high performance computing (HPC), such as familiarity with handling non-uniform memory access (NUMA) and Message Passing Interface (MPI), to mention a few keywords. This work was primarily done by Dr. Diego Rossinelli.

Due to the high contrast-to-noise ratio and resolution, the initial segmentation of the vasculature could be performed by a standard rescaling, denoising and thresholding. The resulting binary mask retained several artifacts from the imaging, which had to be removed.

The first one among those was white adipose tissue, which had taken up part of the 1,3-diiodobenzene used as radiopaque component in PU4ii. This specific issue could have been avoided if vascular casting had been performed using µAngiofil, but this only became apparent after image acquisition and fat removal in post-processing had already been completed. Said post-processing consisted of manually segmenting fat in small regions of interest, which was used as training data for automatic classification of fat. A similar approach was chosen to identify every single glomerulus in the kidney individually. In both cases, providing the training data was labor-intensive, in particular for the fat, as it required manual contouring not only in one dimension, but all three dimensions to create a smooth surface. This could fortunately be avoided for the glomeruli, as the classification was performed on the binary mask and not the raw grayscale data, meaning that borders did not have to be voxel-accurate, but only accurate towards the segmented blood vessels.

The second major issue was the presence of ring artifacts. These are very common artifacts in tomography and are typically caused by limitations in the accuracy of the flat-field correction or non-ideal pixel responses of the detectors or scintillators. In our workflow, these were addressed by manual identification and deletion of ring artifacts in the segmented vessel mask. Better approaches are available, such as improved flat-field corrections including measurement and modeling of the individual detector pixel responses [54], more advanced filtering techniques in the reconstruction workflow [53] or making use of the redundant acquisition of fully overlapping height steps to replace defective pixels.

The third major problem was the formation of large numbers of gas bubbles in the vascular cast during polymerization, leading to equally large numbers of artificial holes in the segmented binary mask. This issue is a common problem amongst all vascular casting resins, including Microfil and µAngiofil, and can only satisfactorily be resolved by using contrast agents with hydrophilic properties, as described in chapter 5.1. In large vessels, these bubbles could be removed by employing connectivity analysis on the segmented binary mask to identify regions of background that were fully enclosed by vasculature on all sides. This approach is however inherently incapable of removing gas bubbles touching a border of the vessels, and cannot fill holes that fully disconnect blood vessels. As a consequence, the vasculature in some regions of the kidney did not connect to the main connected component. The fully connected dataset therefore lost part of the capillary bed of the kidney compared to the initial segmentation.

In general, the chosen approach for vascular segmentation and artifact removal resulted in a fully connected binary mask of the vasculature in a whole mouse kidney. For future applications however, the reliance on manual training data means that the approach does not scale well and may not be robust towards rater variability. The specific issues making manual intervention necessary stem from practical issues in sample preparation and image acquisition, and should ideally be addressed on those levels, rather than in image post-processing.

The initial segmentation of the tubules was performed similarly to the initial vascular segmentation, by scaling, denoising and thresholding. Due to the larger feature size and lower contrast-to-noise ratio however, the reconstructions employing the Paganin-filter [55] served as the raw data basis

instead, which trades edge enhancement and resolution for improved contrast [56]. In that case, ring artifacts and compression of the tubular lumina through overpressure in the vascular compartments resulted in artificial shortcuts and interruptions, respectively. Connectivity analysis on the tubular binary mask did not yield a fully connected tubular tree of sufficient quality to allow determination of kidney tubules by analyzing the path length from the glomeruli. The tubular segmentation can only serve as direction-less map of tubular localization instead.

6.2.6 Limitations of vascular casting and need for alternative approaches

In retrospect, the specific issues of vascular casting of the murine kidney were not well enough described in the available literature, requiring many failed casting attempts to be rediscovered and understood instead. The most detailed description by Vasquez et al. concluded that: “By moderating perfusion pressure and perfusion mass volume, individual investigators may find that further optimization is needed to amend the protocols depicted here for their particular preclinical model specimen.” [37] While accurate, the description somewhat understates the challenges and amount of optimization required when employing vascular casting in specific organs, while providing only little specific information on which parameters should be optimized in what manner. This in part is the reason for including chapter 4.5.4, a detailed protocol of the kidney vascular casting procedure. It has to be noted however that many of the specific details indeed cannot be easily and briefly explained. When attempting to teach other people the vascular casting procedure, it became clear that even if someone was fully capable of performing regular abdominal aorta perfusion with water-based solutions, the infusion with hardening plastic resins created considerable additional challenges that require extensive experience to deal with. Examples include: Recognizing whether the flow rate is sufficient for the size and type of mouse perfused based on the velocity of the outflowing plastic resin, or identifying and resolving potential blockages when flow rate is too low. These are skills mostly dependent on experience, and difficult to describe in written accounts. The difficulty, low reliability and remaining unresolved artifacts of vascular casting with hydrophobic plastic resins were some of the main reasons why the development of a new contrast agent dedicated to *ex vivo* microvascular imaging was resumed, as is described in chapter 5.1. In addition, the use of hydrophilic contrast agents was necessary to ensure compatibility with aqueous tissue clearing methods such as CLARITY and PACT.

6.2.7 Evaluation of existing alternatives to vascular casting and need for a new contrast agent

During the work on optimizing the vascular casting with PU4ii, the evaluation of Aurovist 15 nm surface-functionalized gold nanoparticles as a suitable hydrophilic alternative proceeded in parallel as the limitations of plastic resin-based vascular casting became increasingly apparent. Later on, these experiments were supplemented by similar experiments using the 110 nm large ExiTron nano 12000 alkaline earth metal nanoparticles, as is described in chapter 5.2. Results for both of these were comparable. Without prior filtering, nanoparticle aggregates would clog the capillary loops of the glomeruli, and prevent proper perfusion of the vascular network downstream of the blockage. Filtering markedly improved vessel filling, but aggregates formed after filtration seemed to block further perfusion of downstream kidney regions as well. In addition, nanoparticles would slowly diffuse out of the vasculature into the surrounding medium. All of these issues made nanoparticle-based blood pool contrast agent unsuitable for the purposes of this PhD project, which required reliable capillary filling and long-term sample stability for transport and measurement at synchrotron facilities.

In principle, the aforementioned issues may be resolvable by considerable optimization. The aggregation behavior of the nanoparticles can be altered by the choice of the surrounding medium, as was demonstrated by using a mannitol solution instead of PBS for suspending the ExiTron nano

12000 nanoparticles. Additional optimizations of nanoparticle size and concentration may further increase the reliability of the vessel filling.

Leakage of the blood pool contrast agents over time could not be prevented entirely by coinjecting with gelatin, while vascular filling was negatively impacted. The temperature-dependent gelling behavior of gelatin made it comparably difficult to control and required careful optimization of temperature, flow rate and concentration to yield the results presented in chapter 5.2.4.3. Gelatin may be replaced with hydrogels with different gelling properties such as alginate, which gels in the presence of calcium cations. This would open up a wider range for parameter optimizations, such as higher gel concentrations, which may lead to a workable protocol.

In the context of the whole PhD project, the nanoparticles suffered from an additional drawback that was not discussed in the conference paper, namely their light scattering properties. This would make them ill-suited for further tissue clearing and imaging with 3D light microscopy. Only a fully water-soluble contrast agent would be capable of both resolving the issues with vascular filling and feature a lack of light-scattering interfaces necessary for high-quality lightsheet imaging. Accordingly, nanoparticle-based blood pool contrast agents may have been a solution if only vascular and tubular imaging was required, but the development of a dedicated contrast agent was required if the renal erythropoietin-producing cells had to be imaged on the same sample as well.

6.2.8 Design and synthesis of the cross-linkable, polymeric X-ray contrast agent XlinCA

In principle, the requirements of a dedicated X-ray contrast agent for *ex vivo* high resolution vascular imaging were rather simple. The contrast agent should be highly water-soluble, large enough to avoid extravasation or glomerular filtration and cross-linkable to prevent loss of contrast over time. In theory, these properties can be fulfilled by a large variety of compounds, only a few of which are shown in chapter 5.3. For practical use, there were additional requirements such as material costs and ease of manufacture to consider. Material costs favored the design of a contrast agent derived from 5-amino-2,4,6-triiodoisophthalic acid, which is a common precursor of a variety of different angiography contrast agents [12], [57] and commercially available at relatively low cost. Ease of manufacture was a major factor due to the large amounts of contrast agent required. In our own studies, preparing the kidneys of a single mouse would require about 0.6 g of contrast agent, while a whole mouse would take 2.7 g of contrast agent. This required synthesis at considerably larger scale than in typical research projects, meaning that any complexity in the manufacturing process would be correspondingly amplified. Therefore, a simple approach based on a single, linear polymer was chosen over more difficult to synthesize alternatives to create molecules with high molecular weight, such as dendrimers [58].

Initially, experiments were performed with the non-fixable polymer, i.e. prior to coupling with ethylenediamine, which is designated as compound **3** in chapter 5.4. This was based on wrong estimations of the molecular weight of compound **3** by dynamic light scattering, creating the assumption that the size of the molecules was considerably larger than the targeted 65 000 g/mol. Later measurements by gel permeation chromatography revealed the correct molecular weight of 30 400 g/mol, which was well below the required molecular weight to avoid glomerular filtration. Despite this, glomerular filtration of the contrast agent could be avoided in some instances by co-injection with gelatin. Gelatin had been used to compensate for the lack of cross-linkable functional groups. Similar to the results achieved with the nanoparticle-based blood pool contrast agents, gelatin was not successful at preventing leakage of compound **3** over time. In retrospect however, gelatin was in some instances capable of preventing glomerular filtration of compound **3**. This was not investigated further, since at that time, the lack of glomerular filtration was attributed to the erroneously assumed large size of compound **3**. It can be speculated that fixation of gelatin within the glomerular pores reduced their filtering capability below the point at which retention of

compound **3** became possible. This result may be of interest in demonstrating the potential for alternative solutions to preventing glomerular filtration of contrast agent.

Attempts to increase the molecular weight of compound **3** to above 65 000 g/mol by adjusting the parameters of the RAFT polymerization process were unsuccessful. Increasing the ratio of monomer to radical initiator reduced yields and reliability of the reaction. The solution to this problem could only be implemented when the cross-linkable compound **6**, XlinCA, was developed. The free amine groups not only allowed fixation within the vasculature, but also permitted pre-cross-linking of the 30 kDa large molecules using glutaraldehyde to increase their molecular weight to above the required threshold. With this feature, a compound had finally been developed that was capable of fulfilling the requirements of being a highly water-soluble, cross-linkable X-ray contrast agent with high molecular weight.

As a highly water-soluble compound, XlinCA could avoid the filling artifacts caused by water inclusions or gas formation that had been a major issue for plastic resin-based vascular casting. The quality of the vascular filling with XlinCA was mainly dependent on the extent to which blood could be removed from the vascular lumina by the initial perfusion with saline prior to contrast agent injection. As a consequence, excellent vascular filling could be achieved with a simple transcardial perfusion. Vascular casting with XlinCA thus turns a procedure which may take several months of organ-specific optimization into a method that can be performed successfully within a single attempt.

6.2.9 Combined vascular and tubular imaging with laboratory source X-ray µCT

Since flow rate of the contrast agent injection no longer has to be optimized to avoid premature polymerization, lower perfusion pressures can be employed compared to plastic resin-based vascular casting. In combination with the fact that glomerular filtration can proceed during the injection of a water-soluble compound, and pressure is thus maintained within the tubules, the lower pressure in the blood vessels prevents compression of renal tubules. This resolves the problems encountered when attempting to segment the fully connected tubular tree of an entire mouse kidney injected with plastic resin.

Imaging of renal tubules with µCT was facilitated by the unexpected property of XlinCA to be found in tubular walls in the cortex and outer medulla, as is described in chapter 5.5. The vascular lumina still featured higher concentration of XlinCA, which permitted concurrent vascular and tubular imaging with laboratory source X-ray µCT. Given that similar behavior could not be observed with compound **3**, this is speculated to be caused by limited diffusion of XlinCA into the intracellular space, where it is immobilized by residual aldehydes of the prior perfusion fixation. This behavior reduces the contrast-to-noise ratio between the vasculature and the background, which is a disadvantage if exclusively vascular imaging is desired.

This limitation was of lesser concern in this PhD project, where combined vascular and tubular imaging is required. Imaging of renal erythropoietin-producing cells on the other hand was hampered by the strong fluorescent signal of XlinCA at wavelengths below 500 nm. Since these would prevent accurate imaging of the tdTomato signal by fluorescence microscopy, further developments are unfortunately still required to reach the initially set specific aims of the PhD project. Fluorescence could potentially be reduced by replacing glutaraldehyde by formaldehyde in the XlinCA protocols, and by cleavage of the residual RAFT reagents from the polymer backbone to reduce their contribution to fluorescence. If these approaches prove insufficient, the development of an aliphatic X-ray contrast agent may be required.

6.3 Conclusion

This project was embedded in an overarching research initiative to improve our understanding of the oxygen distribution of the kidney and its effects on oxygen-dependent mechanisms. The initial outline intended for the imaging of renal blood vessels and tubules, the main suppliers and consumers of oxygen, respectively, in their entirety with full connectivity. Those data were then to be used to calculate the oxygen distribution within the kidney with computational modeling. To correlate this oxygen distribution with a physiological response, the location of oxygen-sensing renal erythropoietin producing cells in the same kidneys should be identified as well.

A dataset of the fully connected vasculature and tubules of a whole mouse kidney has been acquired with synchrotron X-ray µCT and is being used for initial computational modeling of oxygen transport and distribution. Previous datasets did not provide any information on the kidney capillaries and were only available for the rat kidney [25], with no equivalent dataset being available for the mouse until now. The herein presented dataset represents major step forward, being the first to finally clear the hurdle of full capillary resolution in the murine kidney. Quantitative analysis and computational modeling are complicated by several artifacts remaining within the dataset, most of which are the consequences of limitations inherent to the plastic-based vascular casting method used.

To overcome these limitations, the water-soluble, cross-linkable, polymeric X-ray contrast agent XlinCA was developed, which allows for simpler, more reliable and filling artifact-free vascular casting. Vascular casting of a whole mouse could be performed with a simple transcardial perfusion without optimization, which demonstrates the potential of XlinCA to turn high resolution vascular 3D imaging with X-ray µCT into a much more widely accessible technique. In the kidney, combined vascular and tubular imaging could be demonstrated with laboratory source X-ray µCT, which allowed for quantification of 3D renal anatomy on the whole organ scale without being constrained by the availability of synchrotron beamtime.

Renal erythropoietin producing cells could be imaged reliably at depth on the whole organ scale using tissue clearing combined with lightsheet microscopy. Staining protocols for marking cell nuclei and blood vessel walls were also developed, allowing identification of individual cells and cell localization in the context of the oxygen supply, respectively.

In conclusion, out of the initial seven specific aims described in chapter 6.1, all but one have been achieved. Imaging of the vascular and tubular system with all the additional constraints imposed by the envisioned application in computational modeling was successful, representing all the goals except aim number 3., localization of renal erythropoietin-producing cells. This last goal could be achieved individually, but not in combination with the other six goals. Through all the developments undertaken in the framework of this PhD-thesis however, most of the challenges have already been overcome, and it should only be a matter of time and optimization of the herein presented protocols until multimodal vascular, tubular and cellular imaging on the same sample is finally within reach.

7 Materials and Suppliers List

Perfusion reagents

Phosphate Buffered Saline (PBS)	Oxoid Phosphate Buffered Saline Tablets (Dulbecco A) BR0014G, ThermoFisher Scientific, United States
Ketamine 100 mg/ml	Ketasol®-100 ad us. vet., injection solution Dr. E. Graeub AG, Switzerland
Xylazine 20 mg/ml	Xylazin Streuli ad us. vet., injection solution Streuli Pharma AG, Switzerland
Paraformaldehyde	Paraformaldehyde prilled, 95% 441244, Sigma Aldrich, Germany
Glycine	Glycine Molecular biology 07132391, Biosolve Chimie, France
Agar	Agar for microbiology 05039, Sigma Aldrich, Germany
Mineral oil	Mineral oil, light oil (neat), BioReagent M8410, Sigma Aldrich, Germany

Surgery Tools

Fine scissors	Vannas Spring Scissors - 2.5mm Blades 15000-08, Fine Science Tools, Germany
Arterial clamp	Micro Serrefine - 10 × 2 mm 18055-01, Fine Science Tools, Germany
Arterial clamp applying forceps	Micro-Serrefine Clip Applying Forceps 18057-14, Fine Science Tools, Germany
Vessel dilating forceps	S&T Vessel Dilating Forceps - 11cm 00125-11, Fine Science Tools, Germany
Angled forceps	S&T 0.3mm × 0.25mm Forceps 00649-11, Fine Science Tools, Germany
Straight forceps	Rubis Switzerland Tweezers 5-SA 232-1221, VWR, United States
Silk suture for ligations	Non-Sterile Silk Suture Thread 5/0 18020-50, Fine Science Tools, Germany

Perfusion Consumables

1 ml syringe	Injekt F 1 ml 9166017V , B. Braun, Germany
26 G needle	Sterican 26 G × ½ “ 466 5457, B. Braun, Germany
10 ml syringe Luer Lock	NORM-JECT 10 ml (12 ml) 4100-X00V0, Henke Sass Wolf, Germany
50 ml syringe Luer Lock	Omnifix 50 ml (60 ml) 4617509F , B. Braun, Germany
1.2 µm syringe filter	Chromafil Xtra PET-120/25 729229, Macherey-Nagel, Germany
3-way stopcock	Discofix C 3-way Stopcock 16494C , B. Braun, Germany

21 G butterfly needle	Venofix Safety G21 4056521-01, B. Braun, Germany
0.5 ml PCR tubes	PCR Single tubes, PP, 0,5 ml 781310, Brand, Germany
1.5 ml centrifugation tubes	Micro tube 1.5ml 72.690.001, Sarstedt, Germany

PACT Tissue Clearing

Acrylamide	Acrylamide A8887, Sigma Aldrich, Germany
Sodium dodecyl sulfate (SDS)	Sodium dodecyl sulfate ≥99.0% (GC), dust-free pellets 75746, Sigma Aldrich, Germany
Histodenz	Histodenz D2158, Sigma Aldrich, Germany
VA-044 radical initiator	2,2'-Azobis[2-(2-imidazolin-2-yl)propane]dihydrochloride FUJIFILM Wako Pure Chemical Corporation, Japan
Isolectin IB4	Isolectin GS-IB4 From Griffonia simplicifolia, Alexa Fluor™ 488 Conjugate I21411, ThermoFisher, USA
CD31 antibody	CD31 Monoclonal Antibody (390), FITC RM5201, ThermoFisher Scientific, United States
DRAQ5	DRAQ5 424101, BioLegend, United States

Vascular casting

PU4ii	PU4ii VasQtec, Switzerland
1,3-Diiodobenzene	1,3-Diiodobenzene 475262, Sigma Aldrich, Germany
1,4-Diiodobenzene	1,4-Diiodobenzene 193526, Sigma Aldrich, Germany
2-Butanone	2-Butanone 360473, Sigma Aldrich, Germany

8 References

[1] G. Kuhlmann, “Observing air pollutants and greenhouse gases with hyperspectral imaging spectrometers on-board aircraft and satellites,” presented at the TOPICAL DAY Imaging and Image Analysis X, Empa, Dübendorf, Apr. 09, 2018, [Online]. Available: https://events.empa.ch/Veranstaltungsarchiv/2018/event.php?vnr=ea-10c.

[2] C. N. Hall *et al.*, “Capillary pericytes regulate cerebral blood flow in health and disease,” *Nature*, vol. 508, no. 7494, pp. 55–60, Apr. 2014, doi: 10.1038/nature13165.

[3] C. E. Shannon, “Communication in the Presence of Noise,” *Proc. IRE*, vol. 37, no. 1, pp. 10–21, Jan. 1949, doi: 10.1109/JRPROC.1949.232969.

[4] D. B. Murphy and M. W. Davidson, *Fundamentals of light microscopy and electronic imaging*, 2nd ed. Hoboken, N.J: Wiley-Blackwell, 2013.

[5] D. S. Richardson and J. W. Lichtman, “Clarifying Tissue Clearing,” *Cell*, vol. 162, no. 2, pp. 246–257, Jul. 2015, doi: 10.1016/j.cell.2015.06.067.

[6] H. Kolesova, M. Capek, B. Radochova, J. Janacek, and D. Sedmera, “Comparison of different tissue clearing methods and 3D imaging techniques for visualization of GFP-expressing mouse embryos and embryonic hearts,” *Histochem Cell Biol*, vol. 146, no. 2, pp. 141–52, Aug. 2016, doi: 10.1007/s00418-016-1441-8.

[7] F. Chen, P. W. Tillberg, and E. S. Boyden, “Expansion microscopy,” *Science*, vol. 347, no. 6221, pp. 543–548, Jan. 2015, doi: 10.1126/science.1260088.

[8] P. Schiebener, J. Straub, J. M. H. Levelt Sengers, and J. S. Gallagher, “Refractive index of water and steam as function of wavelength, temperature and density,” *J. Phys. Chem. Ref. Data*, vol. 19, no. 3, pp. 677–717, May 1990, doi: 10.1063/1.555859.

[9] B. L. Henke, E. M. Gullikson, and J. C. Davis, “X-Ray Interactions: Photoabsorption, Scattering, Transmission, and Reflection at E = 50-30,000 eV, Z = 1-92,” *At. Data Nucl. Data Tables*, vol. 54, no. 2, pp. 181–342, Jul. 1993, doi: 10.1006/adnd.1993.1013.

[10] S. Seltzer, “Tables of X-Ray Mass Attenuation Coefficients and Mass Energy-Absorption Coefficients, NIST Standard Reference Database 126.” National Institute of Standards and Technology, 1995, doi: 10.18434/t4d01f.

[11] F. Stacul *et al.*, “Contrast induced nephropathy: updated ESUR Contrast Media Safety Committee guidelines,” *Eur. Radiol.*, vol. 21, no. 12, pp. 2527–2541, Dec. 2011, doi: 10.1007/s00330-011-2225-0.

[12] H. Lusic and M. W. Grinstaff, “X-ray-Computed Tomography Contrast Agents,” *Chem. Rev.*, vol. 113, no. 3, pp. 1641–1666, Mar. 2013, doi: 10.1021/cr200358s.

[13] E. Archibald, “X-ray Demonstration of Pulmonary Changes in Tuberculosis by Lipiodol Injection,” *Can. Med. Assoc. J.*, vol. 15, no. 10, pp. 1000–1002, Oct. 1925.

[14] K. Iwai, H. Maeda, and T. Konno, “Use of oily contrast medium for selective drug targeting to tumor: enhanced therapeutic effect and X-ray image,” *Cancer Res.*, vol. 44, no. 5, pp. 2115–2121, May 1984.

[15] F. Plouraboue, P. Cloetens, C. Fonta, A. Steyer, F. Lauwers, and J.-P. Marc-Vergnes, “X-ray high-resolution vascular network imaging,” *J. Microsc.*, vol. 215, no. 2, pp. 139–148, Aug. 2004, doi: 10.1111/j.0022-2720.2004.01362.x.

[16] B. Müller, J. Fischer, U. Dietz, P. J. Thurner, and F. Beckmann, “Blood vessel staining in the myocardium for 3D visualization down to the smallest capillaries,” *Nucl. Instrum. Methods Phys. Res. Sect. B Beam Interact. Mater. At.*, vol. 246, no. 1, pp. 254–261, May 2006, doi: 10.1016/j.nimb.2005.12.048.

[17] G. Margaritondo, “A Primer in Synchrotron Radiation: Everything You Wanted to Know about SEX (Synchrotron Emission of X-rays) but Were Afraid to Ask,” *J. Synchrotron Radiat.*, vol. 2, no. 3, pp. 148–154, May 1995, doi: 10.1107/S0909049595001701.

[18] G. Margaritondo, Y. Hwu, and G. Tromba, “Synchrotron light: From basics to coherence and coherence-related applications,” p. 29.

[19] C. Rau *et al.*, “Fast Multi-scale imaging using the Beamline I13L at the Diamond Light Source,” in *Developments in X-Ray Tomography XII*, San Diego, United States, Oct. 2019, p. 68, doi: 10.1117/12.2543405.
[20] E. Pasotti, “Sorting through the Trash: The Waste Management Crisis in Southern Italy,” *South Eur. Soc. Polit.*, vol. 15, no. 2, pp. 289–307, Jun. 2010, doi: 10.1080/13608740903497733.
[21] R. Rodewald, “Porous substructure of the glomerular slit diaphragm in the rat and mouse,” *J. Cell Biol.*, vol. 60, no. 2, pp. 423–433, Feb. 1974, doi: 10.1083/jcb.60.2.423.
[22] J. R. Pappenheimer, E. M. Renkin, and L. M. Borrero, “Filtration, Diffusion and Molecular Sieving Through Peripheral Capillary Membranes: A Contribution to the Pore Theory of Capillary Permeability,” *Am. J. Physiol.-Leg. Content*, vol. 167, no. 1, pp. 13–46, Sep. 1951, doi: 10.1152/ajplegacy.1951.167.1.13.
[23] M. Gekle, “Renal tubule albumin transport,” *Annu. Rev. Physiol.*, vol. 67, no. 1, pp. 573–594, Mar. 2005, doi: 10.1146/annurev.physiol.67.031103.154845.
[24] W. Kuo and V. Kurtcuoglu, “Renal arteriovenous oxygen shunting,” *Curr. Opin. Nephrol. Hypertens.*, vol. 26, no. 4, pp. 290–295, Jul. 2017, doi: 10.1097/MNH.0000000000000332.
[25] D. A. Nordsletten, S. Blackett, M. D. Bentley, E. L. Ritman, and N. P. Smith, “Structural morphology of renal vasculature,” *Am. J. Physiol. Heart Circ. Physiol.*, vol. 291, no. 1, pp. H296-309, Jul. 2006, doi: 10.1152/ajpheart.00814.2005.
[26] Garcia-Sanz Agustin, Rodriguez-Barbero Alicia, Bentley Michael D., Ritman Erik L., and Romero J. Carlos, “Three-Dimensional Microcomputed Tomography of Renal Vasculature in Rats,” *Hypertension*, vol. 31, no. 1, pp. 440–444, Jan. 1998, doi: 10.1161/01.HYP.31.1.440.
[27] F. Imeri *et al.*, “Generation of renal Epo-producing cell lines by conditional gene tagging reveals rapid HIF-2 driven Epo kinetics, cell autonomous feedback regulation, and a telocyte phenotype,” *Kidney Int.*, vol. 95, no. 2, pp. 375–387, Feb. 2019, doi: 10.1016/j.kint.2018.08.043.
[28] K. Chung and K. Deisseroth, “CLARITY for mapping the nervous system,” *Nat. Methods*, vol. 10, no. 6, pp. 508–513, Jun. 2013, doi: 10.1038/nmeth.2481.
[29] B. Yang *et al.*, “Single-cell phenotyping within transparent intact tissue through whole-body clearing,” *Cell*, vol. 158, no. 4, pp. 945–958, Aug. 2014, doi: 10.1016/j.cell.2014.07.017.
[30] F. F. Voigt *et al.*, “The mesoSPIM initiative: open-source light-sheet mesoscopes for imaging in cleared tissue,” Neuroscience, preprint, Mar. 2019. doi: 10.1101/577122.
[31] L. Bergeron, M. Tang, and S. F. Morris, “A Review of Vascular Injection Techniques for the Study of Perforator Flaps:,” *Plast. Reconstr. Surg.*, vol. 117, no. 6, pp. 2050–2057, May 2006, doi: 10.1097/01.prs.0000218321.36450.9b.
[32] R. Beeuwkes, “Efferent vascular patterns and early vascular-tubular relations in the dog kidney,” *Am. J. Physiol.-Leg. Content*, vol. 221, no. 5, pp. 1361–1374, Nov. 1971, doi: 10.1152/ajplegacy.1971.221.5.1361.
[33] F. D. Verli, T. R. Rossi-Schneider, F. L. Schneider, L. S. Yurgel, and M. A. L. de Souza, “Vascular Corrosion Casting Technique Steps,” *Scanning*, vol. 29, no. 3, pp. 128–132, May 2007, doi: 10.1002/sca.20051.
[34] S. Heinzer *et al.*, “Hierarchical microimaging for multiscale analysis of large vascular networks,” *NeuroImage*, vol. 32, no. 2, pp. 626–636, Aug. 2006, doi: 10.1016/j.neuroimage.2006.03.043.
[35] T. Krucker, A. Lang, and E. P. Meyer, “New polyurethane-based material for vascular corrosion casting with improved physical and imaging characteristics,” *Microsc. Res. Tech.*, vol. 69, no. 2, pp. 138–147, Feb. 2006, doi: 10.1002/jemt.20263.
[36] J. Ehling *et al.*, “Quantitative Micro-Computed Tomography Imaging of Vascular Dysfunction in Progressive Kidney Diseases,” *J Am Soc Nephrol*, vol. 27, no. 2, pp. 520–32, Feb. 2016, doi: 10.1681/ASN.2015020204.

[37] S. X. Vasquez *et al.*, “Optimization of microCT imaging and blood vessel diameter quantitation of preclinical specimen vasculature with radiopaque polymer injection medium,” *PLoS One*, vol. 6, no. 4, p. e19099, Apr. 2011, doi: 10.1371/journal.pone.0019099.
[38] J. Czogalla, F. Schweda, and J. Loffing, “The Mouse Isolated Perfused Kidney Technique,” *J. Vis. Exp.*, no. 117, p. 54712, Nov. 2016, doi: 10.3791/54712.
[39] R. Hlushchuk *et al.*, “Cutting-edge microangio-CT: new dimensions in vascular imaging and kidney morphometry,” *Am J Physiol Ren. Physiol*, vol. 314, no. 3, pp. F493–F499, Mar. 2018, doi: 10.1152/ajprenal.00099.2017.
[40] K. M. Hazenfield and D. D. Smeak, “In vitro holding security of six friction knots used as a first throw in the creation of a vascular ligation,” *J. Am. Vet. Med. Assoc.*, vol. 245, no. 5, pp. 571–577, Sep. 2014, doi: 10.2460/javma.245.5.571.
[41] A. Mirone, E. Brun, E. Gouillart, P. Tafforeau, and J. Kieffer, “The PyHST2 hybrid distributed code for high speed tomographic reconstruction with iterative reconstruction and a priori knowledge capabilities,” *Nucl. Instrum. Methods Phys. Res. Sect. B Beam Interact. Mater. At.*, vol. 324, pp. 41–48, Apr. 2014, doi: 10.1016/j.nimb.2013.09.030.
[42] D. Paganin, S. C. Mayo, T. E. Gureyev, P. R. Miller, and S. W. Wilkins, “Simultaneous phase and amplitude extraction from a single defocused image of a homogeneous object,” *J. Microsc.*, vol. 206, no. 1, pp. 33–40, Apr. 2002, doi: 10.1046/j.1365-2818.2002.01010.x.
[43] I. J. Murawski, R. W. Maina, and I. R. Gupta, “The relationship between nephron number, kidney size and body weight in two inbred mouse strains,” *Organogenesis*, vol. 6, no. 3, pp. 189–194, Sep. 2010, doi: 10.4161/org.6.3.12125.
[44] L. Schaad *et al.*, “Correlative Imaging of the Murine Hind Limb Vasculature and Muscle Tissue by MicroCT and Light Microscopy,” *Sci. Rep.*, vol. 7, no. 1, p. 41842, Mar. 2017, doi: 10.1038/srep41842.
[45] W. Kuo, G. Schulz, B. Müller, and V. Kurtcuoglu, “Evaluation of metal nanoparticle- and plastic resin-based x-ray contrast agents for kidney capillary imaging,” in *Developments in X-Ray Tomography XII*, San Diego, United States, Sep. 2019, p. 23, doi: 10.1117/12.2529414.
[46] N. A. Le, W. Kuo, B. Müller, V. Kurtcuoglu, and B. Spingler, “Crosslinkable polymeric contrast agent for high-resolution X-ray imaging of the vascular system,” *Chem. Commun.*, vol. 56, no. 44, pp. 5885–5888, 2020, doi: 10.1039/C9CC09883F.
[47] B. S. Gardiner, D. W. Smith, P. M. O’Connor, and R. G. Evans, “A mathematical model of diffusional shunting of oxygen from arteries to veins in the kidney,” *Am. J. Physiol.-Ren. Physiol.*, vol. 300, no. 6, pp. F1339–F1352, Jun. 2011, doi: 10.1152/ajprenal.00544.2010.
[48] U. Olgac and V. Kurtcuoglu, “Renal oxygenation: preglomerular vasculature is an unlikely contributor to renal oxygen shunting,” *Am. J. Physiol.-Ren. Physiol.*, vol. 308, no. 7, pp. F671–F688, Apr. 2015, doi: 10.1152/ajprenal.00551.2014.
[49] U. Olgac and V. Kurtcuoglu, “The Bohr Effect Is Not a Likely Promoter of Renal Preglomerular Oxygen Shunting,” *Front Physiol*, vol. 7, p. 482, 2016, doi: 10.3389/fphys.2016.00482.
[50] D. S. Perrien *et al.*, “Novel methods for microCT-based analyses of vasculature in the renal cortex reveal a loss of perfusable arterioles and glomeruli in eNOS-/- mice,” *BMC Nephrol.*, vol. 17, no. 1, p. 24, Dec. 2016, doi: 10.1186/s12882-016-0235-5.
[51] R. Wagner, D. Van Loo, F. Hossler, K. Czymmek, E. Pauwels, and L. Van Hoorebeke, “High-Resolution Imaging of Kidney Vascular Corrosion Casts with Nano-CT,” *Microsc. Microanal.*, vol. 17, no. 2, pp. 215–219, Apr. 2011, doi: 10.1017/S1431927610094201.
[52] M. C. Ortiz *et al.*, “Microcomputed tomography of kidneys following chronic bile duct ligation,” *Kidney Int.*, vol. 58, no. 4, pp. 1632–1640, Oct. 2000, doi: 10.1111/j.1523-1755.2000.00324.x.
[53] N. T. Vo, R. C. Atwood, and M. Drakopoulos, “Preprocessing techniques for removing artifacts in synchrotron-based tomographic images,” in *Developments in X-Ray Tomography XII*, San Diego, United States, Sep. 2019, p. 6, doi: 10.1117/12.2530324.

[54] L. C. P. Croton, G. Ruben, K. S. Morgan, D. M. Paganin, and M. J. Kitchen, "Ring artifact suppression in X-ray computed tomography using a simple, pixel-wise response correction," *Opt. Express*, vol. 27, no. 10, p. 14231, May 2019, doi: 10.1364/OE.27.014231.
[55] T. Weitkamp, D. Haas, D. Wegrzynek, and A. Rack, "*ANKAphase*: software for single-distance phase retrieval from inline X-ray phase-contrast radiographs," *J. Synchrotron Radiat.*, vol. 18, no. 4, pp. 617–629, Jul. 2011, doi: 10.1107/S0909049511002895.
[56] G. Rodgers *et al.*, "Optimizing contrast and spatial resolution in hard x-ray tomography of medically relevant tissues," *Appl. Phys. Lett.*, vol. 116, no. 2, p. 023702, Jan. 2020, doi: 10.1063/1.5133742.
[57] N. S. Joshi, P. N. Bansal, R. C. Stewart, B. D. Snyder, and M. W. Grinstaff, "Effect of Contrast Agent Charge on Visualization of Articular Cartilage Using Computed Tomography: Exploiting Electrostatic Interactions for Improved Sensitivity," *J. Am. Chem. Soc.*, vol. 131, no. 37, pp. 13234–13235, Sep. 2009, doi: 10.1021/ja9053306.
[58] Y. Fu *et al.*, "Dendritic Iodinated Contrast Agents with PEG-Cores for CT Imaging: Synthesis and Preliminary Characterization," *Bioconjug. Chem.*, vol. 17, no. 4, pp. 1043–1056, Jul. 2006, doi: 10.1021/bc060019c.